BULLETIN OF THE MINERAL RESEARCH AND EXPLORATION

2024 174 ISSN : 0026-4563
E-ISSN : 2651-3048

CONTENTS

Research Articles

LOCATION OF MANAGEMENT
Bilimsel Dokümantasyon ve Tanıtma Dairesi Başkanlığı
Maden Tetkik ve Arama Genel Müdürlüğü
Çukurambar Mahallesi
Dumlupınar Bulvarı No: 11 06530
Çankaya/ANKARA
e-mail: bilimsel_dairesi@mta.gov.tr

Bull. Min. Res. Exp. is indexed and abstracted in TR Dizin, Emerging Source Citation Index (ESCI), Scopus, The ICI Journals Master List (Copernicus), Directory of Open Access Journals (DOAJ), Open Academic Journals Index (OAJI), Georef, MIAR, EBSCO and Zoological Record.

The Bulletin of the Mineral Research and Exploration is published in three issues in a year. Each volume is published in Turkish and English in pdf format on the website of Bulletin of the Mineral Research and Exploration and English issue published in print. The English volume of the "Bulletin of the Mineral Research and Exploration" can be obtained from "BDT Department" free of charge, either directly or ordered by adding postage fee from the correspondence address. Typesetting and printing operations are carried out and followed by the Publication Service of the Scientific Documentation and Publicity Department. e-mail: bilimsel_dairesi@mta.gov.tr

The section of "notes to the authors", format, copyright and other information can be obtained from www.mta.gov.tr as PDF files.

Printed Date: 19.08.2024
Printing House: Kuban Matbaacılık - İvedik Organize Sanayi Matbaacılar Sitesi 1514. Sokak No: 20
Phone: 0312 395 2070 • Fax: 0312 395 3723 • www.kubanmatbaa.com
Periodical
ISSN: 0026-4563
E-ISSN: 2651-3048

Bulletin of the Mineral Research and Exploration

http://bulletin.mta.gov.tr

Determination of Atterberg Limits using the vane shear test method

Kamil KAYABALI[a*], H. B. NAGARAJ[b], Deniz YILMAZ[a] and Muhammet BEYHAN[a]

[a] *Ankara University, School of Engineering, Geological Engineering Department, Ankara, Türkiye*
[b] *B.M.S College of Engineering, Bangalore, India*

Research Article

Keywords:
Liquid Limit, Plastic Limit, Undrained Shear Strength, Vane Shear Test, Atterberg Limits.

Received Date: 14.12.2022
Accepted Date: 18.09.2023

ABSTRACT

Atterberg limits are important index parameters used to classify soils for various engineering applications. Engineering properties of soils are predicted through simple correlations with index properties and thereby the engineering behavior of soils are qualitatively assessed. There are two popular methods of determining liquid limit, and plastic limit is commonly determined adopting rolling thread methods. To avoid operator related variations in determining plastic limit by conventional method, some researchers have explored using cone method as an alternative. However, there is no consensus about the depth of penetration to reckon the end of plastic state. Though various other test methods have been developed to determine plastic limit (like roll plate device), cone penetration with its limitation of determining plastic limit, is the only method to determine both liquid and plastic limit of soils. Since laboratory vane shear test is a simple and reliable method of determining undrained strength of fine-grained soils, the authors have explored to determine both liquid and plastic limits through correlations developed between undrained strength and water content over a range of consistencies between liquid and plastic states. This would eliminate determining liquid and plastic limit separately without sacrificing the reliability of results.

1. Introduction

Atterberg's original proposal for consistency limits (Atterberg, 1911) included seven qualitative limits, of which only two found more common usage in geotechnical engineering, namely liquid limit (LL) and plastic limit (PL). LL is the water content at which the soil starts to flow under its own weight. PL is the onset of soil brittleness or the water content corresponding to the transition from plastic- to semi-solid state.

The LL and PL, either individually or in the form of plasticity index (PI) have been used in a number of empirical correlations and can be helpful for preliminary estimates in the early stages of design. Such applications include classification of soils (Feng, 2004*a*), prediction of engineering properties like undrained shear strength (Skempton, 1954), consolidation parameters [e.g., the coefficient of compression, coefficient of recompression, preconsolidation pressure, settlement (Terzaghi and Peck, 1967; Azzouz et al., 1976; Leonards, 1976; Nagaraj and Srinivasa Murthy, 1986)], and determination of soil penetration resistance (Stroud, 1974) and the like.

The most common techniques to determine the liquid limit are the Casagrande cup and cone penetration test; and plastic limit are the thread rolling methods. Determination of LL by the Casagrande cup

Citation Info: Kayabalı, K., Nagaraj, H. B., Yılmaz, D., Beyhan, M. 2024. Determination of Atterberg Limits using the vane shear test method. Bulletin of the Mineral Research and Exploration 174, 1-10. https://doi.org/10.19111/bulletinofmre.1362349

**Corresponding author: Kamil KAYABALI, kayabali@ankara.edu.tr*

method involves a number of uncertainties (see, for instance, Wroth and Wood, 1978; Lee and Freeman, 2007; Kayabali and Tüfenkçi, 2010*a*). The fall cone method is advantageous in comparison with Casagrande's method as it has less operator dependent variations and has good reproducibility of results. It also gives much lower standard deviation of the results than the cup test when identical samples are tested at multiple laboratories (Sherwood and Ryley, 1970; Haigh, 2012). Thus, there is not much debate on the uncertainties of fall cone tests. However, determination of plastic limit by the thread rolling method has always been a point of concern due to its operator related variations. Hence, a number of attempts have been made to determine the plastic limit using the fall cone method. Some of such attempts include the works of Towner (1973), Campbell (1976, 1983), Wood and Wroth (1978), Campbell et al. (1980), Feng (2000, 2001), Belviso et al. (1985), Rao (1987), Harison (1988), Sharma and Bora (2003), Feng (2004*a*,*b*), Al-Dahlaki and Al-Sharify (2008), Rashid et al. (2008), Lee and Freeman (2009), Sivakumar et al. (2009, 2014). Shimobe (2010), using various types of cones, concluded that the extended fall cone method is capable of simultaneously determining both the liquid and plastic limits. He further stated that the fall cone test can also be used to determine the liquidity index as a state quantity, the undrained shear strength, and sensitivity of soils in terms of the cone penetration. Extrusion method was also employed as a tool to determine the consistency limits of fine-grained soils. Timar (1974), using the direct extrusion method, obtained partial success towards determining the two most common consistency limits. Whyte (1982), based on the results of preliminary reverse extrusion (RX) tests on a low plasticity clay, showed that RX is a reliable method for determining soil plasticity; also, that it is simple, rapid and economical. Kayabali and Tüfenkçi (2010*b*) showed that the RX test can provide a reasonable degree of success in determining LL and PL and that the RX test eliminates most of the uncertainties involved in both the conventional PL and LL tests, most importantly those that are operator dependent. Kayabali et al. (2016) developed a testing apparatus called the mud press machine (MPM). Using the test results of 275 soil samples, the authors of the study showed that Atterberg limits can be determined in a more rational and quantifiable basis using the MPM.

Vane shear test is one of the most common tools to assess the undrained shear strength of cohesive soils. It can be employed both in the laboratory and in the field. It was originated in Sweden in the early 1900s and became popular towards 1940s. Major advantages of the test are: ease to conduct, simplicity, robustness and speed. It also allows the measurement of peak and residual strength, and therefore, the sensitivity of cohesive soils. It provides an indirect assessment of over-consolidation ratio of a soil deposit as well (Ameratunga et al., 2016). It is recommended to be used on soils with an undrained shear strength less than 100 kPa (American Society of Testing Materials, 2000). The miniature vane test employing four springs with different stiffnesses is capable of measuring undrained shear strength of soils from a few kPa to about 100 kPa, which is the common range for the plastic behavior between the liquid and the plastic limit of fine-grained soils.

Kyambadde (2010) stated that, although VST is not the most attractive method, it provides a degree of validation of liquid limit data where vane shear strength relationships are available.

The scope of this investigation is to illustrate the usability of miniature vane shear test to determine the two major Atterberg limits.

2. Materials and Methods

One hundred soil samples were subjected to Atterberg limits and vane shear tests. Majority of the soil samples used in the study were residual soils produced by weathering of igneous rocks and few soils were lacustrine deposits obtained in the vicinity of Ankara, Türkiye. The soils selected to be used in this study were such that they had a wide range of plasticity. The liquid limits ranged from 23 to 106, and the plasticity index ranged from 7.5 to 50. The positions of soil samples on the plasticity chart are presented in Figure 1.

The various equipment employed for this experimental research includes a fall-cone, a roll-plate device (Figure 3) and a miniature vane shear apparatus

which are respectively shown in Figures 2 to 4. The device for the vane shear test (Figure 4) measures the torque by electronic transducers instead of by springs. It facilitates measurement of torque up to 3.0 N.m. The measurable shear stress using this servo-controlled VST device ranges from 0.1-466 kPa when the blade dimensions are 12.7 mm x 12.7 mm. The rotational speed ranges from 0.001-1200 degrees per minute.

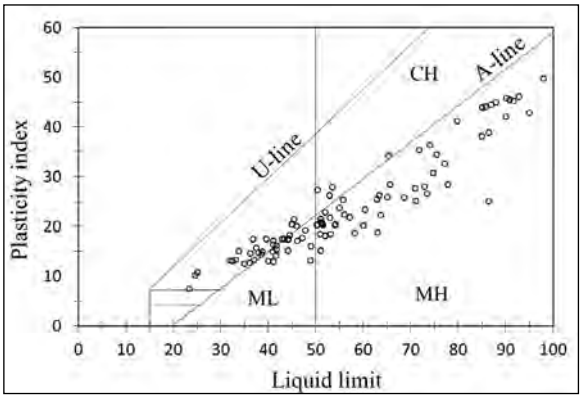

Figure 1- Positions of soil samples on the Casagrande chart.

Figure 2- The fall cone device used in this investigation.

Figure 3- Roll-plate device for plastic limit tests.

Figure 4- Miniature vane shear test device.

All soil specimens were first sieved through an ASTM#40 mesh (American Society for Testing Materials, 2005). Then, sufficient quantity of water was added and the soil was mixed thoroughly before transferring into polythene covers. The mixed soil samples in polythene covers were properly labelled, and were placed in desiccator filled with water at the bottom to maintain 100% humidity. The samples were left for at least 20 h for proper saturation. For each of the soil samples the liquid limit was determined by using a fall-cone device (BS1377-1990). At least five trial points were obtained by varying the water content from dry side to wet side and the corresponding cone penetration was recorded. The range of cone penetration was targeted to be between 15 mm to 25 mm. Water content corresponding to 20 mm penetration was reckoned as the liquid limit of soil (British Standards Institution, 1990). Plastic limit of all the soils was evaluated as per the standard procedure outlined in ASTM D4318-05 Standard (American Society for Testing Materials, 2005) using the roll-plate device. Tests were repeated at least 5 times and the average of five plastic limit tests was taken to represent the soil subjected to the roll-plate test. The test results of liquid limit and plastic limit of all the soils are tabulated in Table 1.

Table 1- The results of Atterberg Limits tests and vane shear tests (LL: liquid limit, PL: plastic limit, PI: plasticity index, USCS: Unified Soil Classification System, a and b: coefficients obtained from the curve fitted to the semi-logarithmic experimental curve of the vane shear test, R^2: the regression coefficient, ML: silt of low plasticity, MH: silt of high plasticity, CL: clay of low plasticity, CH: clay of high plasticity).

No.	LL	PL	PI	USCS	a	b	R^2
1	51.1	35.9	15.2	MH	2E+08	0.377	0.976
2	63.0	44.2	18.8	MH	5.E+07	0.287	0.970
3	77.2	44.6	32.6	MH	14909	0.118	0.976
4	32.4	19.3	13.1	CL	12109	0.271	0.988
5	60.4	37.0	23.4	MH	5968	0.109	0.986
6	43.3	25.8	17.5	CL	44731	0.246	0.988
7	41.0	28.0	13.0	ML	163178	0.275	0.950
8	40.0	26.9	13.1	ML	211404	0.288	0.988
9	47.1	29.4	17.7	ML	21980	0.187	0.980
10	41.7	25.6	16.1	CL	63439	0.259	0.991
11	37.0	23.7	13.3	CL	8959	0.242	0.998
12	42.9	25.4	17.5	CL	17698	0.219	0.990
13	36.2	21.6	14.6	CL	16136	0.25	0.985
14	44.5	26.3	18.2	CL	31014	0.228	0.999
15	51.3	30.5	20.8	MH	8595	0.145	0.978
16	36.0	23.3	12.7	CL	24575	0.255	0.998
17	35.0	22.5	12.5	CL	32018	0.26	0.998
18	41.0	23.9	17.1	CL	96358	0.277	0.993
19	23.3	15.8	7.5	CL	26556	0.323	0.998
20	52.0	29.2	22.8	MH	16740	0.169	0.922
21	86.5	47.6	38.9	MH	6093	0.086	0.966
22	46.0	25.9	20.1	CL	7303	0.166	0.985
23	39.6	22.1	17.5	CL	14016	0.226	0.992
24	45.4	24.0	21.4	CL	6445	0.175	0.998
25	65.6	37.2	28.4	MH	171511	0.192	0.972
26	75.4	40.9	34.5	MH	8817	0.112	0.992
27	72.9	44.9	28.0	MH	5341	0.096	0.971
28	103	62.2	40.8	MH	7639	0.074	0.943
29	41.7	26.3	15.4	ML	22955	0.22	0.997
30	46.1	29.0	17.1	ML	83707	0.246	0.981
31	54.1	33.7	20.4	MH	20170	0.166	0.997
32	56.1	33.6	22.5	MH	88339	0.214	0.996
33	51.5	31.2	20.3	MH	25663	0.192	0.978
34	74.7	43.9	30.8	MH	916	0.058	0.915
35	45.0	24.6	20.4	CL	7024	0.174	0.996
36	68.6	42.8	25.8	MH	34188	0.135	0.967
37	58.2	39.5	18.7	MH	54624	0.163	0.995
38	60.0	39.8	20.2	MH	344266	0.205	0.983
39	50.4	23.1	27.3	CH	3019	0.149	0.990

Table 1- Continued.

No.	LL	PL	PI	USCS	a	b	R^2
40	51.0	30.1	20.9	MH	104103	0.214	0.967
41	95.0	52.1	42.9	MH	2731	0.073	0.996
42	85.0	46.9	38.1	MH	3649	0.084	0.989
43	73.5	46.9	26.6	MH	120860	0.154	0.970
44	71.1	46.0	25.1	MH	11807	0.116	0.990
45	77.8	49.4	28.4	MH	1.E+06	0.174	0.991
46	101	62.2	38.3	MH	922631	0.145	0.934
47	48.9	35.7	13.2	ML	1.E+06	0.263	0.998
48	36.8	19.3	17.5	CL	3165	0.191	0.992
49	33.8	18.8	15.0	CL	6551	0.233	0.992
50	32.0	18.8	13.2	CL	24462	0.311	0.996
51	65.3	31.0	34.3	CH	2761	0.116	0.997
52	57.2	35.4	21.8	MH	56743	0.186	0.976
53	41.6	27.4	14.2	ML	6773	0.165	0.997
54	49.0	33.0	16.0	ML	883887	0.259	0.997
55	44.1	26.8	17.3	ML	75389	0.235	0.993
56	53.5	25.6	27.9	CH	8660	0.171	0.981
57	33.1	19.8	13.3	CL	10956	0.26	0.997
58	38.7	23.8	14.9	CL	1979	0.159	0.999
59	37.5	21.8	15.7	CL	4517	0.208	0.997
60	53.0	31.3	21.7	MH	81326	0.211	0.994
61	54.0	33.7	20.3	MH	424	0.067	0.941
62	85.1	41.1	44.0	MH	10705	0.108	0.986
63	62.9	37.4	25.5	MH	35110	0.161	0.996
64	55.8	30.4	25.4	MH	24486	0.178	0.987
65	38.5	24.1	14.4	CL	1922	0.161	0.993
66	44.1	28.9	15.2	ML	62961	0.229	0.994
67	63.4	37.1	26.3	MH	9868	0.133	0.991
68	44.3	26.8	17.5	ML	45369	0.222	0.991
69	55.0	31.3	23.7	MH	14609	0.159	0.989
70	51.1	29.6	21.5	MH	18762	0.174	0.993
71	52.0	33.9	18.1	MH	2.E+06	0.275	0.987
72	41.0	24.6	16.4	CL	62589	0.261	0.996
73	37.9	23.2	14.7	CL	2567	0.178	0.995
74	65.1	39.2	25.9	MH	164541	0.184	0.986
75	50.2	29.9	20.3	MH	26825	0.194	0.984
76	63.7	41.4	22.3	MH	8.E+06	0.258	0.980
77	40.9	26.0	14.9	ML	136616	0.281	0.988
78	50.9	32.5	18.4	MH	36741	0.191	0.998
79	71.8	36.4	35.4	MH	283563	0.202	0.984

Table 1- Continued.

No.	LL	PL	PI	USCS	a	b	R^2
80	53.1	34.6	18.5	MH	853309	0.247	0.986
81	47.8	28.6	19.2	ML	18210	0.181	0.977
82	52.9	26.7	26.2	CH	5226	0.149	0.984
83	86.5	61.5	25.0	MH	174311	0.127	0.996
84	106	73.8	32.4	MH	49136	0.092	0.997
85	91.7	46.4	45.3	MH	1707	0.072	0.960
86	51.4	30.9	20.5	MH	9713	0.16	0.993
87	102	66.7	35.1	MH	39473	0.098	0.995
88	70.9	43.2	27.7	MH	4576	0.108	0.985
89	24.6	14.4	10.2	CL	9276	0.353	0.999
90	25.1	14.4	10.7	CL	4485	0.271	0.978
91	74.0	37.7	36.3	MH	2981	0.094	0.992
92	79.8	38.6	41.2	MH	4561	0.101	0.992
93	85.8	41.7	44.1	MH	2371	0.085	0.990
94	86.9	42.4	44.5	MH	5409	0.097	0.989
95	88.0	43.1	44.9	MH	3884	0.088	0.991
96	90.2	44.4	45.8	MH	2425	0.078	0.995
97	90.8	45.3	45.5	MH	4599	0.089	0.997
98	92.8	46.7	46.1	MH	2475	0.075	0.996
99	90.0	47.9	42.1	MH	4725	0.084	0.990
100	98.0	48.2	49.8	MH	1905	0.067	0.993

The vane shear tests were performed in accordance with the ASTM D4648-00 Standard (American Society of Testing Materials, 2000). Each of the soils used in the study was prepared in a similar way as done for the liquid limit and plastic limit test. The test procedure involved conducting five trials of vane shear tests using the saturated soil having a consistency between the liquid limit and plastic limit. The measured torques were converted to undrained shear strengths using the relationships given in Equations 1 and 2 (American Society of Testing Materials, 2000):

$$T = \tau \times K \quad (1)$$

$$K = \frac{\pi D^2}{2x10^6}\left[1 + \frac{D}{3H}\right] \quad (2)$$

where T = torque (N.m), τ = undrained shear strength (N/m^2), K = vane blade constant (m^3), D = measured diameter of the vane (mm) and H = measure height of the vane (mm). The measured undrained shear strengths with respective water contents were plotted in a semi-logarithmic plot. One such typical plot for soil No. 58 is shown in Figure 5, from which an equation was obtained in the following form:

$$y = a \exp^b \quad (3)$$

where y is the undrained shear strength (s_u) and a and b are the regression coefficients.

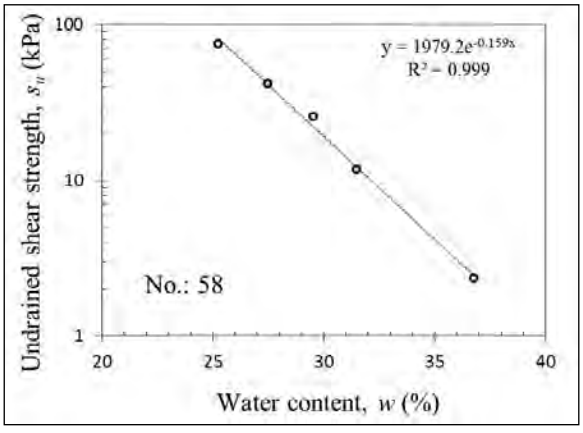

Figure 5- A sample plot constructed upon VST test results.

3. Experimental Results

From Table 1, it can be seen that of the 100 samples collected from different locations, 57 soils are classified as MH (silt of high plasticity), 26 are classified as CL (clay of low plasticity), 13 as ML (silt of low plasticity) and 4 as CH (clay of high plasticity). Thus, the soils covered a wide range of plasticities. As mentioned earlier, each soil sample was subjected to five vane shear tests at different water contents. Thus, the resulting number of undrained shear strength and water content pairs is 500 for 100 soil samples. Listing of such a large data occupies a great deal of space; so, to save space**,** the results of vane shear tests are presented only in terms of a and b coefficients as presented in Table 1.

In order to explore for a possible correlation between undrained shear strengths obtained from the miniature vane shear test and Atterberg limits, the numerical data presented in Table 1 was subjected to a series of statistical analyses. To show if it was possible to determine the liquid limit in terms of the undrained shear strength and water content, a multiple regression analysis was performed using the software DATAFIT (DATAFIT, 2008). This way a series of both complex and rather simple empirical equations were obtained defining the LL in terms of s_u and w. One of the simplest of such relationships are selected and provided as follows:

$$LL = 0.902\ (w^{0.997})\ s_u^{\ 0.138} \quad (R^2 = 0.92) \qquad (4)$$

where s_u is in kPa and w is in %. The maximum coefficient of correlation was 0.95 for highly complex polynomial equations which involved many constants. As a next step, Equation (4) was employed to predict the liquid limit empirically. Figure 6 is a plot of the empirically-predicted liquid limits with those determined experimentally using the fall-cone method. The deviations from the measured liquid limits were evaluated statistically in terms of absolute percent errors. Figure 7 is the histogram of absolute percent errors of the measured liquid limits when determining the liquid limit using the predictive Equation 4. The overall absolute percent error is 6.8%. A quick glimpse on Figure 7 reveals that the amount of error for the predicted liquid limits of 80% of all soils is within ±10%.

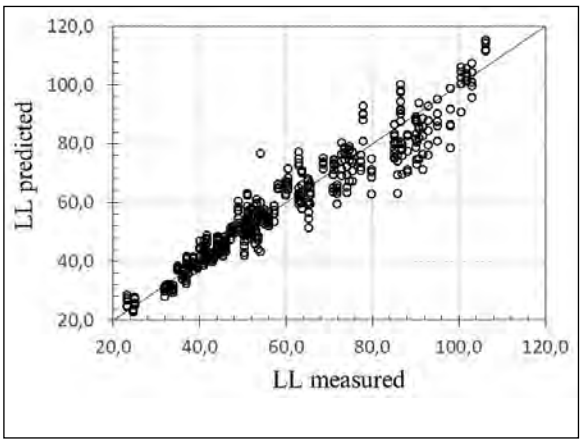

Figure 6- Comparison between the predicted liquid limits versus the measured liquid limits.

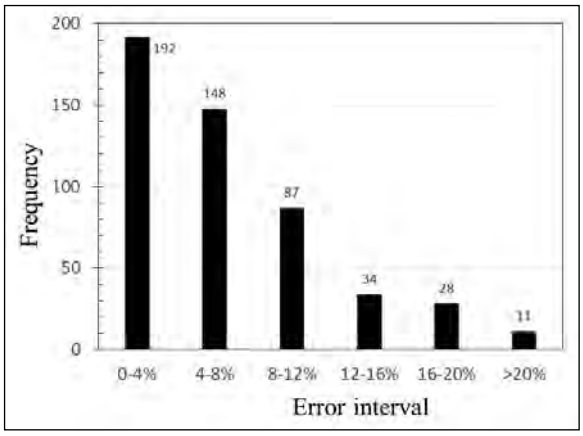

Figure 7- Histogram of absolute errors of predicted liquid limits.

Similarly, 500 sets of water content, undrained shear strength and plastic limit were also subjected to a multiple regression analysis to predict the plastic limit in terms of water content and undrained shear strength. The following simple version of the empirical equation was obtained:

$$PL = 0.609\ (w^{0.959})\ s_u^{\ 0.139} \quad (R^2 = 0.95) \qquad (5)$$

In the next step, Equation (5) was employed to predict the plastic limit empirically. Figure 8 is a plot of the empirically-predicted plastic limits with those determined experimentally using the roll-plate method. The deviations from the measured plastic limits were evaluated statistically in terms of absolute percent errors. Figure 9 is the histogram of absolute percent errors of the measured plastic limits when determining the plastic limit using the predictive Equation 5. The overall absolute percent error is 5.3%.

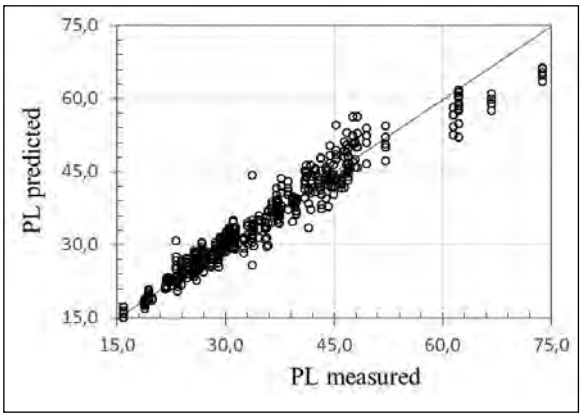

Figure 8- Comparison between the predicted plastic limits versus the measured plastic limits.

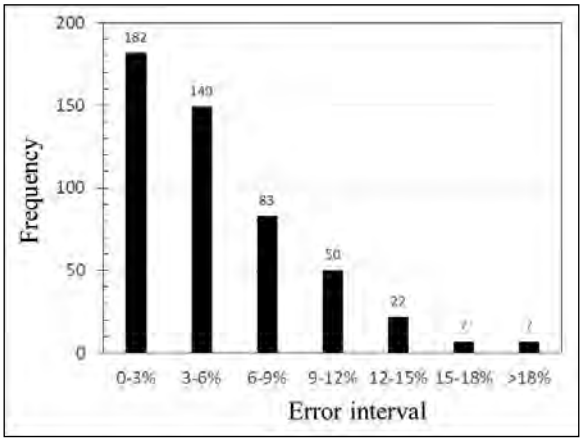

Figure 9- Histogram of absolute errors of predicted plastic limits.

A quick glimpse on Figure 9 reveals that the amount of error for the predicted plastic limits of 86% of all soils is within ±10%.

Equations 4 and 5 are found very useful in that they can be used to predict the two Atterberg limits, namely the liquid limit and plastic limit based on a single trial of VST test which is done at any water content between plastic limit and liquid limit. To avoid error introduced by a single trial of VST test in predicting liquid and plastic limits, it is better to use the results of at least a few trials of vane shear tests conducted at different water contents between PL and LL**,** so that the coefficients a and b are obtained.

The coefficients a and b as presented in Table 1 for each soil sample were also subjected to multiple regression analyses along with the Atterberg limits data. One hundred sets of a and b coefficients and the liquid limit yield the following short version of the predictive equations:

$$LL = 3.62\ (a^{0.106})\ b^{-0.92} \qquad (R^2 = 0.92) \qquad (6)$$

Similarly, plastic limit is defined in terms of a and b coefficients:

$$PL = 1.72\ (a^{0.129})\ b^{-0.91} \qquad (R^2 = 0.92) \qquad (7)$$

The overall absolute percent error between the measured and predicted the liquid limits is 6.3% and that for plastic limit, it is 3.9%, which implies that the Atterberg limits are predicted with a slightly higher degree of accuracy than those predicted by Equations 4 and 5 which make use of water content and undrained shear strength.

4. Results

In order to eliminate determining the liquid and plastic limit separately without sacrificing the reliability of estimating these limiting water contents, the authors have explored to determine both these limits using a laboratory vane shear test through the correlations developed between the undrained strength and water content over a range of consistency between the liquid and plastic states. From the vane test results of 100 natural soils used in this study having a wide range of plasticity properties, attempts to do a multi regression analysis of the two empirical coefficients a and b (obtained from the undrained strength versus water content of individual soils) with the LL and PL led to two separate correlation equations to empirically predict the LL and PL with the undrained strength and water content in terms of the empirical coefficients. Even a single test data from vane shear test at a water content between LL and PL can be just sufficient to predict LL and PL respectively using the correlation Equations 4 and 5. However, to improve the efficiency of predicting LL and PL, one can use the results of at least a few trials of vane shear tests conducted at different water contents between PL and LL, so that, the coefficients a and b are obtained. These coefficients can be used to predict LL and PL respectively using the correlation Equations 6 and 7. The developed correlations becomes handy to have an independent and quick check on the test results of LL and PL while handling large data generated at soil laboratories.

References

Al-Dahlaki, H., Al-Sharify, G. A. 2008. A proposed approach for plastic limit determination using the drop-cone penetrometer device. Journal of Engineering and Development 12(1), 107–117.

Ameratunga, J., Sivakugan, N., Das, B. M. 2016. Correlations of soil and rock properties in geotechnical engineering. Springer India, 228 p.

American Society of Testing Materials, 2000. Standard test method for laboratory vane shear test for saturated fine-grained soil. ASTM D4648-00, West Conshocken, PA, USA.

American Society for Testing Materials, 2005. Standard test methods for liquid limit, plastic limit, and plasticity index of soils. ASTM D4318-05, West Conshohocken, PA.

Atterberg, A. 1911. Lerornas forhallande till vatten, deras plas ticitetsgranser och plasticitetsgrader. Kungliga Lantbruk sakademiens Handlingar och Tidskrift 50(2), 132–158 (in Swedish).

Azzouz, A. S., Krizek, R. J., Corotis, R. B. 1976. Regression analysis of soil compressibility. Soils and Foundations 16(2), 19-29.

Belviso, R., Ciampoli, S., Cotecchia, V., Federico, A. 1985. Use of the cone penetrometer to determine consistency limits. Ground Engineering 18(5), 21–22.

British Standards Institution, 1990. British standard methods of test for soils for engineering purposes, BS 1377. Milton Keynes, British Standards Institution.

Campbell, D. J. 1976. Plastic limit determination using a drop cone penetrometer. Soil Science 27(3), 295–300.

Campbell, D. J. 1983. Discussion. Geotechnique 33(1), 78–79.

Campbell, D. J., Stafford, J. V., Blackwell, P. S. 1980. The plastic limit as determined by the drop cone test in relation to the mechanical behavior of soil. European Journal of Soil Science 31, 11-24.

DATAFIT, 2008. Datafit Version 9.0.59, Oakdale Engineering, RC 101, 23 Tomey Road, Oakdale, PA, 15071 USA.

Feng, T. W. 2000. Fall-cone penetration and water content relationships of clays. Geotechnique 50(2), 181-187.

Feng, T. W. 2001. A linear log d -log w model for the determination of consistency limits of soils. Canadian Geotechnical Journal 38(6), 1335-1342.

Feng, T. W. 2004*a*. Using a small ring and a fall-cone to determine the plastic limit. Journal of Geotechnical and Geoenvironmental Engineering 130(6), 630-635.

Feng, T. W. 2004*b*. Determining the consistency limits of high plasticity clays by the BS fall cone method. Ground Engineering 37(4), 56-57.

Haigh, S. K. 2012. Mechanics of the Casagrande liquid limit test. Canadian Geotechnical Journal 49, 1015-1023.

Harison, J. A. 1988. Using the BS cone penetrometer for the determination of the plastic limit of soils. Geotechnique 38(3), 433–438.

Kayabalı, K., Tüfenkçi, O. O. 2010*a*. Shear strength of remolded soils at consistency limits. Canadian Geotechnical Journal 47(3), 259-266.

Kayabalı, K., Tüfenkçi, O. O. 2010*b*. Determination of plastic and liquid limits using the reverse extrusion technique. Geotechnical Testing Journal 33(1), 14-22.

Kayabalı, K., Aktürk, O., Fener, M., Özkeser, A., Üstün, A. B., Dikmen, O., Harputlugil, F. H., Asadi, R. 2016. Determination of Atterberg limits using newly devised mud press machine. Journal of African Earth Sciences 116, 127-133.

Kyambadde, B. S. 2010. Determination of strength and index properties of fine-grained soils using a soil minipenetrometer. PhD Thesis, University of Brighton 292 p.

Lee, L. T., Freeman, R. B. 2007. An alternative test method for assessing consistency limits. Geotechnical Testing Journal 30(4), 1–8.

Lee, L. T., Freeman., R. B. 2009. Dual-weight fall cone method for simultaneous liquid limit determination. Journal of Geotechnical and Geoenvironmental Engineering 135(1), 158–161.

Leonards, G. A. 1976. Estimating consolidation settlements of shallow foundations on overconsolidated clays. Special Report 163, Transportation Research Board, 13-16.

Nagaraj, T. S., Srinivasa Murthy, B. R. 1986. A critical reappraisal of compression index. Geotechnique 36(1), 27-32.

Rao, H. Y. 1987. Determination of Atterberg limits by cone penetrometer. International Proceeding of 8th Asian Regional Conference on Soil Mechanics and Foundation Engineering 1, 81–84.

Rashid, A. S. A., Kassim, K. A., Katimon, A., Noor, N. M. 2008. Determination of plastic limit of soil using modified methods. Malaysian Journal of Civil Engineering 20(2), 295–305.

Sharma, B., Bora, P. K. 2003. Plastic limit, liquid limit and undrained shear strength of soil - reappraisal. Journal of Geotechnical and Geoenvironmental Engineering 129(8), 774-777.

Sherwood, P. T., Ryley, M. D. 1970. An investigation of a cone penetrometer method for the determination of the liquid limit. Geotecnique 20(2), 203-208.

Shimobe, S. 2010. Determination of index properties and undrained shear strength of soils using the fall cone test. Proceedings of the 7th International Symposium on Lowland Technology, September 16-18, Saga, Japan, 51-59.

Sivakumar, V., Glynn, D., Cairns, P., Black, J. A. 2009. A new method of measuring plastic limit of fine materials. Geotechnique 59(10), 813–823.

Sivakumar, V., O'Kelly, B. C., Henderson, L., Moorhead, C., Chow, S. H. 2014. Measuring the plastic limit of fine soils. An experimental study. Proceedings of Institution of Civil Engineers 168(GE1), 53-64.

Skempton, A. W. 1954. Discussion – sensitivity of clays and the c/p ratio in normally consolidated clays. Proceedings of the American Society of Civil Engineers, Separate 478, 19-22.

Stroud, M. A. 1974. The Standard Penetration Test in sensitive clays and soft rocks. International Proceeding of European Seminar on Penertation Testing, Stockholm, 2(2), 366-375.

Terzaghi, K., Peck, R. B. 1967. Soil mechanics in engineering practice. John Wiley and Sons 2nd Ed., 729 p.

Timar, A. 1974. Testing the plastic properties of cohesive and intermediate-type soils by extrusion. Acta Technica Academiae Scientiarum Hungaricae 76(3-4), 355-370.

Towner, G. D. 1973. An examination of the fall cone method for the determination of some strength properties of remoulded agricultural soils. Journal of Soil Science 24(4), 470–479.

Whyte, I. L. 1982. Soil plasticity and strength - a new approach using extrusion. Ground Engineering 15(1), 16–24.

Wood, D. M., Wroth, C. P. 1978. The use of the cone penetrometer to determine the plastic limit of soils. Ground Engineering 11(3), 37.

Wroth, C. P., Wood, D. M. 1978. The correlation of index properties with some basic engineering properties of soils. Canadian Geotechnical Journal 15(2), 137-145.

Bulletin of the Mineral Research and Exploration

http://bulletin.mta.gov.tr

Determination of the relationship between tectonic and karstification using morphometric indices in Bozburun Peninsula, Marmaris, Türkiye

İsmail EGE[a], Efekan ÖZKAN[b*] and Selahattin POLAT[a]

[a] *Uşak University, Department of Geography, Uşak, Türkiye*
[b] *Uşak University, Graduate Education Institute, Uşak, Türkiye*

Research Article

Keywords:
Karstification, Karst, Tectonic Factors, Morphometric Indices, Bozburun Peninsula, Türkiye.

Received Date: 12.03.2023
Accepted Date: 19.07.2023

ABSTRACT

Bozburun Peninsula (Marmaris) attracts attention due to its various karst shapes on limestones of different ages. It is also located in an important region in terms of tectonic activity. In this study, the distribution of karst shapes determined by satellite images, topographic maps and field studies was examined. In this context, the elevation ranges (m), base and hillslope angles (%), depth (m) and pitting rates (RP), elongation ratio (RE) and directions (EA α) of the relevant shapes were determined. Then, the relationship between the faults and the quantitative results obtained was interpreted. Remote Sensing (RS), Geographic Information System (GIS) technologies, calculations and field observations used in the study; it enabled us to reveal that there is a close relationship between karstic formations such as polje, uvala and doline and geological structures such as faults, diaclasis, folds and Nappe windows. Available data also show that geological structures have a positive effect on karstification in the study area.

1. Introduction

Bozburun Peninsula is an important place due to its location between the Aegean Sea and the Mediterranean coasts. The peninsula hosts many coves and gulfs. The study area is located between latitudes 36°33'-36°55'N and longitudes 27°57'-28°18'E in the southwest (SW) of the Aegean Region. The peninsula is administratively within the boundaries of Marmaris district. The area is surrounded by the Gulf of Hisarönü of the Aegean Sea in the west and the Gulf of Marmaris of the Mediterranean Sea in the east (Figure 1). Doğaner (1999), in a study her work on the Bozburun Peninsula, stated that the northern border of the peninsula can be formed by a line to be drawn between the İçmeler Bay and Hisarönü Gulf. The peninsula extending southwest from here to Rhodes Island covers many settlements (Bozburun, Taşlıca etc.). However, in this study, the border was expanded to the town center of Marmaris based on the basin boundaries. The study area extends in the southwest direction towards Rhodes Island and has a projection area of ~440 km^2 (approximately) (Figure 1).

Bozburun Peninsula is located in the western part of an important karst belt, the Taurus Karst Region of the South Anatolian Karst Belt. Micro and macro sized karst shapes are frequently encountered in the Bozburun Peninsula, as in the rest of the Taurus Mountains.

The degree of influence of the factors (geological/ geomorphological features, processes, climate and

Citation Info: Ege, İ., Özkan, E., Polat, S. 2024. Determination of the relationship between tectonic and karstification using morphometric indices in Bozburun Peninsula, Marmaris, Türkiye. Bulletin of the Mineral Research and Exploration 174, 11-35. https://doi.org/10.19111/bulletinofmre.1329619

**Corresponding author: Efekan ÖZKAN, efekanozkan09@outlook.com*

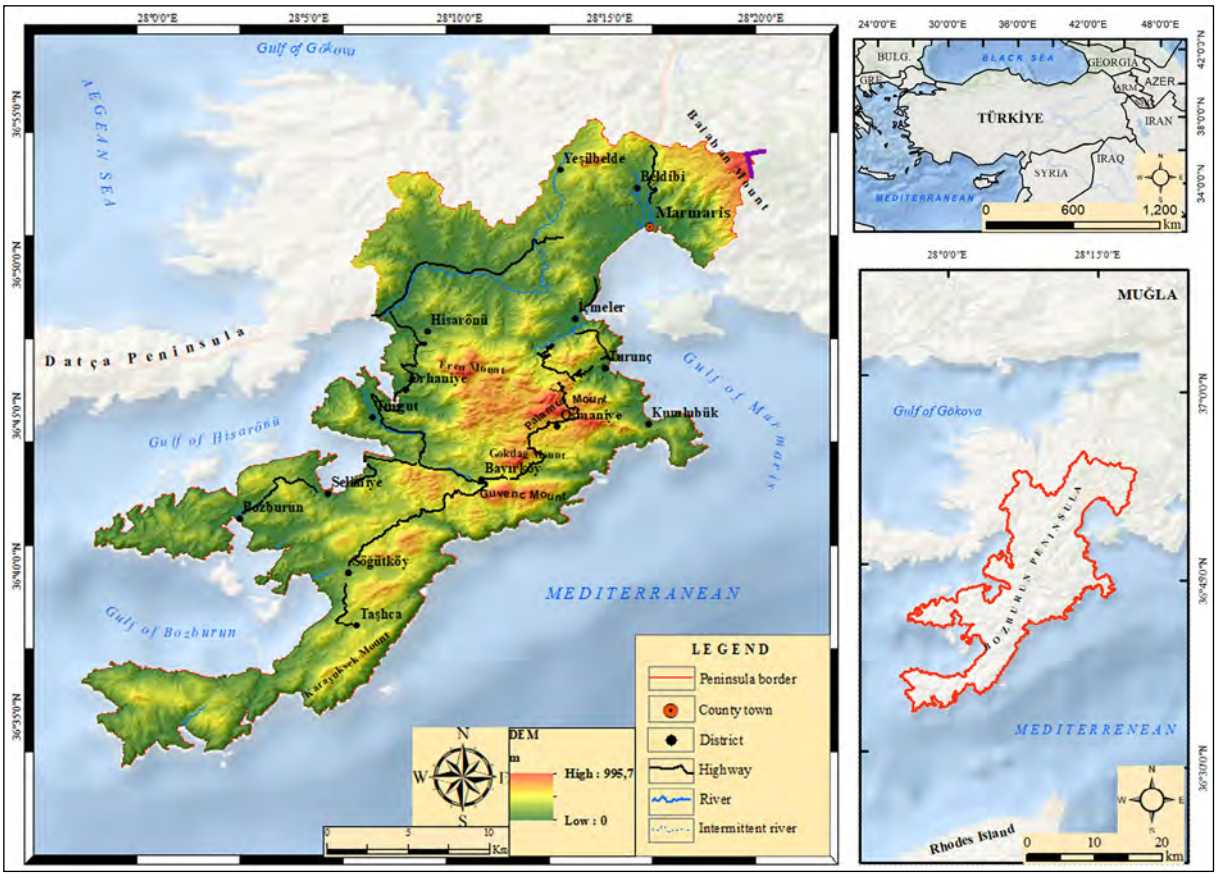

Figure 1- Maps showing the Bozburun Peninsula and its vicinity.

time) effective in the development of karstic lands may vary across regions. Sub-humid characteristic conditions of the Mediterranean climate, the direction, thickness and slope of different lithological layers are known as important factors in karstification (Tuncer and Nazik, 2010; Doğan et al., 2017; Nazik and Poyraz, 2017; Öztürk, 2020; Aydın and Tuncer, 2021). Based on the lithological structure, limestones are known as the most suitable rock for the formation of karstic lands. There are pelagic and neritic limestones formed in different depositional environments inside study area. Their mineral or element composition (calcium, clay, marl, micrite etc.) displays some variations based on location in Bozburun Peninsula.

A large number of karst morphology studies have been carried out in various regions of Türkiye. The studies explain the effect of different geological and climatic conditions on karstification. Although there are many research on geomorphology in the study area and its close vicinity, karst studies are only limited to caves (Günhan and Öner, 2021; Günhan et al., 2018). For this reason, a detailed study is needed on the Bozburun Peninsula having very unique karst shapes.

The morphological appearance of the region have been determined by active tectonism, neotectonism, fluvial erosion and sea level changes due to epeirogenic movements (Doğan, 1996; Tuncer and Nazik, 2010; Akdeniz, 2011; Nazik and Poyraz, 2015). Existing data and observations imply that there is a close relationship between the faults and the elongation directions of the karstic features in the tectonically active region. The faults are generally trends along E-W, ENE -WSW directions. However, these faults are cut by different faults with and acute or right angle. This is clearly observed in the area reflecting the tectonic characteristics of the Southwest Aegea (Tur et al., 2015; Topal, 2018). As a result, a remarkable karst patterns have appeared in the study area. Hence, main purpose of the study is to shed light to the relationship between tectonism and karst formation in the peninsula. Morphometric indices have been used to explain this relationship.

In order to explain this relationship, the main factors affecting topography and geology such as trends, geological/geomorphological features and their relationships have been studied during this study.

In geomorphology studies, morphometric indices have become very important especially in recent years. The collaboration between in Geographic Information Systems (GIS) and Remote Sensing (RS) technologies is very important in this subject. Many studies have been conducted on this issue in Türkiye as well. Some important studies can be listed as (Turoğlu, 1997; Cürebal, 2004; Erginal and Cürebal, 2007; Özdemir, 2007, 2011; Öztürk and Erginal, 2008; Bahadır and Özdemir, 2011; Sarp et al., 2011; Yıldırım and Karadoğan, 2011; Uzun, 2014; Avcı and Günek, 2015; Nazik and Poyraz, 2016; Köle, 2016; Topuz and Karabulut, 2016; Avcı and Kıranşan, 2017; Avcı and Sunkar, 2017; Geçen and Ölmez, 2017; Topal, 2018; Ege and Duman, 2020; Ege et al., 2019; İzmirli and Ege, 2019; Aydın and Tuncer, 2021; Şimşek et al., 2021). Although, the study area presents unique morphological features, no detailed study has been found on the relationship between tectonism- and karstification. It is thought that this study may contribute to this gap.

In explaining the karst patterns of the study area, morphometric analyses have been performed using GIS and RS technologies. In this context, quantitative inferences have been made about the topographical character of the area, its relief and the formation systematic of karstic lands by means of morphometric analyses.

2. Factors Affecting the Formation of the Peninsula

2.1. Material and Method

In order to understand and describe the physical features of the site, 16 topographic maps with 1/25.000 scale and 10 m isohips were digitized using ArcGIS 10.5 package program in GIS environment, and geomorphology map was drawn by the same program. While detecting dolines, uvalas and poljes, images and three-dimensional data in the Google Earth Pro program were used, and the relevant locations were confirmed by field studies. These data were digitized again in GIS environment. While explaining the geological features, the geological map of the 1/100.000 scale Marmaris O20 map of the General Directorate of Mineral Research and Exploration (MTA) was used.

As a result of intensive literature review; it has been observed that morphometric analyses, which can reinforce the outputs of field studies, are used quite frequently, in recent years. It is possible to explain the geomorphological character of the study area from a morphometric perspective and to define it quantitatively in this way (the valleys and drainage systems, lakes, karst terrains, slopes and to explain these geometric pattern etc.). This definition systematically provides support to the studies. One of the most suitable indices to accurately determine the effect of faults on karst shapes are the elongation ratio (R_E) and elongation direction (E_A α) from the morphometric indices (Williams, 1972; Day, 1976, 1983; Bondesan et al., 1992; Thery et al., 1999; Shanov and Kostov, 2014; Öztürk et al., 2018; Ege et al., 2019; Öztürk, 2020; Aydın and Tuncer, 2021; Saroli et al., 2022). In order to understand the characteristics of formation of the karstic shapes in Bozburun Peninsula, apart from the Elongated Ratio (R_E) and elongation direction (E_A α), other geomorphological/morphometric features of the related shapes [area size, elevation, slope values, depth, also Pitting Ratio for poljes (R_p)] were included in the research. While mapping the faults in the region; digitized fault data from MTA were compared with faults detected using Landsat 8 satellite imagery in Geomatica 2016 program. As a result of the observations in the field, some of them were associated with each other, combined and missing ones were added.

In this study, following both the morphometric and general geomorphological characteristics of the area and the karst shapes in the area, Kernel Density Analysis was performed in the GIS environment to understand where the karstification on the peninsula is concentrated. The azimuth angle of the trends of the faults and karst shapes was calculated with the Geo Rose 0.3.0 program. The poljes, the largest of the karst shapes, have been considered in more detail than the others.

2.2. Geological Features

The Bozburun Peninsula is lithologically included in the Western Taurus Karst System/Region. The Western Taurus Karst Region consists of Lycian Nappes, the youngest nappes of the Taurus Mountains and autochthonous carbonate rocks belonging to it (Ekmekçi, 2003; Nazik and Tuncer, 2010; Nazik et al., 2019). Different geological formations have been pushed on top of each other in the field. These structures were formed under the compression regime from the Palaeotectonic period to the present day. The units corresponding to different facies of the tectono-stratigraphic units of the Lycian Nappes have an incompatible appearance and cover a wide area in Southwestern Anatolia (Ersoy, 1990; Tuncer, 2021).

The study area and its surroundings are located in an important region where the Bodrum Nappes, Gülbahar Nappes and Marmaris Ophiolitic Nappes belonging to the Lycian Nappes crop out. Almost all of the formations on the peninsula belong to the Mesozoic Era. Existing units in order from oldest to youngest; Middle-Upper Triassic Çövenliyayla Volcanite (spilite, basalt, tuff), Middle-Upper Triassic Kızılcadağ Melange and Olistostrome (contains ophiolite melange and rarely Jurassic-cretaceous cherty limestones are observed), Middle-Upper Triassic Orluca Formation (sandstone, claystone, calsite), Upper Triassic Bayırköy Formation (commonly dolomite, dolomitic limestone), Upper Triassic- Lias Güverdağı Formation (algal, neritic limestones predominate), Jurassic-cretaceous Orhaniye Formation (pelagic limestones in intensity), Cretaceous Marmaris Peridotite, Upper Senonian Karanasıflar Formation (volcanite units; spilite, basalt), Upper Senonian Karanasıflar Formation (limestone and rarely volcanite breccias), Upper Senonian Karaböğürtlen Formation (volcanite units: spilite, basalt), Upper Senonian Karaböğürtlen Formation (sandstone, claystone, siltstone) (Erakman et al., 1982) (Figure 2). Karstification is mostly was observed inside Orhaniye and Güverdağı Formations.

The Güverdağı Formation (TRJg, Bozburun units/ Bodrum Nappes) has a structure dominated by neritic carbonate rocks. Many karst shapes have formed on the formation surface. The karstic features are also observed within dolomitic limestones in some places. This formation is overlain by the Karanasıflar Formation (*Kkn*, Bozburun units/Bodrum Nappes) unconformably. The formation is observed as extensively deformed inside the study area. Therefore, the thickness of the formation can not be determined precisely. The thickness of the formation has been estimated as about 800 m by some researchers (Bilgin et al., 1997; Şenel and Bilgin, 2010).

The other unit containing karstic features, is Orhaniye Formation (JKo, Turunç units/Gülbahar Nappes). This formation consists of calciturbidite micritic interlayers and chert micrites with thin-medium local thickness. The formation is intensely deformed by tectonics. The thickness of the formation, whose upper relationship is not observed, is about 400 m (Bilgin et al., 1997; Şenel and Bilgin, 2010). The formation is of pelagic origin.

It is understood that pelagic and neritic limestones formed in different periods of the Mesozoic era are important for the karst formation in the study area. The most common of these are neritic limestones. These formed in different periods between the middle triassic and cretaceous time interval (Şenel and Bilgin, 2010). These Mesozoic limestones are quite suitable for karstic occurences due to their lithological characteristics (Şahin, 2005; Öztürk et al., 2018).

The limestones in Bozburun Peninsula are surrounded partly both vertically and horizontally by impermeable (spilit, basalt, etc.) or relatively less permeable and less soluble rocks (such as dolomite). This features form the boundaries of the horizontal and vertical development of the poljes in particular. The impermeable levels (such as serpentine) of the Marmaris Ophiolitic Nappes control the northern boundary of the karstic formations belonging to the peninsula (Şenel et al., 1994; Şenel and Bilgin, 2010; Günhan et al., 2018).

It is estimated that the peninsula acquired its presentday configuration during the neotectonic period (since the latest Oligocene) under different tectonic regimes. These regimes include three compressions and two extensional tectonics. (Tur et al., 2015). It is emphasized in many studies that 13-degree rotation occurred counterclockwise due to

development of the Büyük Menderes Graben inside and vicinity of the study area. It is also mentioned that the dominant shapes and structures are alligned along NE-SW direction throughout the study area and its close vicinity (Tur et al., 2015; Günhan and Öner, 2021) (Figure 2).

2.3. Tectonic Features

The study area is located in the southwestern most part of Türkiye together with the Datça Peninsula.

The peninsula was formed inside the Western Taurus Mountains of the Anatolide-Tauride block during the paleotectonic period. The Western Taurus Mountains start from the Aegean coast and extend to the Kırkkavak Fault Zone in the Isparta angle. The study area is located parallel to the subduction zone formed by the African and Eurasian plates, a product of the Fenno-Sarmatian and Gondwana masses. This feature has gained a NE-trend during the neotectonic period. Common earthquakes occur due to tectonic processes in the South Aegean Arc. In addition, some active volcanoes are observed in this region (Pichon and Angelier, 1979; Tur et al., 2015) (Figure 3).

Moreover, some researchers stated that the faults in the Bozburun area play an important role in the development of the current hydrological system of the study area (Nazik and Tuncer, 2010; Nazik and Poyraz, 2015; Günhan et al., 2018). Based on existing data and new field observations, it is thought that faults play an important role in the formation of karst structures. It is estimated that karst development in the region accelerated during late Pleistocene in relation to both the acceleration of seismotectonic processes and the demise of the last ice age (Tur et al., 2015; Günhan and Öner, 2021). The types of faults in the region are normal, reverse and strike-slip in character (Figure 4, 5). The trends of the faults are mostly aligned along E-W, ENE – WSW directions. However, at many points, a different fault can also cut this trend at a perpendicular or near-vertical angle.

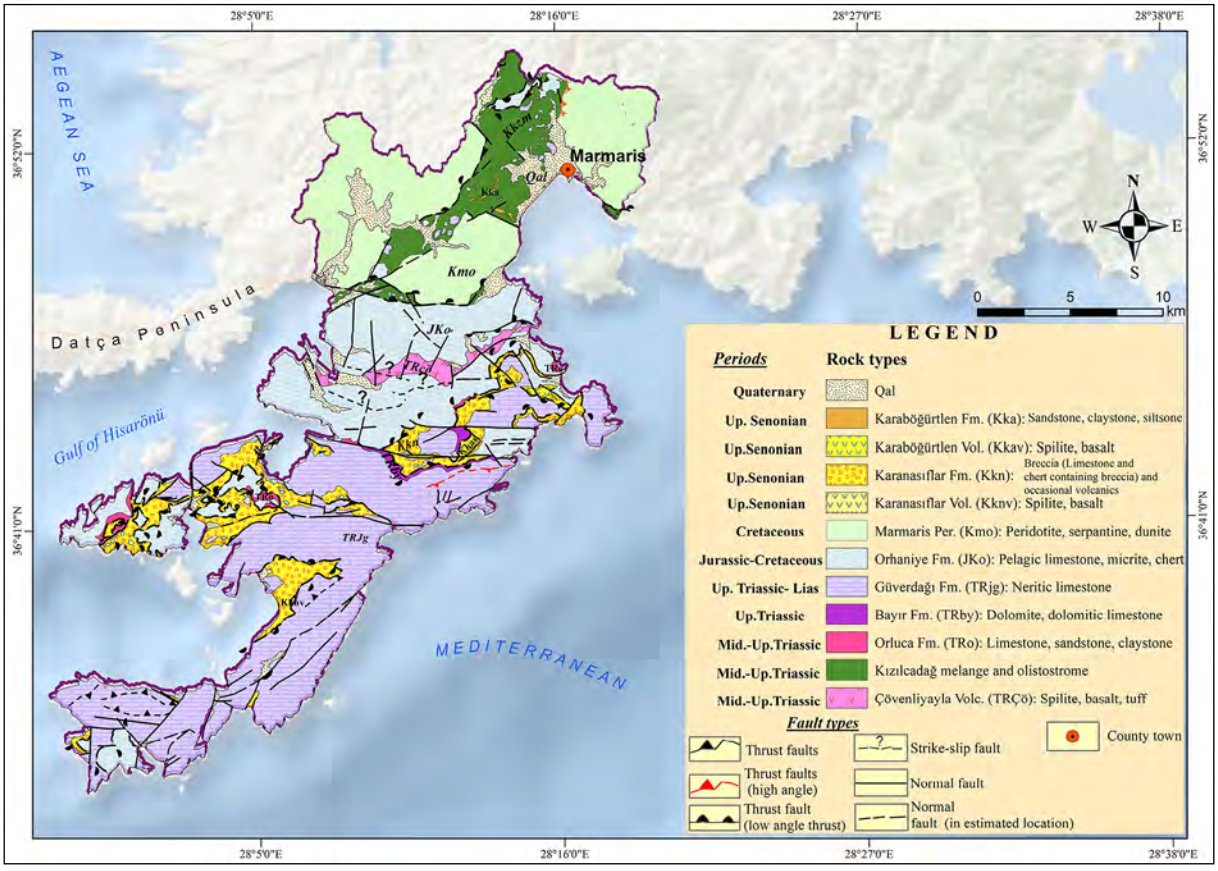

Figure 2- Geological map of Bozburun Peninsula (Şenel and Bilgin, 2010).

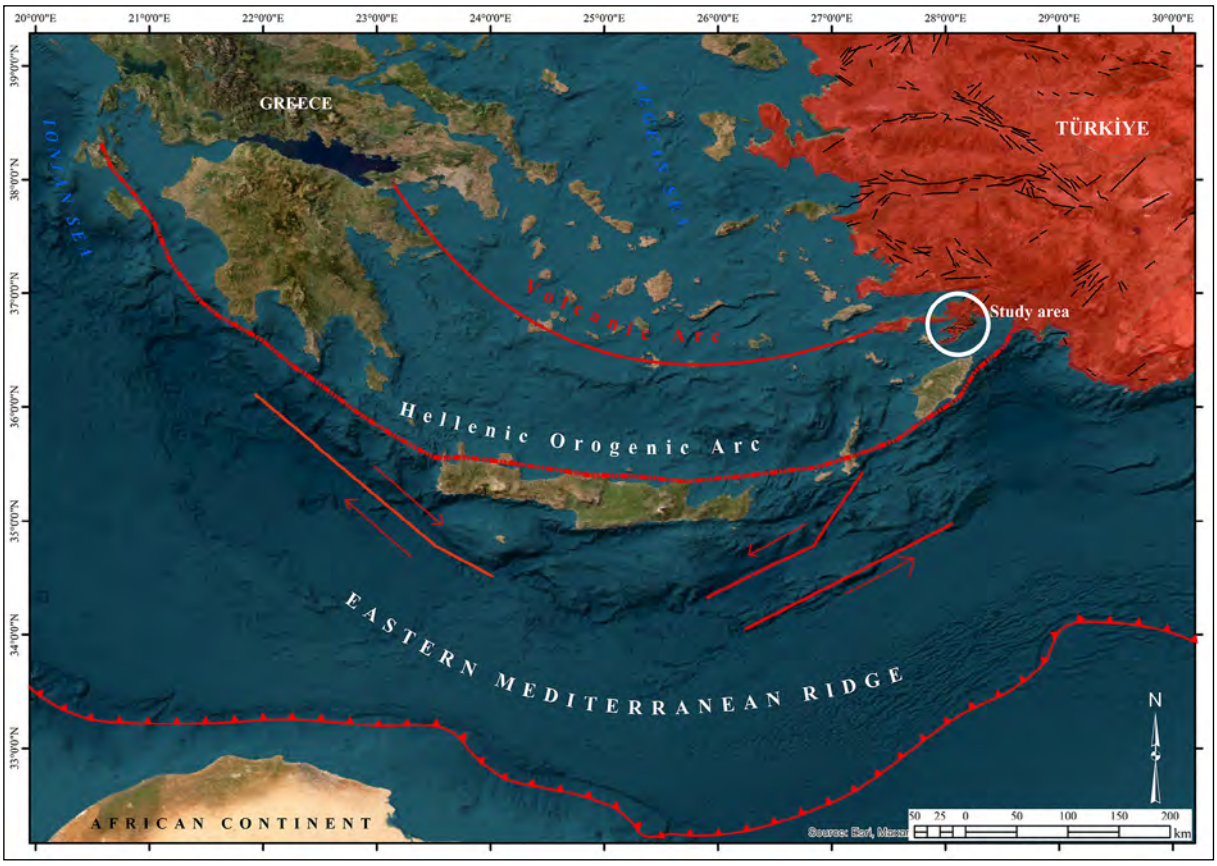

Figure 3- Map showing the main tectonic features of the Southern Aegean Arc and its surroundings.

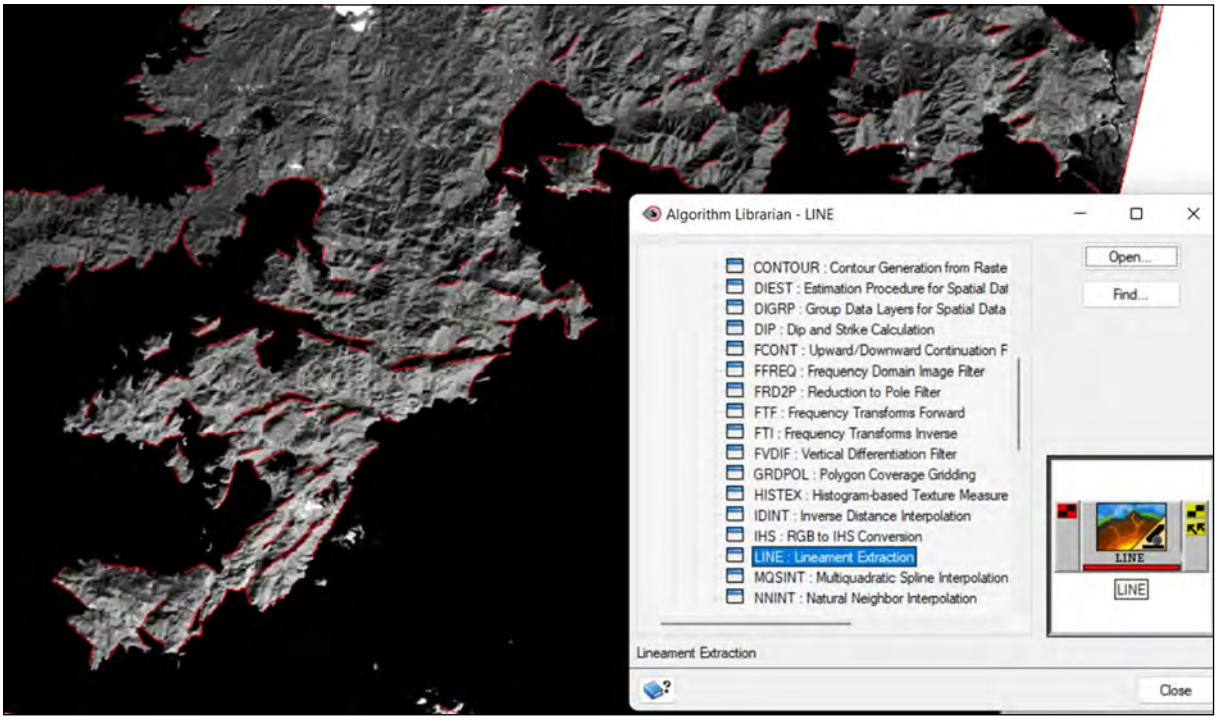

Figure 4- Detection of fault linearity in Geomatica 2016.

Figure 5- Morphotectonic map of the Bozburun Peninsula.

This can be clearly observed on the Bozburun Peninsula reflecting the tectonic characteristics of the Southwestern Aegean Region (Uluğ et al., 2005; Gündoğdu et al., 2015, 2020; Tur et al., 2015; Topal et al., 2016; Günhan and Öner, 2021; Dikbaş et al., 2022).

The Rhodes Fault, one of the most important active faults in the region, produced a 6.3 magnitude earthquake on May 23, 1961 in the offshore Gulf of Marmaris. The P wave focal mechanism, solution of the earthquake indicate that this earthquake was originated from a reverse faulting event (Ersoy et al., 2000). In addition to the Gulf of Marmaris, Gulf of Gökova and Gulf of Hisarönü and their immediate surroundings exhibit high tectonic/seismic activity. Many earthquakes with magnitudes above 5 have occurred in this region. Some ancient earthquakes were reported by some researchers in the region (Kırkan et al., 2023).

2.4. Geomorphic Features

The Taurus belt of Anatolia is very rich in terms of karst shapes. The current shape of the belt occured due to uplift of the submarine carbonate platform and volcanics. The area includes many relatively small scale faults and related micro basins formed by the local tectonism. The karst development continued in relation to physical and chemical decomposition in the research area. The formation of the karstic features seem to be controlled dominantly by faults (Erol, 1983, 1990; Akay and Uysal, 1988; Şimşek et al., 2021). Hills, valleys and many plains have occured in relation to faulting and folding in the study area (Taşlıgil, 2008).

It is suggested that the geomorphological and karst processes in the area has begun with the retreat of the sea since the Lower Miocene and the rise of Anatolia during the Middle Miocene (Şengör et al., 1985). In addition, the humid and warm climatic conditions intensified karst formation during the emplacement of the Lycian Nappes at that time. It is proposed that the karstification ceased during the Pleistocene ice age (Öztürk, 2020). Some studies also suggested that the ending of the Ice Age and the intensified seismic activity also enabled the karstification in the region during the Last Pleistocene. It is thought that the current karstic patterns developed since then (Öztürk, 2020; Günhan and Öner, 2021). Moreover, it is thought that the karst revival in the study area mainly developed along paleovalleys during this period. Some findings suggest that some uvala formations is located along river beds in some locations in the study area. It is also observed that some existing karstic features are degraded along younger folds and fractures in some locations. These were not included in the our study because they had a damaged structure.

Caves are valuable in classifying carbonate aquifers and determining the range of aquifer types (Ford and Williams, 2007). It is observed that some epikarstic processes dominate the karstification in some local areas and many related caves have been observed inside the study area (Table 1, Figure 6). The epikarstic caves are mostly distributed around the Bayırköy Polje and on the Güverdağı Formation in the peninsula. Some of these features also constitute a some water resources in the study area. It is estimated that these caves start to develope during the paleotectonic period. However, some recent studies suggest that the neotectonic processes seem to reshape the existing elements (Nazik and Poyraz, 2015; Günhan et al., 2018). Some sedimentary units support this view.

Although it can be said that the caves in the study area have generally gained a “hanging” structure as a result of the neotectonic activity, the underground-surface drainage relationship has been newly established at some points and limited at others due to the controls of different lithological units. When evaluated from this perspective, they are both perched and rare, small and irregular in pattern.

It is possible to come across small “erosion plains” characteristic of the Menteşe Region, especially in the central and southern parts of the peninsula. Here too, due to faulting, especially uvala and poljes show a specific trend. The list of poljes is as follows: Hacıağaç Polje (P1), Kuyucak Polje (P2), Osmaniye

Table 1- Some know caves and their brief characteristic properties in the study area (See Figure 7. The caves are mosly populated around Bayırköy area) (Günhan et al., 2018 and Günhan and Öner, 2021).

Cave names	Altitude (m)	Direction	Depth (m)	Trend of faults	Known features
Mahalbaşı	430	Horizontal	102	–	–
Bozenyakası	~400	–	–	–	–
Kayaini	477	Vertical	50	N-S	-Fossil cave -*Popcorn* calcite deposition
Katranlı Çengirek	458	–	116	N-S	-The mouth of the cave is in the form of a sinkhole. - Debris present
Torudibeği 1	506	Vertical	51	N-S	-Abundant fault breccias
Torudibeği 2	~450	–	–	N-S	–
Sakızeği	333	Vertical	126	N-S, WSW-ENE	-Debris present
Kirpiyeri	188	–	–	–	In the form of a small cavity.
İkizincirli Çengirek	174	Vertical	131	WNW-ESE	-Cave chimneys (old and still in formation).
Üçgül	~150	Vertical	–	–	–
Armelli	150	Horizontal	62	–	–

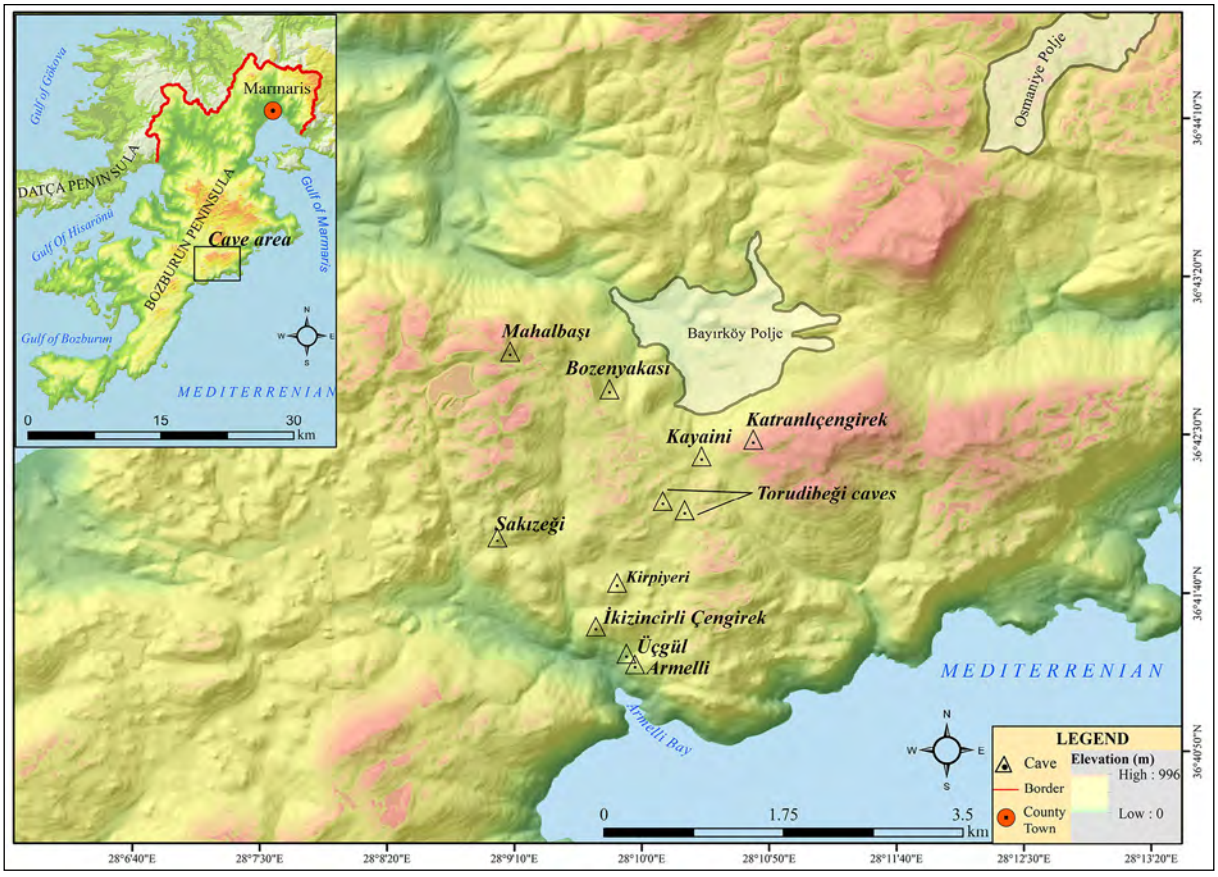

Figure 6- The location of the caves clustered around Bayırköy (modified from Günhan et al., 2018).

Polje (P3), Bayırköy Polje (P4), Kızılköy Polje (P5), Selimiye Polje (P6), Avlana Polje (P7), Ortaören Polje (P8), Söğüt Polje (P9), Ağlan Polje (P10), Taşlıca Polje (P11), Sindilli Polje (P12) and Serçelimanı Polje (P13) (Figure 7).

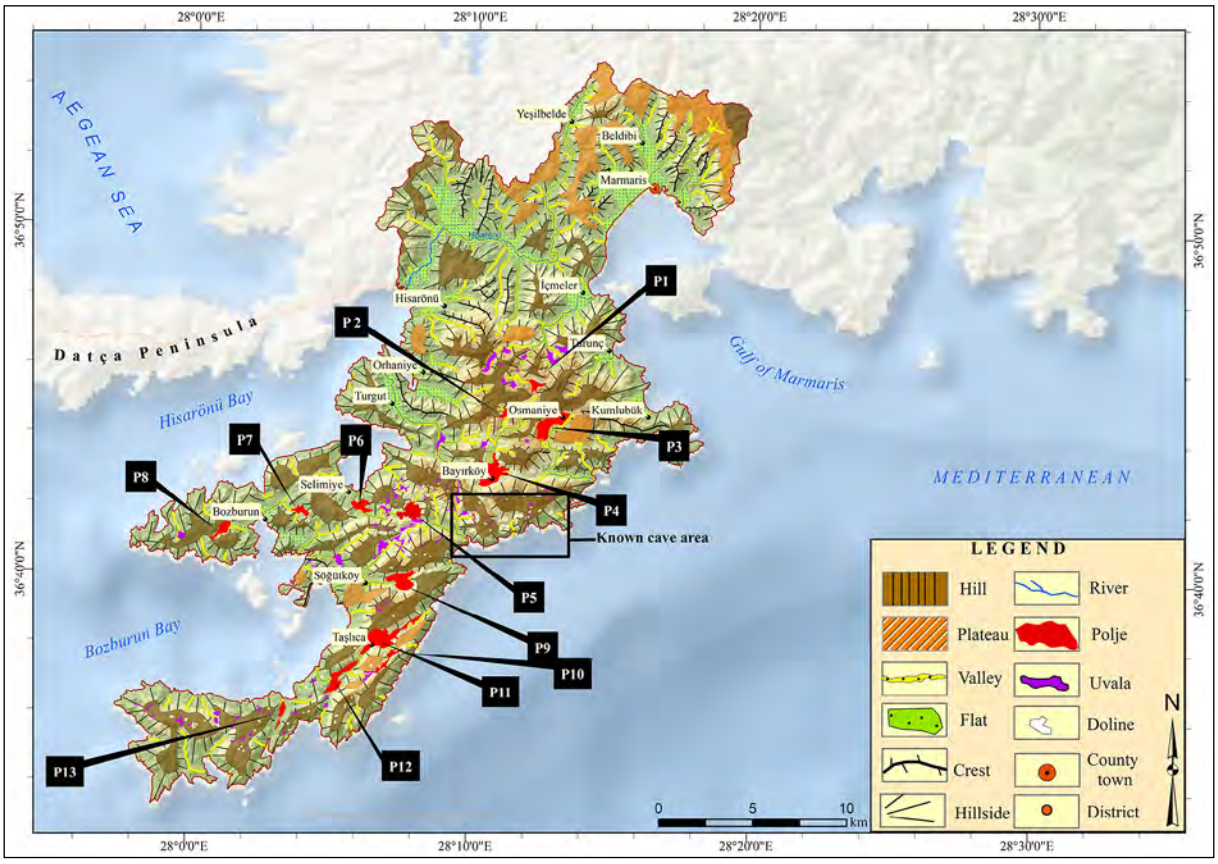

Figure 7- Geomorphology map of Bozburun Peninsula.

3. Discussion

3.1. General Geomorphological Characteristics of Dolines and Uvalas

Dolines, one of the karstic erosion/dissolution forms, have different formation systematics. They are classified as dissolution, collapse, covered and subsidence dolines (Ford and Williams, 1989; Doğan, 2004; Öztürk et al., 2018*a*). Dolines are important morphological shapes. Because they provide specific information about the morphological development of an area. Dolines also may provide quantitative results suitable for geomorphologic analysis (Öztürk, 2018*a*). As a result of the studies carried out using the Google Earth program, 107 characteristic dissolution dolines have been identified in an area of approximately 440 km^2. The distribution of the dolines in the field coincides with highly fractured neritic limestones. These morhological features are distributed along some large-scale or smaller-scale faults.

Uvalas are generally larger depressions than dolines, formed by the merging of dolines close to each other (Cvijic, 1893; Sür, 1994; Kranjc, 2013). Bonacci, an important karst researcher, described poljes as a large karstic features originated from the uvalas with not less than 0.5 km^2 in size (Bonacci, 2004). In this study, following criteria have been taken into account during the determination of the uvalas. The criteria are: 1) the shape should be formed by the merging of at least two dolines, 2) the area should be smaller than 0.5 km^2, 3) base of the shape should be covered with terra rossa, 4) the area should be a depression and 5) the at the base rocks should be soluble. Based on these 81 different uvalas have been determined throughout the peninsula during this study. Uvalas, similar to dolines, are generally observed along joints and fractures located mainly inside neritic limestones. In addition, some uvalas in the study area were found in the contact areas of pelagic and neritic layers, where there were layers with dolomitic interfaces and even intertwined with each other and with different structural units, and in some places they

were superimposed on these other units (volcanites, etc.), settled in the thrust windows and grew with the fluvial effect. These probably also have paleovalley characteristics.

Based on field observations and related studies, the size (m^2, km^2), elevation steps (m), elongation ratio (R_E) and elongation direction (E_A α), density (Kernel density analysis) and depth (m) of dolines and uvalas have been evaluated in the peninsula. This paper also attempts to understand the extent of the relationship between poljes, dolines, uvalas, and tectonism.

3.1.1. Areal Size

The smallest doline in the field has an area of 233 m^2, and the largest doline has an area of 11292 m^2. The average doline size is calculated as 3824 m^2. Dolines identified in the study area have been evaluated using areal size histogram (Figure 8). Based on this data, the areal size of 40 dolines corresponding to the maximum number range varies between 233 m^2 and 2333 m^2. This is followed by a range of 2333.1 m^2- 4433 m^2 with 32 dolines. 67% of the dolines are under 4433 m^2. It is thought that the tectonic effect (continuous reactivation of the land, fragmentation and fracturing along the thrusts and normal faults) played a significant role. In the literature, the dolines smaller than 27.000 m^2 are considered as small dolines (Brinkmann et al., 2008; Öztürk, 2018*b*). In this framework, all dolines in the field are classified as small dolines.

It is known that uvalas, which is a dissolution feature larger than itself, are formed by the merging of dolines. However, as mentioned above, very small dolines that have developed due to tectonic effects and that are very close to each other may easily merge and become uvala. Therefore, very small uvalas can be formed by the merging of the two very small dolines. Such uvalas are also observed in the study area. Based on the available data, 19% of the uvalas in the study area are smaller than the largest dolines. Moreover, the majority of dolines (75%) are larger than the smallest uvala(Figure 8).

It seems that the extensive tectonic deformations have negatively affected the size of the uvalas in the study area. It is detected here that 67 (~70%) of the observed uvalas are smaller than 70600 m^2. The uvalas observed on the peninsula are much smaller than 0.5 km^2. Therefore, it is deemed here appropriate to include the uvalas inside small uvala class (Brinkmann et al., 2008; Aguilar et al., 2016) (Figure 8).

3.1.2. Elevation Steps (Histogram)

Most of the dolines (~61%) in the Bozburun Peninsula are located at altitudes between 201-450 m (Figure 9). It is estimated that climatic conditions will not make a significant difference in this narrow range.

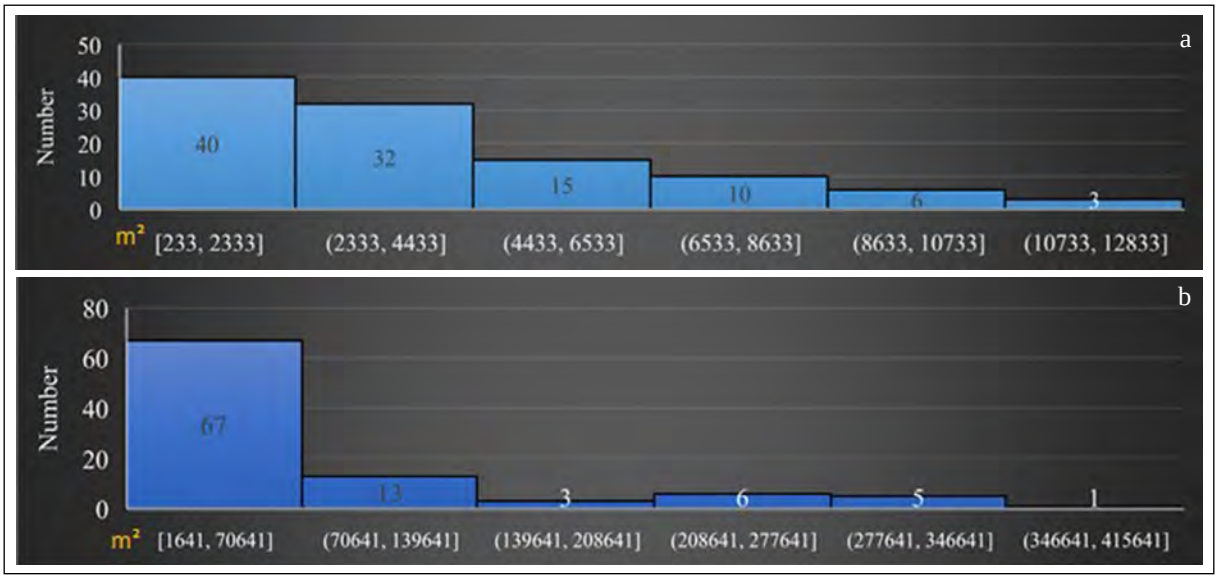

Figure 8- Histogram graphs; a) sizes of dolines, and b) sizes of uvalas.

It can be thought that the fact that the fractures and pits formed along the anticline surfaces, caused by the geomorphological development under the influence of orogenic movements and tectonism that have become more intense since the Miocene, coincide with these elevation ranges is more decisive in the distribution of dolines. The elevation histogram of uvalas is very similar to that of dolines (i.e. 201-450 m). The distribution and elongation directions of uvalas are very similar to dolines due to same structural features. In these levels, partially degraded uvalas and paleo-valleys are observed due to periodic reactivation, especially on medium to high slopes. In addition, it has been also observed that fluvial processes have reactivated the karstic features in some places due to high slope values of the hillsides along the dolines connected to the main uvalas.

3.1.3. Slope

According to the slope analysis performed in ArcGIS 10.5 program, the slope groups determined by using Oakes (1958). Based on this, more than 60% of the peninsula (278 km^2) is located in the slope groups of the very steep slope class between 15% and 40%. The average slope is about 21.2%. It has been observed that most of the karst shapes, including poljes, have slope values exceeding 8%. The presence of knickpoint and fractures is important in this sense. The base slopes of the karstic features are generally included in the slope groups up to 8%. Areas with steeply-sloping (15% and above) includes significant amounts of degraded dolines and uvalas. It is understood that they are still in the formation phase in relation to tectonism along paleo-valley floors (Figure 10).

3.1.4. Depth

The depths of the dolines in the field vary between 1-11 m. In the calculations and observations, it has been understood that the average depth of the dolines in the peninsula is 2.5 m. These shapes, which are included in the dissolution doline group, which has a widespread distribution on karst areas, are quite common in the Taurus Mountains. It has been determined that secondary and tertiary faults rather than main fault lines are effective in the formation of dolines on the peninsula, whose elongation direction do not directly overlap with the main fault lines in general (Figure 11). On the contrary, the depth of the dolines usually reaches 5-6 meters in various locations, especially between two effective fault lines. At another point where different faults intersect, even a doline with a depth of 11 meters was detected (Figure 12).

Uvala depths have a wide range ranging from 1 to 45 m in the study area. The average depth is 11.8 m. Considering that the areal sizes of uvala shapes are generally several times larger than dolines, this value at depth seems normal.

3.1.5. The Morphometric Indices: Elongation Ratio (R_E) and Elongation Direction (E_A α)

In the field, dolines that have been exposed to periodic rejuvenation and degradation in places are frequently encountered in medium-high inclined locations. In this respect, it can be thought that faulting in the neotectonic period affected the elongation ratios of karstic shapes. The elongation ratio is calculated by taking the ratio of the long axis to the short axis of the doline or related karstic shape

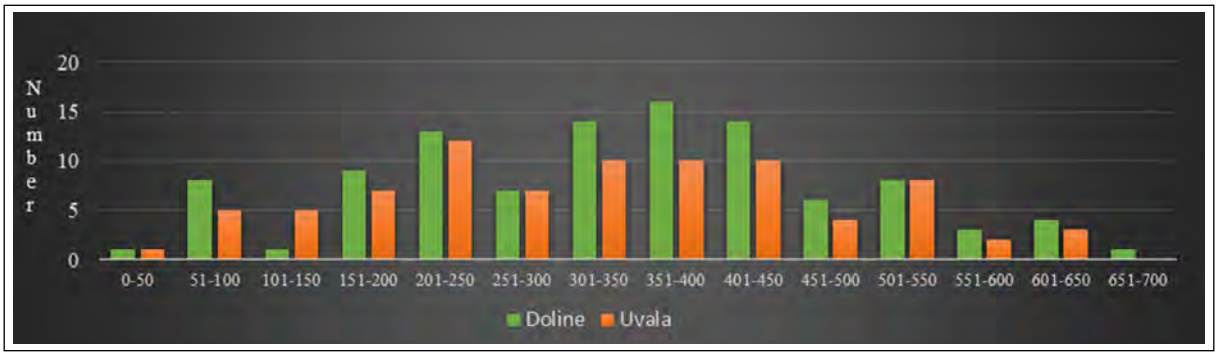

Figure 9- Histogram of the elevation ranges (m) where dolines and uvalas are located.

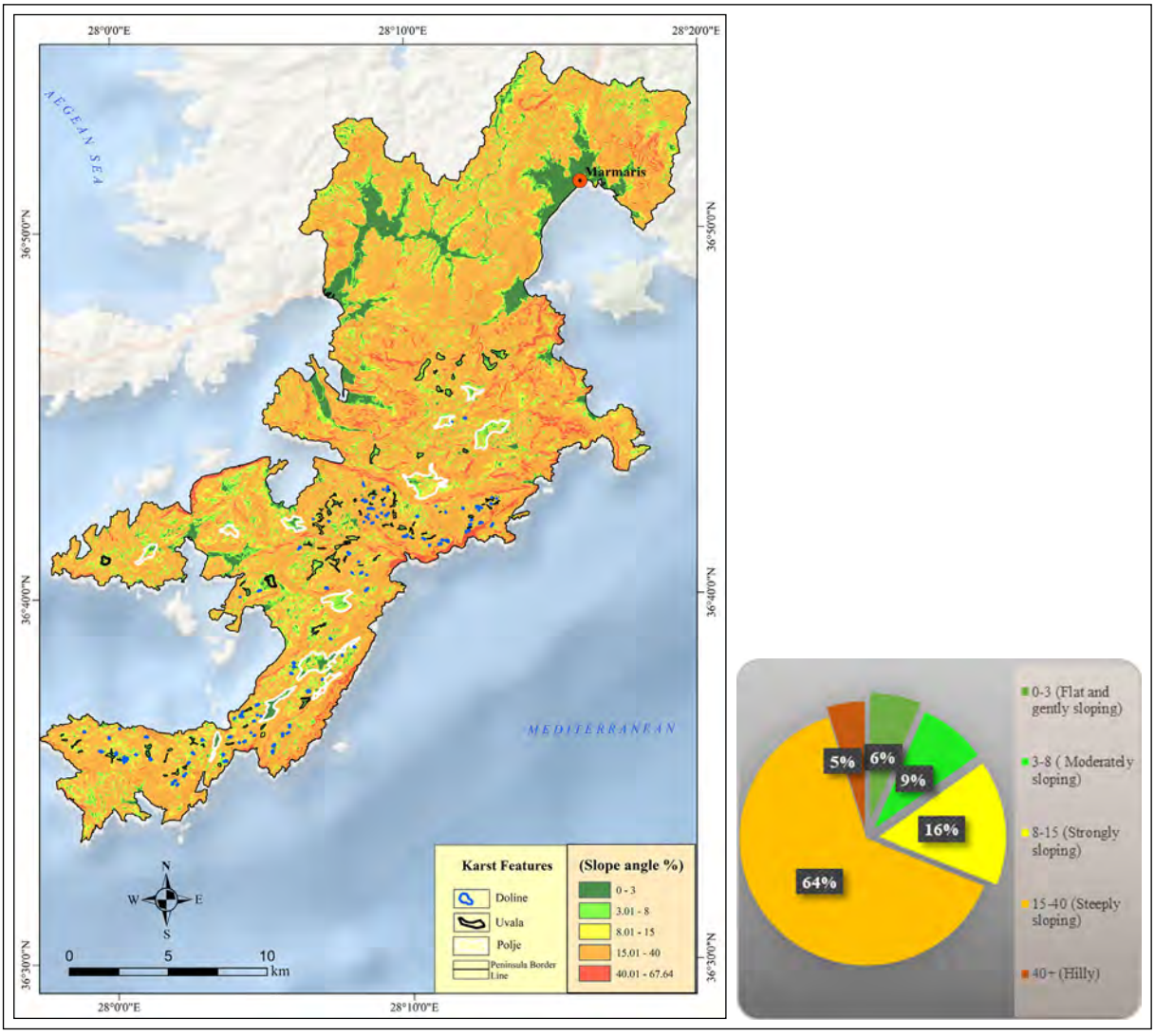

Figure 10- The distribution of slope and karst shapes in the study area.

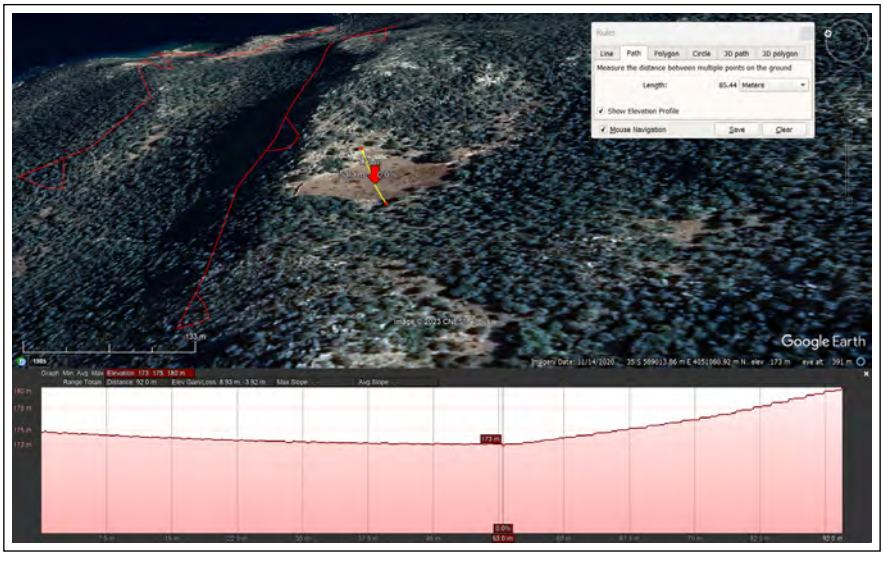

Figure 11- Developed in a crack formed by a fault, example of a dissolution doline reaching 5 m in depth (Google Earth Pro 2020 image).

Figure 12- Resp., a) a Google Earth image of the Bozburun Peninsula., b) The deepest doline (11m) of the Bozburun Peninsula is marked with a black star in the image. This doline is located in the ESE direction of Bayır Village.

in many studies (Bondesan et al., 1992; Aydın and Tuncer, 2021) (Formula 1). At this point, the long and short axis should intersect each other at an angle of 90°. If the value moves away from 1, it means that the shape moves away from circularity and resembles an elliptical feature (Öztürk, 2018*b*). Basso et al. (2013) subdivided the elongation ratio into 4 categories (Table 2). In this context, 65% of the dolines in the field are in the elongated class. There are many elongated dolines in the region that extend diagonally to each other and are sensitive to fluvial degradation. These dolines, also due to the effect of neotectonism, combined to form elongated uvalas. Most of dolines (%65) and uvalas (%76) has an elongated form in the peninsula.(Figure 13). Almost half of the uvalas in the field are located exactly on a fault, and extend parallel to the faults (Figure 14).

$$R_E = \frac{Long\ axis\ (m)}{Short\ axis(m)} \qquad \text{(Formula 1).}$$

Table 2- Classes of elongation ratio (from Basso et al., 2013; Öztürk, 2018*a*, *b*; Aydın and Tuncer, 2021).

Elongation ratio (R_E)	Geometry of Shape
Less than 1.21 ($R_E < 1.21$)	Circular, semi-circular
1.21 to 1.65 ($1.21 < R_E < 1.65$)	Semi-elliptical
1.65 to 1.8 ($1.65 < R_E < 1.8$)	Elliptical
Greater than 1.8 ($R_E > 1.8$)	Elongated

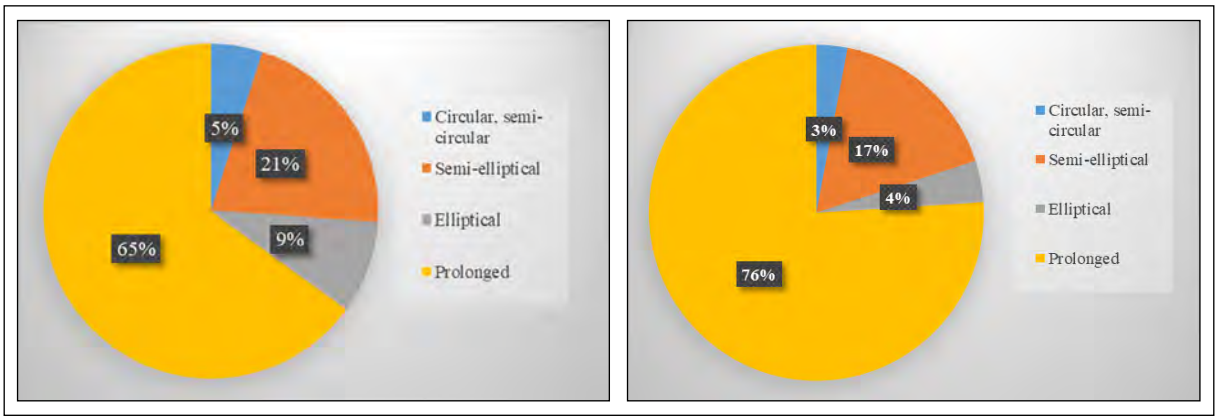

Figure 13- Elongation ratio graphs of dolines (left) and uvalas (right).

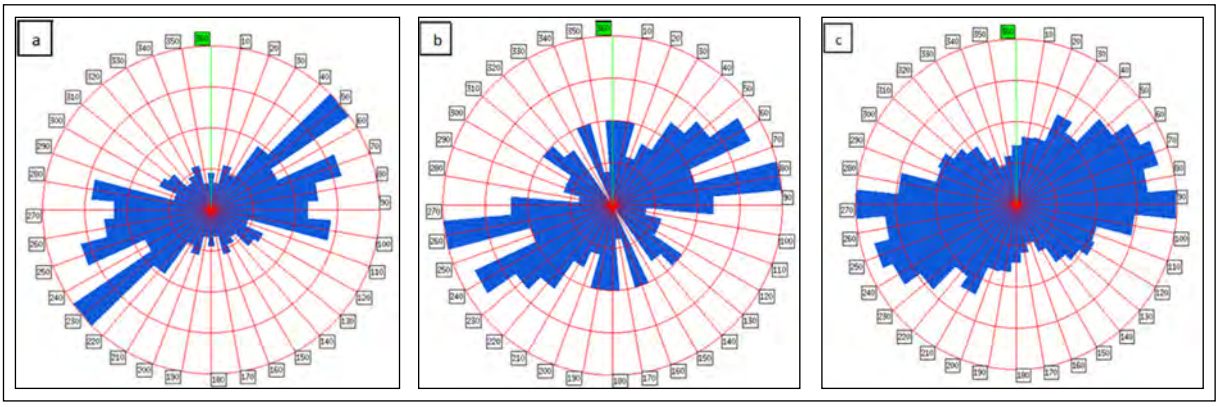

Figure 14- Rose diagrams of the elongation directions of; a) dolines, b) uvalas and c) faults in the study area.

3.1.6. Density

Dissolution dolines are pit-like shapes where the surface-groundwater relationship is established, and are formed as a result of chemical and physical erosion around the diaclasis, faults and layer joints that are weak in terms of karstic dissolution (Sür, 1994; Doğan and Yeşilyurt, 2004). In the study area, fields where these conditions come together at different levels have a determinative effect on the density of dolines. Especially the dolines around the Bozburun and Selimiye faults are located in Nappe windows and the hillslope angles are over 8 percent. This view is supported by fault data obtained from Google Earth image analysis, 1/100.000 scale geological maps prepared by MTA, and field observations. (Figure 15).

The distribution of uvalas in the study area is more compatible with the presence and elongation of the faults compared to the distribution of dolines. It is clear that the weakness of the structural lines as well as the larger fractures following the fault and the depressions formed by the direct fault have a great effect here. Many uvalas sitting on the pelagics between Turunç and Hisarönü Bay, where faults of different characters exist, prove this inference.

The elongation direction of the poljes directly coincides with the locations of the fault lines. This overlap and the general characteristics of the poljes are mentioned in the next section. The names of the poljes identified in the study and named according to their location are from north to south; Hacıağaç Polje, Kuyucak Polje, Osmaniye Polje, Bayır (Bayırköy) Polje, Kızılköy Polje, Selimiye Polje, Avlana Polje, Ortaören Polje, Söğüt Polje, Ağlan Polje, Taşlıca Polje, Sindilli Polje, Serçelimanı Polje (Figure 16-18, Table 3).

3.2. Properties and Morphometry of Poljes

The largest shapes formed as a result of karstification are poljes. Poljes are formed by

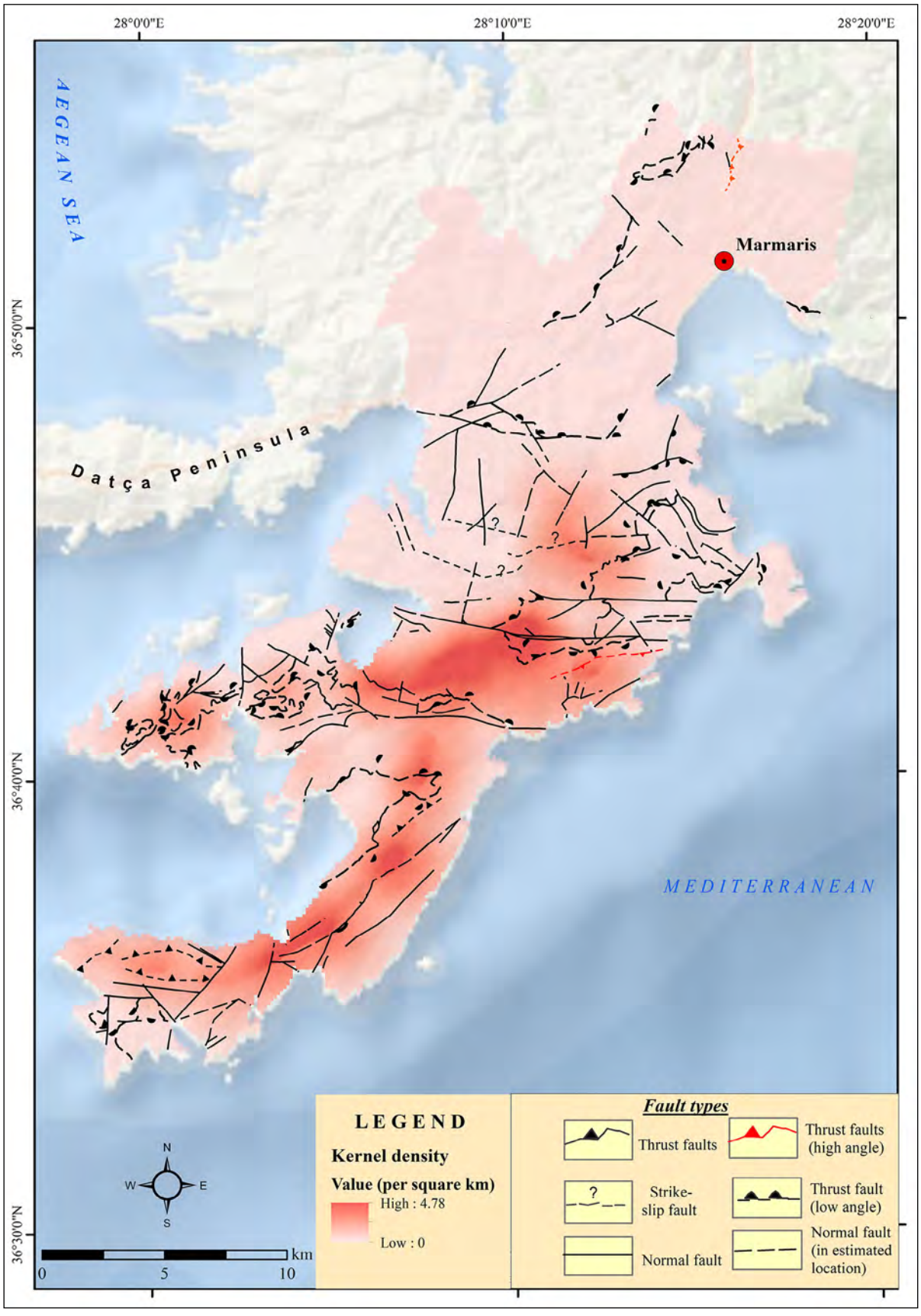

Figure 15- Map showing Polje Kernel density distribution and the faults in the Bozburun Peninsula.

providing optimum conditions for karstification. In addition to the lithological structure, tectonic activities and climatic conditions also play a triggering role for karstification and polje formation. Poljes are generally bowl-like depressions that are close to elliptical shape. (Ford and Williams, 1989; Sür, 1994; Doğan, 2003; Ege, 2015*a*, *b*, 2017).

In this study, before the poljes were identified, the literature on the detection and morphometric properties of poljes were reviewed in detail, just as in the determination of other karstic shapes. Then, the data coming from the field observations were classified and reported with a systematic approach. Poljes have converted to digital data in Google Earth Pro and ArcMap 10.5; it was re-evaluated by using the 1/25000 topographic maps. While determining the boundaries of the polje base, the bedrock remnants, where the slope erosion continues, have been taken as the boundary reference. In addition, care has been taken to clearly distinguish the terra-rossa on the floor of the polje. Gams (1978), on the other hand, emphasizes that three criteria must be met for a depression to be considered as a polje. They are: 1) presence of a flat bottom (may be terraced) in rocks or loose sediments, 2) presence of a closed basin with high flanks (e.g. 18% in this study) and 3) presence of a karst drainage system. In addition to this, Gams (1978) divided the poljes into 5 classes considering these features: 1) Border polje, 2) Peripheral polje, 3) Piedmont polje, 4) Overflow polje and 5) Piezometric level polje.

According to Bonacci (2004), poljes with an area between 0.5 km^2 and 10 km^2 are considered as small poljes. However, considering all the literature, it is seen that the areal size cannot be applied strictly. Mainly, hydrological and geomorphological criteria are taken as a reference during definition (Şimşek et al., 2021). In this study, 13 poljes are classified as small. Their sizes range between 0.25 km^2 (Serçelimanı Polje) and 1.6 km^2 (Bayırköy Polje). The morphometric properties of the detected poljes are important in terms of understanding the tectonic influence on the morphology (Table 3). Polje evaluation starts from the north towards south (Figure 16- 18).

The Hacıağaç Polje (P1) developed at the point where two faults intersect. The diameter/depth ratio of the semi-elliptical and plate-shaped polje was calculated as 12.22. The polje, at the bottom of which alluvial deposits are observed, was originally formed on Cretaceous pelagic limestones. It is bounded by spilites at the bottom and hillsides. The ponors at the bottom are used for agricultural irrigation and animal husbandry.

The Kuyucak Polje (P2) is located approximately 1.5 km southwest of Hacıağaç. The Kuyucak Polje is located on a secondary fault in a syncline. The diameter/depth ratio of the elliptical polje was found to be 19.72. Kuyucak Polje is 1.5 km away from the Senonian aged low angle thrust fault forming another polje (Osmaniye) from the southeast, and its long axis exactly coincides with the strike of this fault. The shape, whose bottom consists of pelagic limestones, has dry drainage.

Another karst shape located 1.5 km southeast of Kuyucak is the Osmaniye Polje (P3). It is surrounded by a Senonian low angle thrust fault from the northwest. The elongated form and direction of the polje were formed by this fault. The diameter/depth ratio was found to be 31.33. This ratio shows that the cavity is less than the Hacıağaç and Kuyucak poljes. The bottom and hillsides of the polje are covered with breccias and limestone blocks in places. Dolomites crop out in this region and spilites and basalts are also encountered in places. A relatively new active drainage was observed southeast of the base of the polje.

The largest polje of the field named Bayırköy Polje (P4), which was formed directly on the Selimiye Fault Zone is located southwest of Osmaniye Polje. In this region, the main faults and secondary fractures with different character cross cut each other. The intersection caused the polje in question to be in circular form, and the polje does not present a certain elongation direction. The diameter/depth ratio is 13.87. There are settlements and gardens in the polje which developed on neritic limestones. The surrounding valleys were probably reactivated during the neotectonic period. Therefore, there is a thick alluvial layer at the base of the polje (Figure 16-18). The polje is a completely closed basin. Probably the aquifer level is higher than

other poljes. There are many karst springs around the shape and active water is observed in its ponors.

Kızılköy Polje (P5) is another polje located 3 km southwest of Bayırköy Polje. The polje has a circular form due to intersection of both low angle thrust fault and normal fault. A large number of hums (residual hill) were found in the Kızılköy Polje. Diameter/depth ratio of this polje is 21.16. There are abundant limestone containing breccias on the slopes and at the bottom. Alluvium also have an important place in the polje base with dry drainage. Ponors were detected at several points, and it is observed that there is water inside these ponors from time to time. There are settlements and gardens in the polje.

The Selimiye Polje (P6) is the another polje observed in the study area. It is located approximately 1.3 km west of Kızılköy. There is a village inside this polje. The polje is 600 m away from the shore line and its maximum depth is 60 m. The elongation direction of the shape is parallel to the trend of the low angle thrust fault and normal fault. Its has is semi-elliptical shape and its diameter/depth ratio is 8.17. The periphery and base of the polje, which developed on pelagic limestones, mostly consists of breccias. Sandstone and mudstones are also observed in the polje. The seismicity due to neotectonic activity reactivated the paleovalley in the basin and allowed it to rise 60 m above the shoreline. The west of the polje seems to have started to experience active fluvial processes again, probably due to the knickpoint that occurred later and the increase in the base slope. There are some karstic springs on the slope separating the polje from the shoreline. It is estimated that the groundwater level of the polje, which is feed by the northern hillsides and karst sources, is high.

Avlana Polje (P7) is the another polje and located approximately 2.3 km southwest of Selimiye. This feature is also controlled by a thrust fault and its elongation direction also conforms to this. This polje is in the elongated class in terms of its form. The diameter/depth ratio is 7.95. This ratio is the lowest compared to other poljes in the study area. This value also shows that the shape has the highest hillslope angle compared to the others. The lithology of the shape consists of pelagic limestones and breccias, as in the others. There is a seasonal stream in the polje. This stream flows through a reactivated paleovalley and reaches Bozburun Bay in the south. Neotectonics appears to play an important role in the development of this shape. In the polje, there are summer cottages used for touristic purposes and a sub-village settlement.

Ortaören Polje (P8) is the another polje observed in the study area. This feature is located about 3 km southwest of Avlana polje. It seems that the development of Ortaören Polje is also controlled by a thrust fault and displays a similar trend compared to this fault. The is in the elongated class in terms of its form. The diameter/depth ratio was calculated as 17.63. The shape appears to develop mainly on pelagics sediments. The base of the polje consists of calcareous breccia.

Another polje on the peninsula is the Söğüt Polje (P9). This is semi-elliptical karst shape and elongated by a thrust fault. The diameter/depth ratio of the figure is 14.64. Neritic limestones and breccia form the main lithological structure of the polje. It is surrounded by high hillslope angle (over 40%). The hillsides were artificially terraced by local people for pasture use. Seasonal drainage is available. In the polje, there are a few houses that form the lower settlement of Söğüt village.

Taşlıca Polje (P10) is the another polje observed in the study area and located in approximately 2 km South of Söğüt Polje. This shape seems to develop on top of a thrust or normal fault. The diameter/depth ratio of the polje is 26.5. The shape has formed on neritic limestones. An intense karstic drainage system has developed in the polje with many ponors and hums. Taşlıca Polje is seperated from Ağlan Polje in the east by a small and narrow cill. It seems likely that these two poljes will merge in the future.

Ağlan Polje (P11), parallel to Taşlıca Polje, formed on the edge of a normal fault. The elongation ratio of this shape (6.76) is the highest compared to the others. The diameter/depth ratio of the polje is 28.09. There is an artificial pond in a ponor belonging to the Polje. This pond is used for irrigation and animal husbandry purposes by the local people.

Another polje that is very likely to merge with the Taşlıca Polje in the feature is the Sindilli Polje (P12). This shape is classified here as the elongated. Sindilli Polje is also separated from Taşlıca polje by a small threshold in the south, and seems to have developed under the control of a thrust and normal fault. The diameter/depth ratio is the highest value in the study area (i.e. 49.96). The shape is rather shallow compared to the others. Beekeeping and animal husbandry are carried out in the polje. There are several ponors, and some remnants of an ancient city on the terraced slopes.

Approximately 2.3 km south of Sindilli Polje, Serçelimanı Polje (P13) is located on a normal fault and has the highest elongation ratio (4.44) in the field. The diameter/depth ratio of the figure was calculated as 34.42. The coast is reached by descending a small threshold (~15 m) from both ends of the polje, which has an average floor height of 27 m (Table 3, Figure 16, 17).

4. Results

With this study, the formation and elongation directions of the karstic features in the study area can be shown as evidence that the seismotectonic processes in the region mostly took place in a counterclockwise direction with a bending movement of approximately 8-13° as emphasized in previous studies (Tur et al., 2015; Günhan et al., 2018). So-called Quaternary thrust faults generally play a major role in the development of the poljes in the study area. The normal faults that develop close to thrust faults also play an important role in the formation of karstic features. The trends of both fault types generally coincide with karst shapes. It is thought that there is a dominant direction in the tectonic evolution of the area and that the torsion movement continues counterclockwise from this axis, which is open to discussion (Pichon and Angelier, 1979; Şengör et al., 1985; Seyitoğlu and Scott, 1991; Uluğ et al., 2005).

The fact that the tertiary lands are not encountered intensively from the Cretaceous until the Quaternary in the research area can be explained in two ways: First, the possibility that the Tertiary formations were largely submerged by sea waters due to the transgression experienced after the Pleistocene glacial period (18000 years BP). The second possiblity is the study area, which started to rise with the Alpine Orogeny that started at the end of the Cretaceous, never experienced marine or lacustrine conditions at that time, and that karstification continued uninterruptedly after the Cretaceous until today. In order to evaluate these possibilities, detailed geological and geomorphological studies are needed throughout the peninsula, including coastal measurements. 107 dolines, 81 uvalas and 13 poljes have been identified during this study in the Bozburun Peninsula. As a result of the evaluations, it is seen that the dolines and uvalas in the peninsula display a highly fragmented appearance, and the dolines and uvalas in the area are classified as small dolines and uvalas (Bonacci, 2004; Brinkmann et al., 2008). In the study, the density of dolines and uvalas in this region, which are concentrated in the altitude steps in the range of 200-450 m, is explained by the presence of neotectonic reactivation and related faults, rather than climatic effects. It is estimated that the erosion cycle will at these slope grades until the karst base level is reached. It has been observed that dolines and uvalas with flanks greater than 15% have a degraded structure. While the average depth of the dissolution dolines are as 2.5 m, the average depth of the uvalas are 11.8 m. Available data suggest that the depth of karst shapes has a positive correlation with the fault presence. It is seen that majority of dolines and uvalas and all of the poljes overlap with faults. The elongation direction (EA α) of dolines and uvalas have a very close relationship with the azimuthal strikes of the faults and overlap in many places. Most of the dolines (65%) and uvalas (76%) in the peninsula are elongated in nature. It has been determined that almost half of the uvalas in the field are located exactly on a fault.

Based on the lithology, it has been observed that there are more karstic shapes on the neritic limestones compared to the pelagic limestones. This is because, neotectonic faults affect neritic limestones more than pelagic limestones. In addition, joints and faults, especially nappes, that developed parallel to the Bozburun and Selimiye faults intensifies and trigger karstification.

Table 3- Some characteristics of poljes determined in this study (Gams, 1978, 1998; Ford and Williams, 1989; Bonacci, 2004).

Name of polje (from north to south)	Area (km^2)	Morphological characteristic	Elongation ratio (R_E) = (Long axis/short axis)	Elongation Direction (E_A α)	The altitude of the deepest point of the sole. (m)	Lithology of the polje.	Polje depth (altitude difference between the highest and lowest point of the polje basin) -m).	Diameter/depth = Pitting ratio (R_P)
Hacıağaç Polje (P1)	0.28	Boundary	1.52 (semi-elliptical)	-	506	Limestone (pelagic)	271	12.22
Kuyucak Polje (P2)	0.29	Structural	1.76 (elliptical)	NE-SW	505	Limestone (pelagic)	155	19.72
Osmaniye Polje (P3)	1.08	Border	4.77 (elongated)	NE-SW	415	Breccia (limestone predominant)	181	31.33
Bayırköy Polje (P4)	1.61	Boundary	1.19 (circular)	-	154	Limestone (Neritic)-Dolomite-Breccia (Limestone predominant)	611	13.87
Kızılköy Polje(P5)	1.32	Boundary	1.23 (circular)	-	232	Limestone (Neritic)-Dolomite-Breccia (Limestone predominant)	241	21.16
Selimiye Polje (P6)	0.46	Boundary	1.53 (semi-elliptical)	-	60	Limestone (neritic)	360	8.17
Avlana Polje (P7)	0.26	Boundary	2.01 (elongated)	E-W	70	Limestone (neritic)	349	***7.95 (Deep)***
Ortaören Polje (P8)	0.40	Boundary	2.45 (elongated)	NE-SW	84	Limestone (pelagic)	192	17.63
Söğüt Polje(P9)	0.85	Boundary	1.6 (semi-elliptical)	-	195	Breccia (Limestone predominant)-Limestone (neritic)	348	14.64
Ağlan Polje (P10)	0.33	Structural	6.76 (elongated)	NE-SW	246	Limestone (neritic)	172	28.09
Taşlıca Polje (P11)	1.5	Structural	3.11 (elongated)	NE-SW	182	Limestone (neritic)	388	26.50
Sindilli Polje (P12)	0.66	Structural	4.19 (elongated)	NE-SW	124	Limestone (neritic)	386	***49.96 (Shallow)***
Serçelimanı Polje (P13)	0.25	Structural	4.44 (elongated)	NNE-SSW	17	Limestone (neritic)	97	34.42

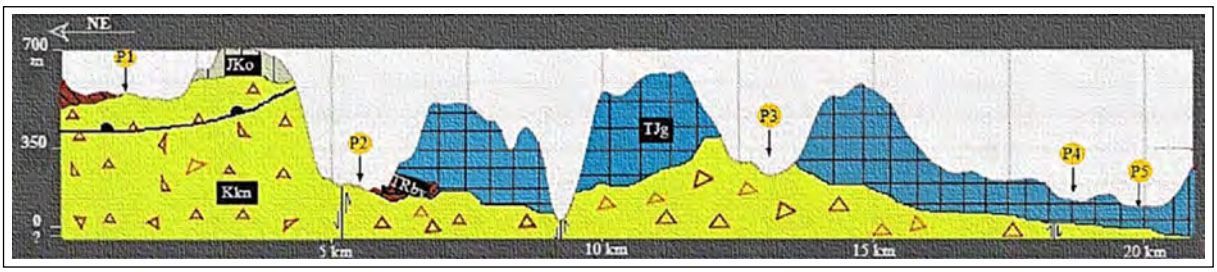

Figure 16- A cross section showing some poljes in the study field Hacıağaç Polje (P1), Kuyucak Polje (P2), Osmaniye Polje (P3), Bayırköy Polje (P4), Kızılköy Polje (P5), NE (Northeast), TRby: Bayırköy Formation, TRJg: Güverdağı Formation, JKo: Orhaniye Formation, Kkn: Karanasıflar Formation; shaped on the section Google Earth Pro and it has been scaled to Şenel and Bilgin (2010).

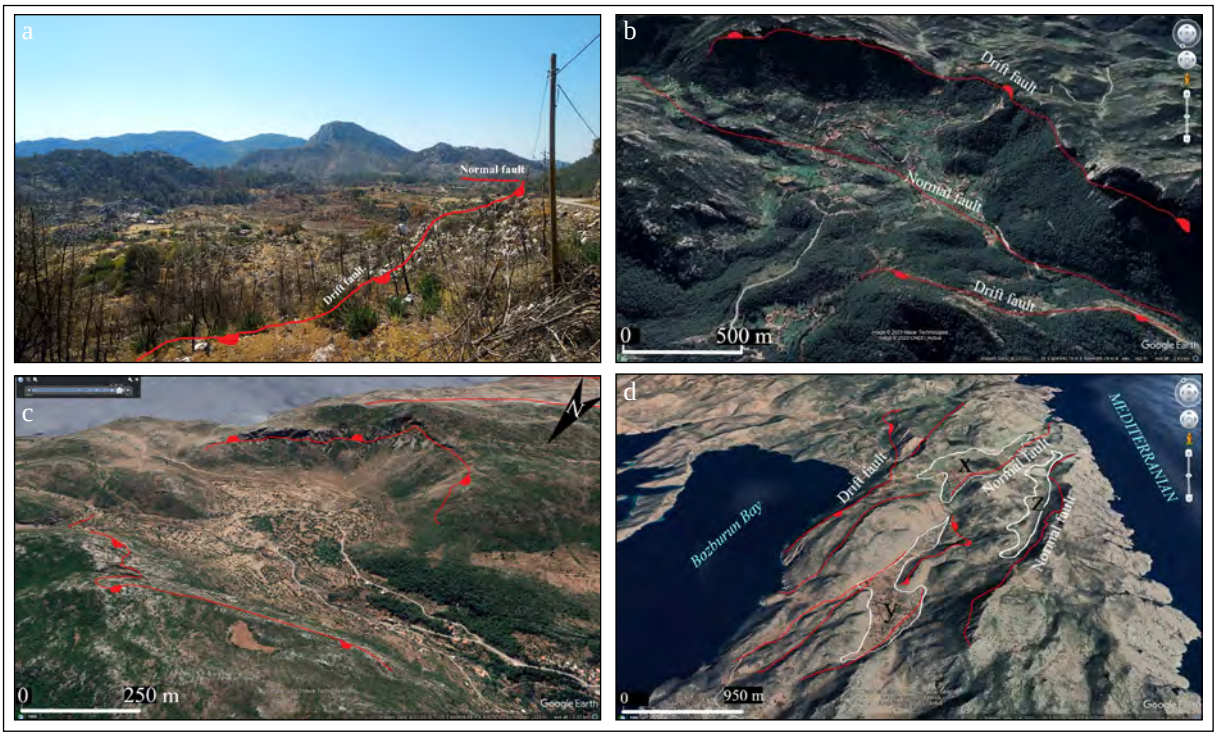

Figure 17- a) View of the Osmaniye Polje from northwest, b) Google Earth image of the Bayır Polje; the largest polje occured in the intersection of the faults in the study area, c) the Söğüt polje occured under the control of a low angle thrust fault, and d) x, y and z (Taşlıca, Sindilli (Aşağı Taşlıca) and Ağlana Polje). A view from the south almost parallel to the faults.

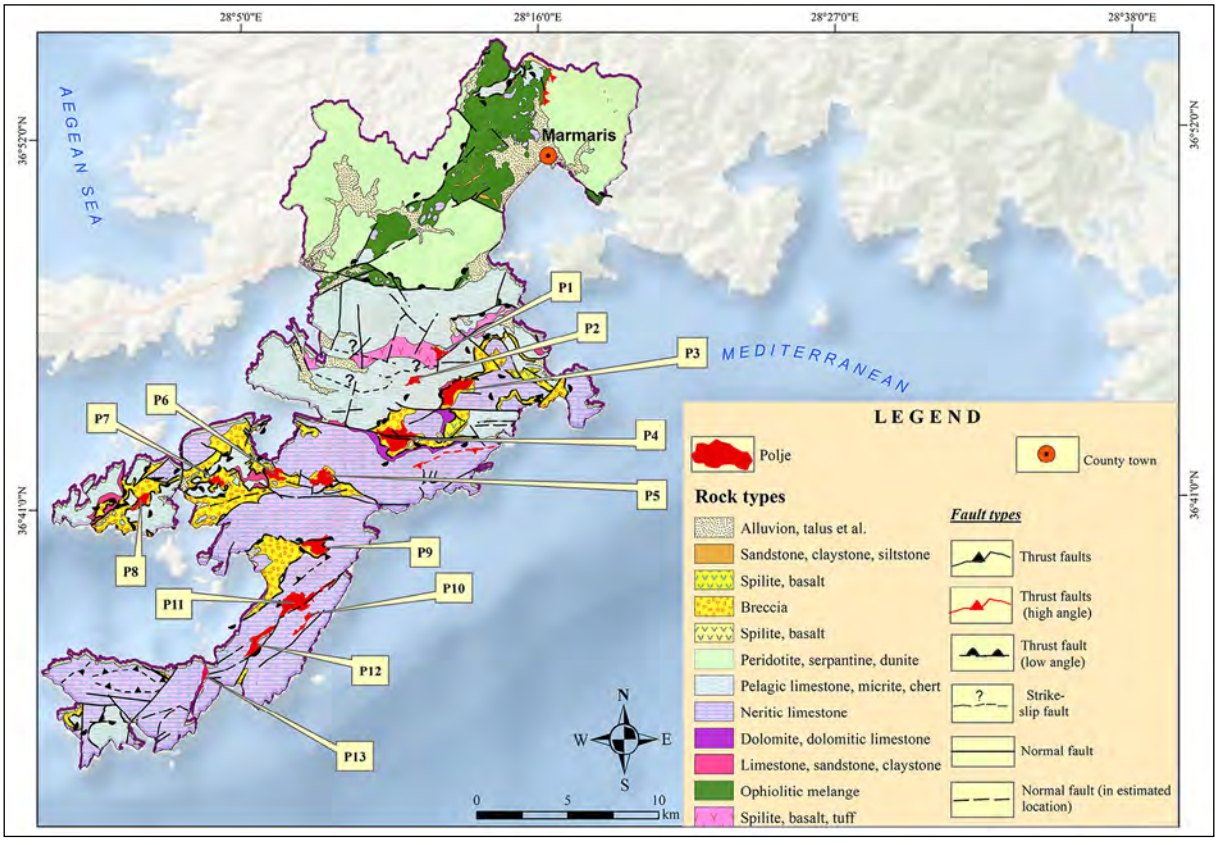

Figure 18- Figure showing the geological elements and polje locations.

Based on the literatüre, poljes with an area between 0.5 km^2 and 10 km^2 are considered as small poljes (Bonacci, 2004). Based on the criteria suggested by Gams (1998), it is suggested here that 0.25 km^2 is more appropriate for the lower limit of small poljes within the scope of this study. 13 poljes meeting these characteristics have been found in the field based on the Gams (1998) and Bonacci (2004). It has been determined that eight of the poljes are classified as boundary while five of them are classified as structural type based on the origin. The main elongation directions are NE-SW in ellipsoidal karst shapes. Circular or semi-elliptical (i.e., non-ellipsoidal) karst shapes predominantly coincide with the different fault intersections in this study.

Acknowledgements

This study was produced within the scope of the doctoral thesis A new suggestion for torrent and flood management: Bozburun Peninsula (Muğla) example completed by Efekan ÖZKAN at the University of Uşak, Department of Geography. İ.E and S.P determined the framework and general lines of the subject and provided literature and technical support.

References

Aguilar, Y., Bautista, F., Mendoza, M. E., Frausto, O., Ihl, T. 2016. Density of karst depressions in Yucatán State, Mexico. Journal of Cave and Karst Studies 78(2), 51-60.

Akay, E., Uysal, Ş. 1988. Post-Eocene tectonics of the Central Taurus Mountains. Bulletin of the Mineral Research and Exploration (MTA) 108, 23-34.

Akdeniz, N. 2011. 1:100.000 Ölçekli Türkiye Jeoloji Haritaları, Denizli-N22, No: 164. Maden Tetkik ve Arama Genel Müdürlüğü Yayınları, No: 164, Ankara.

Avcı, V., Günek, H. 2015. Uludere Havzası'nın (Bingöl) jeomorfolojik özelliklerinin belirlenmesinde morfometrik analizlerin kullanımı. Adıyaman Üniversitesi Sosyal Bilimler Enstitüsü Dergisi 21, 745-766.

Avcı, V., Kıranşan, K. 2017. Darköprü Deresi Havzası'nda (Bingöl) tektonik etkinin morfometrik analizlerle belirlenmesi. The Journal of International Social Research 10(48), 270-284.

Avcı, V., Sunkar, M. 2017. Jeomorfik indislerle Varto Havzası'nda (Muş) tektonik aktivitenin belirlenmesi (Determination of tectonic activity in Varto Basin (Muş) with geomorphic indices). The Journal of International Social Sciences, Fırat University 29(2), 19-38.

Aydın, S., Tuncer, K. 2021. Bozdağ'da (Denizli) dolinlerin morfometrik özellikleri (Morphometric properties of dolines in Bozdağ (Denizli). Turkish Geographical Review 78, 33-48.

Bahadır, M., Özdemir, M. A. 2011. Acıgöl Havzası'nın sayısal topoğrafik analiz yöntemleri ile morfometrik jeomorfolojisi (Morphometric geomorphology of Acıgöl Basin with numerical topographic analysis methods). Journal of International Social Research 4(18), 323-344.

Basso, A., Bruno, E., Parise, M., Pepe, M. 2013. Morphometric analysis of sinkholes in a karst coastal area of Southern Apulia (Italy). Environmental Earth Science 70, 2545–2559.

Bilgin, Z. R., Metin, Y., Çörekçioğlu, E., Bilgiç, T., Şan, Ö. 1997. Bozburun-Marmaris-Köyceğiz- Dalaman (Muğla) dolayının jeolojisi. General Directorate of Mineral Research and Exploration Report, No: 10008, Ankara (unpublished).

Bonacci, O. 2004. Poljes. Gunn, J. (Ed.). Encyclopedia of Caves and Karst Science. Fitzroy Dearborn Publishers. London, 1279-1282.

Bondesan, A., Meneghel, M., Sauro, U. 1992. Morphometric analysis of dolines. International Journal of Speleology 21(1), 1-55.

Brinkmann, R., Parise, M., Dye, D. 2008. Sinkhole distribution in a rapidly developing urban environment. Hillsborough County, Tampa Bay Area, Florida. Engineering Geology 99, 169-184.

Cürebal, İ. 2004. Madra Çayı Havzası'nın hidrografik özelliklerine sayısal yaklaşım. Balıkesir Üniversitesi Sosyal Bilimler Enstitüsü Dergisi 7(11), 11-24.

Cvijic, J. 1893. Das Karstphanomen. Versuch einer morphologichen monographie. Geographische Abhandlungen 5(3), 218-329.

Day, M. 1976. The morphology and hydrology of some Jamaican Karst Depressions. Earth Surface Processes and Landforms 1(2), 111-129.

Day, M. 1983. Doline morphology and development in Barbados. Annals of the Association of American Geographers 73(2), 206-219.

Dikbaş, A., Akyüz, H. S., Basmenji, H., Kırkan, E. 2022. Earthquake history of the Gökova Fault Zone by paleoseismologic trenching, southwest Turkey. Natural Hazards 112, 2695-2716.

Doğan, U. 1996. Polye ve fluvio-karstik depresyonlar (Seydişehir'in güneybatısından örnekler). Türkiye Coğrafyası Dergisi 5, 229-246.

Doğan, U. 2003. Sarıot Polje, Central Taurus (Turkey). A border polje developed at the contact of karstic and non-karstic lithologies. Cave and Karst Science 30(3), 117-124.

Doğan, U. 2004. Dolin sınıflamasında yeni yaklaşımlar. Gazi Eğitim Fakültesi Dergisi 24(1), 249-269.

Doğan, U., Yeşilyurt, S. 2004. Gypsum karst south of İmranlı. Cave and Karst Science 31(1), 7-14.

Doğan, U., Koçyiğit, A., Gökkaya, E. 2017. Development of the Kembos and Eynif Structural Poljes. Morphotectonic evolution of the Upper Manavgat River Basin, Central Taurides, Turkey. Geomorphology 278, 105-120.

Doğaner, S. 1999. Bozburun Yarımadası coğrafi ortam ve insan. Coğrafya Dergisi 7, 29-56.

Ege, İ. 2015*a*. Gezit Polyesi (Kozan/Adana). Akademik Sosyal Araştırmalar Dergisi 3(17), 177-199.

Ege, İ. 2015*b*. Paşalı Polyesi (Feke/Adana) [Paşalı Polje (Feke/Adana)]. The Journal of International Social Research 8(40), 384-402.

Ege, İ. 2017. Polyelerin sınıflandırılması ve Kestelce Polyesi'nin (Kilis) jeomorfolojik özellikleri [Classification of poljes and geomorphological features of Kestelce Polje (Kilis)]. Future Visions Journal 1(1), 33-51.

Ege, İ., Duman, N. 2020. Maymun Dağı (Çardak-Denizli/ Dazkırı-Afyonkarahisar)'nın morfotektonik özelliklerinin Coğrafi Bilgi Sistemleri (CBS) ile belirlenmesi. Turkish Studies 15(1), 278-307.

Ege, İ., Polat, S., İzmirli, E. 2019. Özdemirci (Çivril – Denizli) Havzası'nın morfotektonik özelliklerinin Coğrafi Bilgi Sistemleri (CBS) ile belirlenmesi. Mustafa Kemal Üniversitesi Sosyal Bilimler Enstitüsü Dergisi 16(44), 141-167.

Ekmekçi, M. 2003. Review of Turkish karst with emphasis on tectonic and palaeogeographic controls. Acta Carsologica 32(2), 205-218.

Erakman, B., Meşhur, M., Gül, M. A., Alkan, H., Öztaş, Y., Akpınar, M. 1982. Fethiye-Köyceğiz-Elmalı-Kalkan arasında kalan alanın jeolojisi (Geology of the area between Fethiye-Köyceğiz-Elmalı-Kalkan). Türkiye Sixth Petroleum Congress, April, 1982, Ankara, 23-31.

Erginal, A. E., Cürebal, İ. 2007. Soldere Havzası'nın jeomorfolojik özelliklerine morfometrik yaklaşım: Jeomorfik indisler ile bir uygulama. Selçuk Üniversitesi Sosyal Bilimler Enstitüsü Dergisi 17, 203-210.

Erol, O. 1983. Türkiye'nin genç tektonik ve jeomorfolojik gelişimi. Jeomorfoloji Dergisi 11, 1-22.

Erol, O. 1990. Batı Toros Dağları'nın messiniyen paleojeomorfolojisi ve neotektoniği (Messinian paleogeomorphology and neotectonics of the Western Taurus Mountains). Türkiye Petroleum Congress, 16-20 April 1990, 82-91.

Ersoy, Ş. 1990. Batı Toros (Likya) Napları'nın yapısal öğelerinin ve evriminin analizi. Jeoloji Mühendisliği 37, 5-16.

Ersoy, Ş., Altınok, Y., Yalçıner, C. A. 2000. Güneybatı Anadolu'nun neotektonik yapılarına genel bir bakış ve bölgenin deprem etkinliği. III. Ulusal Kıyı Mühendisliği Sempozyumu, 5 Ekim 2000, Çanakkale, 115-128.

Ford, D. C. Williams, P. 1989. Karst Geomorphology and Hydrology. Springer Dordrecht, 601.

Ford, D. C. Williams, P. 2007. Karst Hydrogeology and Geomorphology. John Wiley, 562.

Gams, I. 1978. The Polje: The Problem of Definition. Zeitschrift für Geomorphologie 22(2), 170-181.

Gams, I. 1998. Geomorphogenetics of The Classical Karst- Kras. Morfogenetika Klasičnega Krasa. Slovenska akademija znanosti in umetnosti, 18.

Geçen, R., Ölmez, İ. 2017. Beyazçay Havzası'nın (Hatay) jeomorfometrik analizler ile değerlendirilmesi. Uluslararası Jeomorfoloji Sempozyumu, 12-14 Ekim 2017, Elazığ, 212-221.

Gündoğdu, E., Özden, S., Güngör, T. 2015. Simav (Kütahya) ve yakın civarının Geç Senozoyik yaşlı jeodinamik evrimi. Türkiye Jeoloji Bülteni 58(1), 23-37.

Gündoğdu, E., Özden, S., Bekler, T. 2020. Sındırgı Fayı ve Düvertepe Fay Zonu yakın civarının kinematik ve sismotektonik özellikleri: Batı Anadolu (Türkiye). Journal of Advanced Research in Natural and Applied Sciences 6(2), 378-395.

Günhan, Ü., Öner, E. 2021. Epikarstik kuşağın denetiminde gelişmiş mağara örneği olarak: İkiz İncirli Çengirek (Marmaris- Muğla), Coğrafya Dergisi 43, 197-216.

Günhan, Ü., Vardar, S., Öner, Ö. 2018. Mağaralar ve Bozburun Yarımadası'ndan örnekler (Marmaris-Muğla), [Caves and examples from Bozburun Peninsula (Marmaris-Muğla)]. International Geography Symposium on the 30th Anniversary of Turkish Geography Research and Application Center, 3-6 October 2018, Ankara, 1289-1304.

İzmirli, E., Ege, İ. 2019. Gökpınar Çayı Havzası'nın jeomorfometrik indisler ile incelenmesi (Investigation of Gökpınar Stream Basin with geomorphometric indices). Future Visions Journal 3(3), 41-57.

Keskin, İ., Yılmaz, I. 2016. Morphometric and geological features of karstic depressions in gypsum (Sivas, Turkey). Environmental Earth Science 75(12), 1040.

Kırkan, E., Akyüz, H. S., Basmenji, M., Dikbaş, A., Zabcı, C., Yazıcı, M., Erturaç, K. M. 2023. Earthquake history of the Milas Fault. An active dextral fault in an extensional province (Southwest Anatolia, Türkiye). Natural Hazards 116 (2).

Köle, M. M. 2016. Devrez Çayı Vadisi'nin tektonik özelliklerinin morfometrik indisler ile araştırılması. İstanbul Üniversitesi Edebiyat Fakültesi Coğrafya Dergisi 33, 21-36.

Kranjc, A. 2013. Classification of closed depressions in carbonate karst. Treatise on Geomorphology 6, 104-111.

Nazik, L., Poyraz, M. 2015. Türkiye karst morfolojisinde neotektoniğin rolü. IV. Ulusal Jeomorfoloji Sempozyumu, 15-17 Ekim 2015, Samsun, 203-213.

Nazik, L., Poyraz, M. 2016. A characteristic zone representing quaternary development of karstic morphology in Turkey: Central Taurides-Central Anatolia-Central Pontides Karstic Zone. The Quaternary Symposium of Turkey, 11 May 2016, İstanbul Teknik Üniversitesi, İstanbul.

Nazik, L., Poyraz, M. 2017. Türkiye karst jeomorfolojisi genelini karakterize eden bir bölge: Orta Anadolu Platoları Karst Kuşağı. Türk Coğrafya Dergisi 68, 43-56.

Nazik, L., Tuncer, K. 2010. Türkiye karst morfolojisinin bölgesel özellikleri. Türk Speleoloji Dergisi, Karst ve Mağara Araştırmaları 1, 7-19.

Nazik, P., Poyraz, M., Karabıyıkoğlu, M. 2019. Karstic landscapes and landforms in Turkey, Landscapes and Landforms of Turkey 5, 181-196.

Oakes, H. 1958. Türkiye toprakları. İzmir Türk Ziraat Mühendisleri Birliği Yayını, 18.

Özdemir, H. 2007. Havran Çayı Havzası'nın (Balıkesir) CBS ve uzaktan algılama yöntemleriyle taşkın ve heyelan risk analizi. PhD Thesis, İstanbul University, 262.

Özdemir, H. 2011. Havza morfometrisi ve taşkınlar, fiziki coğrafya araştırmaları; sistematik ve bölgesel, Türk Coğrafya Kurumu Yayınları 5, 507-526.

Öztürk, B., Erginal, A. E. 2008. Bayramdere Havzası'nda (Biga Yarımadası- Çanakkale) havza gelişiminin morfometrik analizler ve jeomorfolojik indislerle incelenmesi. Türk Coğrafya Dergisi 50, 61-68.

Öztürk, M. Z. 2018*a*. Orta Toroslar'da Dolinlerin Dağılışı ve Morfometrik Özellikleri. Kriter Yayınevi, 102.

Öztürk, M. Z. 2018*b*. Karstik kapalı depresyonların (dolinlerin) morfometrik analizleri. Coğrafya Dergisi 36, 1-13.

Öztürk, M. Z. 2020. Fluvio-karstic evolution of the Taşeli Plateau (Central Taurus,Turkey). Turkish Journal of Earth Sciences 29(5), 733-746.

Öztürk, M. Z., Şener, M. F., Şener, M., Şimşek, M. 2018. Structural controls on distribution of dolines on Mount Anamas (Taurus Mountains, Turkey). Geomorphology 317, 107-116.

Pichon, L. X., Angelier, J. 1979. The Hellenic Arc and Trench System. A key to the neotectonic evolution of the Eastern Mediterranean area, Tectonophysics 60, 1-40.

Polat, S., Güney, Y. 2013. Uşak ili arazisinde karstik şekiller. Marmara Coğrafya Dergisi 1(27), 440-475.

Saroli, M., Albano, M., Moro, M., Falcucci, E., Gori, S., Galadini, F., Petitta, M. 2022. Looking into the entanglement between karst landforms and fault activity in carbonate ridges. The Fibreno Fault System (Central Italy). Frontiers in Earth Science, 10, April 2022, 1-16.

Sarp, G., Geçen, R., Toprak, V., Düzgün, Ş. 2011. Morphotectonic properties of Yeniçağa Basin area in Turkey, 34th International Symposium on Remote Sensing of Environment, April 10-15, 2011, Sydney.

Seyitoğlu, G., Scott, B. C. 1991. Late Cenozoic crustal extension and basin formation in west Turkey. Geological Magazine 128, 155-166.

Shanov, S., Kostov, K. 2014. Dynamic Tectonics and Karst. Springer Berlin, 123.

Sür, A. 1994. Karstik yerşekilleri ve Türkiye'den örnekler. Ankara Üniversitesi Türkiye Coğrafya Araştırma ve Uygulama Merkezi Dergisi 3, 1-29, Ankara.

Şahin, C. 2005. Türkiye Fiziki Coğrafyası. Gündüz Eğitim ve Yayıncılık, 375.

Şenel, M., Bilgin, R. Z. 2010. 1:100.000 scale geological maps of Turkey. Marmaris O20 sheet. Mineral Research and Exploration Directorate of Türkiye (MTA), Ankara.

Şenel, M., Akdeniz, N., Öztürk, E. M., Özdemir, T., Kadınkız, G., Metin, Y., Öcal, H., Serdaroğlu, M., Örçel, S. 1994. Fethiye (Muğla)-Kalkan (Antalya) ve kuzeyinin jeolojisi. Maden Tetkik ve Arama Genel Müdürlüğü, Rapor No: 9761. Ankara (unpublished).

Şengör, A. M. C., Görür, N., Şaroğlu, F. 1985. Strike-slip faulting and related basin formation in zones of tectonic escape: Turkey as a case study. The Society Economic Paleontologist and Mineralogists 37, 227-264, Tulsa.

Şimşek, M., Öztürk, Z. M., Doğan, U., Utlu, M. 2021. Toros polyelerinin morfometrik özellikleri. Coğrafya Dergisi 42, 101-119.

Taşlıgil, N. 2008. Datça-Bozburun özel çevre koruma bölgesi ve turizm, Ege Coğrafya Dergisi 17 (1-2), 73-83.

Thery, J., Pubellier, M., Thery, B., Butterlin, J., Blondeau, A., Adams, C. 1999. Importance of active tectonics during karst formation; a middle eocene to pleistocene example of the Lina Moutains (Irian Jaya, Indonesia). Geodinamica Acta 12, 213–221.

Topal, S. 2018. Quantitative analysis of relative tectonic activity in the Acıgöl fault, southwest Turkey. Arabian Journal of Geosciences 11, April 2018, 198.

Topal, S., Keller, E., Bufe, A., Koçyiğit, A. 2016. Tectonic geomorphology of a large normal fault: Akşehir Fault, southwest Turkey. Geomorphology 259, 55-69.

Topuz, M., Karabulut, M. 2016. Limonlu ve Alata Havzaları'nın (Mersin-Erdemli) jeomorfometrik analizi. Turkish Studies 11(2), 1231-1250.

Tuncer, K. 2021. Aydoğdu, Kızılca, Ovacık ve Kırkoluk Polyelerinin (Tavas, Denizli) morfometrik özellikleri ve jeomorfolojik evrimi. Jeomorfolojik Araştırmalar Dergisi 7, 82-108.

Tuncer, K., Nazik, L. 2010. Türkiye karst morfolojisinin bölgesel özellikleri. Türk Speoloji Dergisi 1(1), 7-20.

Tur, H., Yaltırak, C., Elitez, I., Sankavak, K. T. 2015. Pliocene-Quaternary tectonic evolution of the Gulf of Gökova, southwest Turkey. Tectonophysics 638, 158-176.

Turoğlu, H. 1997. Mühendislik jeomorfolojisi. Marmara Coğrafya Dergisi 1, 257-266.

Uluğ, A., Duman, M., Ersoy, Ş., Özel, F. E., Avcı, M. 2005. Late Quaternary sea-level change, sedimentation and neotectonics of the Gulf of Gökova. Southeastern Aegean Sea. Marine Geology 221 (1-4), 381-395.

Uzun, M. 2014. Lale Dere (Yalova) Havzası'nın jeomorfolojik özelliklerinin jeomorfometrik analizlerle incelenmesi (Investigation of geomorphological parts of Lale Dere (Yalova) basin by geomorphometric analysis). Route Educational and Social Science Journal 1(3), 72-88.

White, W. B. 1969. Conceptual models for limestone aquifers. Groundwater 7(3), 15-21.

Williams, P. W. 1972. Morphometric analysis of polygonal karst in New Guinea. The Geological Society of America Bulletin 83(3), 761-796.

Yıldırım, A., Karadoğan, S. 2011. Raman Dağları güneyinde (Dicle Vadisi) morfometrik ve morfotektonik analizler. Dicle Üniversitesi Ziya Gökalp Eğitim Fakültesi Dergisi 16, 154-166.

Zorer, H., Tonbul, S. 2019. Başkale Havzası'nda havza gelişiminin jeomorfometrik analizlerle incelenmesi. Fırat Üniversitesi Sosyal Bilimler Dergisi 29(2), 19-38.

Bulletin of the Mineral Research and Exploration

http://bulletin.mta.gov.tr

Porphyry and epithermal Au-Cu systems of the Southern Caucasus and Northern Iran

Alexander G. TVALCHRELIDZE[a*]

[a] *Institute of Mineral Resources, Tbilisi State University, 11 Mindeli Str., 0186 Tbilisi, Georgia*

Research Article

Keywords:
Epithermal, Porphyry, Gold, Copper, Paleothermal Field.

ABSTRACT

This article presents tangible geological evidence for the coexistence of porphyry copper and epithermal gold systems within single polygenic deposits and provides a paleothermophysical model for their origins. A brief metallogenic analysis of the Southern Caucasus and Northern Iran has shown that such deposits are confined to long-living calc-alkaline island arcs and were formed during their orogenesis. Examples of complex Sonajil (Iran), Gharta, and Merisi (Georgia) deposits are considered. The investigation has shown that for combined porphyry and epithermal ore formation, some preconditions are suggested to exist: (i) a source of anomalous energy that exceeds the thermodynamics of the enclosing environment; (ii) the existence of a temperature gradient that determines conventional flows of fluids composed of endogenous and meteoric constituents (proven by rhythmical zoning of ore lodes); (iii) the stability of such conditions for a period of sulfide ore formation. However, such a process of sulfide ore formation cannot explain the formation of high sulfidation gold deposits. The precipitation of native gold requires phreatic collapse in the ore conduit channel, already after the formation of hydrothermally altered rocks, and this event results in the creation of either hydrothermal breccias often with jigsaw-fit texture or brecciated vuggy silica where host rocks and hydrothermally altered rocks are cemented by a gold-bearing quartz matrix.

Received Date: 24.04.2023
Accepted Date: 21.11.2023

1. Introduction

By the end of the recent and the beginning of the new centuries, our understanding of the metallogenic setting and genesis of gold, copper, and polymetallic mineralization in the Southern Caucasus and Northern Iran, as well as of the entire Tethys Belt, has dramatically changed. Previously, they were thought to represent perhaps simultaneous but separate products of different ore-forming processes. Today, however, they are considered as deposits united by a common origin and separated from their original magmatic sources by varying distances. For instance, gold and base metal deposits in the Southern Caucasus were traditionally classified into three main types: Volcanogenic gold and base metal massive sulfides of the Kuroko type, hydrothermal gold and polymetallic vein deposits, and porphyry copper (with or without gold) stockwork veins (Tvalchrelidze, 1980 and 1984). This approach significantly limited the possibilities for new discoveries, as exploration was based on incorrect assumptions. As a result, the resource base of the regional stakeholder countries began to deplete. For example, at the beginning of the new millennium, Türkiye gold resource base was considered to be extremely limited, and the prospects for new discoveries were viewed pessimistically (Engin, 2003).

Identification of low, intermediate, and high sulfidation epithermal gold deposits, investigation of

Citation Info: Alexander, G. T., 2024. Porphyry and epithermal Au-Cu systems of the Southern Caucasus and Northern Iran. Bulletin of the Mineral Research and Exploration 174, 37-53. https://doi.org/10.19111/bulletinofmre.1394073

**Corresponding author: Alexander G. TVALCHRELIDZE, sandrotval@gmail.com*

their typomorphic features, and the development of a comprehensive methodology for their prospecting and exploration (Arribas, 1995; Hedenquist, 2000; Goldfarb et al., 2001; Payot et al., 2005; John et al., 2018; Wang et al., 2019) led to fast discoveries of new gold deposits in Türkiye (Oyman et al., 2003; Diarra et al., 2019; Aluç et al., 2020; Gülyüz et al., 2020), the Lesser Caucasus (Bogdanov et al., 2013; Moritz et al., 2017; Veliyev et al., 2018; Imamverdiyev et al., 2021), and Iran (Mehrabi et al., 2008; 2014; Aghazadeh et al., 2015; Heidari et al., 2015; Sholeh et al., 2016). These discoveries were extremely important for improving the resource base of the corresponding countries, which is vital for their economic development (Tvalchrelidze, 2003). Correspondingly, the current state of mining, for instance in Türkiye, has significantly improved (Ersoy, 2022; Hastorun, 2022).

New metallogenic models have proven that both epithermal and porphyry deposits are related to the development of calc-alkaline island arcs during subduction and orogenic stages (Yigit, 2006; 2009; Mederer et al., 2013; Moritz et al., 2016). Therefore, porphyry and epithermal deposits are traditionally described separately, without paying any attention to a possible genetic relation between them (Ghaderi et al., 2018; Kuşcu et al., 2019). Even the models for these types of mineralization are generated separately (Sinclair, 2007; Taylor, 2007; Berger et al., 2008; John, 2010; John et al., 2018). Commonly, these models are based on typomorphic features of world-scale classical mines (see, for instance, Boomeri et al., 2010). However, already in 2000, R.H. Sillitoe outlined a genetic unity of porphyry copper and epithermal gold mineralization (Sillitoe, 2000). During the following years, a lot of evidence of gold presence in porphyry copper deposits was released (Shafiei and Shahabpour, 2008; Hajalilou and Aghazadeh, 2016). Nonetheless, descriptions of real natural examples of telescoping and superposition of porphyry, low, intermediate, and high sulfidation epithermal systems are extremely rare, and I found no comprehensive numeric models of such systems. That is why in this article, I will both present tangible geological evidence for the coexistence of such systems and attempt to provide a corresponding paleothermophysical model for their genesis.

2. Metallogenic Setting of Epithermal and Porphyry Systems

2.1. The Southern Caucasus

The distribution of epithermal gold and porphyry copper (± gold) systems in the Caucasus, as shown in Figure 1, reveals that the deposits are uniquely positioned within the Lesser Caucasus and confined to two tectonic zones. The first is the Late Cenozoic rift zone (known as the Adjara-Trialeti zone), which extends beyond Georgia into Türkiye (Adamia et al., 2011). Originating in the Late Alpine (Paleogene-Neogene) period atop the Cretaceous cover of the Transcaucasian Microplate, today it is overlaid by the intermountain trough (Adamia et al., 1981). Within this zone, Neogene homodrome basalt-andesite-rhyolite volcanism expands from the rift's eastern edge (where tuffaceous sandstones and clays form a rhythmical series) towards the west (where typical basaltic and then andesitic volcanic flows are succeeded by rhyiodacitic and rhyolitic volcanic cones interspersed with tuffites). Alkalinity gradually increases in the same direction. In the Late Neogene, several quartz diorite to quartz monzonite massifs were intruded, predominantly in the rift's central and western, more tectonically active parts. Orogenesis here concluded by the end of the Neogene, just before the Quaternary period. The described volcanic-plutonic affinity is marked by several typomorphic deposits, displaying signs of porphyry copper ores in conjunction with either high sulfidation gold mineralization or intermediate sulfidation gold-polymetallic lodes. These types of mineralization will be briefly described below.

The second zone — the Middle Jurassic-Cretaceous Island arc — is identified as the Somkhito-Karabakh zone of global extent (Tvalchrelidze, 1980; 1984). This volcanic belt spans territories of Armenia, Azerbaijan, Georgia (where it is covered by Cenozoic, Early Quaternary, andesite-basaltic nappes), and then extends to Türkiye and beyond. The modern metallogenic model of this zone has been elaborated by an international team of Swiss, Georgian, Armenian, and Azeri geologists (Mederer et al., 2013; Richards, 2015; Moritz et al., 2016; 2017).

In both zones, two volcanic-plutonic ore-bearing affinities have developed. The Middle Jurassic

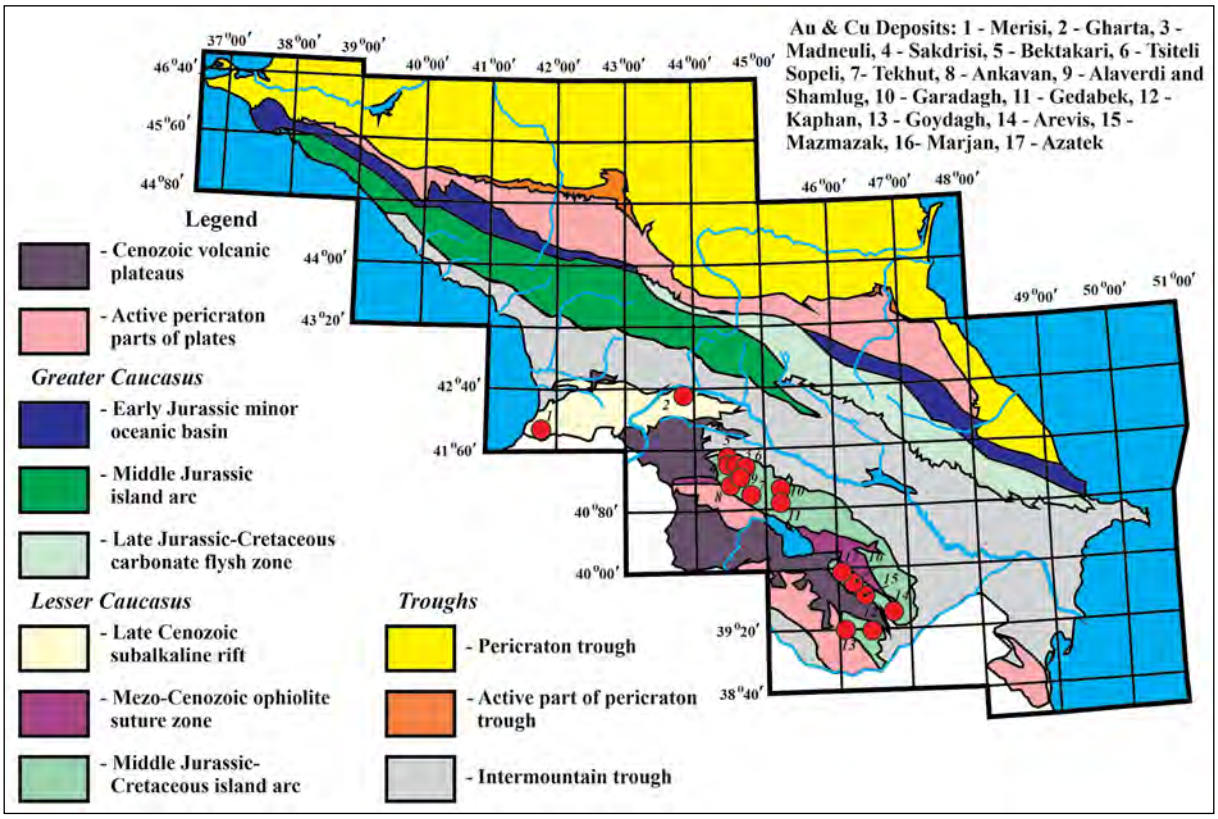

Figure 1- Distribution of the most important porphyry copper (± gold) and high, intermediate, and low sulfidation gold deposits of the Caucasus. Map of metallogenic zoning is modified from Adamia et al. (2011) by author.

rocks, lying directly upon the crystalline basement of the Transcaucasian Microplate, start with a basal conglomerate that overlaps Paleozoic granites. In Armenia and Azerbaijan, a thick calk-alkaline subaqueous andesitic volcanic-sedimentary series has developed. However, north-westward towards Georgia, this island arc affinity decreases in thickness, and Middle Jurassic volcanic rock outcrops become rare. During Bathonian times, this affinity was intruded by vast quartz diorite bodies, one of which, the Shnokh-Kokhp massif, controls the world-class Tekhut Au-Cu porphyry mine (no. 7 in Figure 1) with ore reserves of 460 million tons and copper grade of 0.35% (Marutani, 2003). Cretaceous sediments in Armenia and Azerbaijan are represented only by limestones with insignificant thickness.

Conversely, in Georgia, the thickness of Cretaceous rocks sharply increases, hosting rich ore-bearing Cretaceous andesitic (minor basalt-andesite-dacite-rhyolite) calk-alkaline formation which formed numerous central-type volcanoes and vast fields of acid subaqual pyroclastics in intervocalic areas. This sequence is especially thick (up to 1-1.5 km) within the Bolnisi Mining District, which hosts the great majority of the country's gold and copper reserves (no 3-6 on Figure 1). The sequence is intruded by several quartz diorite bodies the significance of which in ore formation is discussed below.

Among the deposits of the Bolnisi Mining District, the largest one is Madneuli intermediate sulfidation mine with primary ore reserves of 93.1 million tons and metal inventories in them: copper – 542 thousand tons; zinc – 79.8 thousand tons; lead – 8.2 thousand tons; silver – 134 tons; gold – 53.8 tons (Tvalchrelidze, 2003). The mine is the main copper and gold producer in Georgia.

Petrology of both Middle Jurassic and Cretaceous volcanic-plutonic affinities was described in detail some 35 years ago (Tvalchrelidze, 1987).

2.2. Northern Iran

Figure 2 analyses the distribution of typomorphic porphyry copper (± gold) and primarily high

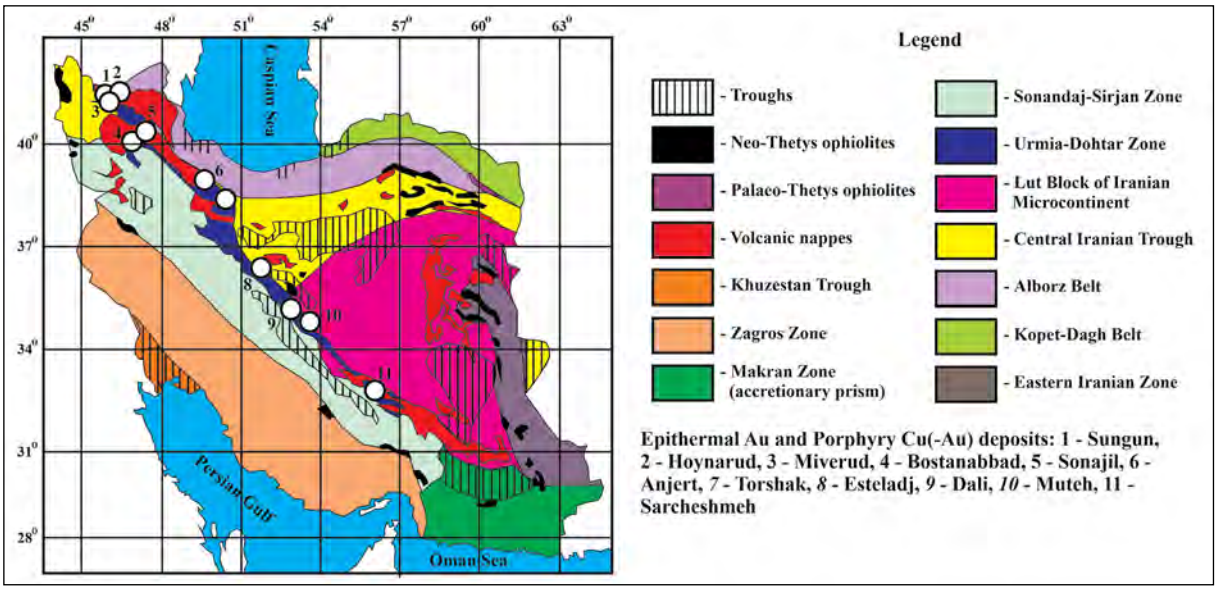

Figure 2- Distribution of typomorphic porphyry Cu (± Au) and epithermal gold deposits of Iran. Map of metallogenic zoning is drawn from Kaviani et al. (2009) modified by author.

sulfidation gold deposits of Iran. These deposits include world-class mines such as Sungun (no. 1 on Figure 2) with recoverable ore reserves of 861 million tons and copper grade of 0.6% (Hosseini et al., 2017) and Sarcheshmeh (no. 11 on Figure 2) with ore reserves of 1538 million tons and a copper grade of 0.58% (Boomeri et al., 2010).

It is evident from Figure 2 that all typomorphic deposits, without exception, are associated with the Urmia-Dokhtar metallogenic zone. This zone represents an andesitic island arc that underwent orogenesis in the Late Neogene – Early Quaternary period. During the 1980s, the extensive development of orogenic magmatism, with still active volcanoes like Sakhand and Sabalan, was not fully understood (Berberian and King, 1981), but it is now clear that this zone continues to be subject to ongoing subduction beneath the Iranian Microcontinent (Kaviani et al., 2009).

In Northern Iran, the Urmia-Dokhtar zone is overlapped by Early Quaternary basaltic nappes and borders the Alborz magmatic belt to the north and the Sanandaj-Sirjan metamorphic zone to the southwest. The latter represented a rift zone that had undergone orogenesis and metamorphism before the Alpine period (Kaviani et al., 2009; Richards, 2015).

Thus, both in the Southern Caucasus and Northern Iran, porphyry copper-gold as well as epithermal ore-forming systems are related to long-lived island arcs that have experienced relatively continuous subduction followed by active development of orogenic magmatism. As a rule, these systems form individual porphyry, high, intermediate, and low sulfidation deposits, but seldom do deposits bear features of different mineralization types. Below, such examples are considered.

3. Combination of Ore-Forming Systems

3.1. Porphyry and High Sulfidation Systems – Sonajil Deposit, Northern Iran

The Sonajil Deposit is located in the East Azerbaijan Province of Iran, near Heris city, approximately 85 km from Tabriz, the province capital. The deposit has been extensively explored by our international team. To date, recoverable reserves of high sulfidation gold ores have been estimated, and gold-producing open pit mines, a heap, and a Carbon-in-Leach (CIL) plant are under construction. The estimated total resources of the gold-bearing site are 7.6 million tons with gold grade of 1.5 g/t, hosting approximately 361 thousand troy ounces of the metal. Porphyry copper ores are currently under extensive exploration. All 12 drilled boreholes have intersected porphyry ores with an average copper grade of 0.4%. The explored vertical interval of mineralization now exceeds 600 m. In

these boreholes, the first indications of gold presence with commercial grades were identified.

Figure 3 presents the model geological map of the Sonajil deposit. The geological structure of the deposit is complex. The geological section begins with an Eocene volcanic suite of basalt-andesitic composition, which consists of basalt and andesite lavas, volcanic breccias of the same composition, tuffs, and tuffaceous volcanic-sedimentary rocks. In the ascending sequence, this suite is replaced by Miocene sandstones and marls. The overall sequence concludes with an Early Quaternary volcanic flow of basalt and dolerite composition, which occupies the highest hypsometric level of the terrain.

The Eocene volcanic sequence is intruded by two stages of an igneous complex. Outcrops of two phases of the Inchekh intrusive body are observed in the central part of the area. The first phase is composed of alkali rocks – monzonites and syenites, whereas the second phase consists of calc-alkaline quartz monzonites and microdiorites. These rocks exhibit porphyritic structures and can be interpreted as a root part of a volcano. The younger Sonajil intrusive stage has a well-expressed hypabyssal character and is represented by mica granites and monzonites.

The deposit comprises two sites. The epithermal high sulfidation gold mineralization site is situated 4.5 km southwestward from the porphyry copper deposit. The ore-bearing structure of this deposit trends northwestward (azimuth 320-340°), with a length of about 1400 m, a width from 10 to 50 m, and an incidence angle of 45-60° to the west-south-west. Ore mineralization is traced up to a depth of 200 m from the surface. Within this deposit, the gold-bearing body is presented by hydrothermal breccia, where fragments of hydrothermally altered (quartz + sericite) andesites are cemented by grey quartz. The quartz matrix of the breccias, occasionally accompanied by calcite, is remarkably thick (more than 200 m) from the surface. The breccia exhibits a jigsaw-fit texture, the origin of which has been detailed in several publications (Figure 4a, Cas et al., 2011).

Porphyry copper deposit, situated in the north-eastern part of the deposit, is presented by typical medium-grade ores in hydrothermally altered (quartz + enargite) intrusive rocks, mainly diorites of both Inchekh and Sonajil intrusive bodies (Figure 4b). The orebody is under extensive drilling campaign because prospects to discover a world class copper-gold deposit are very high.

Thus, the key features of the deposit important for further discussion are as follows:

1. Porphyry and high sulfidation epithermal sites are spatially separated.

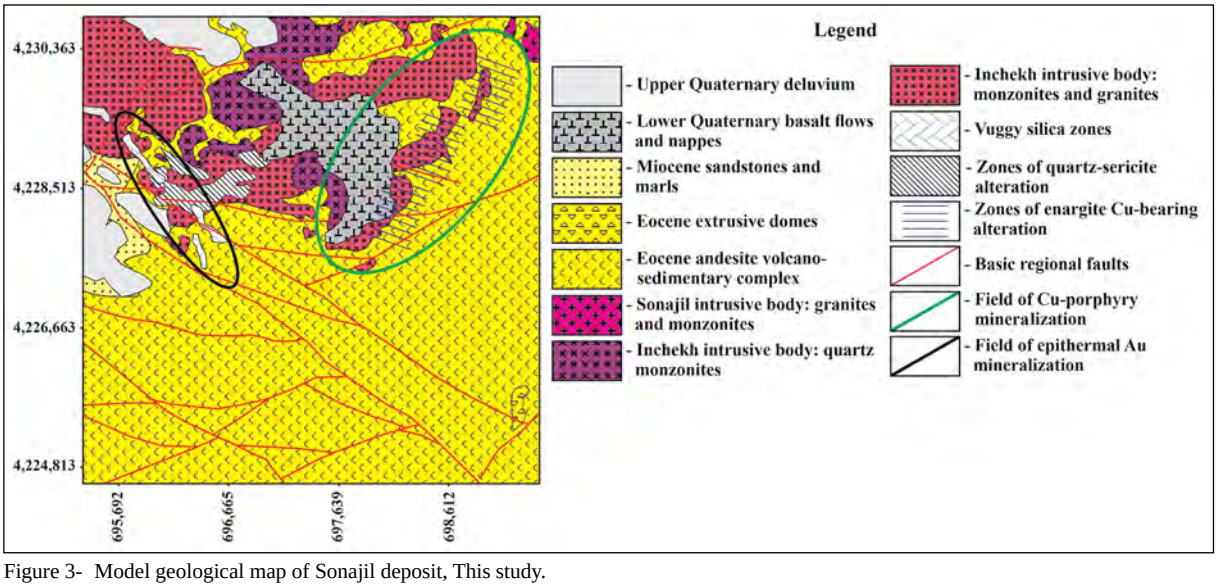

Figure 3- Model geological map of Sonajil deposit, This study.

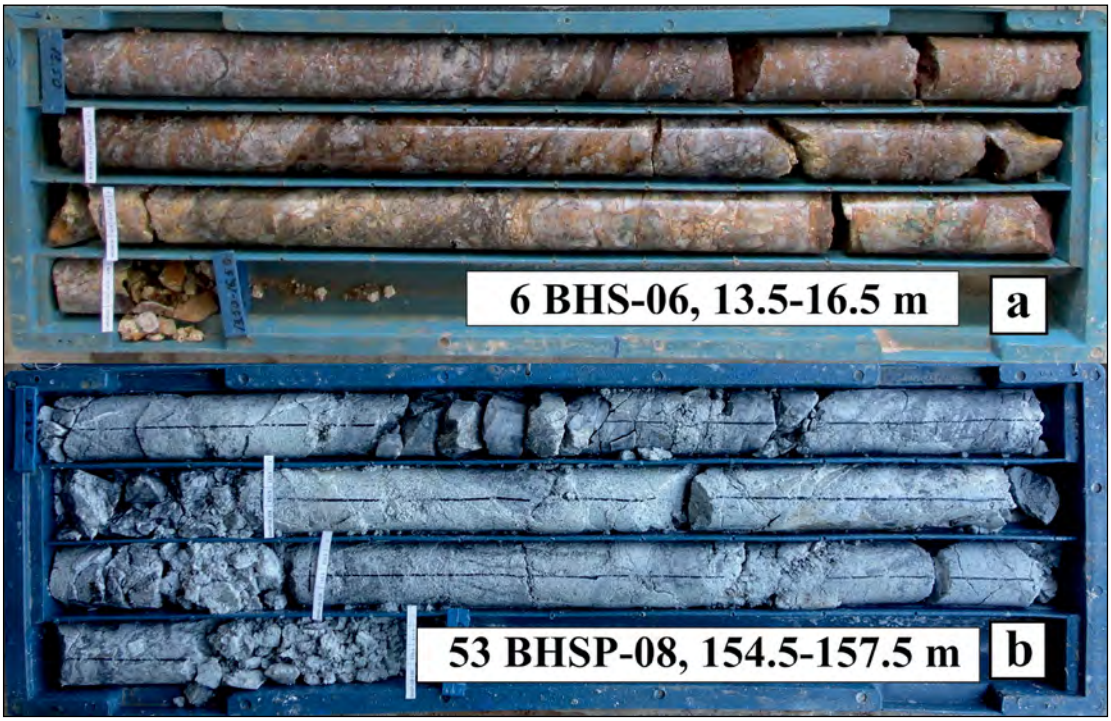

Figure 4- Typical ores of Sonajil deposit, a) gold ores presented by thin impregnation of free gold in the hydrothermal breccia with jigsaw-fit texture; debris of hydrothermally altered quartz-sericite rocks are cemented by quartz. Average Au grade of the interval is 1.41 g/t. b) porphyry gold-copper ores in hydrothermally altered diorites. Average grades of the interval: Copper – 0.56%, gold – 0.74 g/t.

2. Gold mineralization occurs in hydrothermal breccia, formed later than the country andesitic rocks were hydrothermally altered.

3.2. Vertical Zoning of Epithermal High Sulfidation and Porphyry Systems – Gharta Deposit, Georgia

The Gharta deposit is located in the Kareli District, Shida Kartli Region of Georgia, approximately 152.5 kilometers from Tbilisi, the capital city, at the northern slope of the Trialeti Ridge in the Lesser Caucasus. Metallogenically, it is situated at the north-eastern edge of the Adjara-Trialeti rift zone (Figure 1). The deposit has been the subject of extensive exploration by our international team. To date, having covered only about 15% of the deposit's area with a drilling campaign, we have already identified 9.1 million tons of high sulfidation gold with an average gold grade of 0.93 g/t and 62.8 million tons of porphyry copper ores with an average copper grade of 0.42%. A model geological map of the deposit is represented in Figure 5.

The geological structure of the deposit features an area covered by outcrops of Late Neogene intrusive body of quartz diorite composition, which has intruded into Paleogene-Lower Neogene rhythmical slates, argillites, and aleurolites, as well as Upper Cretaceous chemogenic limestones. The host rocks are mainly preserved as relics within the intrusive body and are only visible in the north-western part where the intrusive contact with the mentioned rhythmical slate suite is observed. Numerous mainly sub-latitudinal faults with steep, subvertical dips are present. The entire structure, including the ore zone, is inclined to the east at an angle of 35-45°.

The ore zone has an irregular ellipsoid shape and is presented by hydrothermally altered rocks developed exclusively within the intrusive rocks. Two contrasting types of metasomatic alterations were identified. Within the epithermal gold bonanza zones developed at upper horizons in the western flank of the mineralized zone, hydrothermally brecciated and often fractured vuggy silica is observed (Figure 6a), where debris of quartz diorite and early products of its hydrothermal alteration – quartz-sericite rocks are cemented by grey quartz. At deeper horizons, porphyry copper ores are

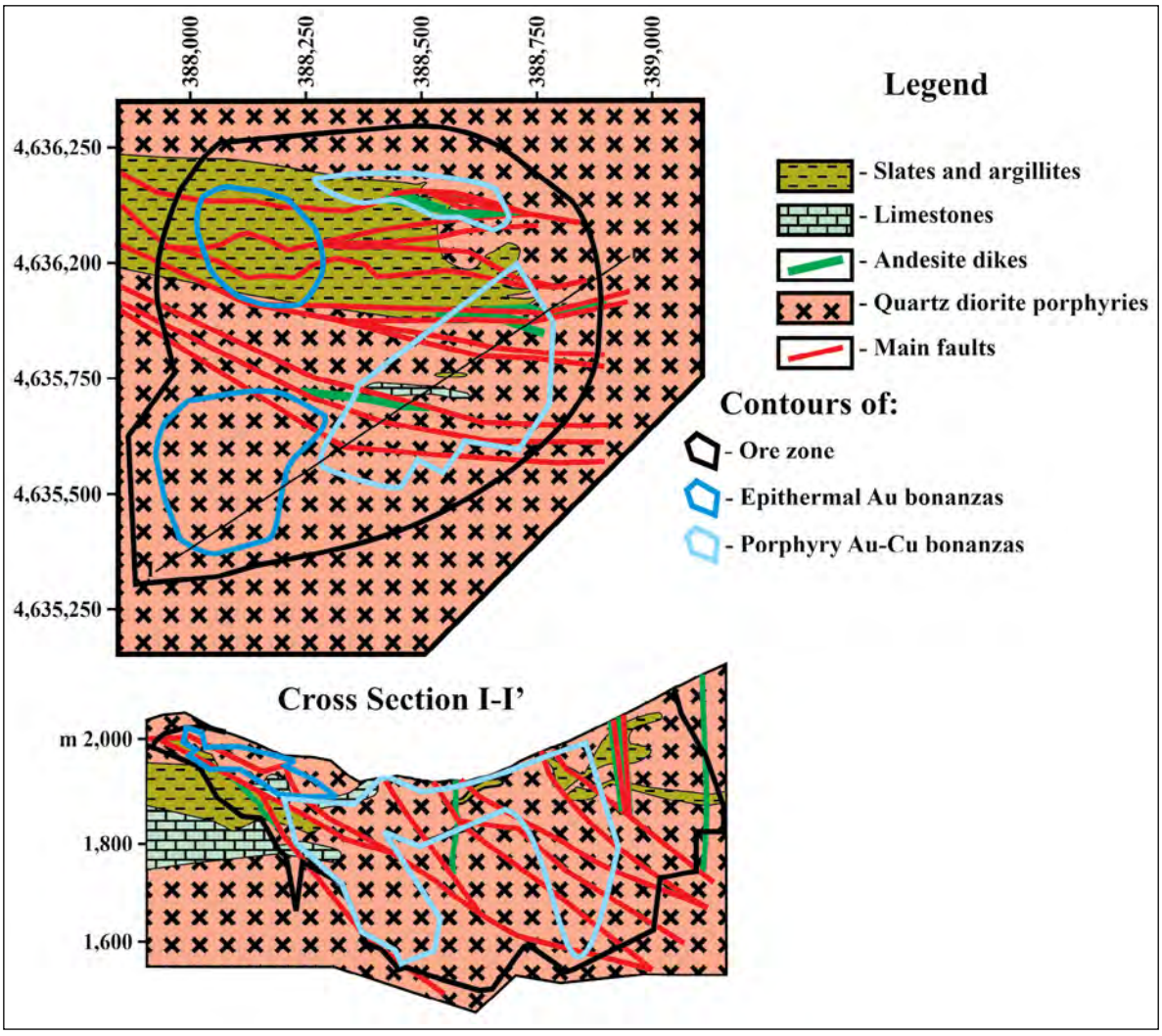

Figure 5- Model geological map of Gharta deposit. This study.

hosted by high-temperature quartz-sericite-garnet-bearing rocks with intense development of epidote. Development of garnet (andradite, as identified diffractometrically) is sometimes so pronounced that quartz diorites are altered to a monomineralic "garnetite" (Figure 6b).

A well-pronounced vertical zoning is characteristic of the deposit (Figure 7). At upper horizons, epithermal high sulfidation gold ores are developed. Beneath 100 meters from the surface, ores are enriched by chalcopyrite, which sometimes creates high-grade ores (Borehole BHG-03 on Figure 7). At deeper horizons, gold-free porphyry copper ores are present. It is crucial to note for further discussion that an ore-free space always exists between gold and copper ores, although this interval is hydrothermally altered in the same manner and with the same intensity as in ore bonanza zones.

3.3. Intermediate Sulfidation and Porphyry Copper Systems – Merisi Mining District, Georgia

The Merisi mining district, identified as no. 1 on Figure 1, is situated in Mount Adjara, approximately 60 km from Batumi, the capital of the Adjara Autonomous Republic of Georgia, and is positioned right on the state border with Türkiye. The district was extensively explored in the 1930s to 1960s, and copper mining was conducted even during the First World War. Currently, only vein-type intermediate sulfidation gold-bearing small deposits have been thoroughly explored, but the primary prospects of the district are related to the porphyry copper system and

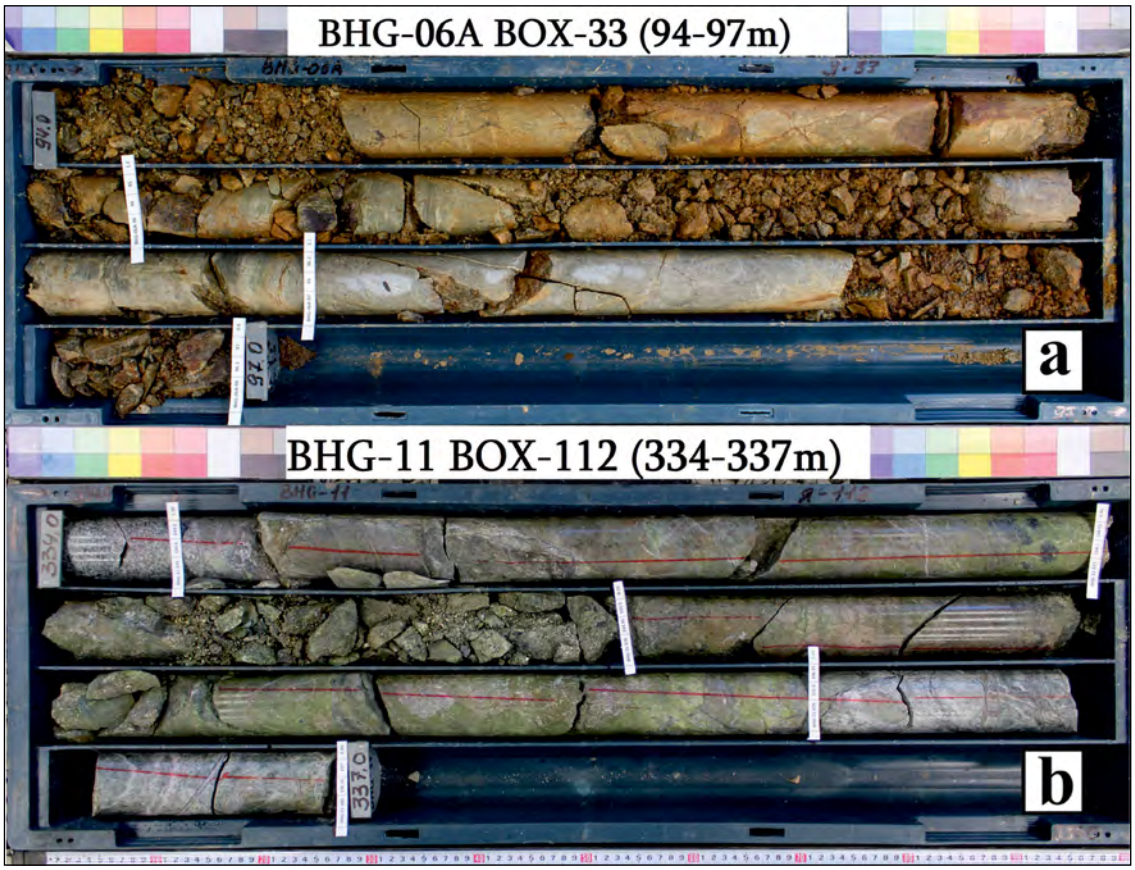

Figure 6- Typical epithermal high sulfidation gold and porphyry copper ores, a) brecciated and fractured vuggy silica; average gold grade of the interval – 3.70 g/t, b) quartz-sericite-garnet (andradite) rock with epidote (green) nests; average copper grade of the interval – 1.38%.

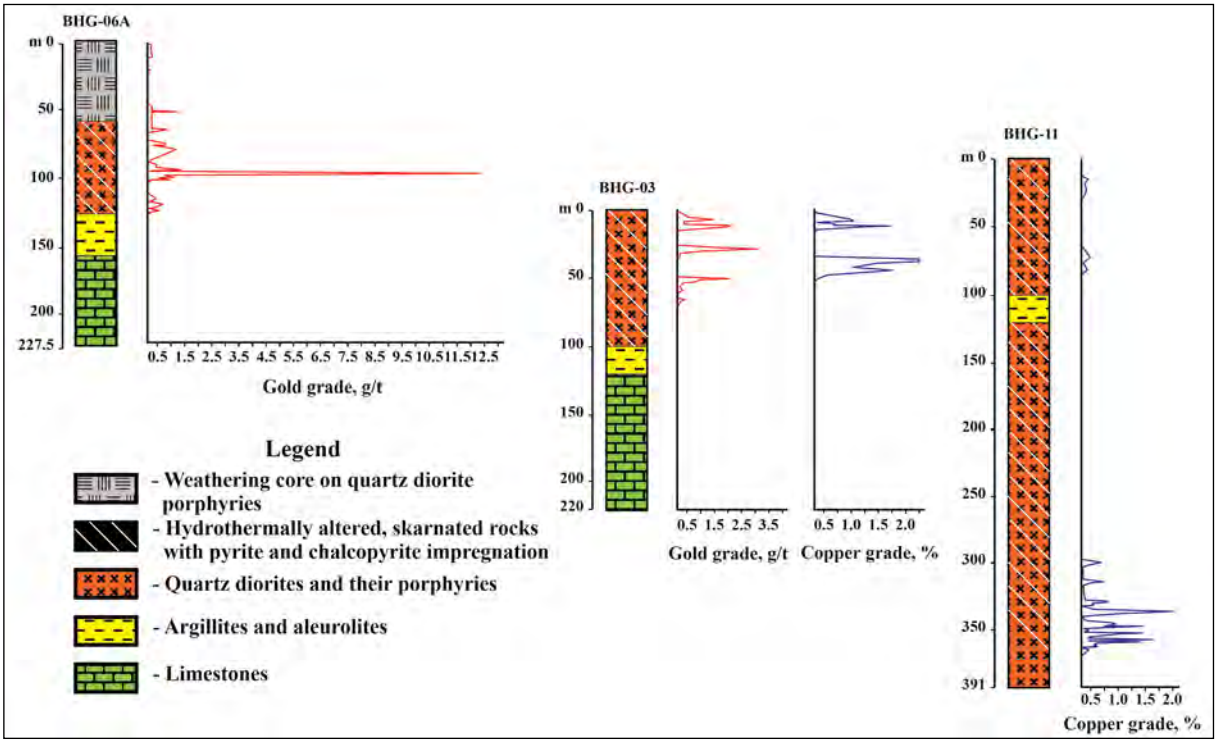

Figure 7- Vertical zoning of Gharta deposit.

the potential presence of high sulfidation gold ores. Thus, the district represents a promising target for exploration.

Figure 8 provides information on the geological structure of the mining district. The district was mapped by the author, alongside his postgraduate student, now Professor Archil G. Magalashvili, and subsequently detailed in my monograph (Tvalchrelidze, 2006). The central part of the mining district comprises the Merisi-Namonastrevi intrusive complex, covering an area of 17 km² and forming three outcrops: (i) Merisi outcrop with an area of 7.5 km², (ii) Namonastrevi outcrop (6.5 km²), and (iii) Chalati outcrop (2.5 km²). Detailed petrochemical investigations, along with fault mapping, have demonstrated that the Namonastrevi and Chalati outcrops were uplifted

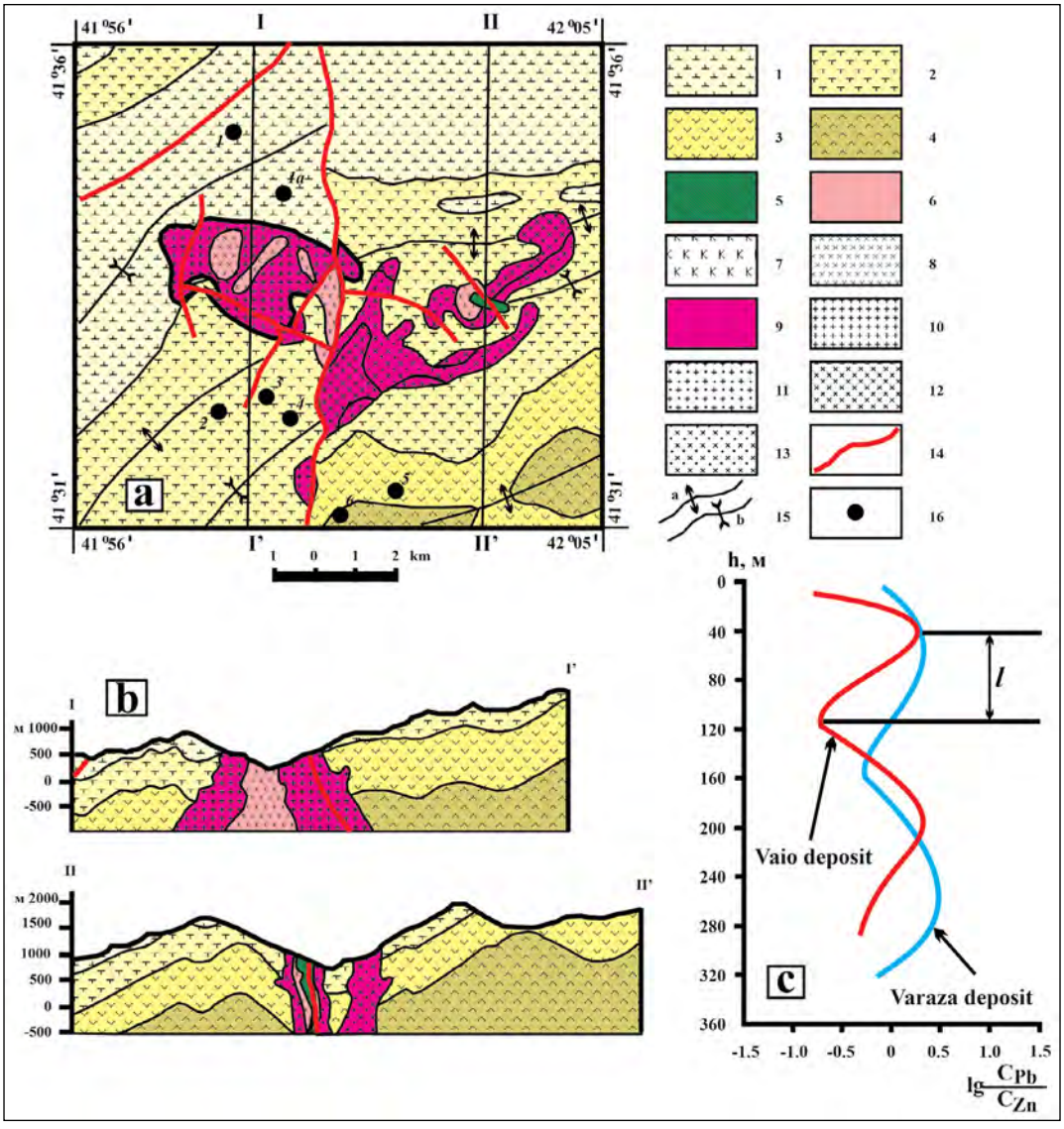

Figure 8- Geological structure of the Merisi mining district, a) geological map; b) cross sections to it. Legend: 1- Upper Eocene – Oligocene: trachybasalt lavas; 2- Upper Eocene: Calc-alkaline basalts and tuffs; 3- Middle Eocene: Subalkaline basalt-andesite-dacite volcanics; 4- Middle Eocene: Andesite tuffs; 5-13- intrusive rocks: 5- Fluid porphyry breccia phase, 6-8: quartz diorite porphyry phase: 6- subvolcanic bodies, 7- quartz diorite porphyries, 8- quartz diorites; 9-13: main intrusive phase: 9- the main intrusive complex, 10- alaskites, 11- granite porphyries, 12- monzonites, 13- diorite porphyries; 14- basic faults; 15- a) anticline and b) syncline axes; 16- intermediate sulfidation gold and base metal lodes: 1- Vaio, 1a- Surnali site of Vaio, 2- Veliburi, 3- Verkhnala, 4- Tskalbokela, 5- Varaza, 6- Obolo-Kanly-Kaia, c) vertical rhythmical zoning of lodes. l- pitch of rhythmicity, C_{Pb} and C_{Zn} – grades of lead and zinc, correspondingly.

along the sub-longitudinal fault by approximately 800 meters (Tvalchrelidze, 2006), causing out-cropping of differing acidic rocks in its western and eastern flanks. These investigations also revealed that the second quartz diorite porphyry phase intruded after the displacement along the mentioned fault had occurred, with rocks of this phase being consistent across each outcrop. The fluid porphyry breccia phase, in my opinion, marks the center of the porphyry ore-forming system and may serve as a significant exploration indicator.

All intermediate sulfidation gold and base metal epithermal deposits and occurrences within the district share a common structure. They are distanced from the contacts of the intrusive body, forming solely in country rocks as subvertical lodes of quartz ± barite composition, with varying thickness from a few meters up to 20 meters, but averaging 2-3 m. The matrix of these lodes bears impregnations and nests of sulfides, predominantly pyrite, chalcopyrite, galena, sphalerite, and also sulfosalts including sulfoantimonites, patrinite, clausthalite, etc. Near the surface, sulfides are oxidized to bornite, hematite, and others. Gold is present both in its native form as thin impregnations within the ores and as an admixture in iron, copper, lead, and zinc sulfides. The ore lodes are accompanied by thin, gouge-like halos of typical medium-temperature hydrothermal alteration, characterized by a quartz-sericite-chlorite rock. The ores are noted for their breccia texture.

The peculiarities of porphyry, high, and intermediate sulfidation systems, as described here, form a solid foundation for further discussion.

4. Discussion

Investigations into the thermodynamic conditions for the evolution of hydrothermal systems from a porphyry stage to the low sulfidation stage have been conducted by Einaudi et al., (2003). I performed a similar type of study sixteen years earlier (Tvalchrelidze, 1986; 1987). For instance, Figure 9 represents a thermodynamic plot demonstrating the equilibria between crystallizing minerals and a model hydrothermal fluid at a temperature of 250°C.

Analysis of this plot leads to the same main conclusion made by Einaudi et al. (2003): The

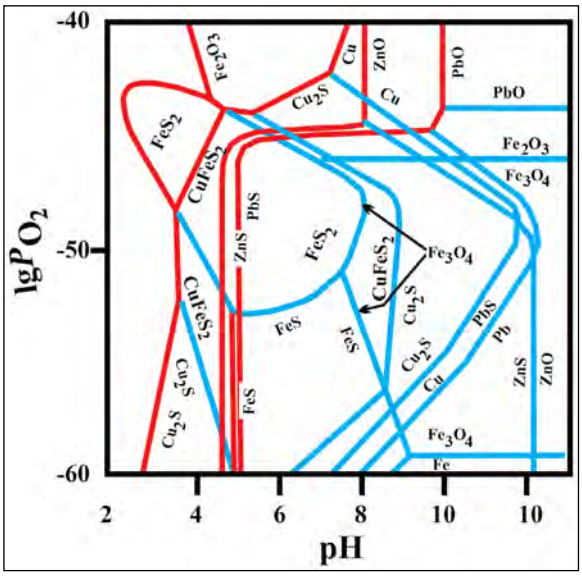

Figure 9- Equilibria of iron and base metal minerals with a model hydrothermal fluid at 250°C. Parameters of the model fluid were published earlier (Tvalchrelidze, 1987). Blue lines – equilibria between solid phases; red lines – equilibria between solid phases and a model fluid.

development of the system and gradual crystallization of minerals occur against the backdrop of fluid neutralization. However, this type of analysis does not explain the origination of convective fluid flows nor ore formation, e.g., mass precipitation of ore minerals within a comparatively limited time period and space. Moreover, the basic typomorphic features of epithermal systems are not addressed.

Some time ago, I analyzed data on an enormous number of vein deposits and demonstrated that practically all of them are characterized by a rhythmical zoning, meaning that the grade ratios of the main ore-forming metals undergo rhythmical fluctuations in the vertical section (Tvalchrelidze, 1993). Here, this phenomenon is demonstrated for two deposits of the Merisi mining district (Figure 8c). The pitch of such zoning, *l*, is proportional to the overall vertical interval of the lode. I further proved that this phenomenon is determined by ore formation in non-equilibrium conditions under the influence of a thermal gradient. In such an environment, metal cations tend to be bound by the sulfide ion, and different reactions of metal sulfides' precipitation compete with each other. Based on this simple assumption, I elaborated mathematical and thermodynamic models of such non-equilibrium reactions and formulated the theory of rhythmical

zoning (Tvalchrelidze, 1993). This theory illustrated the distribution of bonanzas and vertical zoning of ore lodes but was unable to explain the formation of gold ores in high sulfidation epithermal deposits.

$$Zn^{2+} + S_2^{2-} \xrightarrow{k_1} ZnS$$
$$Pb^{2+} + S_2^{2-} \xrightarrow{k_2} PbS \quad (1)$$

Correspondingly, kinetic coefficients k_1 and k_2 depend on the oversaturation degree of corresponding metals. Based on this simple assumption, it has been elaborated mathematical and thermodynamic models of such non-equilibrium reactions and formulated the theory of rhythmical zoning (Tvalchrelidze, 1993). This theory illustrated distribution of bonanza zones and vertical zoning of ore lodes but was unable to explain formation of gold ores in epithermal high sulfidation deposits.

Indeed, as shown in Figure 10, gold remains dissolved in a hydrothermal fluid under a wide range of P-T conditions. This phenomenon is suggested to be related to gold's dual position within the common acid-alkali range of metals. Firstly, gold is encountered together with iron in slightly acidic fluids. Secondly, it is deposited from low-temperature fluids at the final stages of ore formation (Kolonin, 1983). This peculiarity can be explained by the well-expressed chemical affinity of gold with arsenic (Marakushev and Bezmen, 1970), which, in a high-temperature fluid, is presented in the form of the acid at the line of monovariant equilibrium between hydrogen sulfide and sulfuric acid (Figure 10). However, in a low-temperature fluid, arsenic assumes the role of metal. Consequently, gold plays no role in competitive sulfide deposition processes, gradually precipitates from a fluid with a fall in temperature, creating concentrations far below the cutoff grade, and in normal evolution of high sulfidation hydrothermal systems, is unable to form mineral deposits.

Thus, the sole reason for gold precipitation when a high and/or intermediate sulfidation epithermal mineralization forms is a sharp disruption of the consecutive ore formation process due to external influences. One such influence is the phreatic collapse of the ore-hosting structures, followed by the boiling of the hydrothermal fluid and mass precipitation of its ore content.

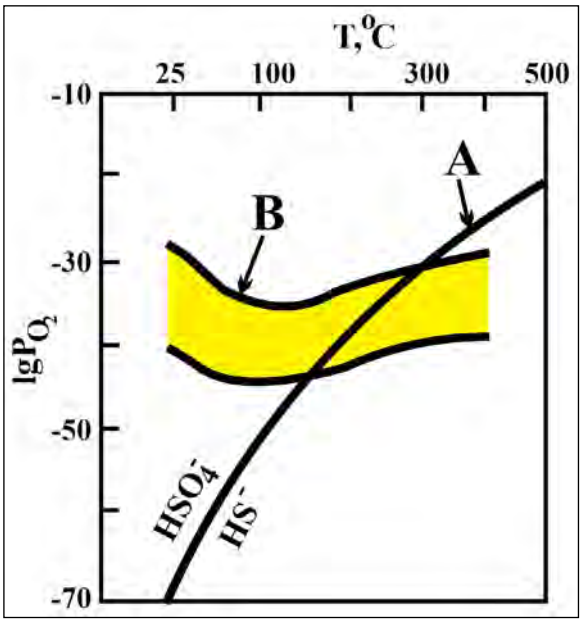

Figure 10- Partial pressure of oxygen during crystallization of base metal sulfides and barite. After Tvalchrelidze (2006), A – monovariant equilibrium Line between S^{6+} and S^{2-} B – field of gold stability in a hydrothermal fluid.

1. The presence of hydrothermal breccias, often with jigsaw-fit texture, specifically highlighted in our studies (Figure 4a), or vuggy silica (Figure 6a), is evidence of such a collapse. This indicates that hydrothermal breccia has a phreatic origin. It should be noted that phreatic breccias are often described in models of high and/or intermediate sulfidation systems. However, several features characteristic of either porphyry or epithermal systems do not align with a purely thermodynamic approach. Specifically: Intermediate and low sulfidation mineralizations are typically located at a certain distance from the contacts of the intrusive body. My earlier statistical analysis of numerous plutonogenic ore districts demonstrated that this distance directly correlates with the dimensions of the plutonic body.

2. A direct transition between porphyry and high sulfidation ores is never observed. In every case I have studied, a distinct ore-free space exists between the two, even though this interval undergoes the same hydrothermal alteration as the ore-rich zones.

3. Porphyry copper ores are often hosted by the main intrusive body, suggesting that they formed simultaneously with or shortly after the crystallization

of the host rock. This observation challenges models that rely solely on a peripheral magmatic source for mineralization.

Given these insights, the significance of employing paleothermophysical models to examine the cooling of intrusive bodies becomes evident. Among the early pioneers of such research was my colleague from Moscow State University, Doctor of Geology and Mineralogy, Vladimir G. Zolotarev. Tragically, Zolotarev and his family met a fatal end in a car accident in the early nineties of the recent century. Honoring his memory and building upon his foundational work, I have continued these investigations and developed a model specifically for the Merisi mining district. This endeavor not only serves as a tribute to Zolotarev's contributions to geology but also advances our understanding of the thermal dynamics and mineralization processes within intrusive geological formations.

Dr. Zolotarev's methodology is predicated on fundamental principles (Zolotarev, 1985): Upon intrusion, the temperature of the magmatic fusion significantly surpasses that of the surrounding country rocks. Consequently, in accordance with the Second Law of thermodynamics, an immediate heat exchange begins between the magma and the host rocks—resulting in the cooling and crystallization of the magma, while simultaneously heating the country rocks. The modeling of such thermal fields necessitates the application of the classical Fourier equation of heat and mass transfer, which encapsulates both convective and conductive heat and mass flows (2). This approach allows for a nuanced understanding of the thermal interactions within geological systems, providing a comprehensive framework for analyzing the cooling patterns of magmatic bodies and their consequent effects on the surrounding geological environment.

$$C\rho(\frac{\partial T}{\partial t}) = -\nabla(q_L h_L + q_S h_S) + \nabla(\lambda \nabla T) + F', \quad (2)$$

Where: ρ = density, C = heat conductivity, T = temperature, t = time, λ = heat conductivity factor, h_L and h_S = enthalpy of fusion's liquid and gaseous phases, q_L and q_S = fusion and liquid phases masses, passing through the elementary 1 cm^2 section, F' = latent fusion heat determining phase change, ∇ = Hamilton's operator. In 3D Descartes space the latter may be expressed as:

$$\nabla = (\frac{\partial}{\partial X} + \frac{\partial}{\partial Y} + \frac{\partial}{\partial Z}), \quad (3)$$

Zolatarev (1985) has proven that in thermophysical models of a cooling magmatic body the influence of the convective member of the Fourier's equation is negligible. In this case, development of the heat field through time may be described by the classical equation of heat transfer:

$$C\rho(\frac{\partial T}{\partial t}) = div(\lambda grad T) + F'(x, y, z), \quad (4)$$

It can be straightforwardly demonstrated that equation (4) is exponential in nature and lacks an analytical solution. Consequently, the modeling of heat fields ought to be conducted in accordance with the methodology proposed by Zolotaev (1985 and subsequent works). This process involves segmenting the entire geological space into a requisite number of elementary blocks, each characterized by a uniform composition and precise coordinates within Cartesian space. Subsequently, the heat transfer equation is to be resolved individually for each of these elementary blocks, ensuring a detailed and accurate representation of the thermal dynamics within the geological setting. This granular approach allows for a comprehensive analysis of heat distribution and its effects on mineralization processes across the spatial extent of the geological environment under study.

$$C\rho(\frac{\partial T}{\partial t}) = \lambda(\frac{\partial^2 T}{\partial t^2}) + F', \quad (5)$$

And for each time interval Δt heat amount (ΔQ) may be calculated for each block having coordinates i, j, k, and the block will have temperature:

$$T'_{i,j,k} = T_{i,j,k} + \Delta T; \Delta T = \frac{\Delta Q}{C_V}, \quad (6)$$

Where: $T_{i,j,k}$ = is a temperature in time moment t, whereas $T'_{i,j,k}$ = is temperature in time moment $t + \Delta t$, C_V = specific heat conductivity of the given block. As far as this method is based on successive temperature calculation along coordinate axes, the

stability condition must be respected: Time pitch shall be followed by a pitch along axes:

$$\partial t \le (\frac{1}{2}k)(\frac{\lambda_{max}}{C.l})l_0; k = 1,2, \quad (7)$$

Where: l_0 = distance between blocks. In 2D models this condition may be satisfied by calculation of heat transfer between blocks:

$$C\rho(\frac{\partial T}{\partial t} + V\Delta T) = div(\lambda gradT) + F', \quad (8)$$

Where: $\vec{V}$ = speed vector of heat transfer.

I have developed a specific model for the Merisi mining district. The thermophysical parameters crucial for these calculations were previously documented (Tvalchrelidze, 2006). Figure 11 illustrates a block model of the geological environment at a depth of 2.5 kilometers, captured before the occurrence of fault tectonics events and the intrusion of the second phase. Figure 12 elucidates the dynamics of crystallization and paleotemperature fields 122,000 years following the intrusion. Indeed, paleotemperature fields underwent analysis across various temporal spans, specifically: 6, 14, 22, 30, 46, 80, 122, 160, 180, and 250 thousand years post-intrusion. Nevertheless, the epoch 122,000 years subsequent to the intrusion is of paramount significance, as by this juncture, the massif had fully crystallized (as depicted in Figure 12a). This complete crystallization precipitated a phase of paleothermal field stabilization extending from, at a minimum, 122,000 to 250,000 years after the intrusion.

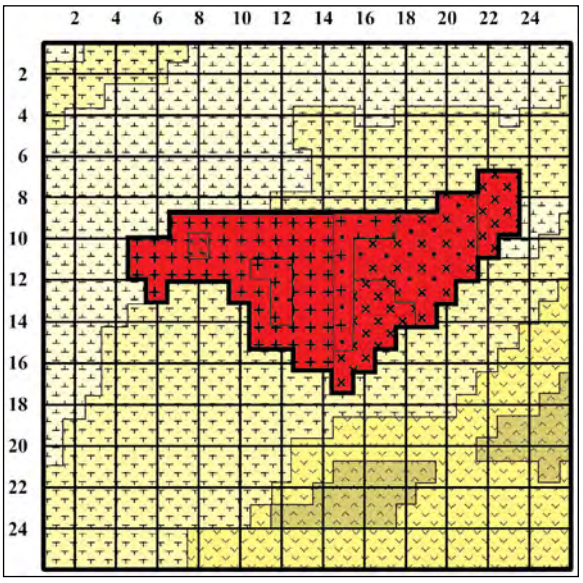

Figure 11- Block model of the Merisi geological environment at a depth of 2.5 km immediately after intrusion of the main phase. Block numbers along coordinate axes are shown. Legend see on Figure 8.

The data presented herein enable the articulation of several foundational postulates, which are discussed in the subsequent sections.

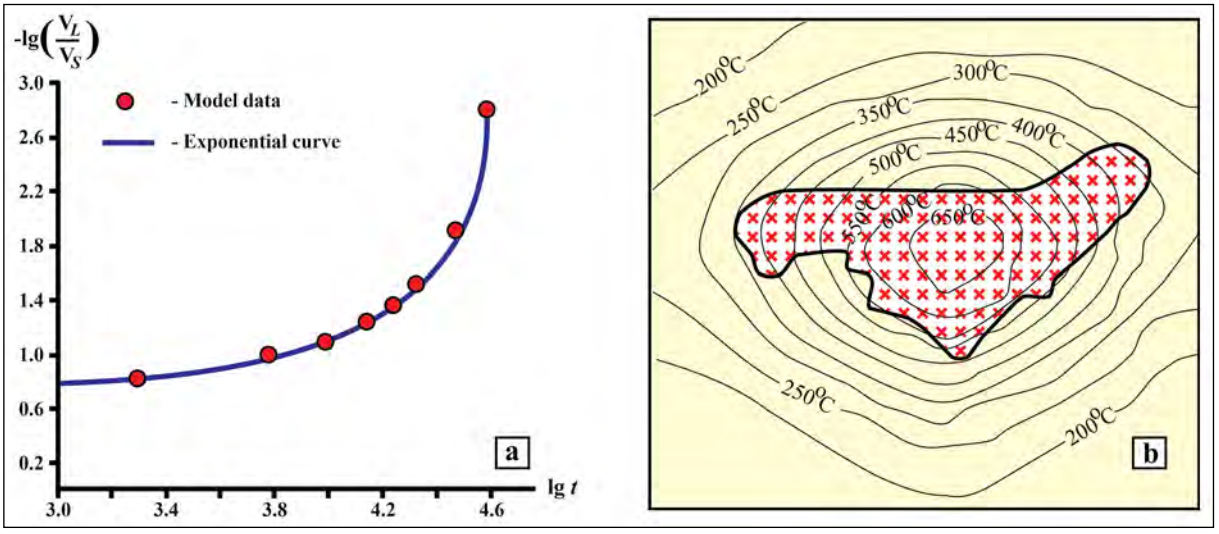

Figure 12- Succession of crystallization, a) and paleotemperature field 122,000 years after intrusion, b) of the Merisi Pluton. V_L and V_S = correspondingly, volumes of the fusion and the crystalized phases; t = time in years.

5. Results

The classical thermodynamic model, which interprets the formation of sulfide minerals as reactions of mineral precipitation under equilibrium conditions, fails to account for the genesis of conventional flows of meteoric waters or the formation of ores of the type under investigation. In the context of porphyry and epithermal ore formation, several prerequisite conditions are proposed to be essential:

1. Source of anomalous energy (heat), which exceeds normal thermodynamics of the enclosing environment.

2. The presence of temperature (and heat!) gradient, which determines conventional flows of fluids composed of endogenous and meteoric constituents (proven by rhythmical zoning of ore lodes).

3. The persistence of such conditions for a period of sulfide ore formation – shorter this stability period is, smaller deposit is formed.

These conditions can be generated through various geological processes, including the transfer of heat from a peripheral magmatic source, a mechanism commonly incorporated into models of epithermal deposit formation. Nevertheless, these models fall short in addressing scenarios involving complex ore-forming systems where porphyry and high and/or intermediate sulfidation ores coexist. In such instances, the requisite heat for ore formation emanates from the paleothermal field associated with cooling magmatic complexes. This specific environment establishes a number of fundamental characteristics inherent to these amalgamated systems, as outlined below:

1. In expansive porphyry copper (± gold) deposits, the porphyry ores are predominantly situated near the contacts (both endo- and exocontacts) of the intrusive massifs. In contrast, within smaller deposits, these ores may be found in the central regions of the igneous body. This distribution pattern becomes intelligible when considering the paleothermal history of the cooling intrusive massifs. As evidenced by Figure 12b, at the juncture when thermal fields reached stability, the temperature within the central part of the large massif remained excessively high for the deposition of ores.

2. This same thermal dynamic also explains the lack of direct telescoping from porphyry ores into high sulfidation mineralization. It has been observed that an interval of ore-free zones exists between these two types of mineralization, corresponding to a reduction in temperature to levels conducive for the formation of epithermal ores.

3. As the cooling magmatic body dissipates heat, it warms the surrounding country rocks. Over time, while the paleotemperature gradient tends to even out, the extent of the heated region expands. Consequently, a distinct gap is present between the initial intermediate sulfidation deposit and the intrusive body's contact. My previous statistical analyses of several plutonogenic ore districts (Tvalchrelidze, 2006) have demonstrated that the size of this gap is proportionate to the dimensions of the magmatic body, with a notably strong correlation. This finding underscores the significant influence of the thermal and structural characteristics of magmatic bodies on the spatial distribution of mineral deposits.

Therefore, the process of sulfide ore formation as outlined cannot account for the genesis of high sulfidation gold deposits. As elucidated, the widespread precipitation of free gold necessitates a phreatic collapse within the ore conduit channel subsequent to the formation of hydrothermally altered rocks. This catastrophic event leads to the formation of hydrothermal breccias, frequently characterized by a jigsaw-fit texture, or brecciated vuggy silica. In these formations, both the host rocks and the hydrothermally altered rocks are bound together by a gold-bearing quartz matrix. This phenomenon underscores the complexity of geological processes involved in high sulfidation gold deposit formation, highlighting the importance of dynamic geological events in the concentration of precious metals.

The model outlined in this article has been validated by the geological characteristics of the deposits discussed herein. This model has facilitated the development of a comprehensive exploration strategy and methodology, resulting in the discovery of multiple porphyry copper and high sulfidation epithermal gold deposits. Currently, four of these deposits are being extensively mined, and construction

is underway at mines on two additional sites. Our team has successfully conducted explorations at several deposits, demonstrating the efficacy of our approach in identifying and developing valuable mineral resources. This success underscores the practical applicability of the model in guiding effective exploration efforts and enhancing the potential for discovering significant mineral deposits.

Acknowledgements

It is my pleasure to acknowledge the international team of economic geologists with whom I am successfully working and performing research for decades, and namely Dr Zurab Kutelia, Dr Revaz Kvatashidze, and Dr Irakli Narozauli (Georgia); Dr. Dmitry Pertel and Dr Paul Hanzl (Australia); Dr. Andrei Kharlashin (Russia), and many others.

It is my sad duty to remember my late colleagues the friendships and collaboration with whom passed through my entire professional life, and namely: Prof. Dr Veniamin Gogishvili, Dr Tina Gogishvili (Georgia); Prof. Dr Bogdan Bogdanov (Bulgaria); Prof. Dr Mirko Vaněček, Prof. Dr Zdenek Pouba (Czech Republic); Prof. Dr Valentin Naumenko, Dr Yuri Koptyukh (Ukraine); Dr Emin Suleymanov, Prof. Dr Vagif Ramazanov (Azerbaijan Republic); Dr Vladimir G. Zolotarev (Russia).

References

Adamia, S. A., Chkhotua, T., Kekelia, M., Lordkipanidze, M., Zakariadze, G. 1981. Tectonics of the Caucasus and adjoining regions: implications for the evolution of the Tethys ocean. Journal of Structural Geology, 3, 437-447.

Adamia, S., Zakariadze, G., Chkhotua, T., Sadradze, N., Tsereteli, N., Chabukiani, A., Gventsadze, A. 2011. Geology of the Caucasus: A review. Turkish Journal of Earth Sciences, 20 (5), 489-544.

Aghazadeh, M., Hou, Z., Badrzadeh, Z., Zhou, L. 2015. Temporal-spatial distribution and tectonic setting of porphyry copper deposits in Iran: Constraints from zircon U-Pb and molybdenite Re-Os geochronology. Ore Geology Reviews, 70 (4), 385-406.

Aluç, A., Kuşcu, I., Peytcheva, I., Cihan, M., von Quadt, A. 2020. The late Miocene Öksüt high sulfidation epithermal Au-Cu deposit, Central Anatolia, Türkiye: Geology, geochronology, and geochemistry. Ore Geology Reviews, 126, 103795.

Arribas Jr., A. 1995. Characteristics of high sulfidation epithermal deposits, and their relation to magmatic fluid. Thompson, J.F.H. (ed.) Magmas, Fluids, and Ore Deposits. Mineralogical Association of Canada Short Course, 23, 419-454.

Berberian, M., King, G. C. P. 1981. Toward a paleogeography and tectonic evolution of Iran. Canadian Journal of Earth Science, 18, 210–265.

Berger, B. R., Ayuso, R. A., Wynn, J. C., Seal, R. R. 2008. Preliminary model of porphyry copper deposits. Open-File Report 2008-1321. U.S. Department of the Interior, U.S. Geological Survey. Reston, 62.

Bogdanov, K., Musaev, S., Ahmedov, A., Salmanli, R. 2013. High-sulphidation (HS) epithermal gold mineralisation in the Chovdar deposit, Lesser Caucasus, Azerbaijan. Proceedings of Bulgarian Geological Society National Conference with international participation "GEOSCIENCES 2013". Sofia, 15-16.

Boomeri, M., Nakashima, K., Lentz, D. R. 2010. The Sarcheshmeh porphyry copper deposit, Kerman, Iran: A mineralogical analysis of the igneous rocks and alteration zones including halogen element systematics related to Cu mineralization processes. Ore Geology Reviews, 38 (4), 367-381.

Cas, R., Giordano, G., Balsamo, F., Esposito, A., Lo Mastro, S. 2011. Hydrothermal Breccia Textures and Processes: Lisca Bianca Islet, Panarea Volcano, Aeolian Islands, Italy. Economic Geology, 106, 437-450.

Diarra, K., Sangu, E., Çiftçi. E. 2019. Ore mineralogy of high sulfidation Çorak-Taç epimesothermal gold deposit (Yusufeli-Artvin-Türkiye). Glagolev, S. (ed.) Proceedings of 14th International Congress for Applied Mineralogy (ICAM2019), Springer Nature Switzerland AG. Cham, 53–58.

Einaudi, M. T., Hedenquist, J., Inan, E. E. 2003. Sulfidation state of fluids in active and extinct hydrothermal systems: Transitions from porphyry to epithermal environments. Volcanic, Geothermal and Ore-Forming Fluids: Rulers and Witnesses of Processes within the Earth. Special Publication 10. Society of Economic Geologists. Ottawa, 285-311.

Engin, T. 2003. Mineral Deposits of Türkiye. Tvalchrelidze, A.G., Morizot, G. (eds). Mineral Resource Base of the Southern Caucasus and Systems for its Management in XXI Century. Kluwer Academic Publishers. Dordrecht-Boston-London, 81-104.

Ersoy, A. 2022. The current status of gold mining in Türkiye: An overview. NOHU Journal of Engineering Sciences, 11(4), 1103-1114.

Ghaderi, M., Narges, Y., Mina, B. K. 2018. Porphyry copper deposits of Iran. Tarbiat Modarres University Press. Tehran, 668.

Goldfarb, R. J., Groves, D. I., Gardoll, S. 2001. Orogenic gold and geologic time: a global synthesis. Ore Geology Reviews, 18 (1-2), 1-75.

Gülyüz, N., Gülyüz, E., Shipton, Z. K., Kuşcu, İ., Lord, L. A. 2020. Geological and mineralization characteristics of the Kestanelik epithermal Au-Ag deposit in the Tethyan Metallogenic Belt, NW Türkiye. Geoscience Journal, 24, 407–424.

Hajalilou, B., Aghazadeh, M. 2016. Geological, alteration and mineralization characteristics of Ali Javad Porphyry Cu-Au deposit, Arasbaran Zone, NW Iran. Open Journal of Geology, 6, 859-874.

Hastorun, S. 2022. The mineral industry of Türkiye. 2019 Minerals Yearbook. Türkiye. U.S. Department of the Interior, U.S. Geological Survey. Manto Park, 47.1-47.19.

Hedenquist, J. W. 2000. Exploration for epithermal gold deposits. SEG Reviews, 13, 245-277.

Heidari, S. M., Daliran, F., Paquette, J. -L., Gasquet, D. 2015. Geology, timing, and genesis of the high sulfidation Au (-Cu) deposit of Touzlar, NW Iran. Ore Geology Reviews, 65, 460–486.

Hosseini, S. A., Asghari, O., Emery, X. 2017. Direct block-support simulation of grades in multi-element deposits: application to recoverable mineral resource estimation at Sungun porphyry copper-molybdenum deposit. The Journal of the South African Institute of Mining and Metallurgy, 117, 577-585.

Imamverdiyev, N. A., Baba-zadeh, V. M., Mursalov, S. S., Valiyev, A. A., Mansurov, M. I., Abdullayeva, S. F. 2021. New perspective Reza gold deposit (Gedabek ore district, Lesser Caucasus, Azerbaijan). Journal of Geology, Geography and Geoecology. 30 (1), 53-64.

John, D.A. (Ed.). 2010. Porphyry copper deposit model. Scientific Investigations Report 2010-5070-B. U.S. Department of the Interior, U.S. Geological Survey, Reston, 170.

John, D. A., Vikre, P. G., du Bray, E. A, Blakely, R. J., Fey, D. L., Rockwell, B. W., Mauk, J. L., Anderson, E. D., Graybeal, F. T. 2018. Descriptive models for epithermal gold-silver deposits. Mineral Deposit Models for Resource Assessment. Scientific Investigations Report 2010–5070–Q. U.S. Department of the Interior, U.S. Geological Survey. Reston, 264.

Kaviani, A., Hatzfeld, D., Paul, A., Tatar, M., Priestley. K. 2009. Shear-wave splitting, lithospheric anisotropy, and mantle deformation beneath the Arabia-Eurasia collision zone in Iran. Earth and Planetary Science Letters, 286 (3-4), 371–378.

Kolonin, G. R. 1983. Acidity and alkalinity evolution character in ore-forming fluid based on experimental data. Dobretsov, N.L. (ed.) Dynamic and Physical-Chemical Models of Magmatic Systems.: Nauka Publisher. Novosibirsk, 57-70 (in Russian).

Kuşcu I., Tosdal, Richard M., Gençalioğlu-Kuşcu, G. 2019. Chapter 8. Porphyry-Cu Deposits of Türkiye. Pirajno, F., Ünlü, T., Dönmez, C., Şahin, B.M. (eds): Mineral Resources of Türkiye. Springer Nature Switzerland AG. Cham, 337-425.

Marakushev, A. A., Bezmen, N.I. 1970. Thermodynamics of sulfides and oxides related to ore formation problems. Nauka Publisher. Moscow, 215 (in Russian).

Marutani, M. 2003. Study on mining sector development master plan in the Republic of Armenia. Final report. Japan International Cooperation Agency (JICA), Steering Committee of Study on Mining Sector Development Master Plan of Government of the Republic of Armenia. Yerevan-Tokyo, 46.

Mederer, J., Moritz, R., Ulianov, A., Chiaradia. M. 2013. Middle Jurassic to Cenozoic evolution of arc magmatism during Neotethys subduction and arc-continent collision in the Kapan Zone, southern Armenia. Lithos, 177, 61-78.

Mehrabi, B., Chaghaneh, N., Fazel, E. T. 2008. Intermediate sulfidation epithermal mineralization of No. 4 anomaly of Golojeh deposit (N. Zanjan) based on mineralography, alteration and ore fluid geochemistry features. Journal of Economic Geology, 6 (1), 1-22.

Mehrabi, B., Sianib, M. G., Azizic, H. 2014. The genesis of the epithermal gold mineralization at North Glojeh Veins, NW Iran. International Journal of Sciences: Basic and Applied Research (IJSBAR), 15 (1), 479-497.

Moritz, R., Rezeau, H., Ovtcharova, M., Tayan, R., Melkonyan, R., Hovakimyan, S., Ramazanov, V., Selby, D., Ulianov, A., Chiaradia, M., Putlitz, B. 2016. Long-lived, stationary magmatism and pulsed porphyry systems during Tethyan subduction to post-collision evolution in the southernmost Lesser Caucasus, Armenia and Nakhitchevan. Gondwana Research, 37, 465-503.

Moritz, R., Reseau, H., Mederer, J., Gialli, S., Hemon, P., Lavoie, J., Calder, M., Hovakimyan, S., Melkonyan,, R., Tayan, R., Popkhadze, N., GuGushvili, V., Ramazanov, V. 2017. Gold

deposits of the Lesser Caucasus: products of successive Mesozoic and Cenozoic geodynamic settings. Mineral Resources to Discover – Proceedings of the 14th SGA Biennial Meeting, 1. Society for Geology Applied to Mineral Deposits. Geneve, 67-70.

Oyman, T., Minareci, F., Pişkin, Ö. 2003. Efemçukuru B-rich epithermal gold deposit (İzmir, Türkiye). Ore Geology Reviews, 23, (1-2), 35-53.

Payot, B. D., Maglambayan, V. B., Dimalanta, C. B., Yumul Jr., G. P., Tamayo Jr., R. A., Matsuda, T., Suzuki, S., Bellon, H. 2005. Geology and hydrothermal alteration of the low sulfidation Pantingan Gold System, Mount Mariveles, Bataan (Luzon), Philippines. Resource Geology, 55 (3), 155-162.

Richards, J. P. 2015. Tectonic, magmatic, and metallogenic evolution of the Tethyan orogen: From subduction to collision. Ore Geology Reviews, 70, 323-345.

Shafiei, B., Shahabpour, J. 2008. Gold distribution in porphyry copper deposits of Kerman Region, southeastern Iran. Journal of Sciences, 19 (3), 247-260.

Sholeh, A., Rastad, E., Huston, D., Gemmell, J.B., Taylor, R.D. 2016. The Chahnaly low-sulfidation epithermal gold deposit, Western Makran volcanic arc, southeast Iran. Economic Geology, 111, 619–639.

Sillitoe, R. H. 2000. Styles of high-sulphidation gold, silver and copper mineralisation in porphyry and epithermal environments. Proceedings of the Australasian Institute of Mining and Metallurgy, 305, 19-34.

Sinclair, W. D. 2007. Porphyry Deposits. Goodfellow, W.D. (ed.) Mineral Deposits of Canada: A Synthesis of Major Deposit-Types, District Metallogeny, the Evolution of Geological Provinces, and Exploration Methods. Geological Association of Canada, Mineral Deposits Division, Special Publication No. 5, 223-243.

Taylor, B. E. 2007. Epithermal gold deposits. Goodfellow, W.D. (ed.) Mineral Deposits of Canada: A Synthesis of Major Deposit-Types, District Metallogeny, the Evolution of Geological Provinces, and Exploration Methods. Geological Association of Canada, Mineral Deposits Division, Special Publication No. 5, 113-139.

Tvalchrelidze, A. G. 1980. Copper metallogeny of the Caucasus. Jankovic, S. (ed.) European Copper Deposits. Belgrade, 191-196.

Tvalchrelidze, A. G. 1984. Main features of metallogeny of the Caucasus, Janelidze, T.V., Tvalchrelidze, A.G. (eds): Proceedings of the Sixth Quadrennial IAGOD Symposium. Vol. 1. E. Schweizerbat'sche Verlagbuchhandlung. Stuttgart, 1-5.

Tvalchrelidze, A. G. 1986. Physico-chemical conditions of base metal sulphide ore formation. Friedrich, G. H., Genkin, A. D., Naldrett, A. J. Ridge, J. D., Sillitoe, R. H. Vokes, F. M. (eds.) Geology and Metallogeny of Copper Deposits. Springer-Verlag. Berlin-Heidelberg-New York-London-Paris-Tokyo, 358-369.

Tvalchrelidze, A. G. 1987. Geochemical conditions of base metal sulfide deposit formation. Nedra Press. Moscow, 188 (in Russian).

Tvalchrelidze, A. G. 1993. Quantitative models of vein type ore deposits and theory of rhythmical zoning. Geological Association of Canada Special Papers, 40, 751-760.

Tvalchrelidze, A. G. 2003. Mineral resource base of Georgia in XXI century. Tvalchrelidze, A.G., Morizot, G. (eds.) Mineral Resource Base of the Southern Caucasus and Systems for its Management in the XXI Century. Kluwer Academic Publisher. Dordrecht-Boston-London, 19-70.

Tvalchrelidze, A. G. 2006. Mineral resources and mineral resource base of Georgia. Rudy I Metally Publishing House. Moscow, 320 (in Russian).

Veliyev, A., Bayramov, A., Ibrahimov, J., Mammadov, S., Alizhadeh, G. 2018. Geological setting and ore perspective of the new discovered Gadir low sulfidation epithermal deposit, Gedabek NW flank, Lesser Caucasus, Azerbaijan. Universal Journal of Geoscience, 6 (3), 78-101.

Wang, L., Qin, K., Song, G., Li, G. 2019. A review of intermediate sulfidation epithermal deposits and subclassification. Ore Geology Reviews 107, 434-456.

Yiğit, O. 2006. Gold in Türkiye – a missing link in Tethyan metallogeny. Ore Geology Reviews, 28 (2), 147-179.

Yiğit, O. 2009. Mineral deposits of Türkiye in relation to Tethyan metallogeny: Implications for future mineral exploration. Economic Geology, 104 (1), 19-51.

Zolotarev, V. G. 1985. Spatial-temporal dynamics of processes related to granite consolidations and their role in ore formation. Sciences de Terre. Série Information géologique, 23, 27-48.

Bulletin of the Mineral Research and Exploration

http://bulletin.mta.gov.tr

Edge enhancement of potential field data using the enhanced gradient (EG) filter

Hazel Deniz TOKTAY[a*], Korimilli Naga Durga PRASAD[b] and Ahmad ALVANDI[c]

[a] *İstanbul University-Cerrahpaşa, Faculty of Engineering, Department of Geophysical Engineering, Büyükçekmece Campus, İstanbul, Türkiye*

[b] *Council of Scientific and Industrial Research -National Geophysical Research Institute, Gravity and Magnetic Studies Group, Uppal Road, Hyderabad, 500007, Telangana, India*

[c] *University of Tehran, Institute of Geophysics, Tehran, Iran*

Research Article

Keywords:
Edge Detection, Gradient, Potential Field, Mapping.

ABSTRACT

Potential field data play a critical role in interpreting various geologic structural features through edge detection filters that aid in mapping subsurface structural features. For this purpose, various filters have been introduced in recent years to determine lateral boundaries. However, each of these filters has its limitations and advantages. This study presents a new edge enhancement filter named Enhanced Gradient (EG) based on the Richards function and applies it to potential field data for structural mapping. The EG is tested on two dimensional (2D) and three dimensional (3D) synthetic magnetic models with sources buried at different depths and variable properties. The results from the EG filter provide more accurate and higher resolution horizontal boundaries and can avoid creating the false edges in the output results. In addition, the proposed filter was examined using aeromagnetic data from the Indiana region in the USA. The primary and secondary faults and geological formations are recognizable in the EG image. The results of the EG map will allow us to improve the qualitative interpretation of potential field anomalies in studying the structural and tectonic geology of the Indiana region in the USA.

Received Date: 01.05.2023
Accepted Date: 14.06.2023

1. Introduction

Gravity and magnetics are widely used geophysical methods for understanding subsurface structures and tectonics. Some of the applications of the method include mineral resource exploration, hydrocarbon exploration, crustal deformation studies, and surface and subsurface structural mapping. Much emphasis can be made on the structural feature delineation that helps us understand various geological structural boundaries buried at depth. Determining the horizontal boundaries of these buried sources and delineating the lateral extents is of prime importance. There are many filters used to determine the edge of potential field anomalies. Each filter has advantages and limitations (Alvandi et al., 2022; Prasad et al., 2022*a*; Ibraheem et al., 2023). A standard method for identifying horizontal boundaries called the total horizontal derivative (THDR), was introduced by Cordell and Grauch (1985). The THDR procedure is less sensitive to noise in the data and is suitable for determining shallow sources (Phillips, 2002; Pham et al., 2021; Alvandi and Ardestani, 2023). The maximum amplitudes of the THDR are located over the boundaries of the geological contact, and it is defined in Equation 1 as follows:

Citation Info: Toktay H. D., Prasad K. N. D., Alvandi A. 2024. Edge enhancement of potential field data using the enhanced gradient (EG) filter. Bulletin of the Mineral Research and Exploration 174, 55-66. https://doi.org/10.19111/bulletinofmre.1386653

**Corresponding author: Hazel Deniz TOKTAY, hazel.deniztoktay@iuc.edu.tr*

$$THDR = \sqrt{\left(\frac{\partial T}{\partial x}\right)^2 + \left(\frac{\partial T}{\partial y}\right)^2} \quad (1)$$

where T is the magnetic or gravity field, $\frac{\partial T}{\partial x}$ and $\frac{\partial T}{\partial y}$ are its first-order derivatives in the x and y directions, respectively (Blakely and Simpson, 1986; Prasad et al., 2022*b*).

The 3D analytical signal amplitude (ASA) is a popular procedure for identifying the lateral boundaries of potential field anomalies, given by Equation 2 (Nabighian, 1984; Roest et al., 1992).

$$ASA = \sqrt{\left(\frac{\partial T}{\partial x}\right)^2 + \left(\frac{\partial T}{\partial y}\right)^2 + \left(\frac{\partial T}{\partial z}\right)^2} \quad (2)$$

where $\frac{\partial T}{\partial z}$ is a first-order vertical derivative of the potential field. On the other hand, maximum ASA values are very sensitive to depth and are only located over the horizontal boundaries when the source's depth is shallow. However, THDR and ASA are ineffective in balancing sources simultaneously at different depths (Pham et al., 2021, 2022; Prasad et al., 2022*a*, 2022*b*; Alvandi et al., 2023).

In order to determine the horizontal boundaries of the shallow and deep anomalies simultaneously, a wide range of phase-based filters has been introduced. The tilt derivative (TDR) filter was introduced as the first to determine the edge of potential field anomalies. (Miller and Singh, 1994). The TDR uses the amplitude of the THDR to normalize the vertical derivative. Although the vertical derivative and THDR are both weak for deeper sources edge detection, the TDR (Equation 3) using the ratio of the vertical derivative to the THDR has overcome this problem and equalized the deep and shallow sources. The amplitude of TDR over the source is positive, with zero amplitude over the edge (Zero vertical derivative and maximum horizontal gradient), and elsewhere, it is negative.

$$\mathrm{TDR} = \mathrm{atan}\left(\frac{\frac{\partial T}{\partial z}}{\mathrm{THDR}}\right) \quad (3)$$

The TDR amplitude variations have a specific range, ±90° (Miller and Singh, 1994). This filter is insensitive to source depth compared to THDR and ASA filters and does not completely balance the source edges buried at various depths. However, with increasing depth, TDR loses its sharpness so that the edges of the anomaly become blurred (Pham et al., 2018).

Wijns et al. (2005) developed another phase-based filter called theta map (TM) filter. The TM uses the ASA to normalize the THDR. The amplitude of the filter is minimal over the source edges. The TM filter is sensitive to depth sources and does not detect deep and thin source edges well (Prasad et al., 2022*a*). The TM amplitude variations have a specific range, between 0°-90° (Equation 4).

$$\mathrm{TM} = \mathrm{acos}\left(\frac{\mathrm{THDR}}{|\mathrm{ASA}|}\right) \quad (4)$$

Cooper and Cowan (2006) have developed modified versions of the total horizontal gradient and vertical derivative to improve the resolution of edges. The horizontal tilt derivative (TDX) filter is a normalized form of THDR amplitude to the absolute value of $\frac{\partial T}{\partial z}$ and is represented in Equation 5.

$$\mathrm{TDX} = \mathrm{atan}\left(\frac{\mathrm{THDR}}{\left|\frac{\partial T}{\partial z}\right|}\right) \quad (5)$$

The TDX filter is the inverse of the tilt derivative filter, as it performs equally well with both shallow and deep anomalies. In addition, these filters do not indicate the edges of interfering sources (Zuo et al., 2018; Prasad et al., 2022*b*).

Castro et al. (2018) introduced another balanced-edge detection method, the combined tilt derivative filters (TDR±TDX) and is defined in Equation 6 as:

$$\begin{cases} \mathrm{TDX} + \mathrm{TDR} = \frac{\pi}{2} & \text{if } \mathrm{TDR} > 0 \\ \mathrm{TDR} - \mathrm{TDX} = \frac{-\pi}{2} & \text{if } \mathrm{TDR} < 0 \end{cases} \quad (6)$$

The TDR-TDX filter produces sharp peaks over the source centers, while the TDR + TDX filter creates a plateau. In TDR±TRX for deep-seated sources, the limits of body edges will appear wider than the actual edges (Castro et al., 2018).

2. Proposed Method

This paper proposes a novel edge detection filter called Enhanced Gradient (EG) based on the Richards function for balancing the edges of magnetic and gravity sources. The EG (Equation 7) filter has a near-

identical shape to the arc-tan function (Richards, 1959), often used for potential field data edge detection.

$$EG = \left(1 + \exp\left(\frac{-\frac{\partial BT}{\partial Z}}{\sqrt{\left(\frac{\partial BT}{\partial x}\right)^2 + \left(\frac{\partial BT}{\partial y}\right)^2}}\right)\right)^{-\alpha} \quad (7)$$

where

$$BT = \frac{(THDR)^{\alpha}}{1+\sqrt{(H_X(THDR))^2 + (H_Y(THDR))^2 + THDR^2}} \quad (8)$$

where H_X and H_Y are the Hilbert transform of the total horizontal gradient amplitude filter (Cooper, 2009) and $\propto$ a positive number.

3. Evaluation of Alpha ($\propto$)

A synthetic gravity model consisting of three prisms, with different physical properties buried at different depths and density contrasts, is created. The physical and geometrical properties of the bodies are represented in Figure 1a. for evaluating the alpha

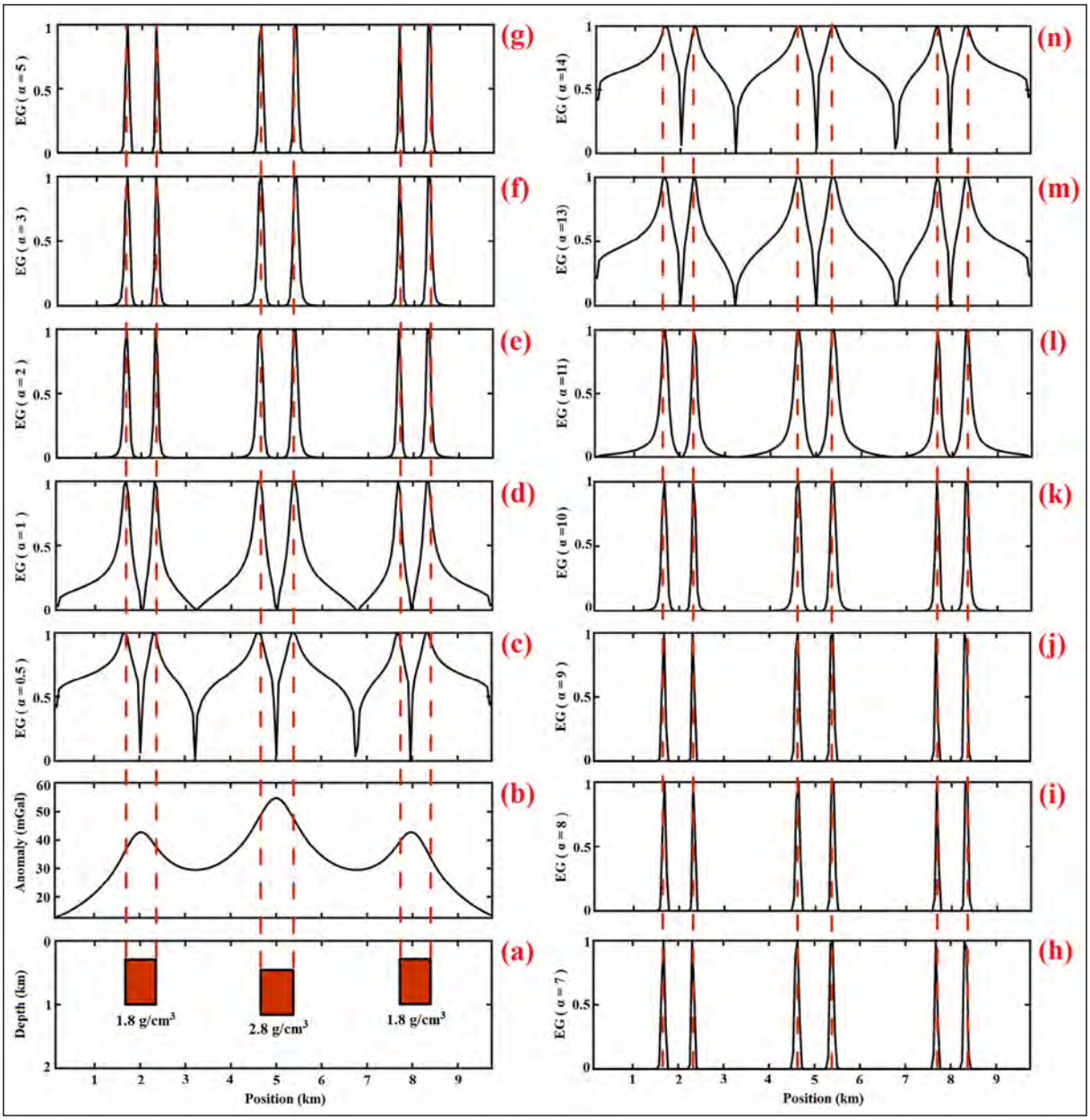

Figure 1- Evaluation of alpha (α) parameter in the EG over synthetic gravity anomaly; a) Schematic representation of synthetic model, b) the gravity anomaly response over the prismatic bodies. The response of the EG at c) α=0.5, d) α=1, e) α=2, f) α=3, g) α=5, h) α=7, i) α=8, j) α=9, k) α=10, l) α=11, m) α=13, n) α=14.

(∝) value to the proposed EG function. The schematic model is shown in Figure 1a, with the computed anomaly response presented in Figure 1b. The EG is applied to the computed gravity anomaly with values increasing from 0.5 to 14 (Figure 1c to Figure 1n). The results show that the amplitude response of the proposed filter is maximum over the edges. The filter produces sharp edges when the ∝ value is two and maintains its sharpness till ∝ the value is 10. The detected edges lose the sharp character and become vague when the ∝ value is more than 10. Therefore, to extract the effectiveness of the filter, a ∝ value of 2-10 can be used for the best results. In the present study, a ∝ value of 2 is fixed to all the synthetic and real data models.

4. Application Over the 2D Synthetic Magnetic Model

A synthetic magnetic model consisting of three prisms with different physical properties buried at different depths is developed. The physical and geometrical properties of the bodies are represented in Figure 2a. The magnetic response of the synthetic model is presented in Figure 2b, and its reduced-to-pole (RTP) magnetic anomaly is presented in

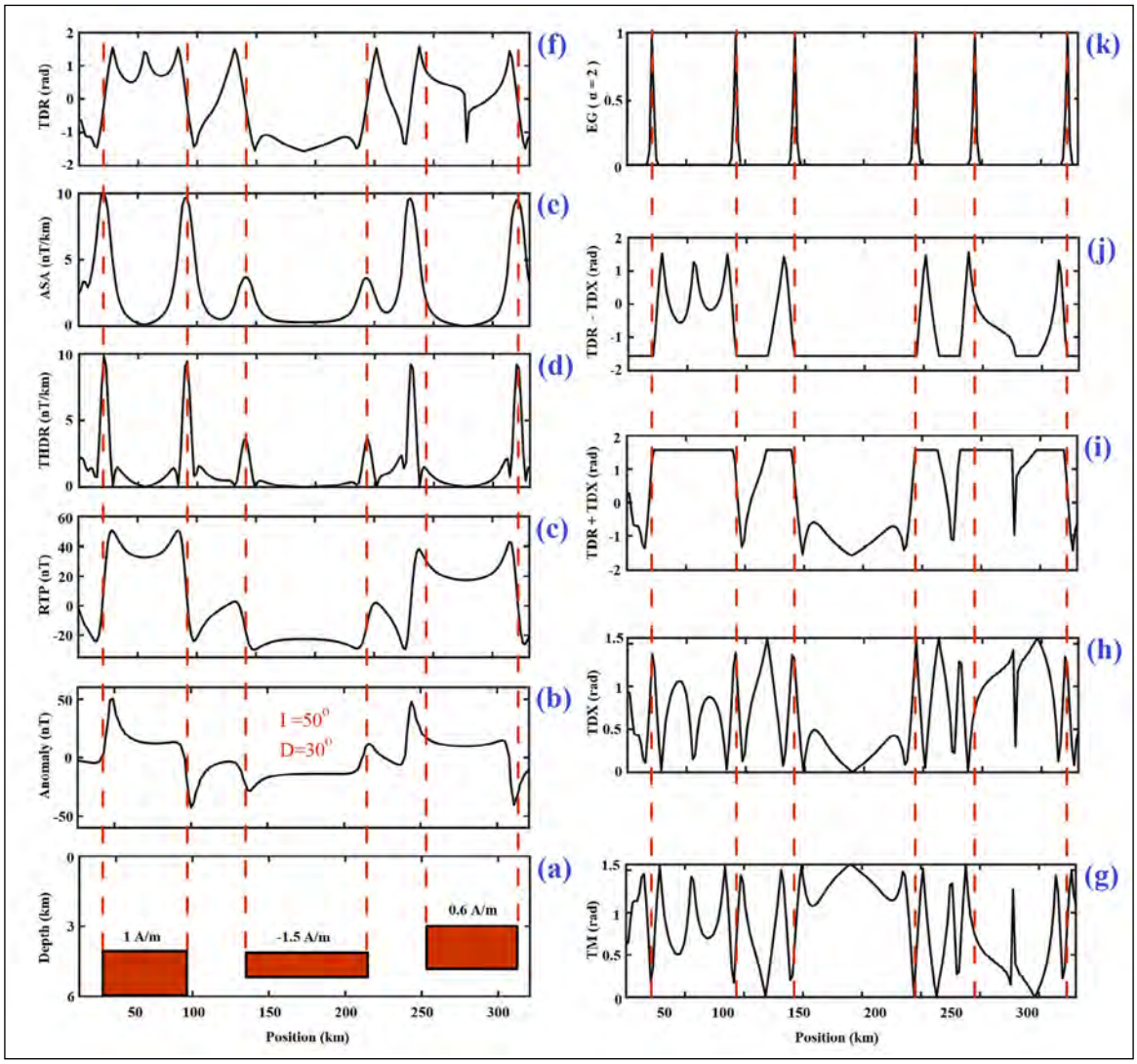

Figure 2 - The response of various edge detection techniques over a synthetic magnetic model; a) Schematic representation of synthetic model, b) the magnetic anomaly response over the three prismatic bodies, c) the reduced-to-pole magnetic anomaly response over the three prismatic bodies. The response of various filters are presented as d) THDR, e) ASA, f) TDR, g) TM, h) TDX, i) TDR + TDX, j) TDR – TDX and k) enhanced gradient filter.

Figure 2c. The response of the various conventional edge detection filters is represented in Figures 2d to 2j. It is obvious from the response that when the magnetic data is subjected to different conventional filters (Figure 2d to 2j), the response is better analyzed in THDR (Figure 2d), ASA (Figure 2e). However, the response is not balanced for the shallow and deeper bodies. The rest of the filters have spurious and false edges, making the interpretation more complex. When the Enhanced Gradient filter with $\propto = 2$ is applied to the RTP magnetic anomaly, the amplitude response maxima show a clear demarcation of the edges of the prismatic bodies (Figure 2k). The maxima of the response are over the edge of the body. Moreover, we can observe a balanced image from the sources buried at shallower and deeper depths.

5. Application Over the 3D Synthetic Magnetic Model

To illustrate the robustness of the proposed filter, a synthetic magnetic model with ten prismatic bodies is constructed. The schematic model of the synthetic magnetic model is shown in Figure 3a, with the nomenclature of the prismatic bodies in Figure 3b. The total magnetic intensity (TMI) is calculated on a 200×200 km^2 grid with a grid spacing of 1 km along the east-west and north-south directions (Figure 4a). The magnetic inclination and declination of all prisms are 90° and 0°, respectively. The magnetic anomaly is reduced to pole. The dimension and properties of the prismatic bodies are shown in Table 1.

The response of the THDR and ASA filters are shown in Figures 4b and 4c, respectively. Shallow

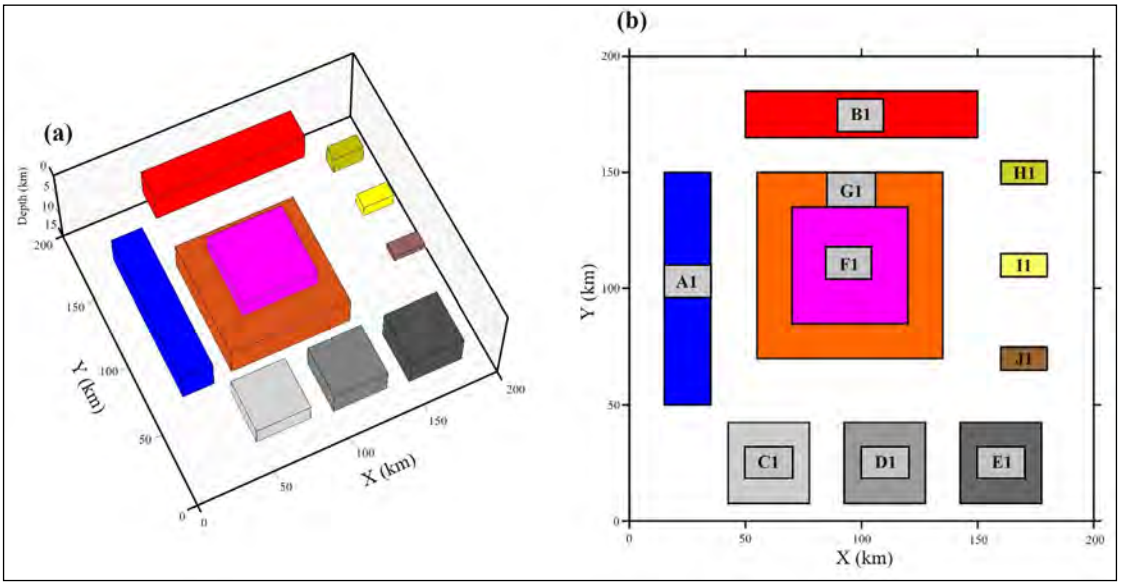

Figure 3- Schematic representation of the synthetic model (magnetic) in a) three-dimensional view and b) planar view with nomenclature of different prismatic bodies.

Table 1- The parameters of the prismatic bodies used to generate magnetic anomaly over the 3D synthetic model. All the dimensions are in kilometers.

Property	A1	B1	C1	D1	E1	F1	G1	H1	I1	J1
Xc	25	100	60	110	160	95	95	170	170	170
Yc	100	175	25	25	25	110	110	150	110	70
Width	20	100	35	35	35	50	80	20	20	20
Height	100	20	35	35	35	50	80	10	10	10
Top Depth	2	2	5	5	5	5	10	3	2	1
Thickness	5	5	3	4	5	3	5	3	2	1

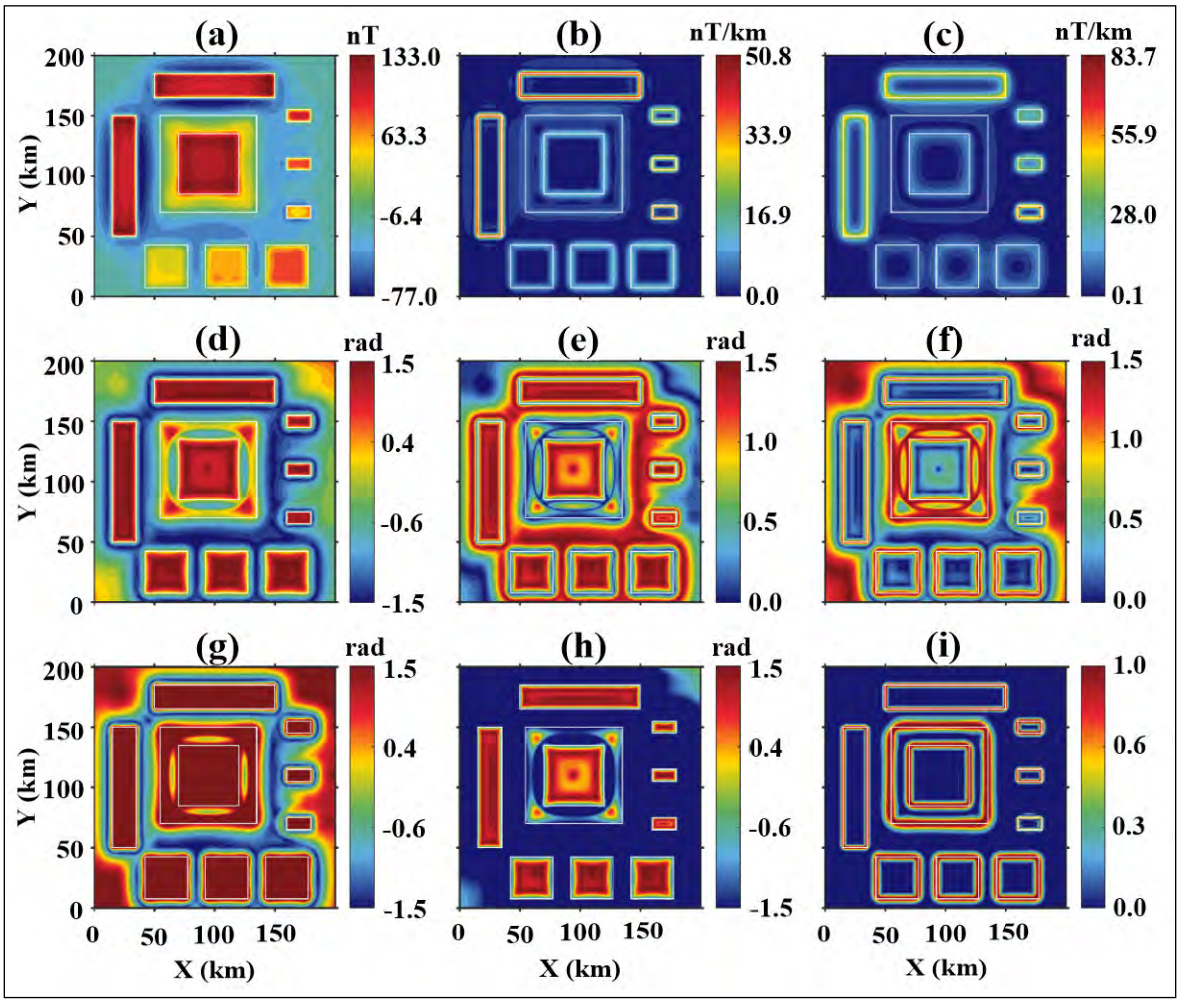

Figure 4- The magnetic anomaly is shown in a); All the 10 bodies are positively magnetized. The response of various edge detection filters are b) THDR, c) ASA, d) TDR, e) TM, f) TDX, g) TDR + TDX, h) TDR – TDX and i) Enhanced gradient filter (The white line represents the real prism edge).

seated bodies dominate the response. The edges detected from the deep-seated bodies are blurred. The filters TDR (Figure 4d), TM (Figure 4e), TXD (Figure 4f), TDR+TDX (Figure 4g), and TDR-TDX (Figure 4h) are found to produce spurious and false boundaries. The response of the EG filter at an alpha value of 2 is presented in Figure 4i shows that the proposed filter successfully delineates the edges of all the prismatic bodies buried at different depths. The filter produced a balanced image of the edges. The stability of the filter is also tested by applying negative magnetization to three bodies (blocks of 2, 4, and 9, as shown in Figure 5) which proved that the EG response was similar to the case discussed above. 4% Gaussian noise to the magnetic anomaly with a standard deviation of 0.5 nT and the results are shown in Figure 6, which shows a noisy response from all the filters where the EG filter proves to be better.

Any edge detection filter applied to the noisy data may not give a clear image of the subsurface structures (Pham et al., 2021; Prasad et al., 2022*a*), so we continued the anomaly to 500 m upward (Figure 7a). Figure 7b-j shows the results of the THDR, ASA, TDR, TM, TDX, TDR+TDX, TDR-TDX and EG after upward continuation of the data. THDR (Figure 7b) and ASA (Figure 7c) produced edges and the noise's influence is not much compared to the rest of the conventional filters. The THDR and ASA filters are dominated by a large-amplitude response from the shallow prism B1, but the small amplitude responses from the deeper sources A1, C1, D1, E1 and F1 are

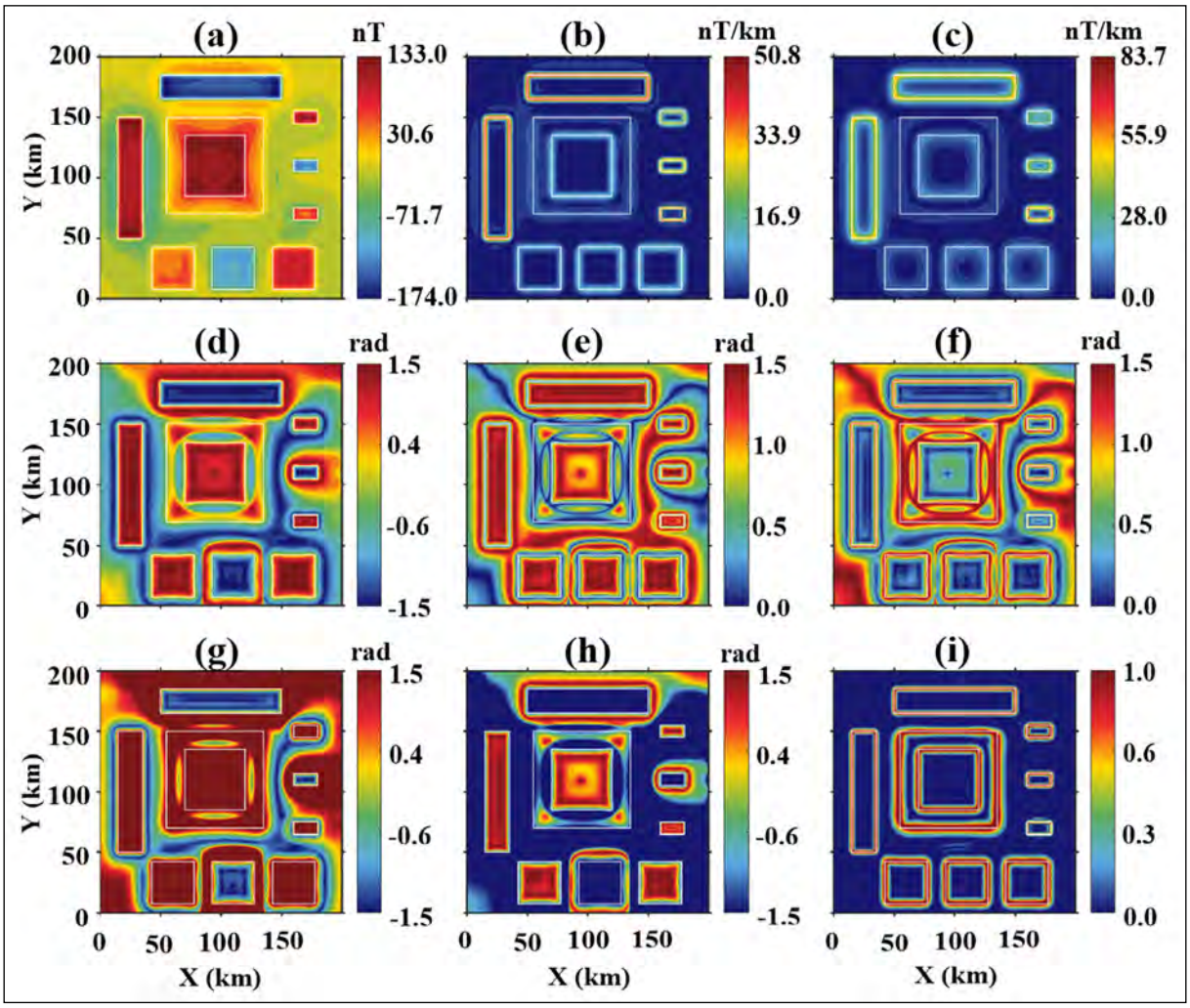

Figure 5- The magnetic anomaly is shown in a); Seven out of 10 bodies are positively magnetized, and the remaining three (2, 4 and 9) are negatively magnetized. The response of various edge detection filters are b) THDR, c) ASA, d) TDR, e) TM, f) TDX, g) TDR + TDX, h) TDR – TDX and i) EG filter (The white line represents the real prism edge).

blurred. Moreover, the maximal amplitude of the ASA filter needs to function better for thin source E1, despite the shallower depth than sources C1, D1 and F1. The TDR (Figure 7d), TM (Figure 7e) and TDX (Figure 7f) filters can balance the edges of the shallow and deep-seated sources well, but they produce such false and spurious edges. The images obtained from using the TDR + TDX (Figure 7g) and TDR-TDX (Figure 7h) filters again show that they do not function well for detecting the sources' edges and produce false contours around and inside of sources. However, their quality and resolution are better than THDR, ASA, TDR, TM and TDX filters. However, the EG filter (Figure 7i) successfully delineates all the edges with minimum influence of the added noise.

6. Application on Aeromagnetic Data

In this section, the ability of the EG filter is tested on the real magnetic data from the northeastern part of the Indiana region situated in North America (Figure 8). The study area consists of gently eastward-dipping sequences of shale, limestone, and sandstone of Paleozoic age formed from material deposited when transgressing shallow seas covered most of the North American continent (Haase et al., 2010). These bedrock units are covered by unconsolidated deposits left from several intervals of glaciation in the Tertiary and Quaternary periods. The bedrock of Indiana experienced erosion at least since late Pennsylvanian time (~300 million years ago). It was

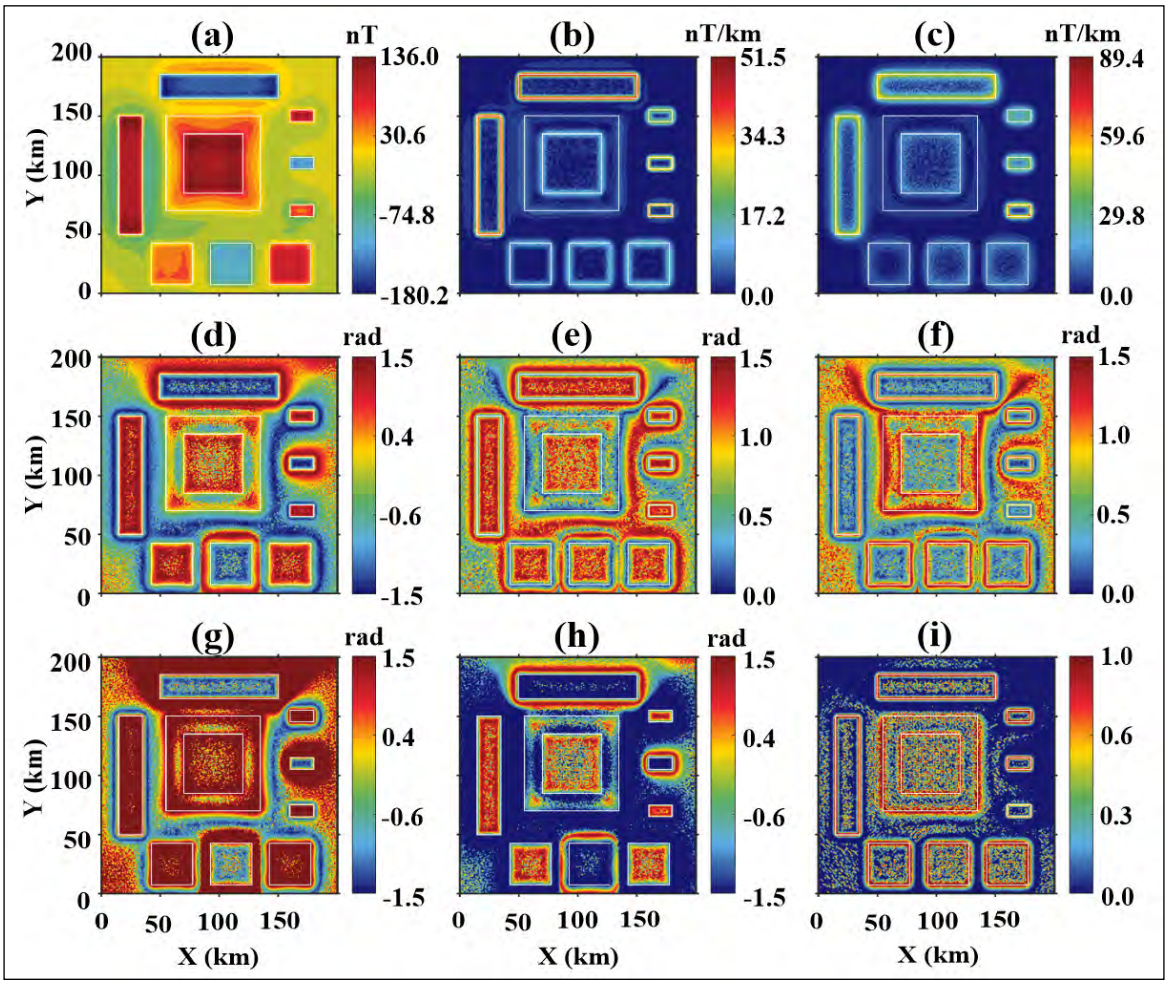

Figure 6- The magnetic anomaly with 4% Gaussian noise added to the synthetic model is shown in a); The response of various edge detection filters are b) THDR, c) ASA, d) TDR, e) TM, f) TDX, g) TDR + TDX, h) TDR – TDX and i) EG filter (The white line represents the real prism edge).

covered by unconsolidated materials only during the past 2 million years when two major glacial advances and retreats crossed the state. Bedrock is exposed only in the south-central part of the state, which was not glaciated, and in localized areas along the Wabash River (Erd and Greenberg, 1960; Huizing and Russell, 1986).

Magnetic anomalies caused by Earth's magnetic field variations make up the upper part of the Earth's crust. The patterns in the magnetic anomalies are used to delineate the locations of buried faults and magnetite-bearing rocks by analyzing the Curie depths and the depth to the base of the sedimentary basin. The analysis of magnetic data is vital for mineral exploration and geological mapping studies. The magnetic anomaly map over the study region, the northeastern part of the Indiana region situated in North America, is constructed from the grids that combine the magnetic data information collected by United States Geological Survey (USGS) during 1947-1994 in 19 separate magnetic surveys due to which the data has varying quality (Henderson and Zietz, 1958; Philbin et al., 1965). These magnetic anomaly maps were digitized along flight-line, considered the most accurate method of recovering the original data. All surveys have been continued to a height of ~300 m above ground and merged to form the States compilation. Index maps show the location of the original surveys, and a data table summarizes the detailed specifications of the surveys. The final magnetic anomaly grid with a 500 m interval and

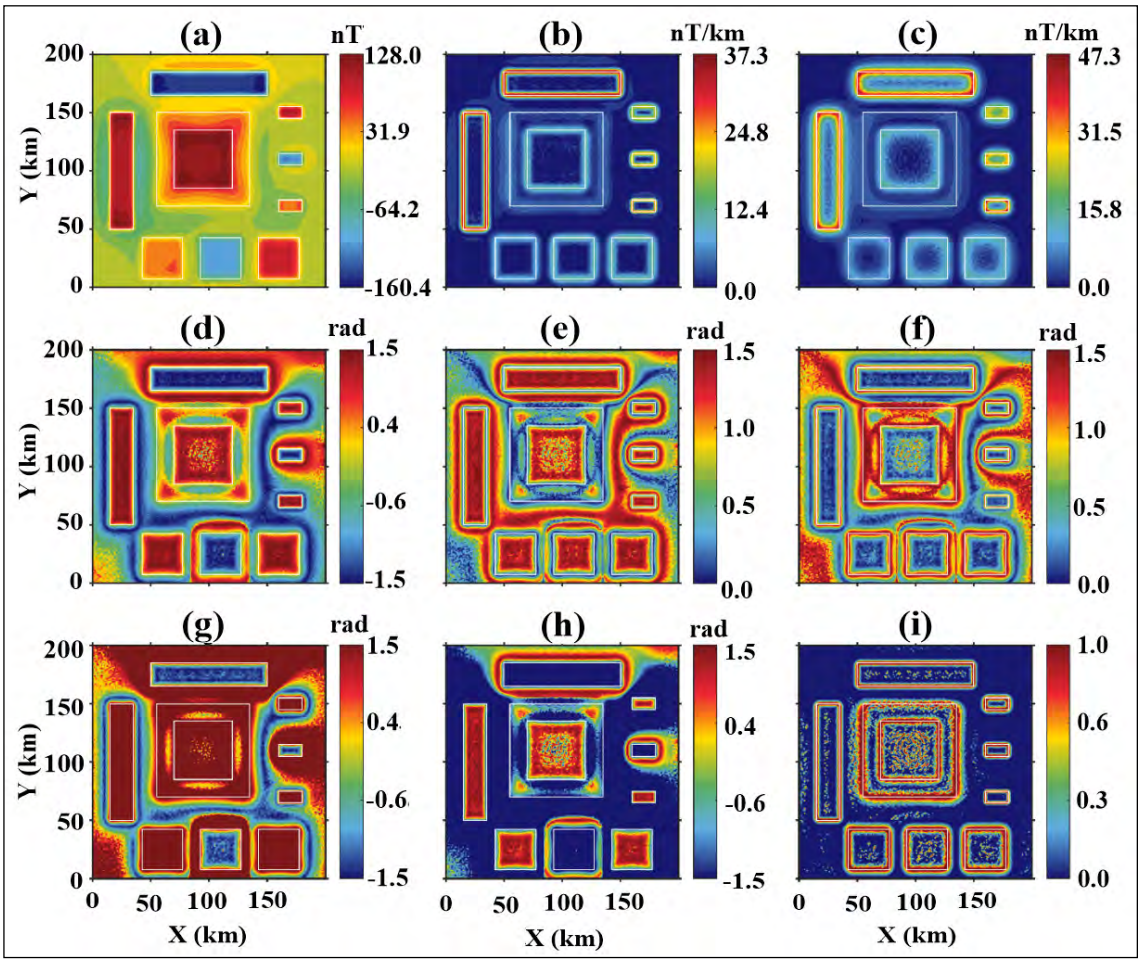

Figure 7- The noise-induced magnetic anomaly continued 500 m upwards is shown in; a) the response of various edge detection filters are b) THDR, c) ASA, d) TDR, e) TM, f) TDX, g) TDR + TDX, h) TDR – TDX and i) EG filter (The white line represents the real prism edge).

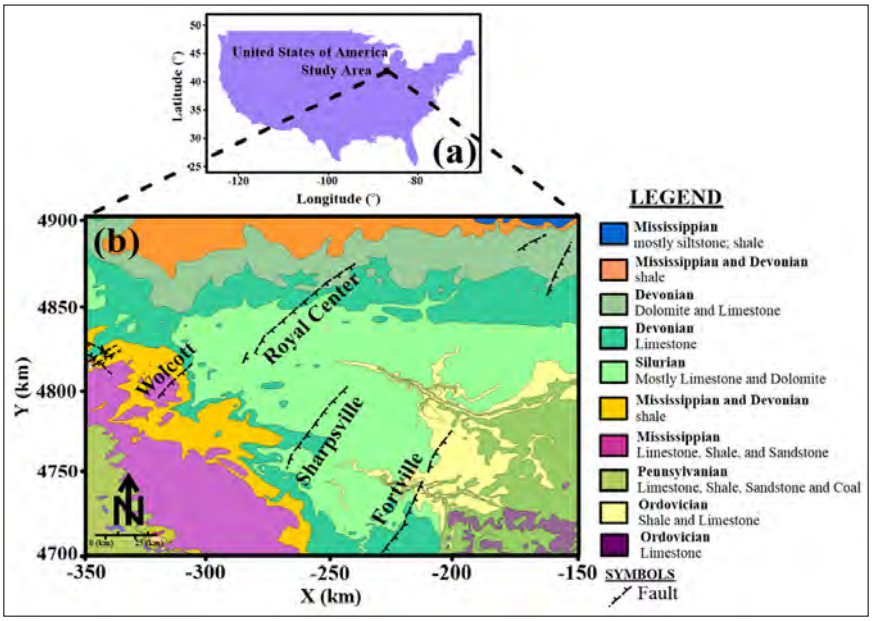

Figure 8- Geological map of the study region with the major tectonic features overlaid (modified from Gray et al., 1987; Gray, 1989 and https://www.usgs.gov).

a part of the magnetic anomaly map is used in the present study and is shown in Figure 9a.

Figures 9b and 9c display the results obtained from using the THDR and ASA filters, respectively. As can be seen, the maps of ASA and THDR are blurred and non-reliable in bringing precise edges for the subsurface sources. Figures 9d, 9e and 9f show the results determined by the TDR, TM and TDX filters, respectively. As seen from these figures, the methods can equalize the amplitudes of large and small anomalies; many adjacent boundaries obtained from this method are connected, making it difficult to detect the geological structures. Figures 9g and 9h show the results of applying TDR+TDX and TDR-TDX, respectively.

The boundaries outlined by the TDR±TDX filters are more precise and accurate than those obtained from other filters. Figure 9i depicts the result obtained by the EG filter on the magnetic data. As observed from the response of the EG filter, it is clear that the detected lineaments have a balanced response from the sources situated at different depths below the subsurface. Moreover, the filter performed better when compared to the other conventional filters used in the present study. Most of the lineaments generated in the study region are trending random direction. The results from the present study are plotted in red, bounded by a sharp blue color line that merely coincides with the existing tectonic features (Figure 10). We can observe that the Fortville fault is directed in almost N-S to N/NE-S/SW has a gravity gradient in the same direction.

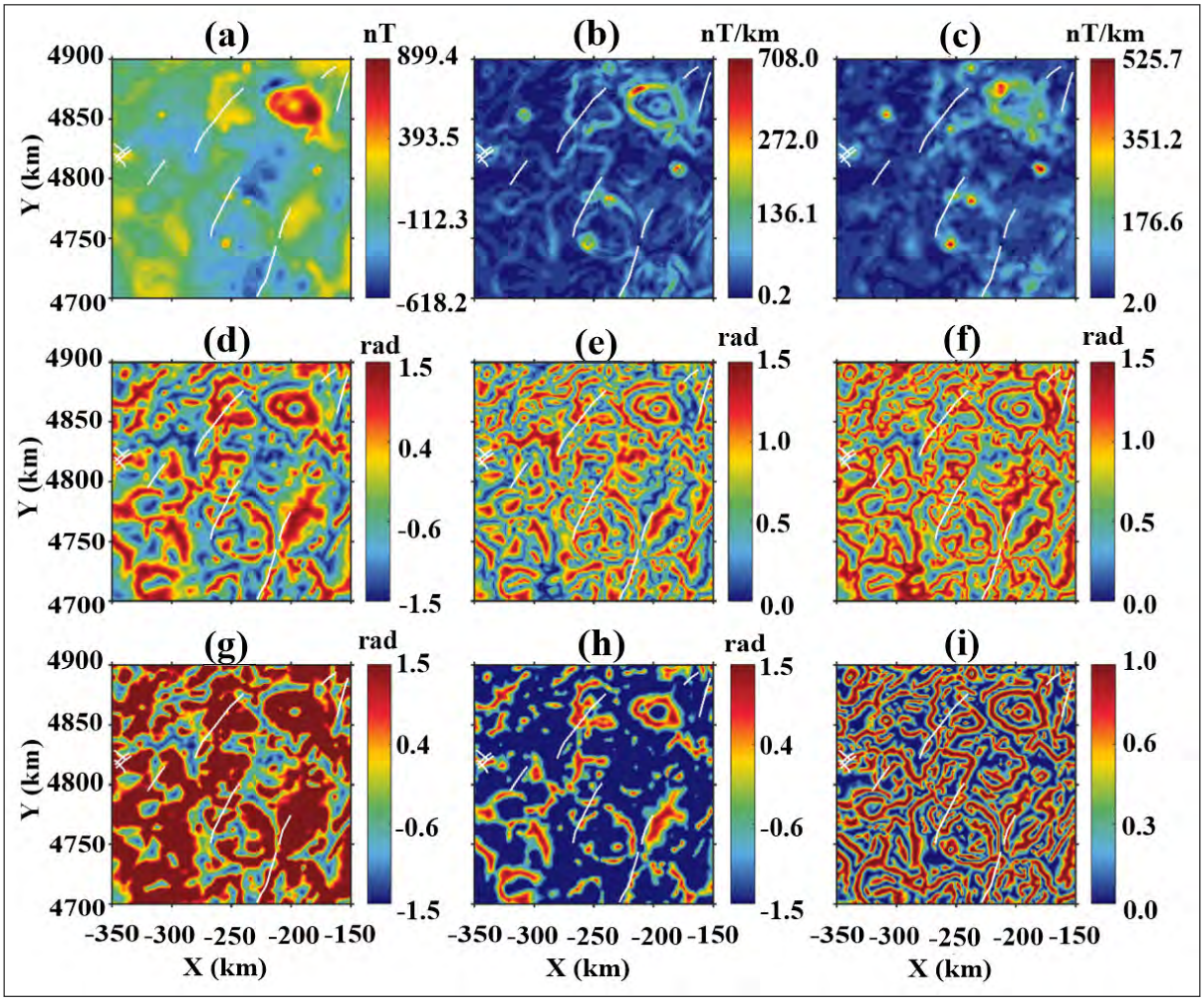

Figure 9- The aero-magnetic anomaly is shown in; a) the response of various edge detection filters are b) THDR, c) ASA, d) TDR, e) TM, f) TDX, g) TDR + TDX, h) TDR – TDX and i) EG filter.

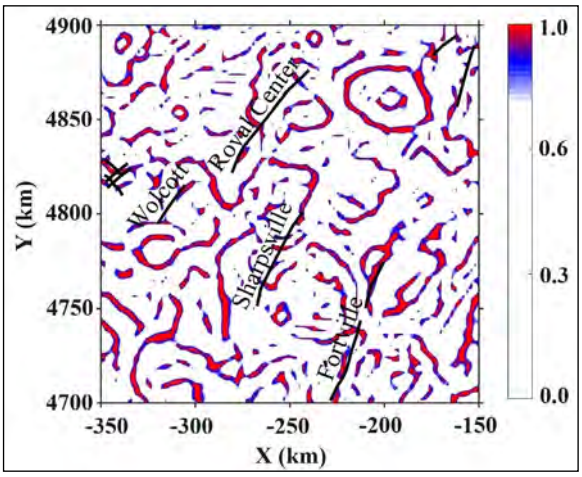

Figure 10-Interpreted lineaments (red color) of the study region overlaid by the major tectonic features (black lines).

However, it has been constrained by a lineament running in the E-W direction towards its northern end. Even though the Sharpsville tectonic fault runs in the N/NE-S/SW direction, we can observe almost crescent-shaped lineaments towards its southern end, followed by an N/NE-S/SW dipping lineament at its northern end. A similar case is seen for the Wolcott tectonic fault. The lineaments beneath the Royal Center tectonic fault are not aligned in the direction of the fault. Instead, the central part of the Royal Center fault is dominated by a N-S trending lineament.

7. Results

Edge detection is a fundamental process in subsurface structural analysis and interpretation. The accuracy increases with noise reduction, making new filters more common. Because the edge enhancement filters are based on the derivative of the anomaly, they amplify the noise signal in the data. However, the EG filter can equalize the weak and strong signals simultaneously and does not bring any false information to the edge map. Also, the EG filter generated a new structural map of the study region in North America, which can help us to draw a new structural and tectonic framework. Finally, the EG is higher resolution, removal of false edges and generates subtler geologic features.

Acknowledgements

The authors would like to thank the US Geological Survey (https://www.usgs.gov) for permission to use the geological information and the aeromagnetic data and Dr. Gordon Robert John Cooper for providing the Hilbert transform calculation scripts.

References

Alvandi, A., Ardestani, V. E. 2023. Edge detection of potential field anomalies using the Gompertz function as a high-resolution edge enhancement filter. Bulletin of Geophysics and Oceanography 64(3), 279-300.

Alvandi, A., Toktay, H. D., Pham, L. T. 2022. Capability of improved logistics filter in determining lateral boundaries and edges of gravity and magnetic anomalies Tuzgölü Area, Türkiye, Journal of Mining Engineering 17(56), 57-72.

Alvandi, A., Toktay, H D., Ardestani, V. E. 2023. Edge detection of geological structures based on a logistic function: A case study for gravity data of the Western Carpathians. International Journal of Mining and Geo-Engineering 57(3), 267-274.

Blakely, R. J., Simpson, R. W. 1986. Approximating edges of source bodies from magnetic or gravity anomalies. Geophysics 51(7), 1494-1498.

Castro, F. R., Oliveira, S. P., De Souza, J., Ferreira, F. J. F. 2018. GRAV-MAG SUITE: An open source MATLAB-based program for processing potential field data. Sociedade Brasileira de Geofísica 8(2), 1-6.

Cooper, G. R. 2009. Balancing images of potential-field data. Geophysics 74(3), 17-20.

Cooper, G. R. J., Cowan, D.R. 2006. Enhancing potential field data using filters based on the local phase. Computers and Geosciences 32(10), 1585-1591.

Cordell, L., Grauch, V. J. S. 1985. Mapping basement magnetization zones from aeromagnetic data in the San Juan Basin, New Mexico. In: The utility of regional gravity and magnetic anomaly maps. Society of Exploration Geophysicists Press, 181-197.

Erd, R. C., Greenberg, S.S. 1960. Minerals of Indiana. Indiana Geological Survey Bulletin 18, 73.

Gray, H. H. 1989. Quaternary geologic map of Indiana: Indiana Geological Survey Miscellaneous Map No: 49, scale 1:500.000, Bloomington, Indiana, United States of America.

Gray, H. H., Ault, C. H., Keller, S. J. 1987. Bedrock geologic map of Indiana, Indiana Geological Survey Miscellaneous Map No: 48, scale 1:500.000, Indiana, United States of America.

Haase, S. H., Park, C. H., Nowack, R. L., Hill, J. R. 2010. Probabilistic seismic hazard estimates incorporating site effects-an example from Indiana, USA. Environmental and Engineering Geoscience 16 (4), 369-388.

Henderson, J. R., Zietz, I. 1958. Interpretation of an aeromagnetic survey of Indiana: US Geological Survey Professional Paper 316-B, 17, scale 1:500,000, Indiana, United States of America

Huizing, T. E., Russell, R. E. 1986. Indiana minerals: a locality index. Rocks and Minerals 61(3),136-151.

Ibraheem, I. M., Tezkan, B., Ghazala, H., Othman, A. A. 2023. A new edge enhancement filter for the interpretation of magnetic field data. Pure and Applied Geophysics 180, 2223-2240.

Miller, H. G., Singh, V. 1994. Potential field tilt—a new concept for location of potential field sources. Journal of Applied Geophysics 32(2-3), 213-217.

Nabighian M. N. 1984. Towards a three-dimensional automatic interpretation of potential field data via generalized Hilbert transforms-fundamental relations. Geophysics 49, 780-786.

Pham, L. T., Oksum, E., Do, T. D., Huy, M. L. 2018. New method for edges detection of magnetic sources using logistic function. Geofizicheskiy Zhurnal 40(6), 127-135.

Pham, L. T., Oksum, E., Do, T. D., Nguyen, D. V., Eldosouky, A.M. 2021. On the performance of phase-based filters for enhancing lateral boundaries of magnetic and gravity sources: a case study of the Seattle uplift. Arabian Journal of Geosciences 14(2), 1-11.

Pham, L. T., Eldosouky, A. M., Oksum, E., Saada, S. A. 2022. A new high-resolution filter for source edge detection of potential field data. Geocarto International 37(11), 3051-3068.

Philbin, P. W., Long, C. L., Moore, F. C. 1965. Aeromagnetic map of the Columbus-Dayton area, Ohio and Indiana: U.S. Geological Survey Geophysical Investigations Map GP-491, scale 1:250,000, United States of America.

Phillips, J. D. 2002. Processing and interpretation of aeromagnetic data for the Santa Cruz Basin-Patagonia mountains area, South-central Arizona. US Geological Survey Open -File Report 02-98, Washington, DC, United States of America.

Prasad, K. N. D., Pham, L. T., Singh, A. P. 2022*a*. A novel filter "ImpTAHG" for edge detection and a case study from Cambay Rift Basin, India. Pure and Applied Geophysics 179(6), 2351-2364.

Prasad, K. N. D., Pham, L. T., Singh, A. P. 2022*b*. Structural mapping of potential field sources using BHG filter. Geocarto International 37, 1-28.

Richards, F. J. 1959. A flexible growth function for empirical use. Journal of Experimental Botany 10(2), 290-301.

Roest, W. R., Verhoef, J., Pilkington, M. 1992. Magnetic interpretation using the 3-D analytic signal. Geophysics 57(1), 116-125.

USGS Science for Changing World (United States Geological Survey). https://www.usgs.gov. 05 August 2024

Wijns, C., Perez, C., Kowalczyk, P. 2005. Theta map: Eedge detection in magnetic data. Geophysics 70(4), L39-L43.

Zuo, B., Hu, X., Liu, S., Geng, M. 2018. Delineation of overlapping magnetic field source boundaries with a 3-D multi-layer convolution model. Journal of Applied Geophysics, 150, 74-83.

Bulletin of the Mineral Research and Exploration

http://bulletin.mta.gov.tr

Structural relationship between subsurface oil fields in the North Dezful Embayment: Qaleh Nar, Lower and Upper Balarud Anticlines (Central Zagros, Iran)

Raana Razavi PASH[a], Mohammad SERAJ[b], Soumajit MUKHERJEE[c*] and Ahmad RADMEHR[d]

[a] *Shiraz University, Faculty of Earth Sciences, Shiraz, Iran*
[b] *National Iranian South Oil Company (NISOC), Ahwaz, Iran*
[c] *Indian Institute of Technology Bombay, Department of Earth Sciences, Mumbai, 400 076, Maharashtra, India*
[d] *National Iranian South Oil Company, Ahwaz, Iran*

Research Article

Keywords:
Hydrocarbon, Tectonics, Seismic Image Interpretation.

ABSTRACT

How subsurface anticlines (oil fields) link structurally with faults is of great relevance in the exploration and development of oil fields. In this context, we investigate the geometric relation between lower Balarud (LBR), upper Balarud (UBR) and Qaleh Nar (QN) subsurface anticlines that are the main oil fields in the Northern Dezful Embayment, central Zagros. The Asmari (As) and the Bangestan (Bng) reservoirs are studied geophysically using seismic profiles, well data and underground contour maps (UGC). Interpretation of 3500 m deep seismic profiles indicates the geometry of the studied subsurface anticlines differs vertically and horizontally to a significant proportion. The interpreted structures much resemble As and Bng horizons in each anticline. The UBR got overturned on the LBR due to thrusting possibly in the Late Miocene. The LBR, like a rabbit-ear structure, is situated at the northern edge of the QN. The lower and upper Chenareh and LBR and UBR resemble structurally and are separated mutually by a steep (strike-slip) fault. The fault separates the LBR and UBR from the QN. Interaction of different factors change in overburden pressure, rate of deformation and uplift in the different parts of the subsurface anticlines moved and accumulated Gachsaran Formation towards both limbs of the anticlines.

Received Date: 02.05.2023
Accepted Date: 23.07.2023

1. Introduction

The Zagros fold-and-thrust belt is one of the prolific petroliferous regions (Cooper, 2007) with ~ 12% of the global oil reserves (Bordenave and Burwood, 1990). Fold and thrust belts have otherwise been questioned to be the suitability for hydrocarbon exploration (review in Hammerstein et al., 2020). Notwithstanding, such a question never arose for the Zagros orogenic belt (Asl et al., 2019). Previous studies in the Zagros belt (especially in the North of Dezful Embayment) reveal that the oil reservoirs are located at several Formations and depths (Safari and Bagas 2021). Major hydrocarbon reserves in the Zagros belt are hosted by anticlines in the Late Cretaceous rocks within the Bangestan (*Bng*) Group and the Oligo-Miocene Asmari (*As*) Formation (Sherkati and Letouzey, 2004; Bordenave, 2014). Ductile evaporitic Gachsaran Formation covers the fractured competent *As* Formation at shallow depths (McQuarrie, 2004; Safari and Bagas, 2021). The Qaleh Nar (*QN*), Lower Balarud (*LBR*), upper Balarud (*UBR*), Kabood and Lab-e Safid subsurface anticlines

Citation Info: Pash, R. R., Seraj, M., Mukherjee, S., Radmehr, A. 2024. Structural relationship between subsurface oil fields in the North Dezful Embayment: Qaleh Nar, Lower and Upper Balarud Anticlines (central Zagros, Iran). Bulletin of the Mineral Research and Exploration 174, 67-83. https://doi.org/10.19111/bulletinofmre.1344433

**Corresponding author: Soumajit MUKHERJEE, soumyajitm@gmail.com*

are the most important oil fields in the north of Dezful Embayment. These are located just south of the main Balarud fault zone (Figure 1).

Previous studies in this area have shown that the Balarud fault has significantly affected these anticlines (Razavi Pash et al., 2020; 2021*a*). The subsurface anticlines define most of the hydrocarbon traps in this region (Allen, 2010; Sarkarinejad et al., 2017; Razavi Pash et al., 2020; Razavi Pash et al., 2021*b*). Interpretation of subsurface data using seismic lines, well data and contour maps are the efficient ways to study blind anticlines (Sarkarinejad et al., 2017; Razavi Pash et al., 2020, 2021*b*). Investigating the structural relation between subsurface anticlines and faults has assisted manifold in petroleum geoscience (Sarkarinejad et al., 2017; Razavi Pash et al., 2020; 2021*b*).

Previous studies conducted in the studied area have investigated the effect of the Balarud fault and the detachment horizons on the geometry of the anticlines (e.g. Hajialibeigi et al., 2015; Sarkarinejad et al., 2017; Razavi Pash et al., 2021*a*, 2021*b*).

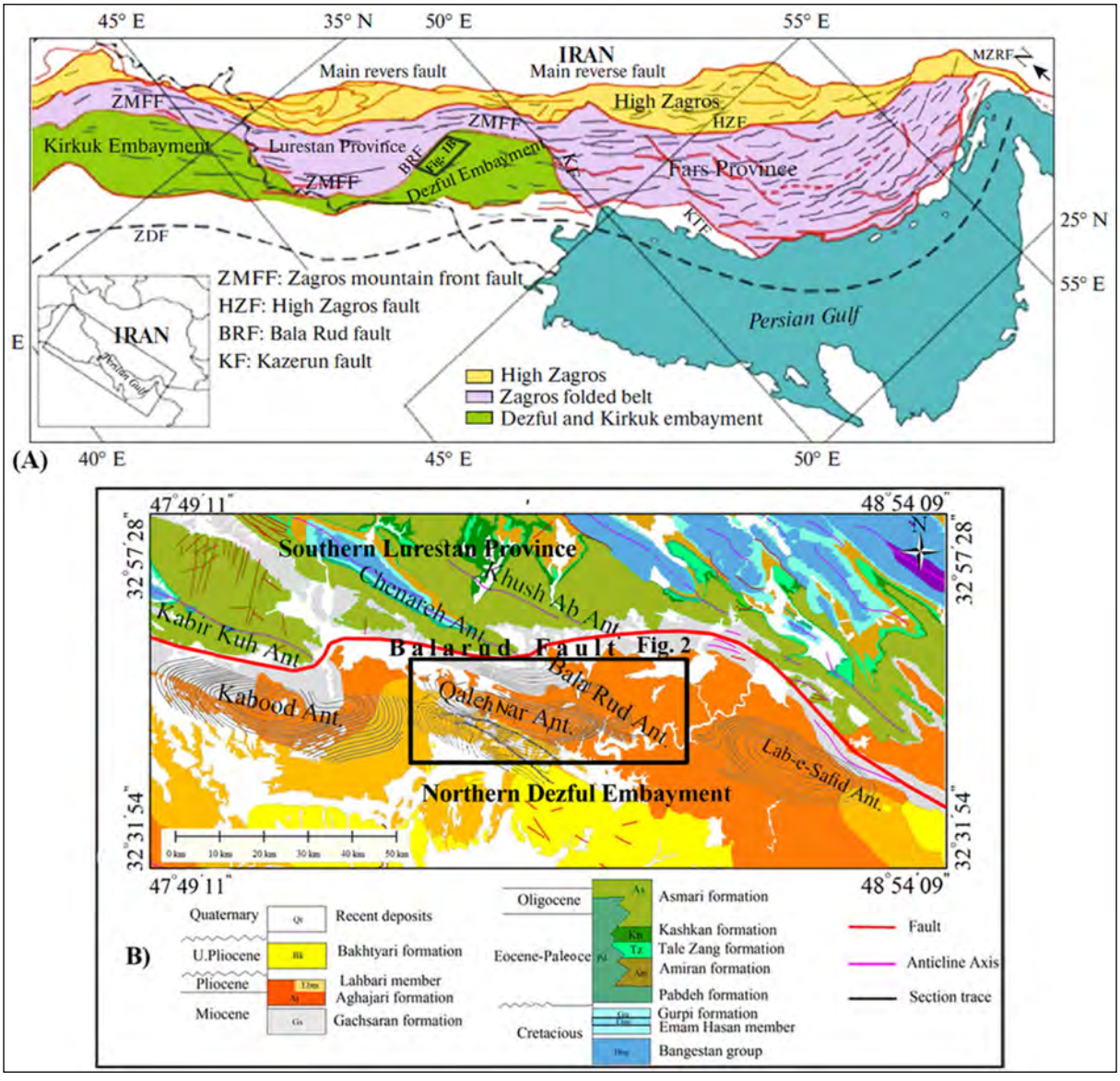

Figure 1- a) Location of the studied anticlines in the central Zagros b) simplified geologic map of the study area and location of the subsurface anticlines with respect to the Balarud fault (Razavi Pash et al. 2021 *a*). Rectangle: location of the studied anticlines. Contours show the underground map of the *As* Formation for anticlines.

However, the structural relationship between these subsurface anticlines has not been investigated. In this research, high-quality seismic profiles [produced by the National Iranian South Oil Company (NISOC)] have been interpreted and the structural relationship between the structures has been investigated. We investigated the geometric relation of the *LBR*, *UBR* and *QN* subsurface anticlines in the footwall of the Balarud fault (Figure 1 and 2). These structures are the major oil fields in the Northern Dezful Embayment. We interpret seismic images, well data and underground contour maps (UGC).

It is worth mentioning that the interpretation of the *LBR* anticline (as an oil field in the region located in the repeated layers below the *UBR* anticline) and its structural relationship with the *UBR* and *QN* have been investigated for the first time in this research.

2. Geology

The Zagros Fold-and-Thrust Belt (ZFTB) is a portion of the Alpine-Himalayan belt located in the SW Iran. The Zagros belt is a product of first the opening of the Neo-Tethyan ocean at the Late Permian–Early Triassic (Stocklin, 1968) and subsequently closing at Tertiary time (Late Miocene) (Berberian and King, 1981; Sherkati et al., 2006). Iran converged with the Arabian plate in the Late Cretaceous (Agard et al., 2005). In the Late Miocene, the main folding took place in the Zagros (Homke et al., 2004; Emami et al., 2010; Razavi Pash et al., 2021*b*).

The Dezful embayment (central Zagros) is bound in the northeast by Mountain Front Fault (MFF), in the north by Balarud Fault, in the east to southeast by Kazerun and Izeh transverse faults, and in the southwest by the Zagros fore-deep (Frontal) Fault (ZFF) (Berberian, 1995; Hessami, 2002; Safari et al., 2009) (Figure 1a). Most of Iran's oil fields are situated in this embayment.

The Dezful Embayment is the main foreland basin since the Late Cretaceous (Sepehr et al., 2006). The interaction between the basement faults, folding and faulting of overlying rock units during and after deposition of Oligocene-Miocene carbonate beds (*As*) evolved the Dezful Embayment (Allen and Talebian, 2011). The folded *As* Formation is situated below the Gachsaran evaporate Formation in the Dezful Embayment. This has provided suitable conditions for creating the oil fields (Sepehr et al., 2006; Sherkati et al., 2006; Abdollahie Fard et al., 2011). The Aghajari and Bakhtyari Formation above the Gachsaran Formation deposites syn-tectonically due to the uplift and erosion of the hinterland part of the Zagros belt (Sherkati et al., 2006; Pirouz et al., 2011). Figure 3

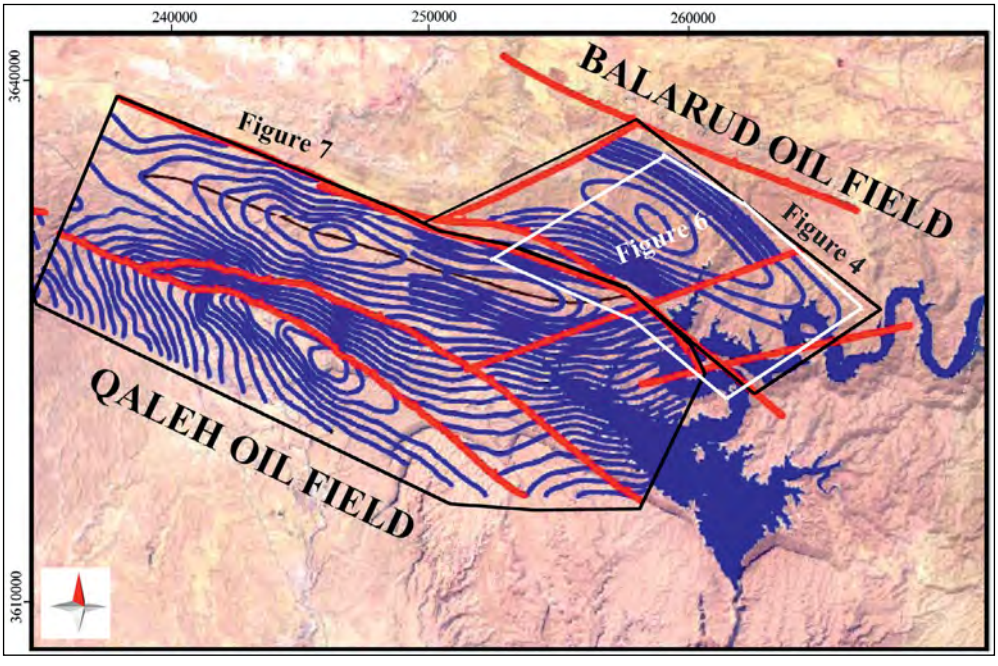

Figure 2- UGC map of the studied anticlines on the satellite image. The location of this Figure is shown in Figure 1b.

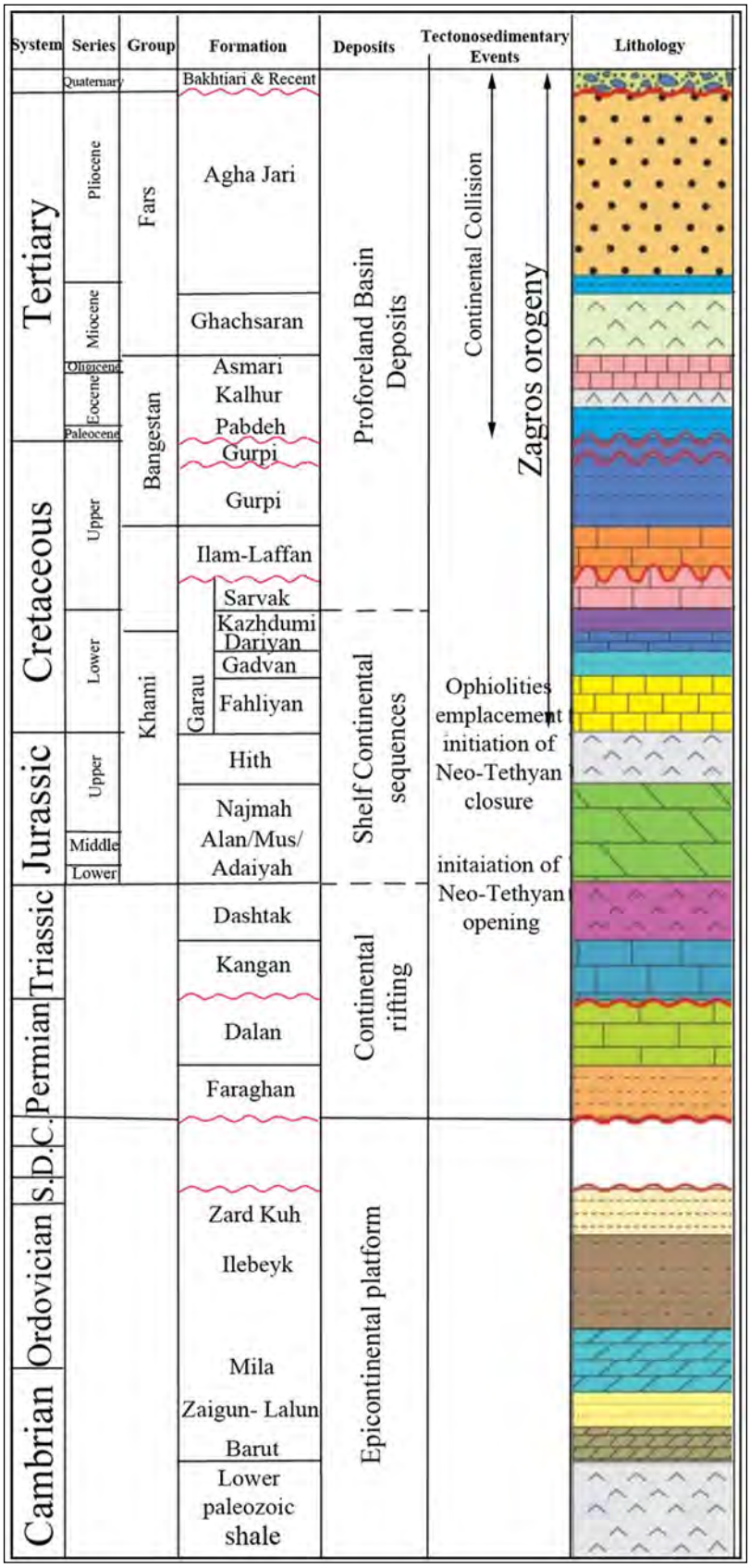

Figure 3- Stratigraphic column of the northern Dezful Embayment based on surface and well data (Abdollahie Fard et al., 2011).

presents the stratigraphic succession of the northern Dezful Embayment. The sinistral Balarud shear zone separates Lurestan province from the North Dezful Embayment (Sherkati et al., 2006; Sarkarinejad et al., 2017; Razavi Pash et al., 2021*a*). Deformation in the north Dezful Embayment has happened mainly by the Balarud left-lateral shear zone (Razavi Pash et al. 2020; Razavi Pash et al., 2021*a*). Faults and folds at both sides of the Balarud fault have the en-echelon geometry (Sarkarinejad et al., 2017; Razavi Pash et al., 2020; 2021*a*). Curved anticlines axes (e.g., NW-trending Kabir Kuh and Chenareh anticlines) in the southern part of Lurestan province can be deciphered at the surface (Bahroudi and Koyi, 2003; Sarkarinejad et al., 2017; Razavi Pash et al., 2020; 2021*a*).

3. Methods

To study the lateral variations of the structural style of folding in this area, geologic maps scale 1:100,000 scale, underground contour maps (UGC), seismic profiles and well data were interpreted for the sub-surface fold geometry and to construct the cross-sections using the Petrel software (version 2014). Since the two most important reservoirs are *Bng* and *As* Formation (As) (Sherkati and Letouzey, 2004; Sherkati et al., 2005; Bordenave and Hegre, 2005; Bordenave, 2014), we interpret them for structures. UGC maps were prepared based on interpreted seismic lines and well data.

4. 2D Structural Analyses of the *QN*, *UBR* and *LBR* Subsurface Anticlines

The *QN*, *UBR* and *LBR* anticlines define the main structures (Figure 4). The *LBR*, like a rabbit ear structure, is located at the northern edge of the *QN*. The *UBR* with a thrust fault is completely driven on the *LBR*.

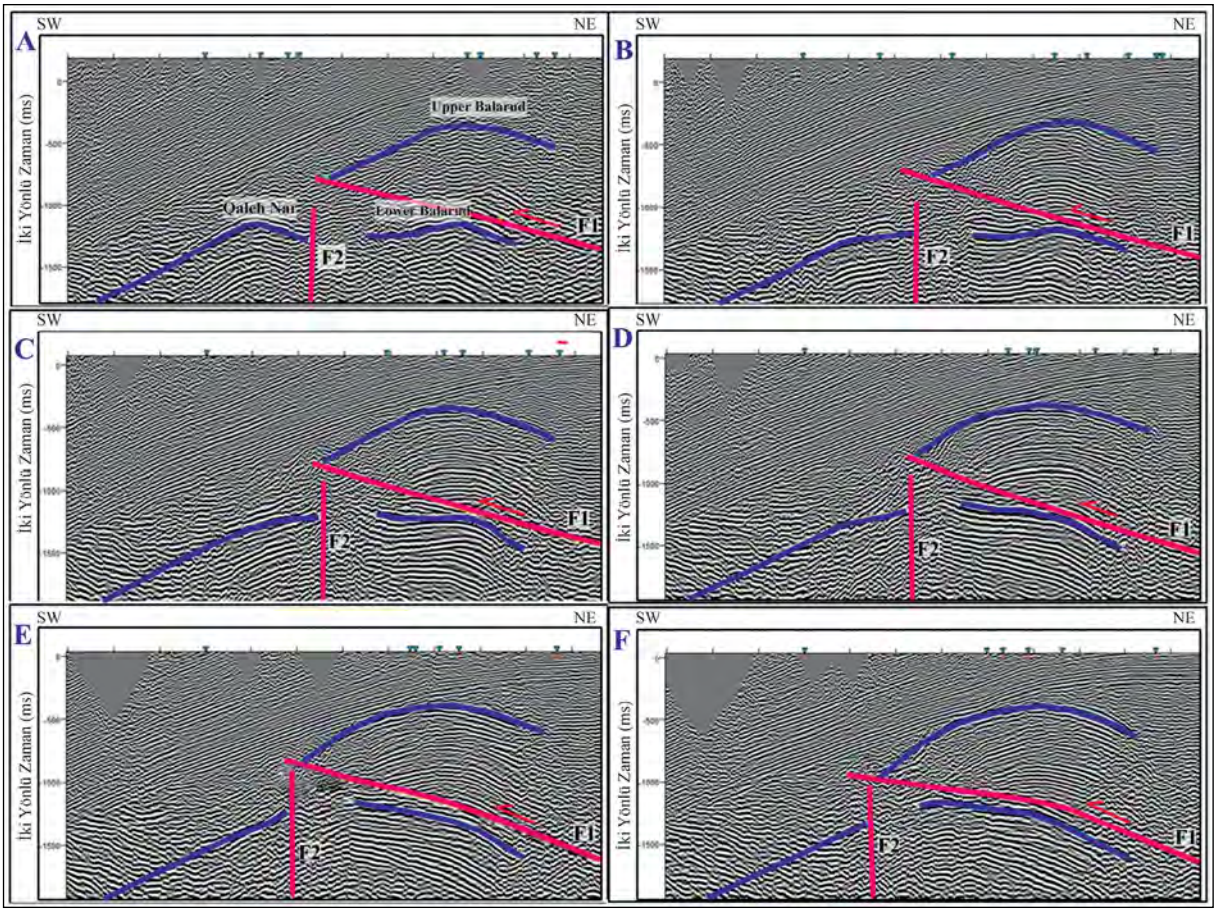

Figure 4- Structural relationship between the *UBR*, *LBR* and *QN* anticlines [based on interpreted seismic lines of the *As* horizon (blue lines)] from the west (A) to east (F). Red lines show the faults (F1 and F2). Uninterpreted images in Repository Figure 2.

The *QN* is an asymmetric anticline with WNW-ESE trending hinge line with double culminations. Its southern forelimb dips steeper than the northern limb. The geometric pattern varies along this anticline. On the east and central sides, is a rounded fold and on the west side, gradually becomes a box fold with average aspect ratio 0.1. It is classified as wide fold. The average interlimb angle in the central part of this anticline is 145°, thus it is a gentle anticline. Forelimb of the *QN* got faulted. The south limb is cut by two faults. Faults are restricted to the middle décollement downward and the Gachsaran Formation as an upper décollement horizon. A footwall syncline developed.

The *UBR* is an asymmetric anticline with NNW-SSE trending fold axis and it is formed in the hanging wall of thrust. The dip of its southern limb or forelimb is more than the northern limb. Since it has an aspect ratio 0.11, it is classified as wide anticline. The interlimb angle is 155°, thus, it is a gentle anticline.

Drilled wells in the crest of the *UBR* indicate repetition of the Gachsaran and *As* Formations downward, after passing through the Sarvak Formation that confirms the presence of the thrust fault on the seismic profile. Based on the seismic profile interpretation, in the footwall of this fault has been developed another anticline in the repeated horizons, called the *LBR*. This anticline is also asymmetric and with respect to the *QN* has lower elevation.

4.1. Structural analysis of the LBR, UBR and QN anticlines on the Bng horizon

The *Bng* UGC map (2100 to 4200 m depth range) and seismic profiles are interpreted to analyze the geometry of the *UBR* (Figure 5). As in Figure 4, in the *Bng* horizon, the forelimb of the *UBR* is cut by a thrust. The dip of this fault in the Gachsaran evaporate Formation is very gentle. The geometry of this anticline is a gentle fold in all sections. In the western part (Figure 5c), a back thrust cuts the anticline's back limb. The thrust fault (F1), at the SW of the *UBR* anticline is identified on the interpreted seismic profiles (Figure 5). It can be a reactivated basement fault (Seraj, 2021).

In the UGC map of the *Bng* horizon, a fault (F2), sinistral strike-slip fault, defines the boundary between the *LBR* and the *QN* anticlines (Figure 6). This fault is a reactivated basement fault (Seraj, 2021). The boundary between the *UBR* and *LBR* at the base of the Bng is a thrust (F1) (Figure 7). The *Bng* horizon in the *LBR* structure has two culminations defining an *en-echelon* structure. This structure to the northwest is also traceable through the Chenareh anticline. Figure 8 presents a UGC map of the *Bng* horizon of the *QN*. Two thrusts cut the southern limb of the *QN*. Also, a large syncline has developed in the southern portion of this anticline.

4.2. Structural analysis of the LBR, UBR and QN anticlines on the As horizon

The *LBR* is adjacent to the *QN* anticline (in the north of *QN* and in the footwall of the *UBR* anticline). A steep fault (F2), sinistral strike-slip fault, between them (Figure 4) is plausibly a reactivated basement fault (Seraj 2021). Like Bng, the boundary of the *LBR* and *UBR* anticlines is a thrust (F1) on the *As* horizon. The horizon in the *LBR* anticline has three en-echelon culminations and shows the effect of the deep-seated fault between the *UBR*, *LBR* and *QN* anticlines (Figure 4). The *en-echelon* structure towards the northwest part also occurs in the Chenareh anticline. The Chenareh anticline is located in the southern Lurestan province and at the hangingwall of the main Balarud fault (Figure 9). The Balarud fault, as an oblique-slip reverse fault has a strike-slip component (Razavi Pash et al., 2021*a*). This fault skirts the Chenareh anticline and the *UBR* anticline.

The *UBR* symmetric anticline trends NW-SE. The *LBR* anticline is located at more depth and is along the *QN* anticline. The *UBR* anticline in the *As* horizon, on the UGC map, is 8.5 km long and 5.5 km wide on average, while the *LBR* anticline in the interpreted *As* horizon is 4.5 km long. The southern limb of the *UBR* has a dip of 20-37°and is steeper than the northern limb (a dip of 12-27°). The *LBR* limb has a dip of 5-30°.

The *As* horizon of *QN* is interpreted from 3D seismic data. A sinistral strike-slip fault (F2) defines the boundary between the *LBR* and *QN* anticlines, which might be a reactivated fault (Seraj, 2021). Interpreted seismic profiles of *QN* indicate fold varies spatially in terms of geometry. Different parts of the *QN* anticline show various geometry (Figure 10). Additionally, the

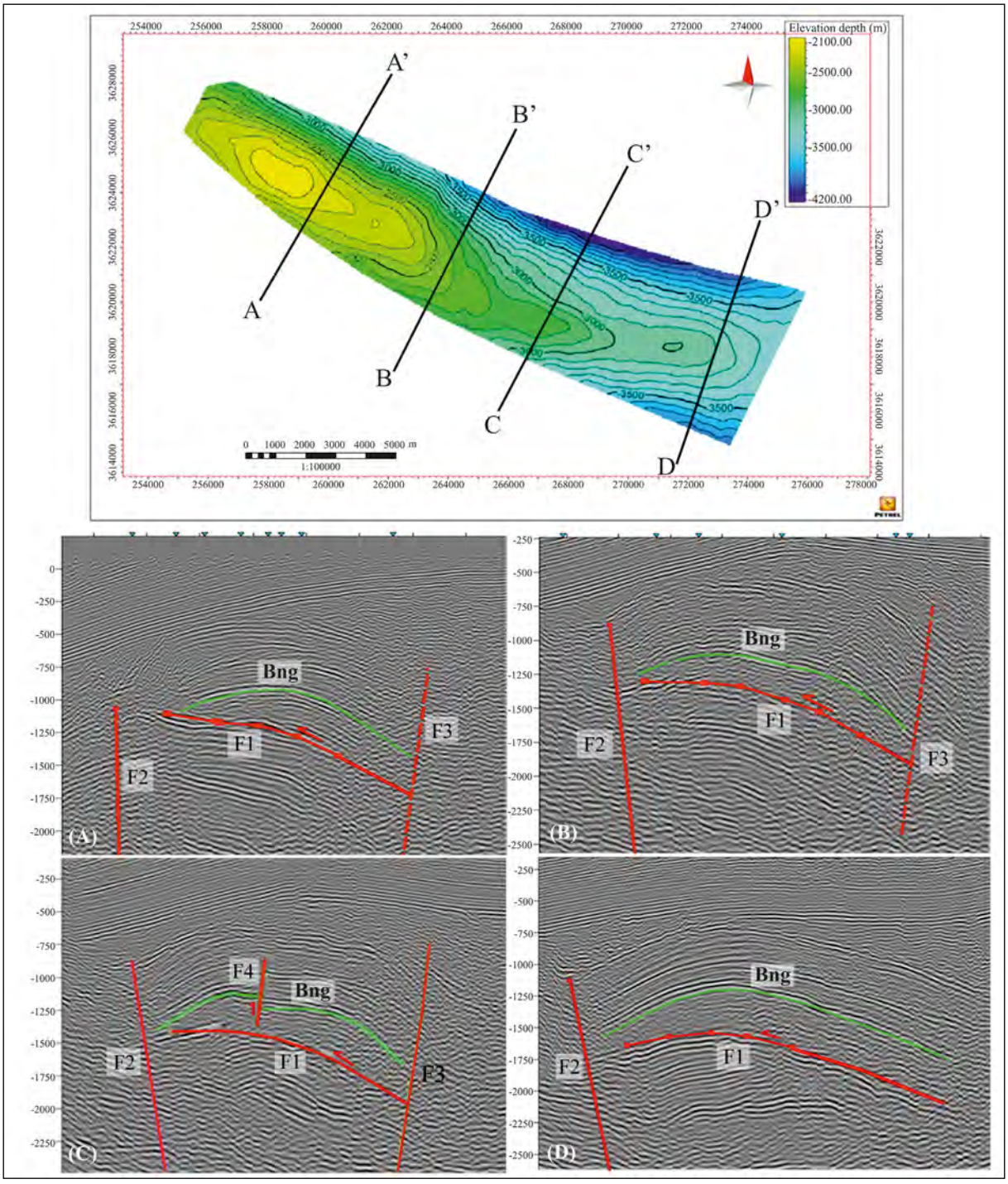

Figure 5- UGC map and interpreted seismic profiles indicating structural geometry of *Bng* horizon throughout the *UBR* anticline. The location of this Figure is shown in Figure 2. Lines AA'- DD' on the UGC map indicate the location of the interpreted seismic profiles. Uninterpreted images in Repository Figure 1. Green lines are the top of the Bangestan group (*Bng*) horizon and the red lines are faults.

southern forelimb is longer and steeper than the back limb. Based on the transverse seismic profiles of the *QN* anticline, there are two thrusts (T1 and T2) in the southwest limb of the *QN* anticline (Figure 10). The highest slip is the result of maximum deformation in the culmination of the anticline. This is true, especially in the western culmination (Sarkarinejad et al., 2017). However, the slip at the noses of this anticline is less.

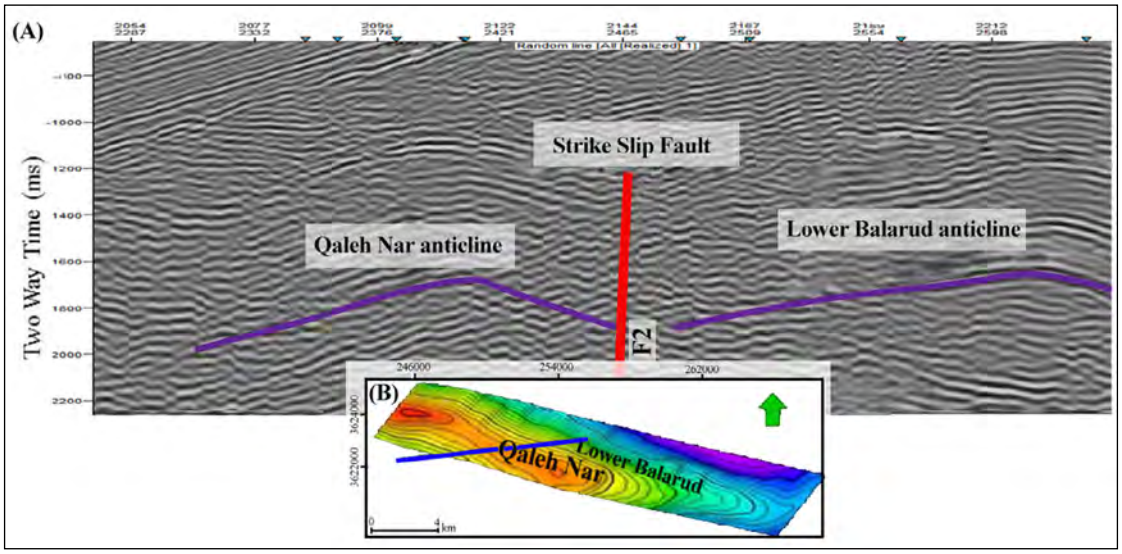

Figure 6- Bangestan horizon (purple lines) in the *LBR* and *QN* anticlines on the (A) seismic profile and (B) UGC map. The red line indicates F2. The blue line shows the location of the seismic profile on the UGC map.

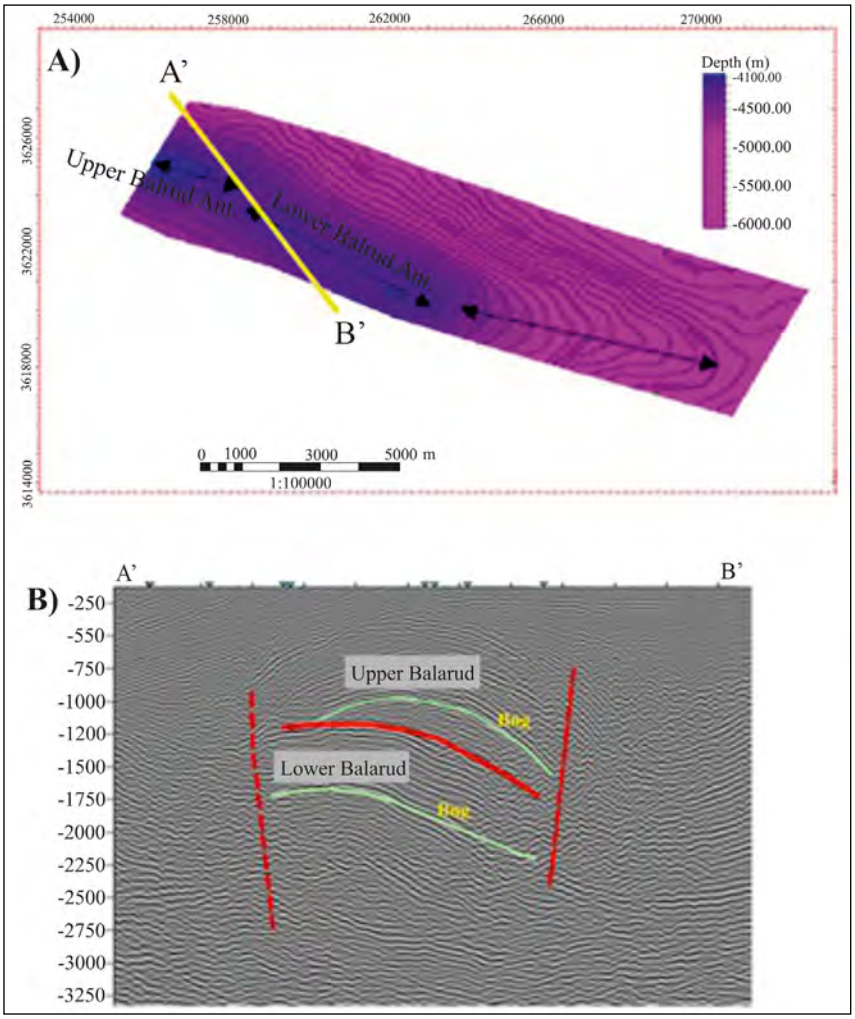

Figure 7- En-echelon structure on the Bng horizon between UBR and LBR anticlines based on a) UGC map and b) seismic lines. Yellow line in Figure 7A shows the location of the seismic profile on the UGC map.

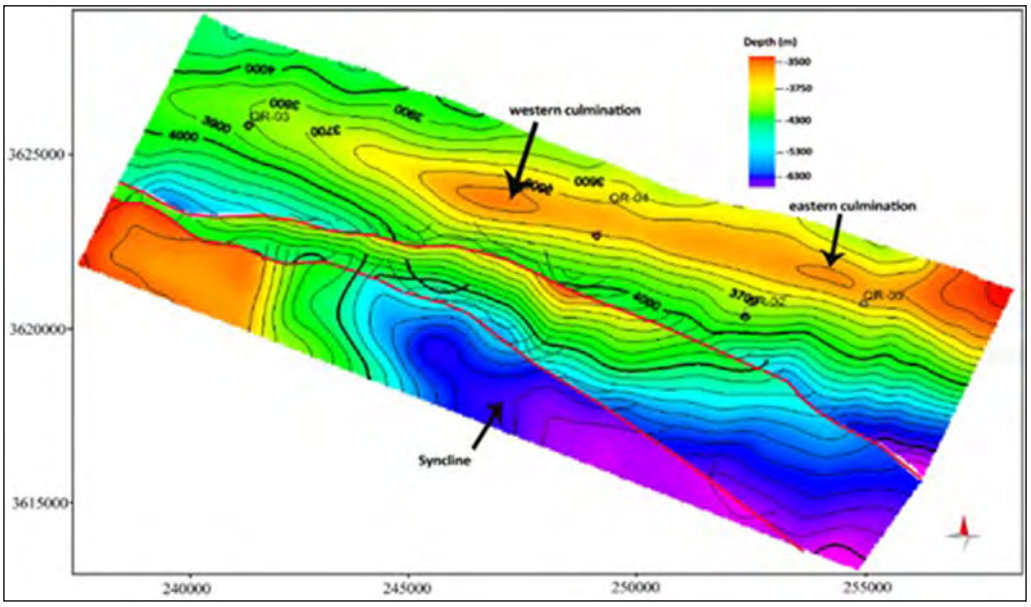

Figure 8- UGC map of *Bng* horizon of the *QN* anticline.

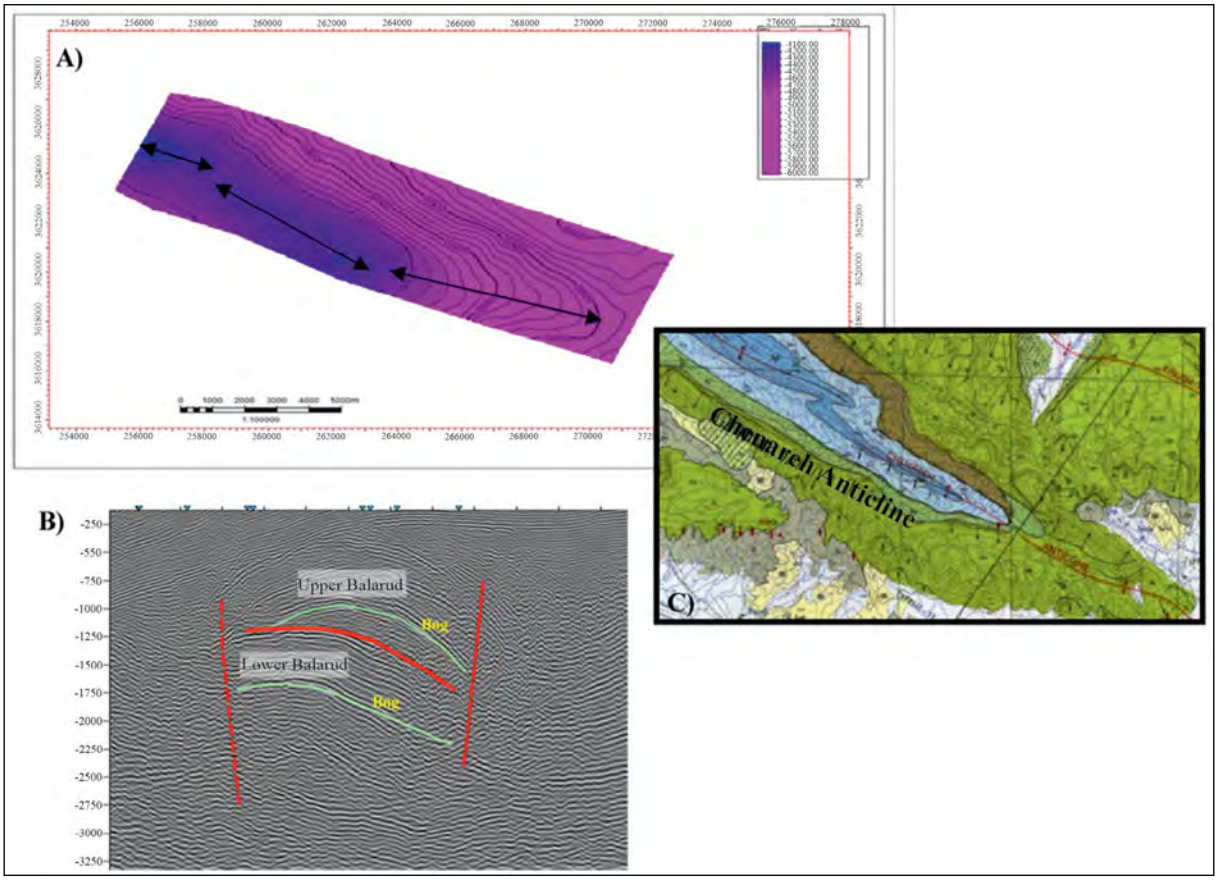

Figure 9- a) En-echelon structure in the As horizon of the LBR on the UGC map, b) the Chenareh anticline at the surface on the geology map (legend in Figure 1b) and c) structural geological map of the study area. Location shown in Figure 2.

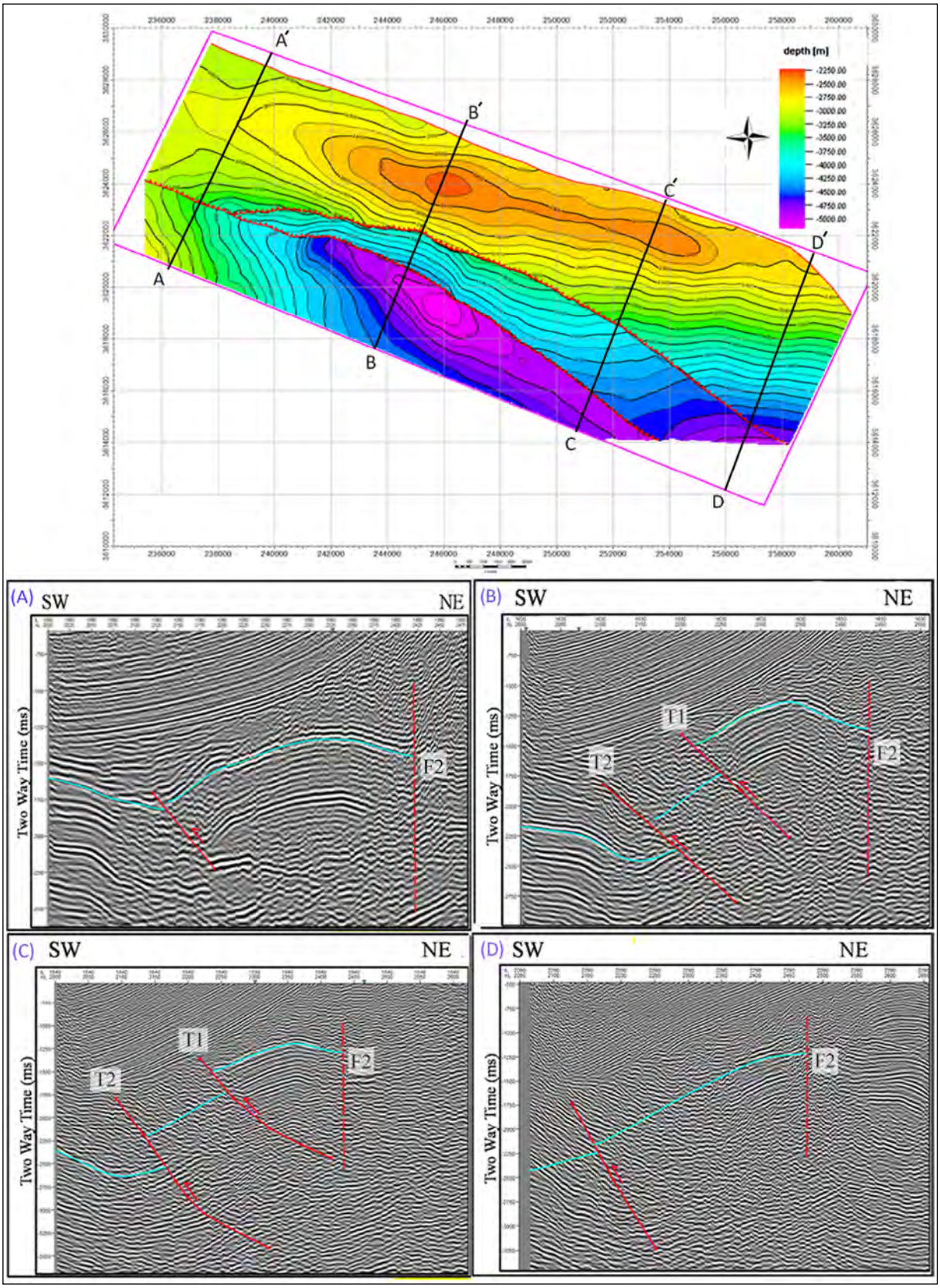

Figure 10- Structural changes of *As* horizon (blue line) along *QN* anticline based on the interpreted seismic sections. Lines AA'-DD' show the location of the interpreted seismic sections (up to 3500 m depth). Red lines indicate the faults. Location in Figure 2. Uninterpreted seismic profiles in Repository Figure 3.

The main structure of *QN* is formed between two faults (T1 and F2). One is a thrust (T1), and the other is a basement reactivated fault (F2) (Figure 10) (Seraj, 2021). The thrust trends NW-SE and the basement fault is steep /sub-vertical) (Seraj, 2021). The basement fault is between the *QN* and *LBR* anticlines (Figure 4). It is one of the main branches out of the Balarud fault zone (Seraj, 2021).

The limbs of the *QN* anticline have a dip of ~ 5°, and a maximum of 25°. The southern limb of the *QN* anticline has a dip of 15-25° and it is 5-10° for the northern limb. The *QN* anticline has two culminations. A very gentle syncline separates the two culminations. NW-SE trending *QN* field on the *As* horizon is 25 km long with ~ 5 km width on average. The *QN* anticline on the *As* horizon is an asymmetric doubly plunging fold. Two thrust faults (T1 and T2) cut in the southern limb of this anticline (Figure 10).

Three transverse sections (AA', BB' and CC') and one structural longitudinal section (DD') (Figure 11, 12) from the surface to the basement are prepared. Based on transverse and longitudinal structural sections and after comparing the 3D views of the *UBR*, *LBR* and *QN* anticlines, deformation intensity along the *UBR* anticline is found to decrease toward the east (Figure 13). As the displacement of the Chenareh and the *UBR* anticlines increase towards the northwest, so is the generally increasing trend of uplift of the *UBR* towards the east. This explains why the flow of the Gachsaran Formation (to the southwest) in

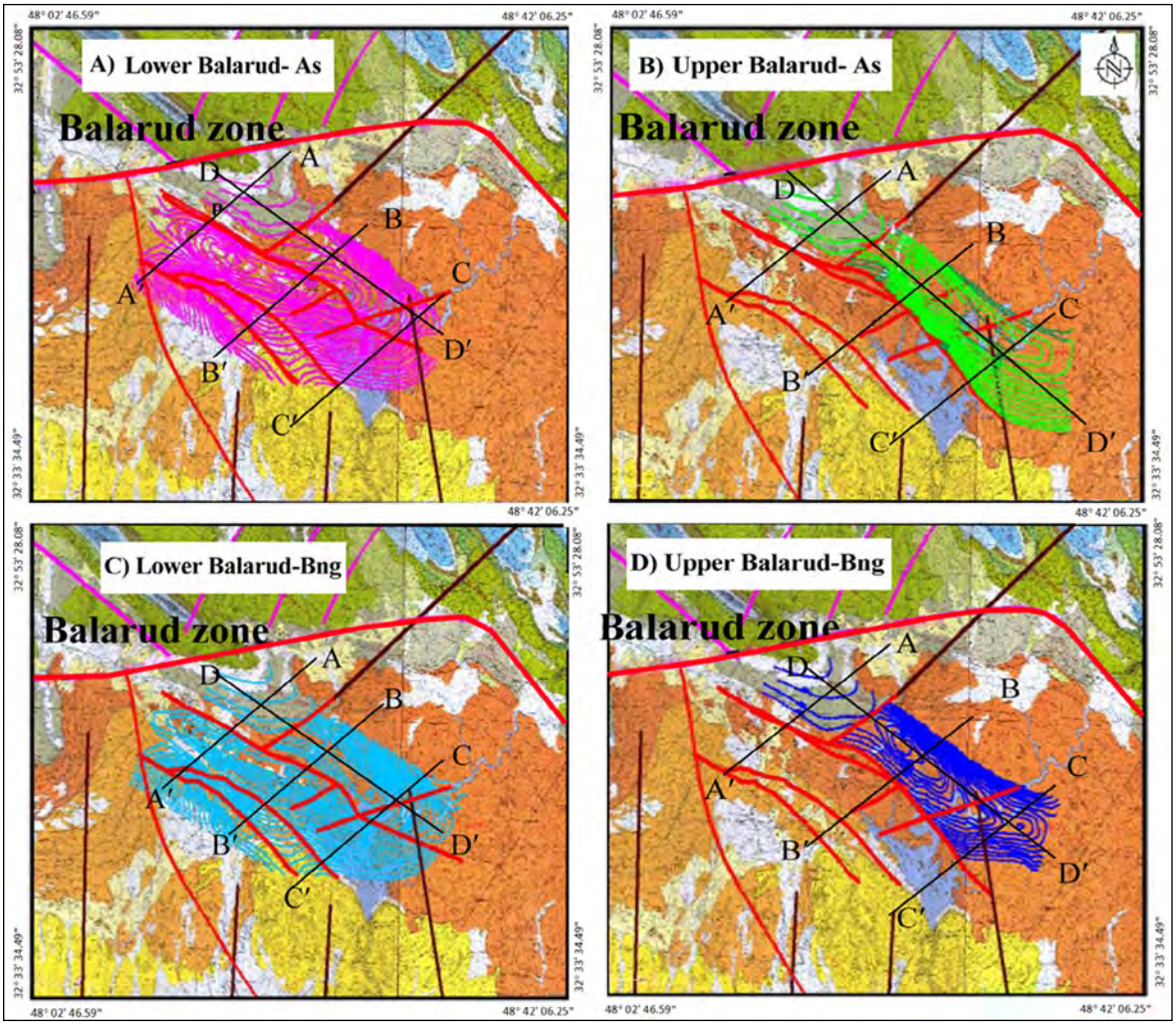

Figure 11- Geological map (with a scale of 1:100000) of the study area (Legend in Figure 1B) and location of the structural sections (AA'-DD'). Contours are the UGC map (*As* and *Bng*) for *UBR*, *LBR* and *QN* anticlines and indicate the location of these anticlines. Red lines show faults.

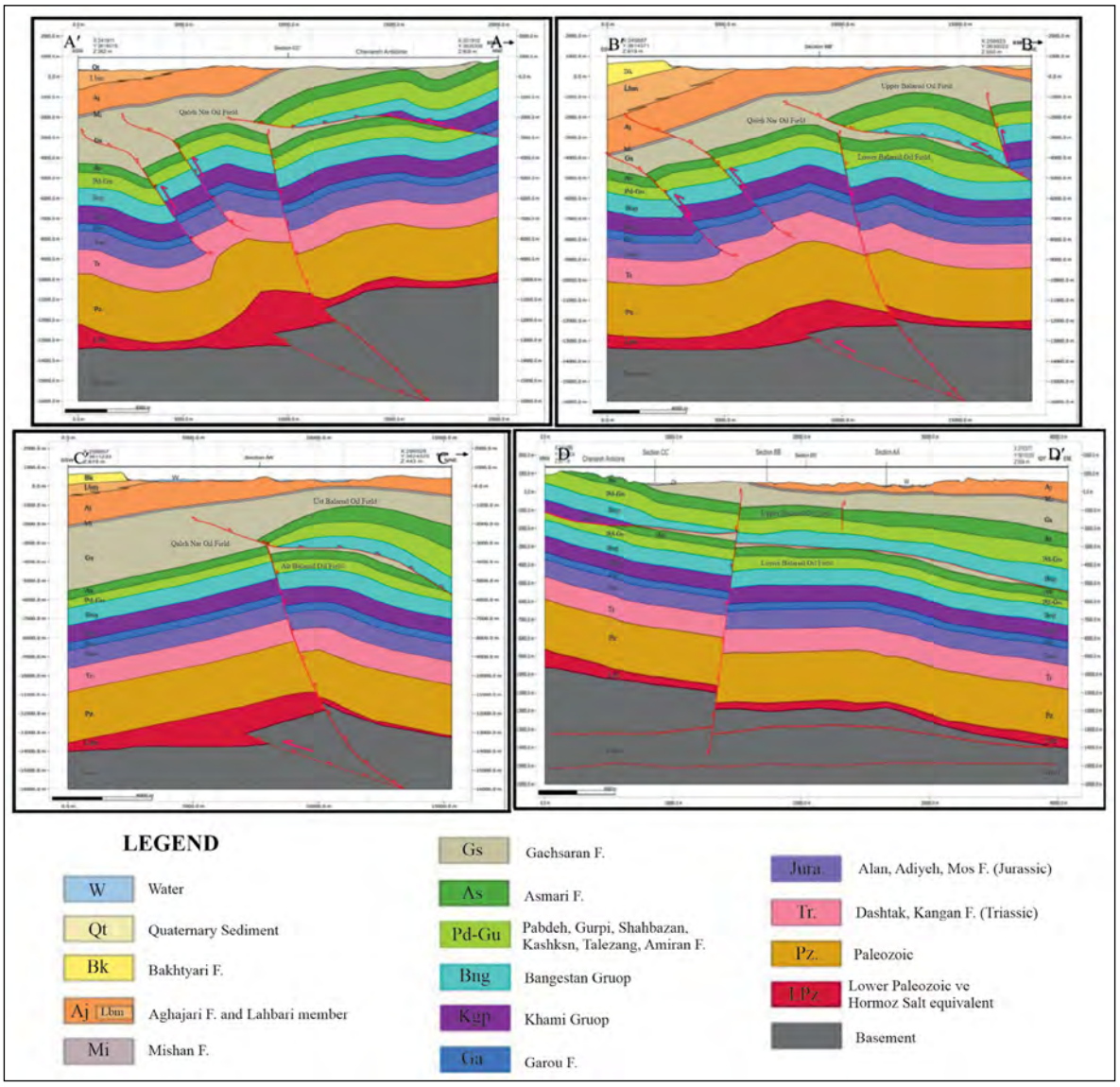

Figure 12- a) Cross-section AA', b) Cross-section BB', c) Cross-section CC'; and d) Cross-section DD'. Locations of the cross-sections are seen at Figure 11.

the west and northwest exceed than that at the center and at the east in this area. Furthermore, the increase of sedimentary overburden (Aghajari Formation to the present-day deposits) and the rate of deformation (and uplift) in the *UBR* moved and accumulated Gachsaran Formation. In other words, higher overburden pressure and greater rate of deformation and uplift are associated with the flow of the Gachsaran Formation towards both NE and SW limbs of anticlines. Therefore, the interaction of the three factors (increase and decrease the rate of overburden pressure, rate of deformation and uplift) in different parts has caused the movement and accumulation of the Gachsaran Formation. More shortening rate indicates more structural relief in the studied anticlines (Sarkarinejad et al., 2017; Razavi Pash et al., 2021*b*). Based on Sarkarinejad et al. (2017), the minimum shortening in the eastern and western parts of the *QN* is ~3% and the maximum amount in the western culmination is ~22%.

4.3. Structural Modelling

After interpreting subsurface information from various sources (surface maps, subsurface and longitudinal-transverse and regional structural sections), digital information on the structures of these horizons were prepared using Petrel software. Six sections were prepared from different parts of the anticlines as in Figure 14a.

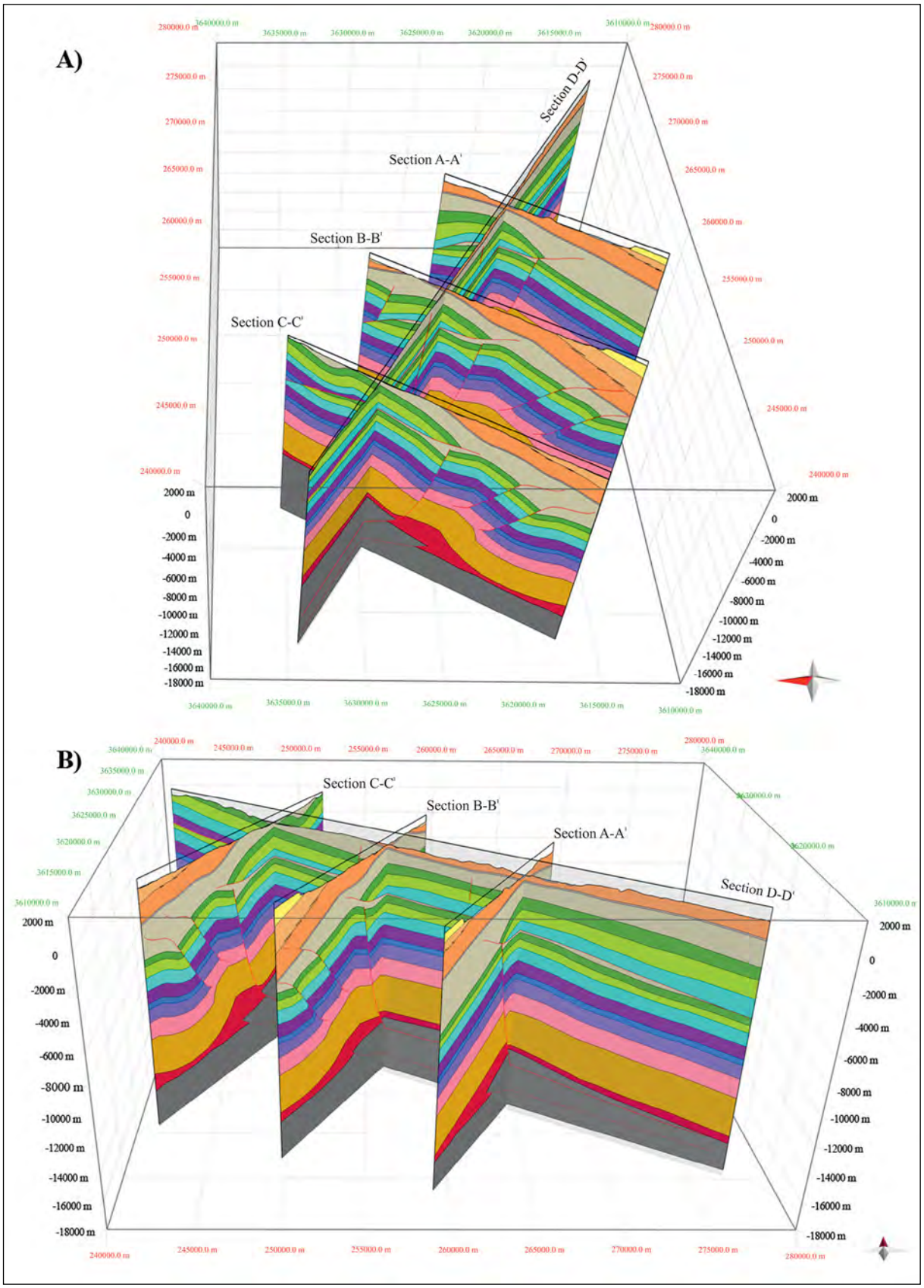

Figure 13- 3D view of transverse and longitudinal structural sections. a) View from northwest to southeast and b) view from southwest to northeast.

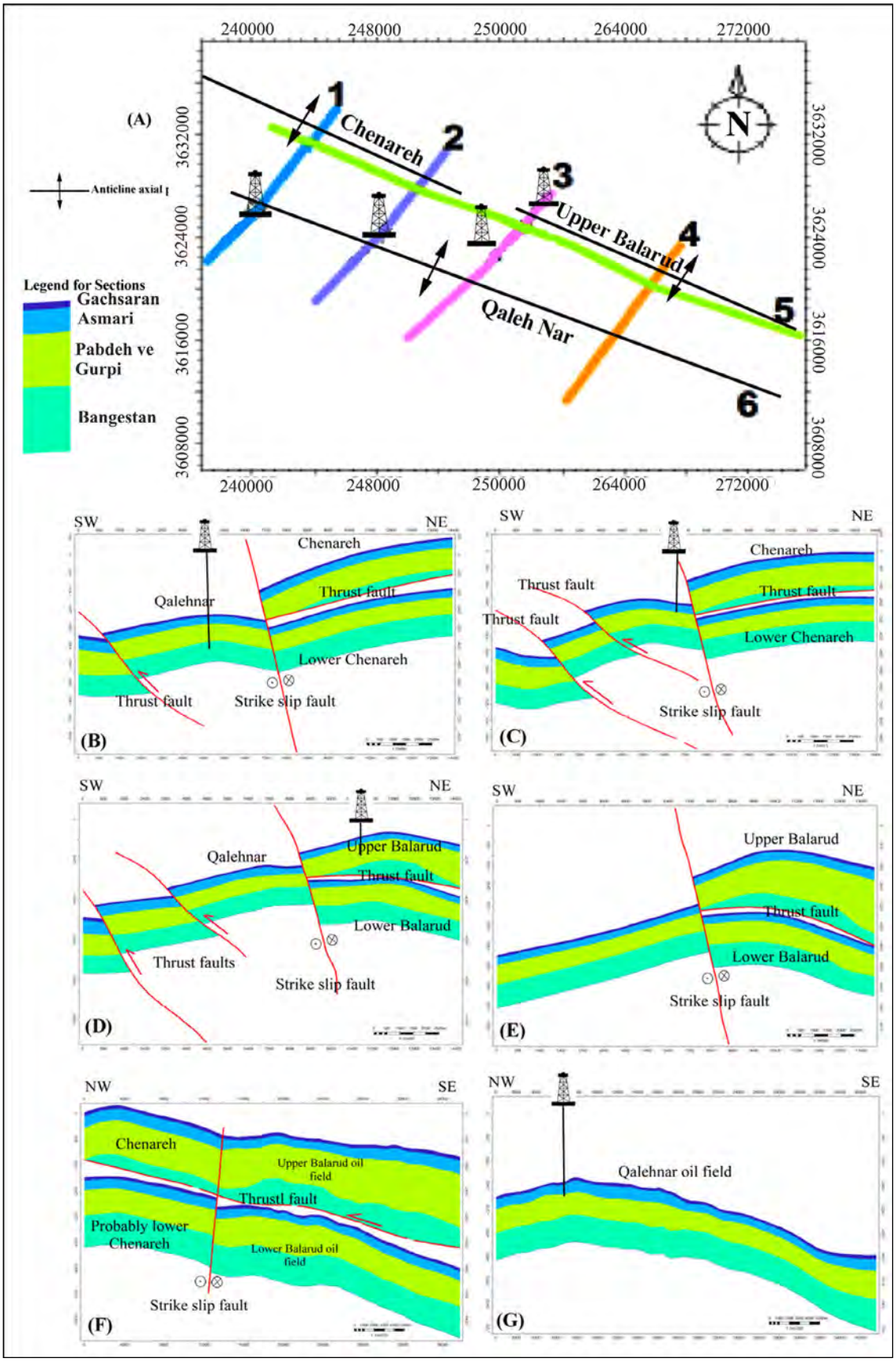

Figure 14- Position of the sections relative to the axis of the folds a, and schematic view of sections 1-6 (b-g).

Section-1 (Figure 14b) passes through the northwestern end of the study area, southeast of the Chenareh anticline and northwest of *QN*. The structural pattern of the section shows that the Chenareh anticline is probably overturned similar to the *LBR* (known as the Lower Chenareh). This structural feature is separated from the *QN* towards the southwest by a steep fault [sinistral strike-slip fault (F2)]. Structural section- 2 (Figure14c) parallels section-1. Structures resemble these sections. The only difference is that in the southern limb of *QN*, two thrust faults are parallel and dip towards the northeast.

Structural section-3, parallel to sections 1 and 2, from northeast to southwest, shows the thrusting of the *UBR* on the *LBR* by a low-dipping thrust. As in sections 1 and 2 and after this structural section, a steep fault (sinistral strike-slip fault (F2) separates the *UBR* and *LBR* folds from the *QN* anticline. The *QN* is characterized by two parallel reverse faults at its southwest limb (Figure14d).

In section-4, (Figure 14e), a transverse section in section-3 (Figure14d), the *UBR* fold is thrust over the *LBR*, and a basement fault separates these anticlines from the *QN*. Sections 5 and 6 are longitudinal with NW-SE trends (Figure 14f, g).

Section-5 (Figure 14f) is along the axial plane of the Chenareh anticline in the southern Lurestan province and the *UBR* anticline in northern Dezful Embayment. As in Figure 14f, a thrust separates the *UBR* and the *LBR* anticlines as well as the upper and lower Chenareh anticlines. In other words, the *UBR* and the upper Chenareh anticlines have been overturned by this thrust fault over the *LBR* and lower Chenareh anticlines, respectively. Due to the complicated structure created and the repetition of layers with the formation of oil fields atop each other, exploratory drilling targets should be decided carefully.

5. Results

Investigating the structural relation between subsurface anticlines/oil fields and the faults that affected them will be a great help in developing oil fields. The main structures in the study area are the *QN*, *UBR* and *LBR* anticlines in the northern Dezful Embayment. These anticlines are the subsurface oil fields. The *Bng* and *As* horizons are the main reservoirs. This study investigated the geometric relationship between the mentioned anticlines based on Bng and As horizons. Interpretation of the seismic profiles indicates the geometry of the studied subsurface anticlines differs vertically and horizontally. The interpreted structures much resemble in As and Bng horizons. The *UBR* anticline overturned on the *LBR* anticline by a thrust. The *LBR* anticline, resembling a rabbit ear structure, is situated at the northern edge of the *QN*. The upper and the lower Chenareh anticlines in the southern Lurestan province and *UBR* and *LBR* anticlines in the northern Dezful Embayment are much similar. The main Balarud fault (a basement fault) separates the mentioned anticlines. Also, the *LBR* anticline is separated from the *QN* by a sinistral strike-slip fault (F2). Interaction of three factors, change in overburden pressure, the rate of deformation and uplift in different parts of the subsurface anticlines moved and accumulated Gachsaran Formation. More overburden pressure and more intense deformation and uplift are associated with flow of the Gachsaran Formation towards both limbs of the anticlines towards the NE and SW.

The structural relation of adjacent anticlines/oil fields can be complex. The existence of thrust faults caused the repetition of reservoirs (As and Bng), as in the *UBR* and *LBR* anticlines. Drilling locations and depths must be determined by considering the sub-surface structures.

Acknowledgements

We thank Prof. D. Chandrasekharam (Associate Editor) and two anonymous reviewers for providing insightful comments that improved the work.

References

Abdollahie, fard ia, Sepehr, M., Sherkati, S. 2011. Neogene salt in SW Iran and its interaction with Zagros folding. Geological Magazine 148 (5-6), 854-867.

Agard, P., Omrani, J., Jolivet, L., Mouthereau, F. 2005. Convergence history across Zagros (Iran): constraints from collisional and earlier deformation. International Journal of Earth Sciences 94 (3), 401-419.

Allen, M. 2010. The nature of the Dezful Embayment and the Balarud Line in the Iranian Zagros. In EGU General Assembly Conference Abstracts, 10438.

Allen, M. B., Talebian, M. 2011. Structural variation along the Zagros and the nature of the Dezful Embayment. Geological Magazine 148 (5-6), 911-924.

Asl, M. E., Faghih, A., Mukherjee, S., Soleimany, B. 2019. Style and timing of salt movement in the Persian Gulf Basin, offshore Iran: Insights from halokinetic sequences adjacent to the Tonb-e-Bozorg salt diapir. Journal of Structural Geology 122, 116-132.

Bahroudi, A., Koyi, H. 2003. Effect of spatial distribution of Hormuz salt on deformation style in the Zagros fold and thrust belt: an analogue modelling approach. Journal of the Geological Society 160 (5), 719-733.

Berberian, M. 1995. Master "blind" thrust faults hidden under the Zagros folds: active basement tectonics and surface morphotectonics. Tectonophysics 241 (3-4), 193-224.

Berberian, M., King, G. C. P. 1981. Towards a paleogeography and tectonic evolution of Iran. Canadian journal of earth sciences 18 (2), 210-265.

Bordenave, M. L. 2014. Petroleum systems and distribution of the oil and gas fields in the Iranian part of the Tethyan region. In: Marlow L, Kendall CCG, Yose LA (Eds) Petroleum Systems of the Tethyan Region. AAPG Memoir 106.

Bordenave, M. L., Burwood, R. 1990. Source rock distribution and maturation in the Zagros orogenic belt: provenance of the Asmari and Bangestan reservoir oil accumulations. Organic Geochemistry 16(1-3), 369-387.

Bordenave, M. L., Hegre, J. A. 2005. The influence of tectonics on the entrapment of oil in the Dezful Embayment, Zagros Fold belt, Iran. Journal of Petroleum Geology 28 (4), 339-368.

Cooper, M. 2007. Structural style and hydrocarbon prospectivity in fold and thrust belts: A global review. In: Ries AC, Butler RWH, Graham RH (Eds) Deformation of the Continental Crust: The Legacy of Mike Coward. Geological Society, London, Spec. Pub. 272, 447-472.

Emami, H., Vergés, J., Nalpas, T., Gillespie, P., Sharp, I., Karpuz, R., Blanc, E. P., Goodarzi, M. G. H. 2010. Structure of the Mountain Front Flexure along the Anaran anticline in the Pusht-e Kuh Arc (NW Zagros, Iran): insights fromsandbox models. Geological Society, London, Special Publications 330 (1), 155-178.

Hajialibeigi, H., Alavi, S. A., Eftekharnezhad, J., Mokhtari, M., Adabi, M. H. 2015. The Geometric Analysis of the Fault-Related Folding, A Case Study: Kaseh Mast Anticline, the South of the Lurestan Zone.

Hammerstein, J. A., Dicuia, R., Cottam, M. A., Zamora, G., Butler, R. W. H. 2020. Fold and thrust belts: structural style, evolution and exploration–an introduction. In: Hammerstein JA, R. Dicuia, Cottam MA, Zamora G, Butler RWH (Eds.) Fold and Thrust Belts: Structural Style, Evolution and Exploration, vol. 490, Geological Society, London, Special Publications 490, 1-8.

Hessami, K. 2002. Tectonic history and present-day deformation in the Zagros fold-thrust belt. Doctoral dissertation, Acta Universitatis Upsaliensis.

Homke, S., Vergés, J., Garcés, M., Emami, H., Karpuz, R. 2004. Magnetostratigraphy of Miocene–Pliocene Zagros foreland deposits in the front of the Push-e Kush arc (Lurestan Province, Iran). Earth and Planetary Science Letters 225 (3-4) 397-410.

Mcquarrie, N. 2004. Crustal scale geometry of the Zagros fold–thrust belt, Iran. Journal of Structural Geology 26 (3) 519-535.

Pirouz, M., Simpson, G., Bahroudi, A., Azhdari, A. 2011. Neogene sediments and modern depositional environments of the Zagros foreland basin system. Geol. Mag 148 (5–6), 838–853.

Razavi Pash, R., Sarkarinejad, K., Ghoochaninejad, H.Z., Motamedi, H., Yazdani, M. 2020. Accommodation of the different structural styles in the foreland fold-and-thrust belts: northern Dezful Embayment in the Zagros belt, Iran. International Journal of Earth Sciences 109 (3) 109, 959–970.

Razavi Pash, R., Sarkarinejad, K., Zarehparvar Ghoochaninejad, H., Motamedi, H. 2021*a*. Application of 3D Structural Modeling to Analyze the Structural Geometry and Kinematic Evolution: A Case Study from Lab-e-Safid and Qale Nar QN Subsurface Anticlines in the Northern Dezful Embayment, Iran. Geotectonics 55(2), 261-272.

Razavi Pash, R.R, Sarkarinejad, K., Sherkati, S., Motamedi, H. 2021*b*. Analogue model of the Bala Rud Fault, Zagros: an oblique basement ramp in a fold-and-thrust belt. International Journal of Earth Sciences 110(2), 741-755.

Safari, H.O., Bagas, L. 2021. A transpressional model for deformation patterns in the northern part of Dezful Embayment's oil fields in Zagros (Iran), using geo-information technologies. Marine and Petroleum Geology 123, 104736.

Safari, H.O., Pirasteh, S., Pradhan, B. 2009. Uplifting estimation in Zagros Transverse faults Iran:

An application of Geoinformation Technology. Remote Sensing 1, 1240–1256.

Sarkarinejad, K., Razavi Pash, R., Motamedi, H., Yazdani, M. 2017. Deformation and kinematic evolution of the subsurface structures: Zagros foreland fold-and-thrust belt, northern Dezful Embayment, Iran. International Journal of Earth Sciences 107(4), 1287-1304.

Sepher, M., Cosgrove J., Moieni, M. 2006. The impact of cover rock rheology on the style of folding in the Zagros fold-thrust belt. Tectonophysics 427(1-4), 265-281.

Seraj, M. 2021. Structural relationship study of Balarud and Qaleh Nar oi fields. National Iranian South Oil Company. Report, 70.

Sherkati, S., Letouzey, J. 2004. Variation of structural style and basin evolution in the central Zagros (Izeh zone and Dezful Embayment), Iran. Marine and Petroleum Geology 21(5), 535-554.

Sherkati, S., Letouzey, J., Frizon de lamotte, D. 2006. Central Zagros fold-thrust belt (Iran): New insights from seismic data, field observation, and sandbox modeling. Tectonics 25(4), TC4007.

Sherkati, S., Molinaro m, D. E., Lamotte, D. F., Letouzey, J. 2005. Detachment folding in the Central and Eastern Zagros fold-belt (Iran): salt mobility, multiple detachments and late basement control. Journal of Structural Geology 27(9), 1680-1696.

Stöcklin, J. 1968. Salt deposits of the Middle East. Geological Society of America, Special Issue 8, 157-181.

Bulletin of the Mineral Research and Exploration

http://bulletin.mta.gov.tr

Investigation of the change in the characteristic properties of epoxy and silane coated natural stone surfaces

Z. Ebru SAYIN[a*], Hakan ÇİFTÇİ[a] and Mustafa GÜRSOY[a]

[a] *Afyon Kocatepe University, Engineering Faculty, Mining Engineering Department, Afyonkarahisar, Türkiye*

Research Article

Keywords:
Travertine, Silane, Epoxy, Surface Protection, Porous Structure.

ABSTRACT

Travertine is a natural stone with macro and micropores; these pores are connected by capillary means. Their visual appearance and porous structure add a different style and diversify their usage areas. However, the large pore structure of travertine brings some limitations in determining the usage areas. In the study, protective solutions called silane and epoxy, which provide protection against water, were used to prevent and/or minimize decomposition in areas of use, depending on the porosity of the travertine, and their effects on travertine were compared. Treatment of both chemicals separately on the travertine surface was carried out by spraying, applying with a brush, and dipping into chemicals. With the findings obtained from the physical examinations after curing, the work continued using the applying and dipping method. The dipping method was evaluated with the chemical's 10, 20, and 40-minutes waiting times. The study found that the best application condition was chemical immersion for 10 minutes. However, in SO_2 wear experiments, it was understood that surfaces treated with epoxy were more durable due to the high viscosity of the chemical. As a result, it has been determined that silane application provides more effective surface protection results than epoxy.

Received Date: 25.05.2023
Accepted Date: 25.03.2024

1. Introduction

Travertine is carbonate sedimentary rocks containing calcium bicarbonate $Ca(HCO_3)$ that precipitate after the volatilization of carbon dioxide (CO_2) in contact with the air of spring waters containing calcium carbonate ($CaCO_3$) and especially hot water sources. Its precipitation generally contains calcite and aragonite crystals (Chafetz and Folk, 1984; Polat, 2011). Travertine has a fossiliferous and porous morphology due to its structure resulting from its formation, and it creates more problems, especially during processing, compared to the other natural stones (marble, granite etc.). It is thought that the controlled use of tools and equipment used in the process of making sized products in factories can help increase production quality (Kamacı, 2013). While the fossiliferous and porous (porous-porous) structure of travertine is considered a disadvantage in factories (Kamacı, 2013), it should not be forgotten that this structure will be an advantage for thermal insulation. Altay et al. (2001) examined some of the natural stones found in Türkiye in terms of thermal conductivity coefficient. They determined that the thermal conductivity coefficients of travertines, which they chose to represent rocks with high porosity, were lower than other rocks.

Citation Info: Sayın, A. E., Çiftçi, H., Gürsoy, M. 2024. Investigation of the change in the characteristic properties of epoxy and silane coated natural stone surfaces. Bulletin of the Mineral Research and Exploration 174, 85-98. https://doi.org/10.19111/bulletinofmre.1458331

**Corresponding author: Z. Ebru SAYIN, zerkan@aku.edu.tr*

In recent years, the increase in buildings in the construction and tourism sector and the demands for using natural stone in the environments have created great activity in the use of natural stone. With the developments in surface processing technologies of natural stones and the construction industry's tendency towards raw materials as buildings surface covering materials, natural stones have begun to be used more than other covering materials. However, the widespread use of building stones, especially porous stones such as travertine, causes limitations according to the region where they will be applied (Erdem, 2016; Hasbay and Hattap, 2017; Tayşi, 2021).

Building materials deteriorate with external factors such as time, environment, and climatic conditions, so they lose their physical and mechanical properties (MEB, 2013). The primary deficiencies in the building blocks used in the construction sector are the changes that may occur in the material characteristics under the influence of moisture and water (Dal and Yılmaz, 2015). It is influential in determining the building material's porosity value. The water absorption value by weight, where this value is intense, increases (Öztank and Bacakoğlu, 2001; Öcal and Dal, 2012) due to wear and tear on non-protective surfaces. However, the capillary channels in the natural stone continue the water movement with the effect of capillary pressure, which affects the water permeability of the travertines and occurs in the veins. Possible temperature changes in the environment and humidity rate also change, transforming from liquid to solid state at water temperature, leading to dew and freezing house (Dal and Yılmaz, 2015). In case of freezing, it is essential to examine the capillary water permeability properties and fill it with a protective material that prevents the water from entering the body to protect the discharge against freezing-thawing since the water exposed to the volume causes internal stresses in the natural stone structure. It is known that the use of travertine, as mentioned earlier as a flooring, facade, or decoration addition, reveals its phenomenon even though it is slow during atmospheric environments. It accelerates this situation in its chemical and physical effects. For example, the impact of sulfate (wearing in SO_2) not only reduces the strength of the natural stone by creating cracks on the surface but also causes the internal cohesion loss of the hydrated structure and a decrease in the adherence between the building fasteners (Erdoğdu, 1998). With the increase in sulfate concentration, natural stone caused high levels of corrosion. As a result, swelling and disintegration will occur on the surface. The effect will manifest with the spread of fragments from its components and breakage at the edges and corners. (Uğurlu, 2003; Öcal and Dal, 2012; Dal and Yılmaz, 2015). It will cause significant damage to the internal structure by keeping it inside the earth during exposure (Uğurlu, 2003).

Application examples of repairing porous and cracked natural stones and the additional gains these applications bring to businesses are examined in this study. Since crack repair and pore filling is the last stage of production, production losses experienced at this stage increase the cost. All the expenses spent so far on the stone that has been cut and prepared for polishing will be completely wasted if the necessary repairs are not carried out. On the other hand, when we look at the cost of lost materials and labor, it is seen that repair and filling operations are not as costly as expected. On the contrary, it has been stated that they are important tools for generating profits by providing additional added value (Çetin, 2001; Acar, 2003). Making natural and artificial materials resistant to environmental effects has become one of the most important research and application issues, especially in the construction sector and subsequently in various production lines. Among these research products, epoxy and silane were used within the scope of the study.

Epoxy prevents the adverse effects that may occur in the surface coating works of the materials to be used on wet and dry floors, in exposure to atmospheric conditions, eliminates the negativities that arise during production under various mechanical, physical, and chemical effects, and protects the produced material surfaces (internal and external) against all kinds of results by covering them with aesthetic materials. It is a technological building material group developed for Materials coated with epoxy-based products that are used for years, without undergoing any structural changes, to create surfaces that are resistant to chemicals, oil, friction, and abrasion and are used with

advantages such as being easy to clean, hygienic and aesthetic. It has a longer protective feature than most alternative floor coverings, and its most important benefit is that surface renovation can be done at meager costs. Due to these features, it is used in a wide area with increasing demand daily.

Some of the disadvantages of epoxy resins include the need to heat the material before processing and the curing rate being slower than that of unsaturated polyesters. Moreover, it requires special expertise in the epoxy resin system and base epoxies and hardeners may need to be sourced from different manufacturers (Gibson, 2017).

Conversely, silane is a siloxane-added, low-viscosity, colorless, transparent, ready-to-use protective material. As it is an impregnation material with high penetrating properties, it is used in building materials used in exterior cladding, on water-absorbing surfaces such as natural and artificial stone surfaces, on historical artifacts to protect them from the effects of atmospheric gases, on concrete and cement-based surfaces caused by water, salt, chlorine, and alkalis and used for protection. Adding a solid water-repellent (hydrophobic) feature to the surfaces of the construction elements ensures that they remain dry, reduces heat losses and heating costs, and has the advantage of protecting against atmospheric gases by making the surfaces impermeable and preventing the spread of cracks (Tekno Construction Chemicals, 2023).

Travertines present patterned structures depending on their formation environments. This textural feature can be preferred in the applications of travertine in the construction sector. For this reason, protecting and revealing the structure during production may be desired. In this context, in the study in which the effect of textural properties on capillary water absorption and uniaxial compressive strength parameters of the stone is discussed, it is stated that textural properties affect both capillary water absorption and uniaxial compressive strength. The results have revealed that the technical features depending on the cutting shape should be considered when using travertine (Çobanoğlu, 2020). Natural stones, which have a porous structure and therefore hydrophilic character, should be transformed into products that do not produce bacteria utilizing additives to obtain a water-repellent feature by making their surfaces hydrophobic, to obtain smooth surfaces and to increase their usage areas and to use them healthily (Çetin, 2001). In this context, the construction chemicals named epoxy and silane were permeated separately on the surface of the travertine selected from porous natural stones in specific proportions to be protective. Their suitability for the usage areas was evaluated by examining the changes in their characteristic features.

Natural stones used in various sectors, particularly travertines, absorb water through capillarity (voids, cracks, cracks, etc.). Over time, natural stones also cause deterioration depending on the amount of water and the penetration time. These deteriorations not only reduce the life of the stone but also cause visual disturbances. The amount of capillary water absorption varies depending on the type of natural stone. The study investigated how much silane and epoxy-coated travertine samples were affected by this situation. Samples treated with silane and epoxy; Water absorption at atmospheric pressure, capillary water absorption, determination of resistance to salt crystallization, and wear tests in SO_2 were performed to investigate the protective solution that is more effective in surface protection against deformation.

2. Material and Method

The travertine sample used in the study belongs to Konya Karaman location. Six hundred specimens of 10x10x2 cm plate and 10x10x10 cm cube samples were obtained from a company operating in İscehisar in Afyon. The specimens brought to the laboratory was subjected to drying at 70°C, then prepared, and XRD (X-Ray Diffraction Analysis) and XRF (X-Ray Fluorescence) analyses were made. Among the protective solutions used on the travertine surface, silane was obtained from Tekno Construction Chemicals (Teknosil product), and epoxy was obtained from Tenax. The guidance and methods to be followed in processing subjects vary according to the characteristics of the subjects mentioned.

Chemical analysis of the sample (in Rigaku/ZSX Primus II brand XRF device) and determination

of resistance to salt crystallization (performed according to TS EN 12370 standard, the prepared solution contains 14% sodium sulfate decahydrate by weight) experiments were carried out in Afyon Kocatepe University, Mining Engineering Department Accredited Natural Stone Analysis Laboratory. Whole rock mineralogical analysis was performed in the Technology Application Research Center (TUAM) laboratory (2θ=0˚-80˚). X-ray analyzes were made using Shimadzu 6000 model and Bruker D8 Advance X-ray diffractometers, and mineral identifications were made using JCPDS (Joint Committee on Powder Diffraction Standarts) (1993) cards. The mercury porosimetry analysis of natural travertine, epoxy, and silane-treated samples was performed in a MICROMERITICS brand mercury porosimetry device in the same laboratory.

The contact angle values of the travertine samples was measured using the One Attension Theta Optical Goniometer with the drop diffusion method. Before the measurements, the surfaces of the raw travertine samples were sanded, washed with distilled water, and dried at 105°C for 24 hours. The curing of the silane-coated samples was carried out in two different ways drying at room temperature for 12 hours and at 105°C for 4 hours. In the epoxy coating process, the travertine samples were preheated to 50°C, then coated with epoxy and kept at room temperature for 24 hours to cure. Preheating the samples at 50°C was performed to accelerate epoxy curing.

In the study, epoxy, and silane were mixed separately in a mechanical mixer for not less than 3 minutes and impregnated with a brush on the surface of the washed and dried samples. The impregnation process was applied in two different ways. The first group of work was completed by applying just one coat to the surfaces with the help of a brush. In the second group study, the samples immersed in silane and epoxy were removed and dried after being kept in protective solutions for 10 minutes. In addition to the studies with silane, it was held for 20 and 40 minutes. Since the impregnation made by spraying does not give the appropriate image, the analyses related to this method have been abandoned. The samples were used in the investigation after drying for 48 hours at 24°C to ensure the polymerization process. The grouping of the samples prepared for the studies and the treatment times with epoxy and silane are given in Table 1.

Table 1- Types of samples prepared for study.

Type of application to the Sample Surface		Duration, min
Epoxy	Applying to surface	-
	Dipping to epoxy	10
Silane	Applying to surface	-
	Dipping to silane	10 20 30

3. Discussion

The result of the X-ray diffractometry analysis of the untreated travertine sample is given in Figure 1. It was determined that the content of the sample was calcite in XRD analysis.

As a result of the chemical analysis of the sample, it was determined that the heat loss was 43.8%, and the CaO content was 55% (Table 2).

In the contact angle measurements of raw and epoxy and silane-coated travertine samples, the contact angles of the samples were measured with distilled water from several different points on the surface, and the average values were recorded. The results are given in Table 3.

As can be seen from Table 3, the contact angle of the raw travertine increased significantly after the silane coating process and gained hydrophobic properties. Coating with epoxy did not cause a severe change in contact angle. Epoxy contains two carbons and oxygen, forming a three-membered ring structure. Epoxy resins have pendant hydroxyl (-OH) groups along their chains that can create strong polar attractions and, therefore, have high surface tension. Due to this characteristic structure, when water is dropped on the epoxy surface, water molecules establish relationships with the functional groups on the surface and spread across the surface, thus giving a low contact angle. The curing method after coating with silane is also effective on the contact angle.

It is known that travertine has very high porosity values among natural stones. This situation brings many limitations in its usage areas. Porosity is most

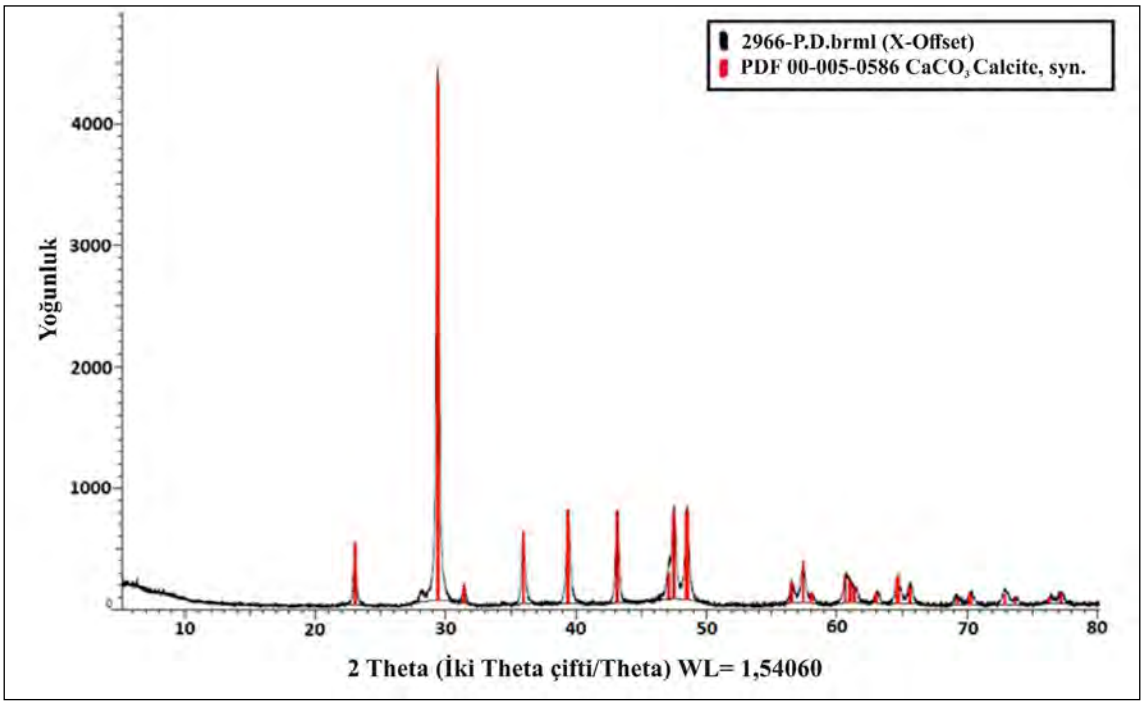

Figure 1- XRD analysis result.

Table 2- Chemical composition of travertine sample.

Compound	Unit	Results
SiO_2	%	0.339
Fe_2O_3	%	0.085
AlO_3	%	0.095
CaO	%	55.00
MgO	%	0.395
SrO	%	0.089
SO_3	%	0.130
Na_2O	%	0.016
MnO	%	0.065
K_2O	%	0.019
P_2O_5	%	0.012
Loss of Ignition	%	43.80

evident in the water absorption value. For this reason, the change in water absorption values by using silane and epoxy chemicals on the sample was determined according to the TS EN 13755 standard. The raw sample was studied on travertines treated with epoxy and silane for the water absorption test. The results obtained in the water absorption test studies carried out in various parameters are given in Figures 2 and 3.

According to the water absorption test results, the water absorption value of the raw sample was calculated as 0.773. The water absorption value of the epoxy was obtained as 0.582 with a standard deviation of 0.36, and the water absorption value of the silane was obtained as 0.296 with a standard deviation of 0.20 with the same method as a result of the application of epoxy to the surface. When the values were examined, the water absorption value of the raw sample was higher than those treated with epoxy and silane. Silane, on the other hand, has lower water absorption than epoxy. This shows that silane

Table 3- Contact angles of raw and surface coated travertine sample.

Sample	Raw Travertine	Epoxy coated travertine	Silane coated travertine (curing: 12 hours, 25°C)	Silane coated travertine (curing: 4 hours, 105°C)
Average contact angle	64.9°	61.62°	109.3°	130.9°

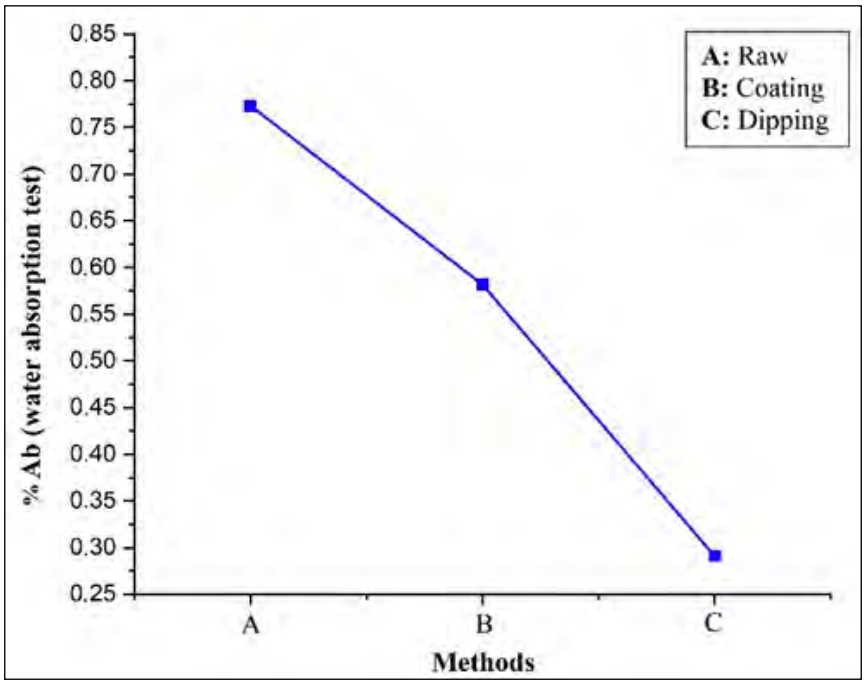

Figure 2- Water Absorption Test Results with Epoxy Applications.

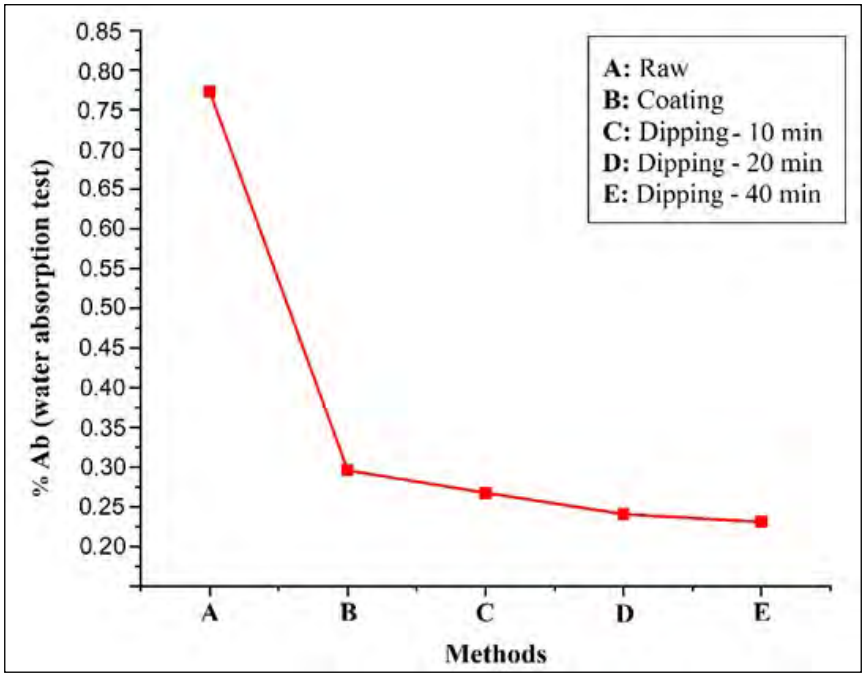

Figure 3- Water absorption test results with silane applications.

and epoxy effectively reduce the water absorption value. Under normal conditions, epoxy surface coating provides complete sealing and zero water absorption. However, as a result of this study, observing some water absorption in epoxy-coated samples is entirely related to the coating process. In other words, since the air bubbles in the epoxy resin were not removed in a vacuum environment before the coating process, they formed partial porosity during curing, which caused the sample to absorb a small amount of water.

The effectiveness of the dipping method was investigated after the application of impregnation with the application. As a result of immersing the samples in epoxy and silane for 10 minutes, water absorption values of 0.291 with a standard deviation of 0.05 in epoxy and 0.278 with a standard deviation of 0.20 in silane were obtained. In this study group, it was determined that the water absorption value of silane gave more effective results than epoxy. In the continuation of the study, the silane immersion time was changed to 20 and 40 minutes, and the results were examined. It was observed that the water absorption values of 0.240 with a standard deviation of 0.18 and 0.231 with a standard deviation of 0.22 respectively, were slightly better against immersion for 10 minutes, but these time changes were not very effective for the study.

The capillary water absorption potentials of the travertine sample were examined, and the relationships between the determined capillary water absorption coefficients and other index properties of the materials were evaluated according to the TS EN 1925 standard. The changes in the capillary water absorption value due to the treatment of travertine used in the research with silane and epoxy with different methods were examined. The results are given in Figures 4 and 5.

When the capillary water absorption test results were examined, the capillary water absorption value of the raw sample was calculated as 0.841. While the capillary water absorption value of the epoxy was 0.648 with a standard deviation of 0.31 due to the application of rubbing on the surface, the capillary water absorption value of the silane obtained by the same method was 0.383 with a standard deviation of 0.22. When the values were examined, the capillary water absorption value of the raw sample was higher than those treated with epoxy and silane. On the other hand, the capillary water absorption value of silane was lower than epoxy. This shows that epoxy and silane effectively reduce the capillary water absorption value.

The effectiveness of the dipping method was investigated after the application of impregnation with the application. As a result of immersing the sample in epoxy and silane for 10 minutes, the capillary water absorption value was obtained as 0.414 with a standard deviation of 0.10 in epoxy and 0.295 with a standard

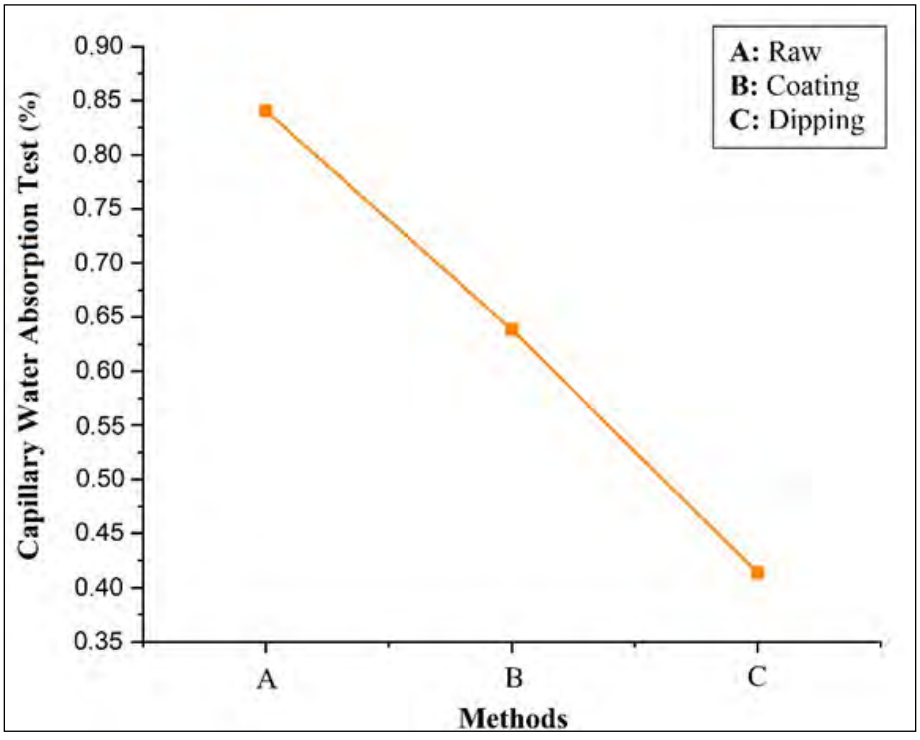

Figure 4- Capillary water absorption test results with epoxy applications.

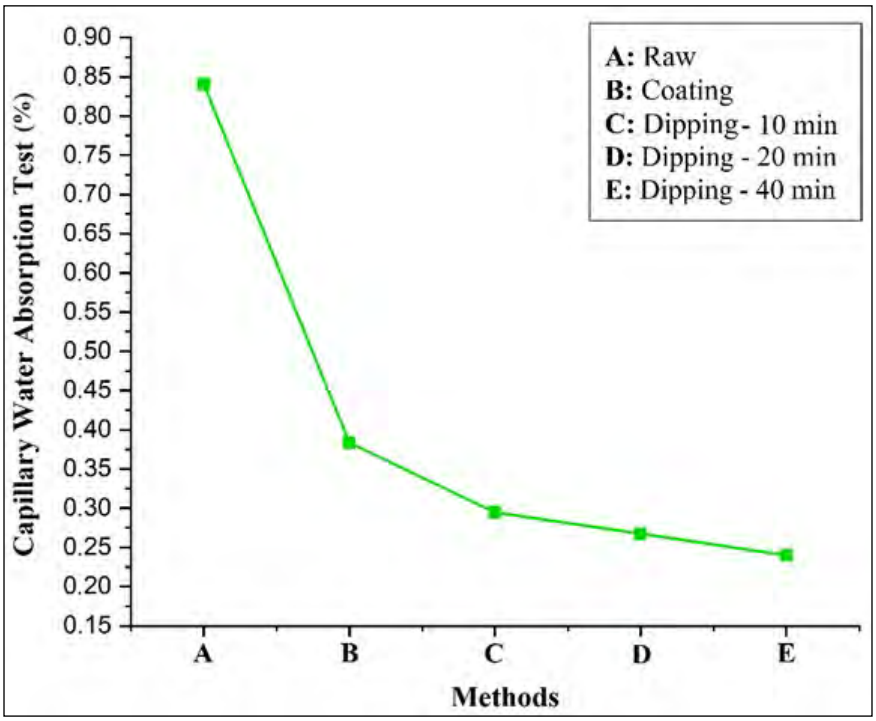

Figure 5- Capillary water absorption test results with silane applications.

deviation of 0.04 in silane. The study determined that the capillary water absorption values of silane were more effective than epoxy. Then, the silane immersion time was changed to 20 and 40 minutes, and the results were examined. However, although the results were slightly better than 10 minutes, it was determined that it was not very effective, with 0.268 with a standard deviation of 0.09 and 0.239 with a standard deviation of 0.17 for the study.

After examining the water absorption and capillary water absorption test results, the ongoing studies on applying epoxy and silane to the surface and immersing the sample in silane for 20 and 40 minutes were canceled. Since the water absorption and capillary water absorption test results made by engaging the samples in epoxy and silane for 10 minutes and then drying them at room conditions gave the best values, another set of these samples was prepared.

To define the resistance of the travertine samples to be used in the study against salt crystallization and to observe the effect of epoxy and silane on salt crystallization, Salt Crystallization Resistance Tests were carried out according to the TS EN 12370 standard. Figures 6, 7, and 8 show the samples immersed in epoxy and silane for 10 minutes before, during, and after the study and the study results.

By the determination of Resistance to Salt Crystallization of Epoxy and Silane, and it was determined that the Average Mass Change (%) of the sample kept in epoxy for 10 minutes was 0.090, the standard deviation was 0.119, the Average Mass Change (%) of the sample kept in silane for 10 minutes was 0.018 and the standard deviation value was 0.021. The results show that the silane-treated samples had higher resistance to salt crystallization. In addition, in the observations made on the samples after the experiment, no decomposition and crack formation were observed due to the exposure of the travertine samples to salt crystallization.

Samples taken from the sample group, immersed in epoxy and silane for 10 minutes and then dried at room conditions, were used to determine the resistance to SO_2 attrition in a humid environment. The study was carried out according to the TS EN 13919 standard in 2022. A visual of the experiment process is given in Figure 9. In Figure 10, the results obtained from the experiments are given.

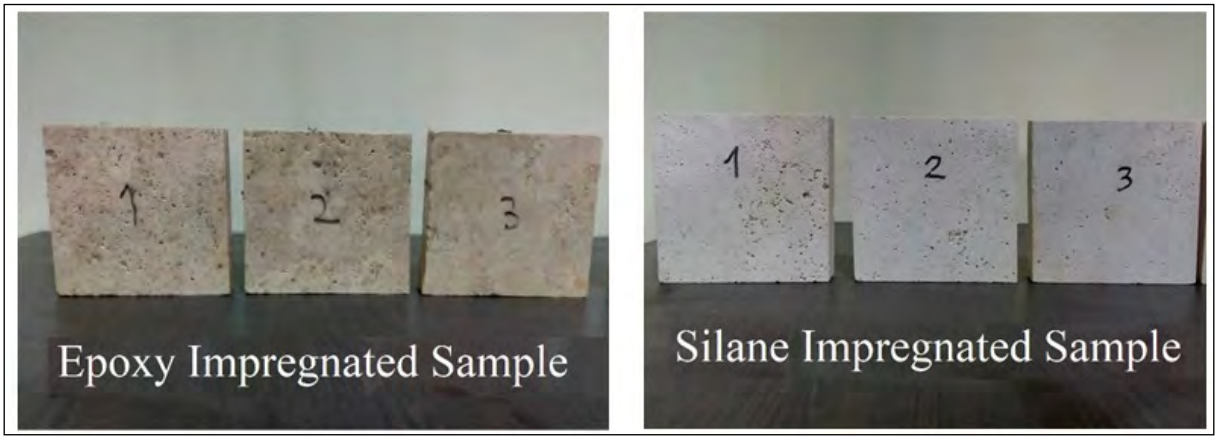

Figure 6- Pre-run image of a few of the samples dipped in epoxy and silane.

Figure 7- Visuals of samples dipped in epoxy and silane during and after the experiments.

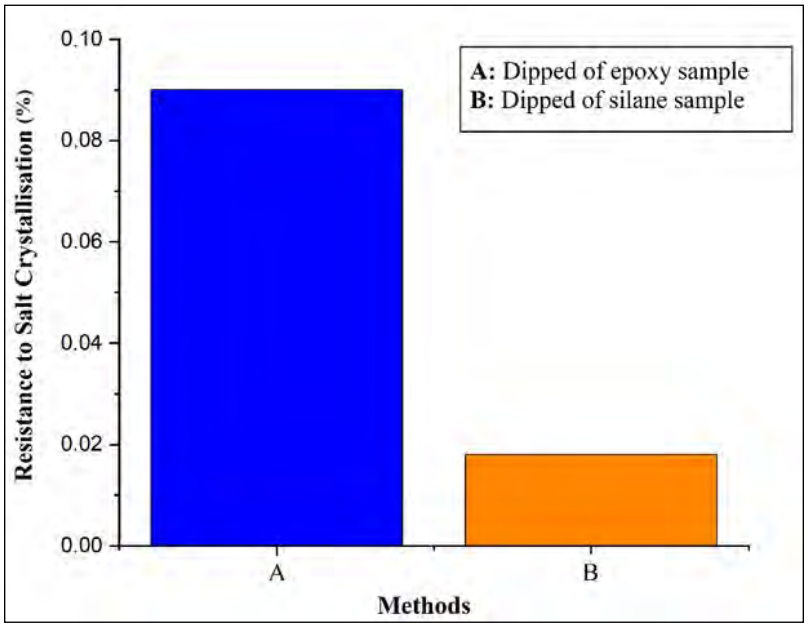

Figure 8- Results of determination of resistance to salt crystallization of epoxy and silane immersed samples.

Figure 9- Image of the test for the determination of resistance to ageing by SO_2 in a humid environment.

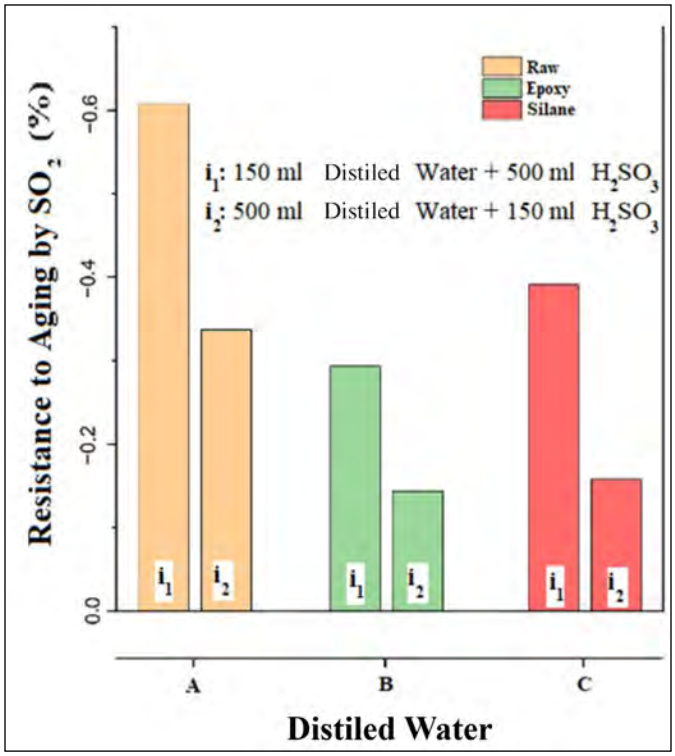

Figure 10- Results of the determination of resistance to ageing by SO_2 in a humid environment of raw, epoxy and silane immersed samples.

On the raw sample in the resistance to ageing by SO_2 in a humid environment test, the Average Mass Change (%) in the mixture formed with 150 ml distilled water + 500 ml H_2SO_3 was -0.608, and the standard deviation value was 0.101. In the mixture, it was determined that the Average Mass Change (%) was -0.337, and the standard deviation value was 0.014.

In the study carried out with epoxy and silane for the determination of the resistance to SO_2 attrition in a humid environment, the sample, which was kept in epoxy for 10 minutes, was found in a mixture of 150 ml distilled water + 500 ml H_2SO_3 and the Average Mass Change (%) was -0.293. The standard deviation value was 0.049 in 500 ml of distilled water. In the mixture formed with water + 150 ml H_2SO_3, the Average Mass Change (%) was found to be -0.144, and the standard deviation value was 0.182. The Average Mass Change (%) of the sample, which was kept in silane for 10 minutes, was -0.391, and the standard deviation value was 0.138 in the mixture formed with 150 ml distilled water + 500 ml H_2SO_3, and the Average Mass Change (%) in the mixture formed with 500 ml distilled water + 150 ml H_2SO_3 was found to be -0.391. It was determined that the standard deviation value was -0.158 and 0.159.

It has been seen by the Determination of Resistance to SO_2 Attrition in Humid Environment that the epoxy-treated samples gave more durable results than the silane-treated samples. This shows that epoxy-treated surfaces have higher SO_2 resistance. In Figure 11, the image of the raw sample is given before and after the test. As can be seen from the figure, the color of the processed samples is quite dark, while the color of the raw sample is light. This showed that the sample caused a color change by absorbing SO_2 due to its porous structure. However, no effect was observed to disrupt the integrity of any part.

Mercury porosimetry is used for mass density determination by measuring pore size, pore size distribution, and surface area in powder or bulk samples. As a result of the mercury porosimetry analysis, the porosity value of the raw travertine sample was 11.99%, the porosity value of the epoxy-treated sample was 6.11%, and the porosity value of the silane-treated travertine was determined as 10.92%. According to the results obtained, it was determined that silane formed a thin layer in the pores of travertine, while epoxy formed a thicker layer, causing the pores to be closed. It has been determined that silane changes the surface area of the

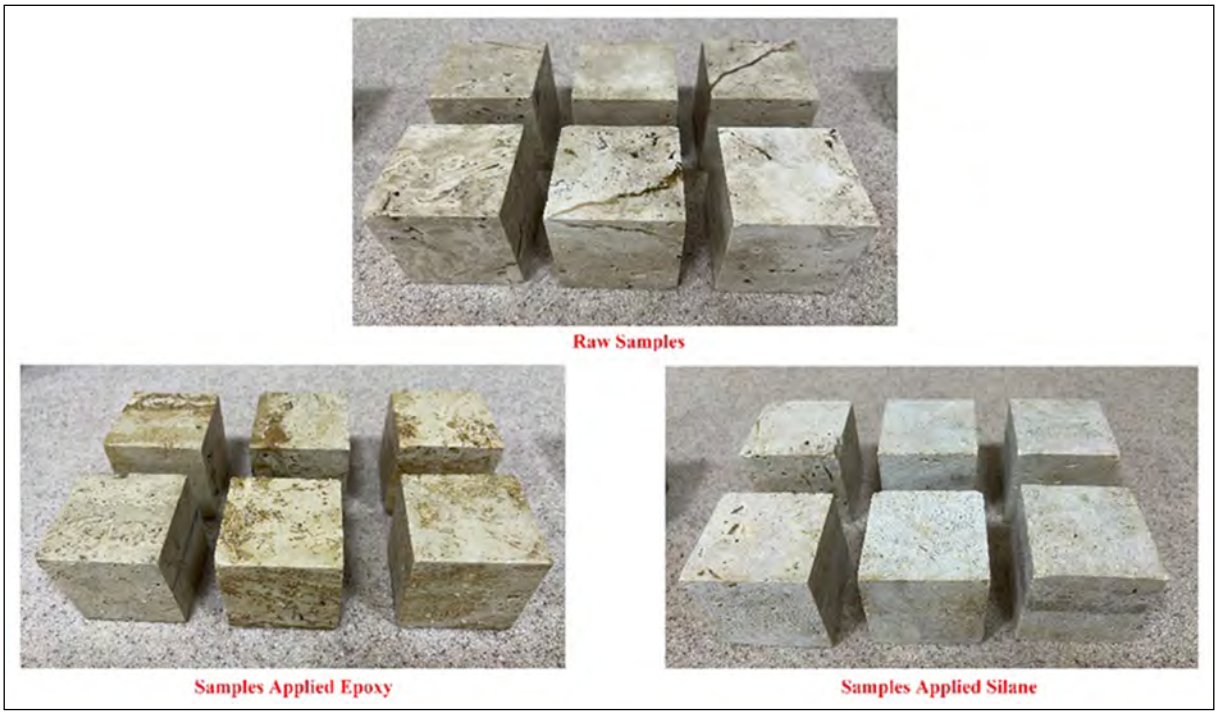

Figure 11- Samples before and after.

raw travertine at a low value. Analysis results of the samples are given in Tables 4, 5, and 6.

Table 4- Mercury porosimetry analysis results of raw travertine sample.

Parameters	Results
Infiltration into the total volume	0.0520 ml/g
The total pore area	0.767 m^2/g
Average pore diameter (volume)	40.3418 µm
Average pore diameter (area)	0.0248 µm
Average pore diameter (4V/A)	0.2711 µm
Bulk density 0.52 psia	2.3072 g/ml
Apparent (skeletal) density	2.6216 g/ml
Porosity	%11.99
The root volume used	%39

Table 5- Mercury porosimetry analysis results of the sample kept in silane for 10 min.

Parameters	Results
Infiltration into the total volume	0.0474 ml/g
The total pore area	0.478 m^2/g
Average pore diameter (volume)	47.2065 µm
Average pore diameter (area)	0.0382 µm
Average pore diameter (4V/A)	0.3966 µm
Bulk density 0.52 psia	2.3065 g/ml
Apparent (skeletal) density	2.5893 g/ml
Porosity	%10.92
The root volume used	%34

Table 6- Mercury porosimetry analysis results of the sample kept in epoxy for 10 min.

Parameters	Results
Infiltration into the total volume	0.0278 ml/g
The total pore area	8.725 m^2/g
Average pore diameter (volume)	0.0130 µm
Average pore diameter (area)	0.0108 µm
Average pore diameter (4V/A)	0.0127 µm
Bulk density 0.52 psia	2.2000 g/ml
Apparent (skeletal) density	2.3431 g/ml
Porosity	%6.11
The root volume used	%22

4. Results

The more porous the natural stone is, the greater the exposure to external factors and the deformation effect. The increase in porosity shortens the natural stone's life due to its tendency to absorb water. It causes the integrity of the stone to deteriorate where it is used (Erdem, 2016; Hasbay and Hattap, 2017; Tayşi, 2021). The water-soluble salts in the natural stone dissolve with the effect of moisture and heat and are transported in capillary cracks, they are recrystallized by the evaporation of water in the new place they are transported, and while these events take place, various deformations such as exfoliation, cavity formation, flowering, crusting occur (Öcal and Dal, 2012; Akbay et al., 2017). For these reasons, the effects of travertines, which are in the natural stone class, were compared by using protective solutions called silane and epoxy, which protect against water, in the study, which was carried out in order to prevent and/or minimize segregation in the places of use depending on the porosity and to eliminate their limitations.

The water absorption value and porous structure of natural stones determine the condition of the stone against external factors that cause deterioration and decomposition. Therefore, the porosity structure of natural stone is a factor that needs to be paid more attention in to geographical regions where the temperature is very low, especially in humid environments. Because water expands in volume during frost, it can cause internal pressures to increase in the cavities and decomposition that begins with the expansion of the void volume. In the study of water absorption at atmospheric pressure, the value of 0.268 obtained in the study performed by impregnating the silane with travertine for 10 minutes gave more effective results than epoxy. In the capillary water absorption study, the value of 0.295 obtained by immersing silane in travertine for 10 minutes gave a more effective result than epoxy.

Salt crystallization is the most damaging event to natural stones. Soluble salts are the main factors that cause disintegration in structures and peeling of surface decorations. Therefore, it needs to be examined carefully. In the study to determine the resistance to salt crystallization, it was determined that the Average Mass Change (%) obtained by impregnating the silane with travertine for 10 minutes was 0.018, and the standard deviation value was 0.021. The results show that the silane-treated samples had higher resistance to salt crystallization. In addition, no decomposition or crack formation was observed when the treated samples were physically examined.

It has been seen by the Determination of Resistance to aging SO_2 in a Humid Environment that the epoxy-treated samples gave more durable results than the silane-treated samples. This shows that epoxy-treated surfaces have higher SO_2 resistance.

In the studies on contact angle measurement, it has been determined that the contact angle of raw travertine gains hydrophobic character by exhibiting a significant increase after the silane coating process.

When the mercury porosimetry analyzes were examined, it was determined that the porosity value of the sample treated with silane was 10.92%. In comparison, the porosity value of the sample treated with epoxy decreased to 6.11%. It has been determined that since the epoxy adheres as a thicker layer on the used surface, it also covers the delicate pores and reduces the porosity value compared to the silane treatment.

When the changes in the characteristic properties of epoxy and silane impregnated with different methods on the travertine surface are examined after the applications, the effects of water absorption in the atmosphere, capillary water absorption, and resistance to salt crystallization showed that silane is more effective in surface protection. On the other hand, in SO_2 wear tests, it has been determined that the protective feature is more effective because epoxy has a denser consistency than silane.

Although the porous structure of travertine is advantageous as a thermal insulation material and decorative product, it is quickly affected by atmospheric conditions due to its porous state, which limits its usage areas. With the study, it was seen that the disadvantageous situations in using natural stone raw materials of sedimentary origin could be turned into an advantageous niche product with high added value, and the value of the study was demonstrated once again.

Acknowledgement

This study was supported by Afyon Kocatepe University Scientific Research Projects Coordination Unit within project number 16.FEN.BİL.28.

References

Acar, H. 2003. Doğal Taşlarda Çatlak Tamir ve Gözenek Dolgu Sistemleri. Türkiye IV. Mermer Sempozyumu (MERSEM 2003) Bildiriler Kitabı, 18-19 Aralık 2003, Afyonkarahisar, Türkiye, 415-434.

Akbay, D., Şengün, N., Altındağ, R., Demirdağ, S. 2017. Doğaltaşların Tuz Kristallenmesine Karşı Direncinin Fiziksel ve Mekanik Özellikleri ile İlişkisinin İncelenmesi. Türkiye 9. Uluslararası Mermer ve Doğaltaş Kongresi ve Sergisi (MERSEM 2017) Bildiriler Kitabı, 13-15 Aralık 2017, Antalya, Türkiye, 411-420.

Altay, S., Çalapkulu, F., Tavman, İ. H. 2001. Bazı Türk Doğal Taşlarının Isı İletim Katsayıları. 4. Endüstriyel Hammaddeler Sempozyumu, 18-19 Ekim 2001, İzmir, Türkiye, 308-315.

Chafetz, H. S., Folk, R. L. 1984. Travertines: Depositional Morphology and The Bacterially Constructed Constituents. Journal of Sedimantary Petrology, 54 (1), 289-16.

Çetin, F. 2001. Gözenek ve Çatlak Tamir Uygulama Örnekleri ve Bu Uygulamaların İşletmelere Getirdiği İlave Kazançlar. Türkiye 3. Mermer Sempozyumu Bildiriler Kitabı, 3-5 Mayıs 2001, Afyonkarahisar, Türkiye, 445-449.

Çobanoğlu, İ. 2020. Su Yollu Yapıya Dik ve Paralel Kesilmiş Travertenlerde Kapiler Su Emme ve Basınç Dayanımı Özelliklerinin Anizotropik Değişimlerinin İncelenmesi. Journal of Scientific Reports –B, E-ISSN:2687-6167 (2), 55-67.

Dal, M.,Yılmaz, D. 2015. Su-Nemin Yapı Elemanlarına ve Yapı Konforuna Olumsuz Etkileri. International Journal Pure Applied Science (1), 89-99.

Erdem, H. O. 2016. Koruma ve Onarım Uygulamaları Öncesinde Tarihi Taş Yapılarda Bozulmaların Teşhisi: Phrygia Hierapolis'inden Bir Örnek. Pamukkale Üniversitesi Arkeoloji Enstitüsü Kültür Varlıklarını Koruma ve Onarım Anabilim Dalı, Kültür Varlıklarını Koruma ve Onarım Yüksek Lisans Programı, Denizli, 169.

Erdoğdu, K. 1998. Su Yapılarındaki Betonlarda Bağlayıcı Malzeme Seçimi. Çimento ve Beton Dünyası, 2(12), 17–23.

Gibson, G. 2017. Epoxy Resins, in: Brydson's Plastics Materials (Eighth Edition). Butterworth-Heinemann, 773-797.

Hasbay, U., Hattap, S. 2017. Doğal Taşlardaki Bozunma (Ayrışma) Türleri ve Nedenleri. Munzur Üniversitesi, Bilim ve Gençlik Dergisi 5(1), 26-45 ISSN: 2148-0273.

Kamacı, C. 2013. Traverten İşlenmesi Sırasında Karşılaşılan Problemler. Yüksek Lisans Tezi, Eskişehir Osmangazi Üniversitesi Fen Bilimleri Enstitüsü, 97.

MEB, 2013. Taş Bozulmalarını Teşhis Etme, İnşaat Teknolojisi, Ankara, 55.

Öcal, A. D., Dal, M. 2012. Doğal Taşlardaki Bozulmalar, Mimarlık Vakfı İktisadi İşletmesi Yayınları, İstanbul 109.

Öztank, N., Bacakoğlu, T. F. 2001. Mermer-Kireçtaşı ve Konglomeraların Yapılarda Kullanımını Denetleyen Parametreler. Türkiye III. Mermer Sempozyumu (MERSEM 2001) Bildiriler Kitabı, 3-5 Mayıs 2001, Afyonkarahisar, 123-131.

Polat, S. 2011. Türkiye'de Traverten Oluşumu, Yayılış Alanı ve Korunması. Marmara Coğrafya Dergisi 23, 389-428.

Tayşi, Y. 2021. Otel Yapılarında Doğal Taş Bozulmalarına İlişkin Bulguların Örnekler Üzerinden İrdelenmesi ve Analizi. Işık Üniversitesi Lisansüstü Eğitim Enstitüsü İç Mimarlık Yüksek Lisans Programı, Yüksek Lisans Tezi, 151.

Tekno Construction Chemicals, 2023, 2023. Teknosil, (https://teknoyapi.com.tr/tr/urunler/arama?q=teknosil&action=do)

TS EN 1925, Nisan 2000. Doğal Taşlar-Deney Metotları-Kılcal Etkiye Bağlı Su Emme Katsayısı Tayini. Türk Standartları Enstitüsü, Ankara, 9.

TS EN 12370, Mart 2020. Doğal Taşlar-Deney Metotları-Tuz Kristallenmesine Direncin Tayini. Türk Standartları Enstitüsü, Ankara, 5.

TS EN 13919, Şubat 2004. Doğal Taşlar-Deney Metotları-Nemli Ortamda SO_2 Yıpratmasına Karşı Direncin Tayini. Türk Standartları Enstitüsü, Ankara, 7.

TS EN 13755, Haziran 2014. Doğal Taşlar-Deney Yöntemleri-Atmosfer Basıncında Su Emme Tayini. Türk Standartları Enstitüsü, Ankara, 10.

Uğurlu, A. 2003. Sulama Kanallarında Sülfat Problemleri ve Çözüm Önerileri. 5. Ulusal Beton Kongresi, 1-3 Ekim 2003, İstanbul, 567-574.

Bulletin of the Mineral Research and Exploration

http://bulletin.mta.gov.tr

Archaeoseismology: Earthquake traces studies in ancient settlements; a chronological evaluation from the World focusing on Türkiye

Ökmen SÜMER[a,b*] and Volkan KARABACAK[c]

[a] *Dokuz Eylül University, Faculty of Engineering, Department of Geological Engineering, İzmir, Türkiye*
[b] *Dokuz Eylül University, Center of Earthquake Research and Implementation, Buca, İzmir, Türkiye*
[c] *Eskisehir Osmangazi University, Department of Geological Engineering, Eskişehir, Türkiye*

Research Article

Keywords:
Archaeoseismology, Archaeoseismologist, Ancient human structures, Chronological development, Anatolia.

Received Date: 14.07.2023
Accepted Date: 11.03.2024

ABSTRACT

Archaeoseismology is a field of science that investigates the remains of ancient human structures of destructive earthquakes that occurred in their ancient history and in this respect makes inferences on the possible effects of earthquakes whose origins will be may occurred in the future. Although many authors wrote the effects of ancient earthquakes in various periods, the first modern archaeoseismology studies in the world gain momentum starting from the end of the 19th century at the same time with Türkiye. In this understanding, the geography of Anatolia (Asia Minor), which has hosted a wide variety of cultural layers since its Mesolithic end, is an open-air research laboratory for modern archaeoseismological studies. This study is a reference work that summarizes the historical past of the discipline of archaeoseismology chronologically in the perspective of studies on Earth and Anatolia, presents suggestions about the future of archaeoseismology and is a literature summary for the new generation of archaeoseismologists.

1. An Overview Of Archaeoseismology

During the transition to settled life, human beings preferred areas that were topographically, geologically and hydrogeologically suitable for settlement, containing the blessings bestowed upon them by nature. In this sense, when the settlements on the seashores are kept separate, areas that lean their back on a high topography for safety, contain agricultural plains in front of them, close to water resources and preferably with plenty of thermal water outlets have become indispensable. At the same time, corridors that facilitate transportation from land to sea coasts have also hosted very dense settlements. From an earth science perspective, these areas mostly correspond to areas shaped or indirectly affected by faults. Today, as in the past, human beings establish their settlements in areas made more suitable for life by courtesy of faults. In this direction, just like today, ancient settlements were also affected by the past earthquakes. These effects occur during earthquakes, in the form of direct cutting of structures on surface faulting, with severe convulsions of seismotectonic and/or farther or nearby structures and seismogravitationally damage to two main types according to the simple classification of Dramis and Blumetti (2005). In this sense, it is also connatural that many major earthquakes that caused damage in historical or prehistoric periods affected the ancient structures, which are located on or near the faults, causing destructions and postponements in them, and left important traces in the history of ancient

Citation Info: Sümer, Ö., Karabacak, V. 2024. Archaeoseismology: Earthquake traces studies in ancient settlements; a chronological evaluation from the World focusing on Türkiye. Bulletin of the Mineral Research and Exploration 174, 99-128. https://doi.org/10.19111/bulletinofmre.1450741

**Corresponding author: Ökmen SÜMER, okmen.sumer@deu.edu.tr*

settlements. While the elemental traces of these earthquakes disappear significantly after the erosional and depositional processes, ancient buildings carry the traces of earthquakes to the present day. These earthquake traces preserved in ancient structures are a unique and important data source in understanding the seismicity of that region and the characteristics of the faults that may be related. The field of science that deals with the traces of these historical and prehistoric earthquakes in archaeological structures is called archaeoseismology (Stewart and Hancock, 1994). In terms of etymological origin, 'Archaeoseismology' is opened in the form of 'scientific studies on ancient earthquakes' as the integrity of meaning with the combination of the ancient Greek words ἀρχαῖος (arkhaîos) 'old/ancient', σεισμός (seismós). Galadini et al. (2006) defines archaeoseismology as a range in the time window of Paleosiesmology, and states that it is a safer scientific branch in terms of ensuring control with many different methods and data in terms of methodological, both archaeological and geological and dating. In this context, the application intervals and chronological efficiency of paleoseismological, archaeoseismological, historical and instrumental seismological records are summarized in Figure 1. While archaeoseismology easily reveals the types of earthquake traces preserved in archaeological structures, events that cause damage can also be dated when the dates of construction and renovation of the structures are known (Stiros and Jones, 1996). Archaeoseismology primarily systematically documents the damage/effects in an archaeological site during and after an earthquake the relevant archaeological period, and tries to relate the earthquake records in historical and archaeological data. The most important point that should not be forgotten and paid attention to here is that the observed damage or deformational structures must be addressed and considered with all possible thinkable alternative causes. Besides, it tends to data the deformation elements caused by the earthquake by using many different absolute dating methods. It clearly determines the type of faulting and the amount of offset by examining the structures cut by the surface rupture. At the same time, when the construction, repair and/or abandonment dates of these structures are known, confines the earthquake that occurred within a time interval. In addition, based on the damage caused during the earthquake, the intensity of the earthquake and from there its magnitude with certain approaches, it also aims to determine the seismic source by performing deformation analysis of damage distributions (Figure 2). Thus, by making use of archaeoseismological studies, it is possible to obtain information about prehistoric and historical earthquakes that occurred especially from the emergence of sedentary human life to the present day. Such information can also be used in earthquake risk analysis related to devastating earthquake activity that faults in that region can produce in the future; It contributes to the creation of data sets of parameters such as earthquake size, impact area and earthquake

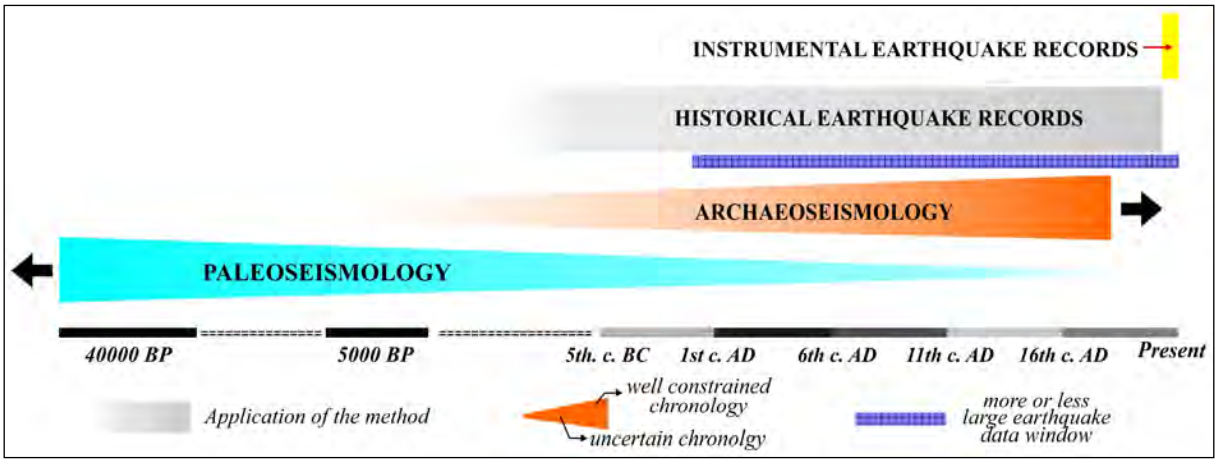

Figure 1- Application intervals and efficiency of paleoseismological, archaeoseismological, historical and instrumental period seismological records in Anatolia (slightly modified and colored from Galadini et al., 2006).

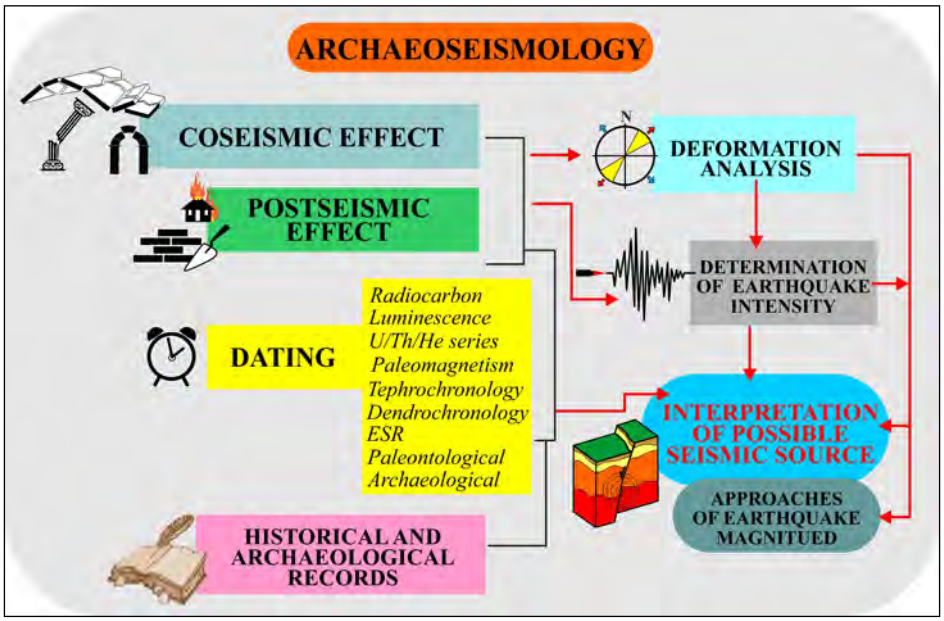

Figure 2- A simple flow chart of the use of archaeoseismological data and the steps of the methods applied (combined and modified from Galadini et al., 2006; Giner-Robles et al., 2009; 2012 and 2018).

recurrence period. Therefore, archaeoseismology is not only a field of science related to historical and prehistoric earthquakes in itself, but also a scientific discipline that sheds light on a better understanding of earthquakes that will occur today and in the future.

2. The First Archaeoseismological Observations In The World And Chronological Development Of Modern Scientific Studies

The first progress stages of the interpretation of the earthquake phenomenon as a natural event, especially in the memory of human beings, took place from about the end of the Archaic period (5th century BC). Pythagoras of Samos is the first person known to observe and convey the deformations and effects created by earthquakes (Sümer et al. 2018). In the different chapters of the 4th, 5th, 6th, 7th, and 8th books of The Historia, which consists of 9 books written by Herodotus in ancient times ~ BC 430, he noted the earthquakes that occurred especially in the land of Skyth, Aigina, Delos and Thessalia (Godley, 1928; 1930; 1938 translations). The 1st, 7th, 8th, 12th, 13th, 14th, and 15th books of Strabo's 17-volume huge work Geography, written at the beginning of the 1st century AD, include sections on earthquakes in Anatolia (Asia Minor), Greek mainland and Aegean islands (Jones, 1917; 1924; 1927; 1928; 1929; 1930 translations). In particular, quoting the words of Democles in paragraph 17 of chapter 3 of the book 1, he stated that earthquakes occurred a long time ago in Lydia and Ionia, and even as far north as Troy. This approach is important as it is an indicator of awareness that similar regions are affected by earthquakes with repeated periods. Gaius Cornelius Tacitus, in his work Annales (Church and Brodribb, 1906 translation), described how the damage caused by the event that we know today as the 17 AD earthquake in Western Anatolia in 13 ancient cities, in particular Sardis was rebuilt with the help of Roman Emperor of the time Tiberius Caesar Augustus. Many chapters of Gaius Plinius Secundus' 37-volume work, The Natural History, contain approaches to the causes and effects of earthquakes, and simple descriptions of earthquake-structure relationships. In fact, the 84th chapter of the 2nd book (Bostock and Riley, 1855 translation) includes approaches that can be considered as the first evaluations in terms of earthquake engineering within the framework of earthquake-soil interaction and that the angular relations of arched structures or load-bearing walls with each other increase earthquake resistance. The 24th chapter (Jones, 1933 translation) of the 7th book of the Greek traveler and geographer Pausanias, in which he describes the Achaia province in his book Description of Greece, written around

the middle of the 2nd century AD, is quite interesting. While the author divides the earthquakes into two according to their types and the way they occur, he states that these types cause different damage and deformations in buildings and architectural structures.

The foundations of modern archaeoseismological studies in today's understanding begin in the second half of the 19th century. While De Rossi (1874) presents data showing that the Basilica of S. Petronilla near Rome was destroyed by an ancient earthquake, he states that the directions of the deformation caused by the earthquake are parallel to the axes of the Tiber and Almone valleys which are located within large volcanic fractures/fissures in central and southern Italy. Especially the NE-SW extension of the Tiber River in Rome is similar and compatible with the deformations in the archaeological structure. Perhaps this study can be qualified as the first archaeoseismological study in the modern sense that examines the morphological data for determining the seismic source of an ancient earthquake in an archaeological structure. While Lanciani (1899) states in his work entitled "The Destruction of Ancient Rome" that the walls and some architectural structures were systematically destroyed in the same direction and that this was caused by an earthquake, he pointed out that the obelisk of the Sallust Gardens was destroyed during the shaking and was found as it was during the excavation and he also adds a drawing documenting it to his work (Figure 3a). This figure is perhaps the first image to document an ancient earthquake inside an archaeological excavation site. Similarly, Lanciani (1918) presents the data of the last excavation season in 1871, in the form of a drawing, showing that two granite columns

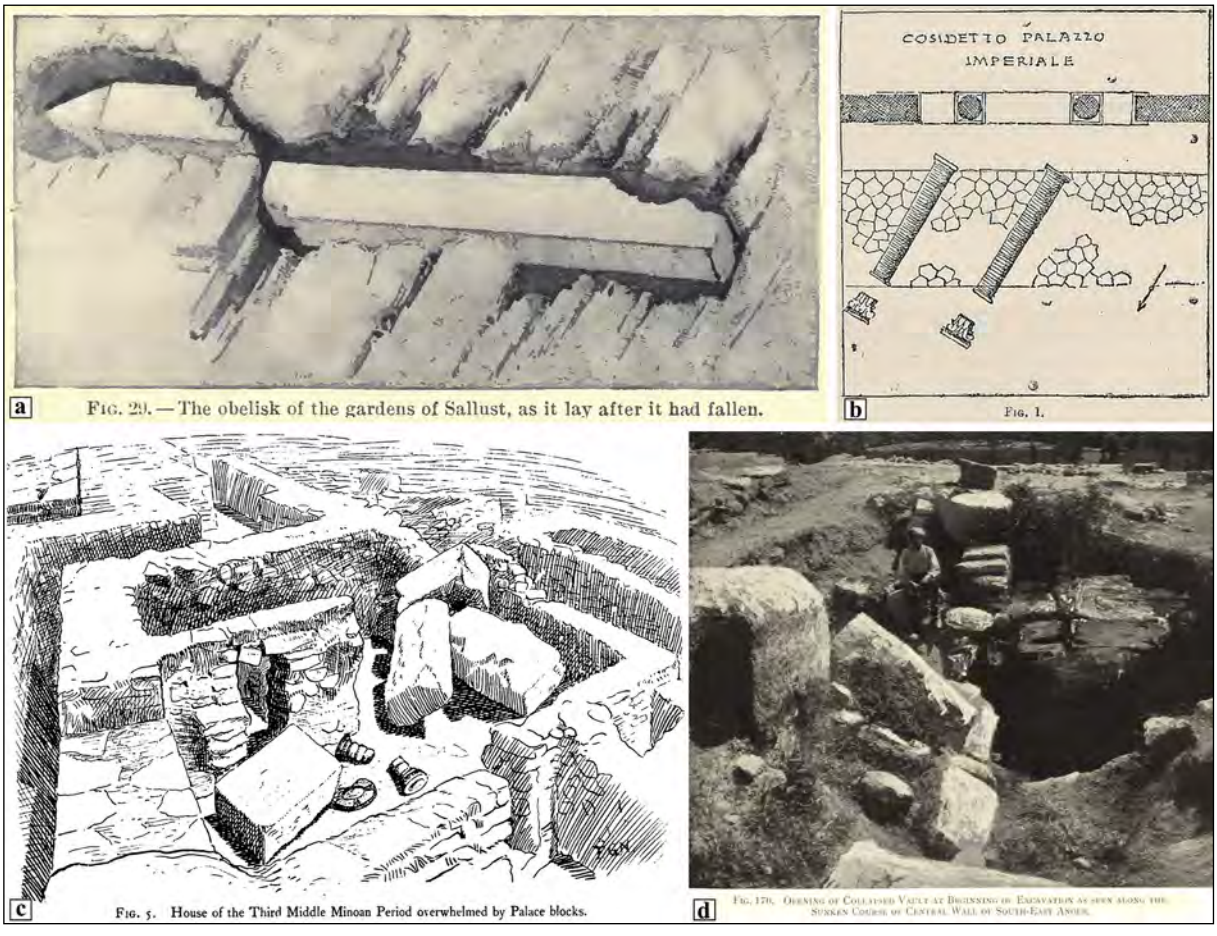

Figure 3- Images/photos presented in some important scientific studies that have pioneered archaeoseismological research on Worldwide. a) Rodolfo Lanciani's work, which deals with the destruction in ancient Rome, the drawing of the overturned obelisk in the Sallust Gardens, b) Illustration of systematically falling in the same direction columns of the Imperial Palace. Drawing, c) photo, d) of earthquake data observed by Arthur Evans in Knossos.

were found separated from their pedestals at the rear entrance of the imperial palace facing the river, and were found toppled in the N-NE direction, parallel to each other (Figure 3b). This schematic drawing is one of the first images of systematic series of aligned fallen columns, one of the best-known data we frequently use in modern archaeoseismology today. Evans (1922), during his archaeological excavations in Knossos, for the first time found that the blocks belonging to the Minoan Palace wall were blocks that reached 1 ton, some of which were thrown 20 feet (about 7 meters) away, and this could only be caused by a large earthquake, and this case is documented by a drawing by F.G. Newton (Figure 3c). Afterwards, Arthur Evans experienced the effect of the earthquake on the building while he was reading in bed in the basement of the excavation house on June 26, 1926, and by understanding the destructive power of the earthquake and its effect on the building, he expressed that he became more aware of the destruction of the Palace of Knossos by an earthquake (Evans, 1928). As a result of this event, Evans prepared a chapter in his book in which he approached that the historical earthquakes of 1508 and 1856 and the earthquakes of 1921 affecting Crete could be have same epicenters, and the effects of earthquakes on Minoan Culture (Evans, 1928). This book chapter is the first approach in which historical earthquakes and a current earthquake are evaluated and interpreted together in terms of archaeoseismology. While these events allowed Knossos, where he directed the archaeological excavations, to lean more in terms of earthquake phenomena, it was instrumental in photographing the data of possible earthquake traces for the first time in the new excavation finds (Figure 3d).

Increasing excavation work between second half of 19th century and beginning of 20th century, awareness of traces of ancient earthquakes in archaeological sites begins to accelerate (e.g. Schliemann, 1880 and 1884; Butler, 1922 and 1925). From the 1940's, with Dinsmoor (1941) and Kunze and Weber (1948), an "Archaeological Earthquake" terminological approach was developed for the first time, while the earthquake traces observed in structures in archaeological sites were defined more clearly and numerically. The book "Stratigraphie comparée et chronologie de l'Asie Occidentale", published by French archaeologist Claude Frédéric Armand Schaeffer in 1948, is a milestone in comparing earthquake traces in archaeological sites with both chronological and regional correlations. In the evaluation chapter of this magnificent book, which is mainly focused on the Ugarit cities, Schaeffer examines the destruction data in separate chronologies of different archaeological sites in Palestine, Syria, Persia, Caucasus, Cyprus, Aegean and Anatolia, while marking the ancient cities on the relevant intensity maps in *Erdbebengeographie* published by August Heinrich Sieberg in 1932. This work is also the first to pioneer publications that suggest catastrophic natural events related to the end of some archaeological periods, such as Bronze Age (e.g. Drews, 1993; Nur and Cline, 2000; Bachhuber and Roberts, 2009). Especially since the 1950's, we entered a period in which historical earthquake catalogs became widespread and traces of these data began to be sought in archaeological sites. In this period, the determination of ancient earthquakes in archaeological sites and the association of every unusual situation with earthquakes without applying specific and accurate scientific methods lead to great debates. Charles Richter (1958)'s statement "Ancient accounts of earthquakes do not help us much; they are incomplete, and accuracy is usually sacrificed to make the most of a good story" in 1958 may seem partially valid for his era, but in fact it is a document of how much we need modern archaeoseismology.

Towards the end of the 1970's, Karcz and Kafri (1978) conducted a study that questioned and compared consistent and questionable archaeoseismological data for the first time within the framework of the logic and methods we use today, and proposed a general mainstream framework in this direction. In the light of these developments, the late 1980's and early 90's can be defined as the birth of modern archaeoseismology. Stiros (1988) publishes his work revealing how much of an effective and important role archaeological data plays in active tectonic studies. In this way, the importance of ancient earthquake traces for understanding current earthquakes is revealed much more clearly. In addition, while the "The Engineering Geology of Ancient Works, Monuments and Historical Sites Preservation and Protection"

series, which was published in 4 volumes, was published in 1988, chapter 4 of volume 3, containing 19 articles entitled "Earthquakes, vibrations and other hazards in relation to the study and the protection of monuments and historical sites; Marinos and Koukis 1988", is very valuable in terms of determining the importance to be taken in the name of engineering and protection of the damage caused to ancient structures by both ancient and modern earthquakes. At this point, for the first time, it paves the way for the evaluation of archaeological structures in terms of earthquake and engineering geology. Simultaneously, in the same year, in 1988, Japanese geomorphologist and archaeologist Akira Sangawa (1988, 1993) published a Japanese publication titled "Declaration of earthquake archaeology" emphasizing the importance of using liquefaction structures in archaeological sites (in fact, seismites with the meanings known today) as a tool for the determination of ancient earthquakes. Its 1993 publication, also in Japanese, is titled "地震考古学" "Earthquake archaeology", but also tries to establish a relationship in terms of approaching the recurrence period of earthquakes by combining historical and instrumental earthquakes in southern Japan with data from archaeological cities. International conference held in Athens in 1991 used the term "Archaeoseismology" as it is used today for the first time and it is described as "the study of ancient earthquakes from the complementary standpoints of their social, cultural, historical and physical effect" as quoted by Stiros and Jones (1996) in their foreword. Towards the mid-90's, in 1996, the British School at Athens published by the Fitch Laboratory and edited by Stathis Stiros and Richard Jones, the first joint studies aimed at developing the discipline of archaeoseismology, the foundations of which have just sprouted, were combined and published for the first time in book form under the title "Archaeoseismology" as we use today. For many scientists, this special issue becomes a stepping stone for the recognition and dissemination of modern archaeoseismology. At this point also, the branch of Quantitative Archaeoseismology, which also emerged in 1990's and developed in the first decade of the 21 century, begins to use engineering seismological techniques to measure quantify ground motion parameters based on observed damage features (Papastamatiou and Psycharis, 1996; Alexandris et al., 2004). The 2000's represent a period of increase and acceleration in archaeoseismological studies. For the first time in Türkiye, Ferry etc. (2004) an Ottoman period buried water channel in İzmit, Similox-Tohon et al. (2004) in Sagalassos, Hinzen (2005) in Tolbiacum in Germany, Drahor (2006) in Sardis, Negri and Leucci (2006) in Hierapolis, and then Silva et al. (2009) at Baelo Claudia in Spain, shallow geophysical data begins to be used in the discipline of archaeoseismology. Sintubin et al. (2007) and a project titled "Archaeoseismology along the Alpine-Himalayan seismic zone" is developed within the scope of the International Geoscience Programme (IGCP-567). With this project, which has the participation of more than 50 scientists from 20 countries, the steps of the first scientific project are taken internationally and regionally. The work done with this project brings results and studies that lay the foundations of today's modern archaeoseismology are published in the INQUA-IGCP 576 workshop held in Cádiz/Spain in September 2009. For example, after using the LIDAR system for the first time in ancient water structures cut by active fault arms in Karabacak et al. (2007) and displacement measurements on roads; studies such as Yerli et al. (2009) and Schreiber et al. (2009) use LIDAR for numerical modeling architectural structure deformations in archaeological sites. Hinzen et al. (2009) proposes a schematic flow chart of quantitative methods that can be used in archaeoseismological studies. Caputo et al. (2011) applied that scheme and used synthetic seismograms in their study. Sintubin et al. (2009) draws attention to the trends of archaeoseismology's focus in different disciplines today and in the future. Giner-Robles et al. (2009) proposes a method of identifying the possible seismological source by bringing a perspective from the kinematic analysis to deformation structures previously seen in different archaeological sites and studies. Finally, Rodríguez-Pascua et al. (2009) develops a comprehensive classification called Earthquake Archaeological Effects (EAE), based on the INQUA ESI 07 (Environmental Seismic Intensity – 2007), which Michetti et al. (2007) began to develop since 2003. After this classification, Rodríguez-Pascua et al. (2013) is developed by adding it in The European Macroseismic Scale (EMS-98) proposed by Grünthal (1998). Giner-Robles et al. (2018) revises the post

seismic part of this classification. In the light of all these developments, the Earthquake Archaeological Effects (EAE) classification we use today becomes the most up-to-date (Figure 4). On similar subject, in classical monuments and buildings, arches are a frequently used indicator in determining the effects of earthquake ground motion, Hinzen et al. (2016) also proposed a scheme to evaluate the damage of arches called "Arch Damage Grade (ADG)" based on three categories. In the same years, Schweppe et al. (2017) introduced the concept of Precariously Balanced Archaeological Structures (PBAS) to estimate ground motions that were not exceeded since the structure is in its delicate state. Schweppe et al. (2021) were the first to estimate dynamic source parameters of an earthquake based on damage to an archaeological structure. The latest developments in the world show that archaeoseismology is in the common monk cluster of some disciplines in the field of archaeology, geology, geophysics, architecture, civil engineering, earthquake engineering and even sociology.

3. Archaeoseismological Chronology and the Potential of Anatolian Geography

The potential of the inventory of ancient buildings in geography is directly related to the history of the transition to settled life in that region. For example, the human settlement in North America defined by several centuries but the settlement in Anatolia goes back to the end of the Mesolithic (~ 11000 years). In this sense, especially the geographical area where Türkiye is located has a relatively dense inventory of ancient buildings with a chronologically older record of settled life (for example, the Mediterranean coast, the Aegean islands, Anatolia, the Levant, and Mesopotamia, etc.). In addition, Türkiye and especially Anatolia are one of the most important areas on Earth that have been geologically shaped by active faults with very high earthquake activity and are still continuing to be shaped. The combination of these two main elements puts Türkiye in a unique position in terms of archaeoseismological richness. At this point in Türkiye, especially the archaeological studies that started after the second half of the 19th century which increased rapidly also have a great impact. The formation of new data sets with the acceleration of systematic archaeological research after the 1950's contributed to the growth and development of archaeoseismology in Türkiye. In this direction, sections and developments from important studies that are the source of modern archaeoseismology studies in our country are summarized below with a chronological approach.

Although the first archaeological excavations in Türkiye were started in Halicarnassus in October 1856, the first simple earthquake observations in an ancient city are found in the excavation reports of Heinrich Schliemann, who conducted excavations in Troy. Schliemann (1880) emphasizes a severe earthquake related to the scattered finding of blocks belonging to the wall of a house under the ruins of the Hellenistic period at a depth of about 10 meters in a trench on the northern slope of Hissarlık. In Schliemann (1884), he noted that in the trench geometry trench with a length of 110 m and a width of 3 m, which they opened in the southern part of Hissarlık, columns in syenite composition with Chorint-type marble heads stretched to the NW on a rubble of 30 cm and fell, emphasizing that these data may be related to a late-stage earthquake. In fact, in the notes of 1884 excavation report stated Mr. Calvert's warnings him that Pliny informed about the earthquakes in Asia that coincided with the reign of Tiberius are quite remarkable. The observations of Howard Crosby Butler from Princeton University pointing to the repairs in the Temple of Artemis during the excavations of Sardis and the pause in attempts to finish the temple in ancient times have been associated with possible earthquakes of 17 AD and older (Butler, 1922). In particular, William Warfield, who wrote the additional geology section of the 1922 excavation report, mentions the possibility of earthquakes affecting Sardis based on mass movements in the Acropolis and sedimentological observations in Paktolos. This section has chronological importance in terms of laying the basic foundations of geoarchaeological approaches, as it also includes geological observations as a contribution to an archaeological excavation report in Türkiye and even in the world. Salomon-Calvi (1940) presents how the columns of the Asclepieion Temple collapsed in the same direction in an ancient earthquake, in the 2nd part of the report titled "Studies Related to Earthquakes in Türkiye", about the 1939 Dikili - Bergama earthquake, while presenting with an

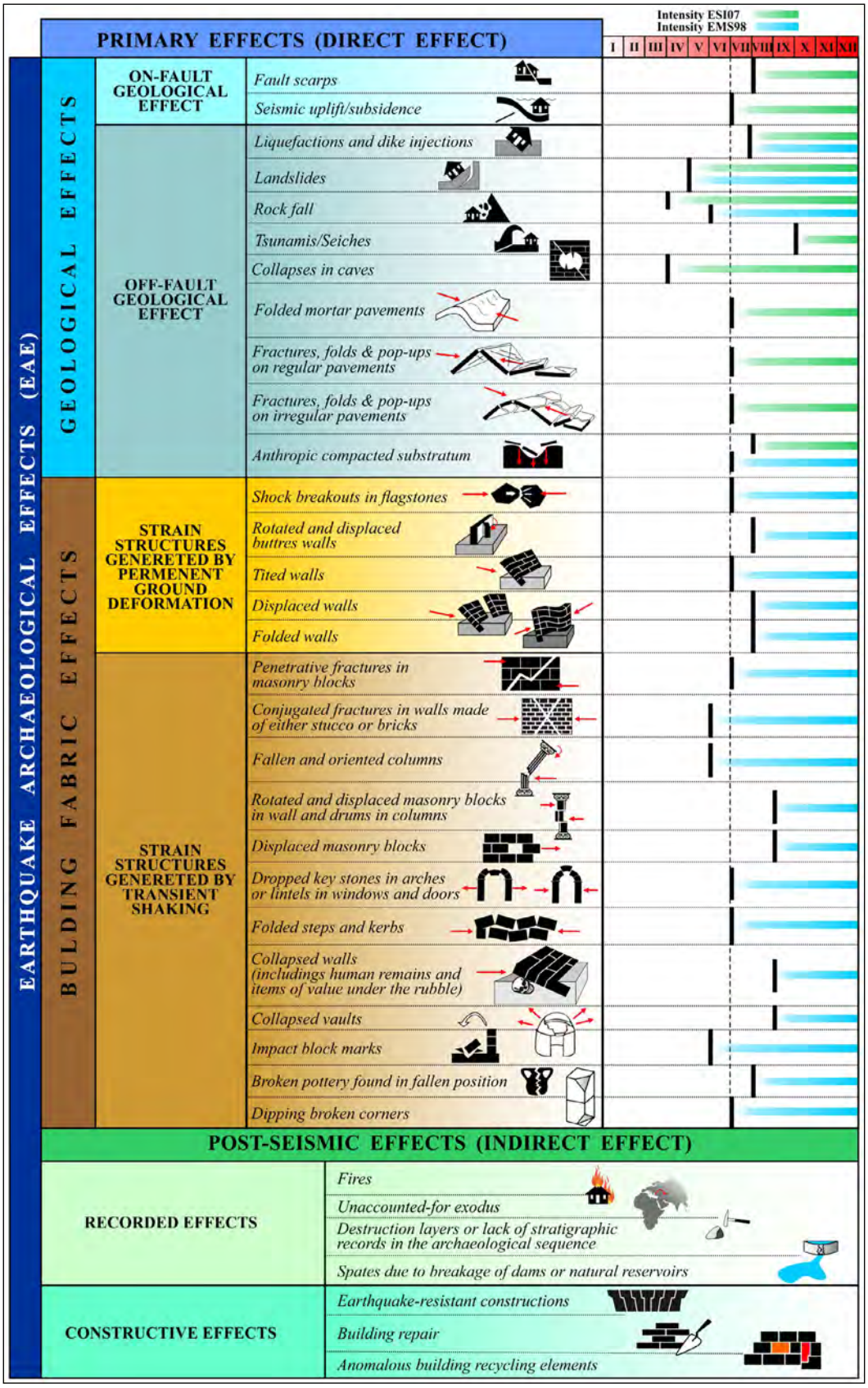

Figure 4- The Earthquake Archaeological Effects (EAEs) classification (combined from Rodríguez-Pascua et al., 2009, 2011 and 2013 and Giner-Robles et al., 2018).

archive photograph the columns that were restored and rebuilt shortly before the earthquake. While he states that the earthquake did not affect the columns (Figure 5a and b), he draws attention to the fact that the ancient earthquake should have also been very strong. This study is very important in terms of representing the first example of two different earthquakes in historical and instrumental periods in an archaeological city, where their effects on the same architectural structure are documented side by side. Duyuran (1945) stated that the large column on the southern leg of the eighth arch, which was revealed on the ground floor of the Basilica during the 1944 excavations in İzmir Agora, was destroyed by an advanced earthquake in the direction of NW from SE, but pointed out that more data was needed to date the earthquake. İzmir Museum Director Rüstem Duyuran who was the first person to document an ancient earthquake data uncovered by excavations at an archaeological site in Türkiye with photographs (Figure 5c). By publishing a more detailed report after Naumann and Kantar (1950), they evaluate the possibility of this event being an 178 BC earthquake by placing the artifacts made after the earthquake and spolia, plan changes and superior rapid repairs on different architectural structures in the reconstruction of the Agora. Carl William Blegen presents the earthquake data he determined during the 1932-1938 excavation periods in Troy in his 1951-1958 excavation reports. While considering the earthquake data, which is also emphasized in the foreword of Blegen et al. (1953), where the Troy VI layer presents its data, under separate headings in the excavation report, it combines the data and allocates an archaeological level in the form of "Earthquake stratum", he states that this earthquake is likely to occur in the middle of the 13th century BC. He also lists the photos of this earthquake data in the second part of the report (Figure 5d). In the 1960's, data begins to come in Sardis (Modern Sart), which contains the traces of earthquakes of different periods in terms of archaeoseismological data richness and which is the one of the archaeoseismology laboratories in Türkiye. The most important reason for the pause of data production in this ancient city can be the suspension of excavations after 1922 until 1958. During the excavations that started under the direction of Harvard University Archaeology Professor George M. A. Hanfmann, Hanfmann (1961) mentioned the suspicion of a possible early 7th century earthquake other than the 17 AD, while he collected photographs of earthquake data from different areas of the city, especially during the 1962-1972 excavations, in the excavation archive (Figure 5e-f) and most of them published in Hanfmann (1963). Collecting all the data in Hanfmann and Mierse (1983), he chronologically lists the earthquakes of 17 AD, early 7th century, 12th century, 16th and/or 17th century that influenced Sardis. New earthquake data for Sardis are also reported during excavations led by Crawford H. Greenewalt in the 1980's (Figure 5g). Although earthquake data were also recorded during archaeological excavations in Hierapolis (Modern Pamukkale) in the same period, these data were removed from the archives much later and evaluated by D'Andria et al. (2008) (Figure 6a). In the early 1970's, the Nature article titled ''Value of Historical Records of Earthquakes'' was published by Nicholas Ambraseys (1971). With this regional-scale study, which touches on the relationship between the historical earthquake records affecting Western Anatolia, especially the Gediz River and around 17 AD, and İstanbul's earthquakes, the importance of bringing a perspective by including the structural elements in the relevant area, apart from looking at the ancient records within the phenomenon of earthquakes, is emphasized. This publication would actually be the study that sprouted today's archaeoseismological perspective and guided the necessary right angle. Rudolf Naumann, an expert on Ancient Anatolian Architecture, who had previously worked in many ancient cities and worked in the earthquake effects in archaeological sites in the İzmir Agora, transferred to the area after the 1970 Gediz earthquake and reported the damage to architectural structures in both the modern and Aizanoi ancient city (Modern Çavdarhisar), emphasizes the earthquake affected modern structures other than ancient ones. He documented the deformations in the Theater, the Temple of Zeus, the Bath and some floor coverings with photographs (Figures 6b and c). Naumann (1971) is one of the first examples in the world where the effect of an instrumental period current earthquake on an ancient city is studied in this detail.

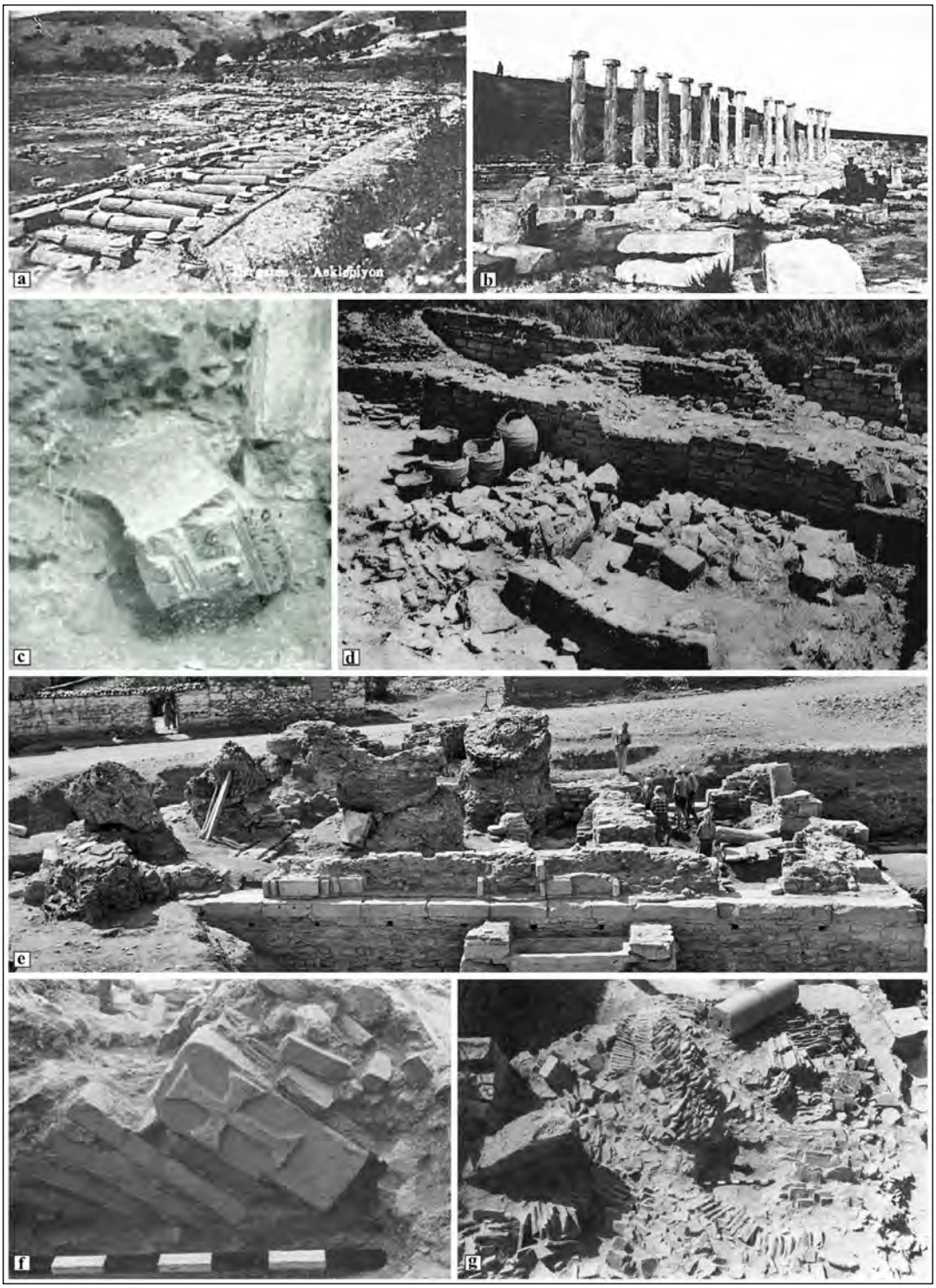

Figure 5- Old and new photographs (a and b), respectively, presented by Wilhelm Salomon-Calvi of the Shrine of Asklepieion in Pergamon, c) The head of the overturned column and column photographed by Rüstem Duyuran in the İzmir Agora, d) One of the photographs that Carl William Blegen observed in the Troy VI layer and presented about the earthquake data on the defensive wall. Photographs of earthquake findings presented in Sardis excavation reports and archive; e) The great destruction in Church E, which dates back to the Byzantine Period (11 – 12 century AD), this photograph belongs to the 1962 excavation archive, it was also used for the possible AD 1595 earthquake data in Buchwald and McClanan (2015). f) This photograph is from the 1970 excavation archive and presented in Hanfmann and Thomas (1971) the excavation report; imbricated marble keystone with Cross from major brick arch of the Colonnaded Street. g) Fallen brickwork and inscribed columnar monument in south colonnade of Marble Road, from the 1979 and 1980 excavation periods and presented in Greenewalt et al. (1983).

Figure 6- a) Photo presented in D'Andria et al. (2008) showing the deformations that occurred during the 7th century earthquake on the Plateia (city square) extending to the Frontino Gate, which was taken during the 1963 excavations in Hierapolis. Some photos in Rudolf Naumann's work documenting damage after the March 28, 1970 Gediz Earthquake in the ancient city of Aizanoi; b) systematic aligned fallen columns of the Temple of Zeus, c) deformations in the cavea of Theater and lateral displacements in large buried marble blocks.

Ünal (1977) draws attention to 3 main events by referring to earthquakes between 2000 BC and 1000 BC based on Hittite tablets and data in the literature. These are in chronological order according to the author; (1) In 1365 BC, in Ugarit during the time of I. Suppiluliuma, (2) in 1290 BC, that is, in Samuha in the last reign of Urhi-Teîmb, and (3) in the end of the III. Hattusili era or at the beginning of the IV. Tuthalya era (~ 1250 BC) are likely to have occurred in Ninive. In the early 1980's, George Rapp publishes Troy's work (Rapp, 1982), which deals with earthquakes in Troy and draws attention as the first chapter to compile earthquake data in an archaeological site in a monograph in which the Archaeological Geology (Geoarchaeology in the sense we use today). In this section, based on the data of author Carl William Blegen and John Manuel Cook, he lists various demolitions in Troy, especially in layer VI, while synthesizing current earthquake data for the destruction in the region and archaeological site. The author also highlights the roof in Karcz and Kafri (1978), bringing a 5-point analytical methodological framework proposal for identifying structural damage to archaeological sites. Finally, the author notes in his chapter that the most valid hypothesis for great destruction at the Troy IV level lies in the underlying immigrations caused by ground movements during the earthquake in the bottom unconsolidated materials. In his studies at Ephesus, Stefan Karwiese comments that the architectural building deformations, especially in terrace houses, may have occurred in the 3rd quarter of the 3rd century AD using numismatic data from the Gallienus period, and that this event may be related to the 262 AD earthquake in historical earthquake catalogs (Karwiese, 1985). While evaluating the possibilities of the Got attack, which coincided with

the same period in Ephesus, the researcher also touches on the changes in the post-earthquake use of different structures in the city, such as the eastern Stoa of the Agora. The excavation team of Sagalassos (Modern Ağlasun), led by Marc Waelkens, reports possible post-earthquake restorations in the Temple of Apollo Clarios, addition on the Roman Bath and deformations in Hellenistic aqueducts in the 1989 excavation results report (Waelkens et al., 1990). He then makes a proposition to this earthquake in Waelkens (1993) based on archaeological finds 138/139 AD or 139/140 AD. Following the developments in the world in the mid-1990's, Türkiye's archaeoseismology also becomes a leap point for. Chapter 6 of Erhan Altunel's doctoral thesis (Altunel, 1994) represents the first example of modern archaeoseismology studies within the borders of Türkiye. In this section, where geological, geomorphological and structural elements are blended with deformations in ancient urban architecture, the deformation elements in the architectural structures of the ancient city of Hierapolis are shown in the city plan for the first time, and the NNW trending left lateral component oblique-slip surface rupture passing through the city is also mapped. At this point, he is stated that this surface crack is also compatible with the general structural geological main discontinuities of the region. Although there is no clear opinion on the history of this earthquake in the study, it is recommended that it may be related to the 60 AD earthquake, which is frequently mentioned in the literature. Another importance of this study is that the term 'Archaeoseismology' was used for the first time in a study in Türkiye. After this study, archaeoseismological interest in Hierapolis increases and studies such as Altunel and Barka (1996); Hancock and Altunel (1997); Hancock et al. (2000) are produced, respectively. In these studies, it is emphasized that the city may have more than one earthquake history such as 60 AD, possible 4th century AD, 7th century AD or 14th century AD by interpreting the data in historical earthquake catalogs and deformations in architectural structures belonging to different archaeological periods. In the same period, a 7-page extended abstract titled "A discussion on some concepts of the archaeoseismology" was published in the booklet of the 4th National Earthquake Engineers Conference in 1997 by Engin Karaesmen and Erhan Karaesmen, who have been dealing with archaeological architectural structures in terms of earthquake engineering since the late 1980's. (Karaesmen and Karaesmen, 1997). In the conclusion section of this work, it is emphasized that the phenomenon of earthquakes is not considered important in archaeological protection and that the measures of the protection of architectural structures should be discussed in terms of earthquake engineering. While modern archaeoseismological studies have started to focus in different ancient cities since the end of the 1990's, it is seen that these studies have been manly distributed with in the Western Anatolian Extensional Province, and mostly in Hellenistic and Roman cities. Altunel (1998) maped a NE-SW trending damage corridor within the city, pointing to deformations in the sacred hall, street, agora and Athena Temple and some lateral displacements in the ancient city of Priene, which is located at the northwestern end of the Büyük Menderes Graben System. He states that these damage in the city may occur with earthquake(s) in the 12th century AD and beyond. In the early 2000's, two archaeoseismology-based Tübitak projects were carried out (Altunel, 2000; Altunel et al., 2001). The first contains limited data from the ancient cities of Priene and Miletus within the Büyük Menderes Graben System, and the second from the ancient cities of Ephesus, Sardis and Philadelphia within the Gediz and Küçük Menderes graben systems. The biggest reason why these projects remain poor in terms of archaeoseismological data rich is that there are no researchers of archeology origin in the team conducting the projects. At this point, it becomes once again manifested that archaeoseismology is a multidisciplinary scientific study. Waelkens et al. (2000), based on the different data they have collected during the Sagalassos excavations, it produces a separate and only archaeoseismology-specific work for the city since 1989. In this publication, they drew attention to the deformation patterns in the architectural structures of the city from various periods dated from Hellenistic to Byzantium, especially the library floor and theater. They reported the probability of at least 4 earthquakes in the city; in the second half of the 1st century AD, the middle of the 3rd century AD, the first quarter of the 6th century AD, and the middle of the 7th

century AD. Akyüz and Altunel (2001) in the ancient city of Cibyra (Modern Gölhisar), located in the middle part of the Fethiye – Burdur Fault Zone which is an important structural discontinuity for the Southwest Anatolia, reported the deformation of the southern flank of the Roman Stadium and the damage of some other architectural structures. Evaluating from the historical earthquake catalog data that the city was affected by the possible 417 AD earthquake, they state that the surface rupture of this earthquake originated from the Kibyra Fault Zone within the city border. Altunel et al. (2003) In their archaeoseismological observations in the ancient city of Cnidos at the westernmost end of the Datça Peninsula, they divided the deformations in architectural structures of different periods in the city, especially the Temple of Aphrodite and the Demeter Sanctuary, into faulting phases, and emphasized that the first earthquake should have been occurred between 2nd or 3rd centuries BC in the Hellenistic period and the second earthquake might be related to the 459 AD earthquake on the Knidos Fault, which developed surface faulting. Şimşek and Ceylan (2003) associated their archaeological excavation results in the ancient city of Laodicea with historical earthquake catalogue, stating that the city was affected by earthquakes such as 27 BC, 47 AD, 60 AD, late 3rd century AD, early 4th century AD and 494 AD. In the following period; From 2003 to 2006, the works were produced by similar teams in Sagalassos, Sintubin et al. (2003); Similox-Tohon et al. (2004); Similox-Tohon et al. (2005); Similox-Tohon et al. (2006) is seen to be concentrated in such studies. From these studies, which point to earthquakes dated using archaeological chronology and similarly compressed between the 6th and 7th centuries, Similox-Tohon et al. (2004 and 2005) are important in terms of applying shallow geophysical and trench-based paleoseismological studies together in archaeoseismology for the first time. Crawford H. Greenewalt, the Sardis Excavation Director at the time pointed out to the earthquake findings in Field 55, where it has been concentrated since the early 2000's, and the presence of a fracture extending 10 cm wide and 2.5 meters deep in Greenwalt (2003; 2006 and 2007), while evaluating the earthquake affecting this area with archaeological finds and associating it with a possible 7th century and/or later event. Drahor (2006) refers to archaeologists in his publication, in which he gave the results he obtained from shallow geophysical studies in the same field, pointing to the existence of the same fracture. At this point, Karabacak (2007) produces a doctoral study in Türkiye by combining both geological, geophysical, LİDAR using, and trench-based paleoseismological data were used by combining historical earthquake catalog data. This study is also a turning point as it is the first archaeoseismological study conducted in Türkiye in a location other than Western Anatolia, and the integrated use of almost all methods in modern archaeoseismology studies today. While Sintubin and Stewart (2008) re-evaluate the data of previous studies in Sagalassos within the framework of an archaeoseismological logic tree, and propose a new measurement method in practice, in the form of Archaeoseismic Quality Factor (AQF), in this approach, it is stated that the earthquake hypothesis in Sagalassos contains some weaknesses and uncertainties, and indicate that they need to be re-evaluated. Another importance of this study is that before them, methodological staged diagrams, suggestions for archaeoseismology studies, propose a much more harmonious, efficient new and developed methodological scheme on the foundations of all studies. Since the late 2000's, studies in different archaeological cities and tectonic regions have gained momentum. Some of these studies are; Birinci (2006) and Piccardi (2007) in Hierapolis, Akan (2009) and Akan et al. (2012) in Rhodiapolis, Altunel et al. (2009) at the northern end of the Dead Sea Fault Zone, Çetin-Yarıtaş (2009) in Termessos, Yönlü et al. (2010) in Priene and Ramazanpaşa Bridge, Karabacak (2011) in Cibyra, Hinzen et al. (2010, 2013*a* and *b*) and Yerli et al. (2010 and 2011) in Pinara. Here, Hinzen et al. (2010)'s work in Pinara is distinguished from other studies in terms of being an archaeoseismological study based on deformation analysis using ground motion simulations. Perinçek (2010) and Bony et al. (2012) take an archaeoseismological approach by using the data of a Byzantine period shipwreck and tsunami within the ruins of Theodosius Port in the north of Istanbul Yenikapı, and interpret that this event was related to the 557 AD earthquake. These publications are the first studies in Türkiye where underwater data is used and an archaeoseismological

approach is made. Yönlü (2012), at the south-west end of Eastern Anatolian Fault Zone; he makes evaluations by blending its archaeoseismological observations in Anavarza, Kastabala, Toprakkale, Ayas, Magarsos with trench-based paleosmological data. This study is the first study in which archaeoseismological studies are carried out in the Eastern Anatolia Fault Zone. Karabacak et al. (2013), on the other hand, states that while performing absolute dating method with the Optical Stimulated Luminescence (OSL) technique on different types of materials such as sediments and ceramics, which are under the architectural structures destroyed by the earthquake in the Cibyra. They suggested the earthquake caused great damage to the city in the 10^{th}- 11^{th} centuries AD. This study is the first example of the use of the OSL method, which has also started to be used in trench-based paleoseismology studies, in an archaeoseismology study. Passchier et al. (2013) from a different point of view, attributing the deformations on the ancient water channels connecting to Ephesus caused by an earthquake originating from the İçme Tepe Fault, and presented an approach based on both the archaeological data and the annual laminated carbonate precipitation rate in the channel. For the timing of the vertical displacement on the channel, they suggested that this event occurred in the second half of 2^{nd} century AD, it may be related to the AD 178 earthquake. Aydan and Kumsar (2015) show an approach to the 17 AD earthquake by evaluating geotechnical data such as acceleration and liquefaction potential recorded in current earthquakes together in regions close to archaeological sites with earthquake history in Western Anatolia. Benjelloun et al. (2015), on the other hand, carries out a study focusing on the dating of the restorations made after the deformation of the Antioch water channels in Antakya. In terms of this study dating method, although the age results are very weak, it is very remarkable in terms of the first use of archaeomagnetism data other than radiocarbon data within the Anatolia. Since the mid-2010's towards the present day, there has also been a diversity in the studies and fields carried out. Some of these works are; Söğüt (2014) in Stratonikeia, Buchwald and McClanan (2015), Cahill (2016, 2019), Hallmannsecker (2020), Sümer et al. (2022) in Sardis, Bachmann et al. (2017) and Pirson (2017) in Pergamon, Kumsar et al. (2016) in Hierapolis and Laodicea, Karabacak (2016) in Lagina, Benjelloun (2017) and Benjelloun et al. (2018) in Nicaea, Stewart and Piccardi (2017) offering data from some ancient cities in a large area covering the Aegean Region and Greece, Softa et al. (2018) in Myra, Altunel and Pınar (2021) in Ephesus. At the same time, the studies conducted outside of Western Anatolia (classical ancient cities in the Aegean and Mediterranean regions) are Drahor et al. (2016, 2017 and 2023) and Sümer et al. (2019, 2021), which documents the deformations in Hittite cities such as Ḫattuša and Šapinuwa and Barış et al. (2021), which evaluates the archaeoseismological data in Bathonea together with ancient earthquake data. Benjelloun et al. (2021), who documented the archaeoseismological deformations of defensive walls, towers and other different architectural structures in the ancient city of Nicaea, on the borders of İznik in the area of the Northern Anatolian Fault Zone middle branch, differs in terms of evaluating deformation structures for the first time within the scope of Earthquake Archaeological Effects (EAEs-98) in Türkiye.

All these archaeoseismological studies, briefly summarized above and carried out on the borders of Türkiye, have been brought together for the first time in terms of both their location of the ancient settlements, dominate archaeological provenance, and their relationships with active fault perspective. In this direction, we also present a chart (Table 1) and the relevant map (Figure 7). Readers can access the details of these related scientific studies from the archaeoseismological perspective by means prepared in chronological order and presented in the appendix of this study (Appendix-1). Additionally, a timeline visual, highlighting the milestones of archaeoseismology studies carried out specifically for Türkiye, is presented in Figure 8.

4. Approaches and Suggestions For The Future

While this paper presents a chronological approach to the development of archaeoseismological studies up to the present, it largely focuses on presenting an inventory of studies conducted in Türkiye. In addition, these studies, which are cataloged together for the first time in the literature, have offered the chance to make some inferences that can contribute to a critical evaluation of archaeoseismological studies.

Table 1- Distribution of archaeoseismological studies carried out in Türkiye, which were mentioned in this study. Please follow up the archaeological tectonic and geographical distribution of location numbers from Figure 7 and follow the Reference numbers from the "No*" column of the chart presented in Appendix-1.

Location Numbers (LN)	Archaeological Site/ Region / City	References	Total Number of Studies
1	Troy, Çanakkale	1, 5, 6, 12, 51	8
2	Sardis, Manisa	2, 7, 23, 26, 56, 58, 59, 69, 73	15
3	Pergamon, Asklepieion, İzmir	3, 63	3
4	Agora of Smyrna, İzmir	4	2
5	Tralleis, Aydın	9	1
6	Hierapolis, Denizli	9, 15-18, 21, 32, 35, 60, 65	11
7	Ephesus, İzmir	13, 23, 54, 56, 65, 71	6
8	Sagalassos, Burdur	14, 22, 27, 30, 31, 33, 36	8
9	Priene, Aydın	19, 20, 44	3
10	Miletos, Aydın	20	1
11	Philadelphia, Manisa	23	1
12	Cibyra, Burdur	24, 45, 53	3
13	Cnidos, Muğla	25	1
14	Laodicea, Denizli	28, 60	2
15	Colossae, Denizli	35	1
16	Rhodiapolis, Antalya	37	2
17	Amik Plain Sıçantarla Hill and ancient road, Antakya	34, 38	2
18	Termessos, Antalya	39	1
19	Yenikapı, İstanbul	41, 50	2
20	Pinara, Muğla	42, 43, 46, 52	5
21	Ramazanpaşa Bridge, Priene, Aydın	44	1
22	Anavarza, Kastabala, Toprakkale, Ayas, Magarsos	48	1
23	Seyitömer Mound, Kütahya	49	1
24	Stratonikeia, Muğla	55	1
25	Magnesia, Aydın	56	1
26	Antioch water channels, Antakya	57	1
27	Šapinuwa, Çorum	61	2
28	Lagina, Stratonikeia, Muğla	62	3
29	Nicaea, İznik	64, 66, 72	3
30	Myra, Antalya	67	1
31	Ḫattuša, Çorum	68, 74	3
32	Bathonea, İstanbul	70	1

The archaeological potential of a region opens a new windows into the seismotectonics of that region. The most important key data in terms of the seismotectonics of a region, older than instrumental earthquakes, can be provided by paleoseismological studies and analytical dating methods. Sites with archaeological potential provide us with the historical record, often without the need for analytical methods. Unlike paleoseismology, much smaller budgets and observational analyses allow us to access seismotectonic data with increasing resolution as we approach the present (see Figure 1). For example, seismotectonic records, which were insufficient along the Fethiye-Burdur Fault Zone due to the limited paleoseismological data in southwestern Anatolia, filled this gap with data from ancient cities such as Sagalossos, Cibyra and Pinara. In this regard,

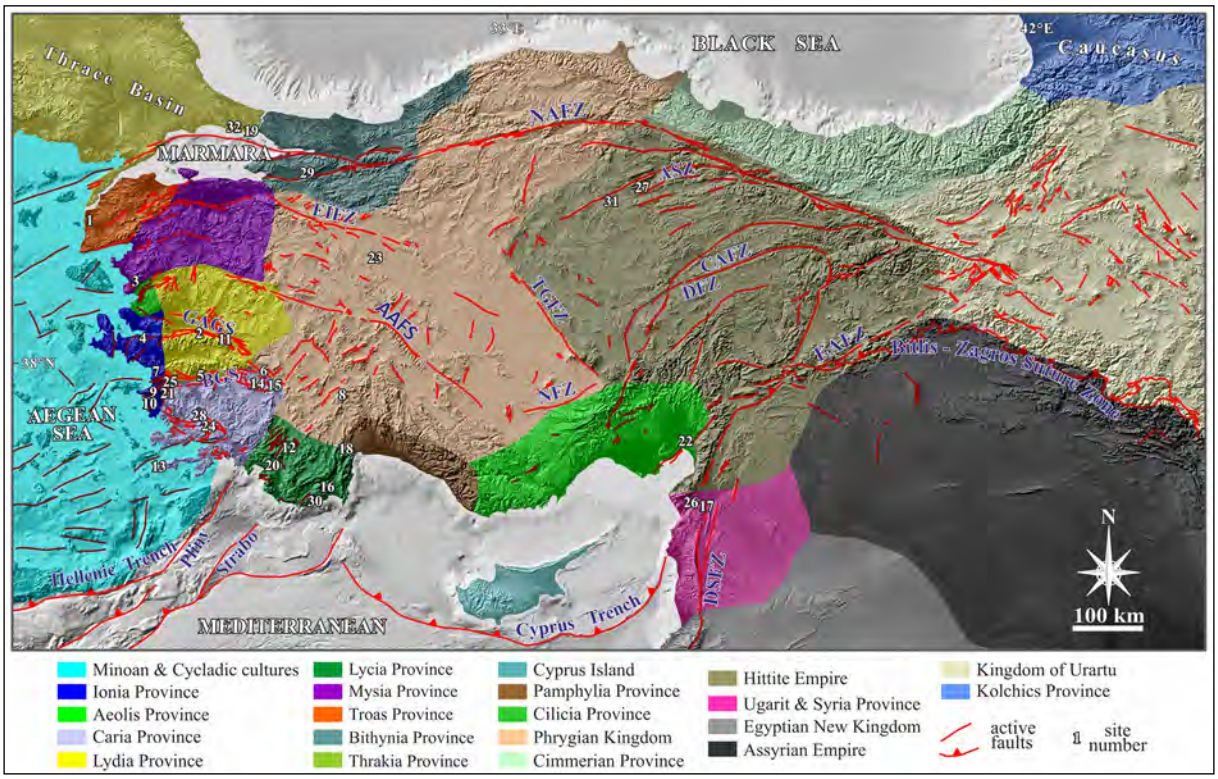

Figure 7- Integrated Archaeotectonic Map of Türkiye and its surroundings, specially prepared for this study for the first time, showing active fault zones and dominant archaeological provinces together. The approximate boundaries of archaeological province (were combined using data from Shepherd, 1923; Freeman, 1996; Sabin et al., 2007; Morris and Scheidel, 2009; Picón and Hemingway, 2016; Schachner, 2019). Active tectonic structures (compiled from Şengör et al., 1985; Koçyiğit, 2003; Emre et al., 2018; Pavlides et al., 2014 and Sümer et al., 2019). For location numbers please take advantage of the first column of Table 1. AAFS: Afyon Akşehir Fault System; ASZ: Amasya Shearing Zone; BGS: Büyük Menderes Graben System; EAFZ: Eastern Anatolia Fault Zone; DFZ: Deliler Fault Zone; EIFZ: Eskişehir İnönü Fault Zone; GAGS: Gediz Alaşehir Graben System, NAFZ: North Anatolian Fault Zone; CAFZ: Central Anatolian Fault Zone; DSFZ: Dead Sea Fault Zone; TGFZ: Tuzgölü Fault Zone.

one of the most important outcomes that the inventory created within the scope of this study shows us is the scarcity of archaeoseismological studies carried out in the ancient settlements on and around the most important active fault zones of Anatolia, such as North Anatolian Fault Zone (NAFZ), East Anatolian Fault Zone (EAFZ) and Dead Sea Fault Zone (DSFZ). At this point, it is clear that archaeoseismological studies must be expanded in settlements different archaeological periods around these main structural lines.

Archaeoseismological investigations also provide data for seismic hazard assessment. Not only the dating of earthquake-related deformations, but also the precise measurement of deformation amount offers the chance of a precise projection of future earthquakes. At this point, the seismic source of the earthquake, the relationship of this sources with the archaeological site or structure, the soil characteristics of the relevant area, and inferencess about the intersity and magnitude of the earthquake provides very important data sources for future seismic hazard analyses. Data from the ancient cities such as Cibyra, Lagina and Hierapolis can be counted among the successful examples in this respect. Although approximately 150 years have passed since the production of the first simple archaeoseismological data in the world and in Türkiye, and about 30 years have passed since the beginning of the first modern archaeoseismological studies, it is seen that numerical data production in this branch of science is still in its infancy. It is clear that today's technologies (laser and spectral imaging techniques, shallow geophysical methods, archaeo-engineering/archaeo-architecture and absolute dating methods, to study the dynamic behavior of structures

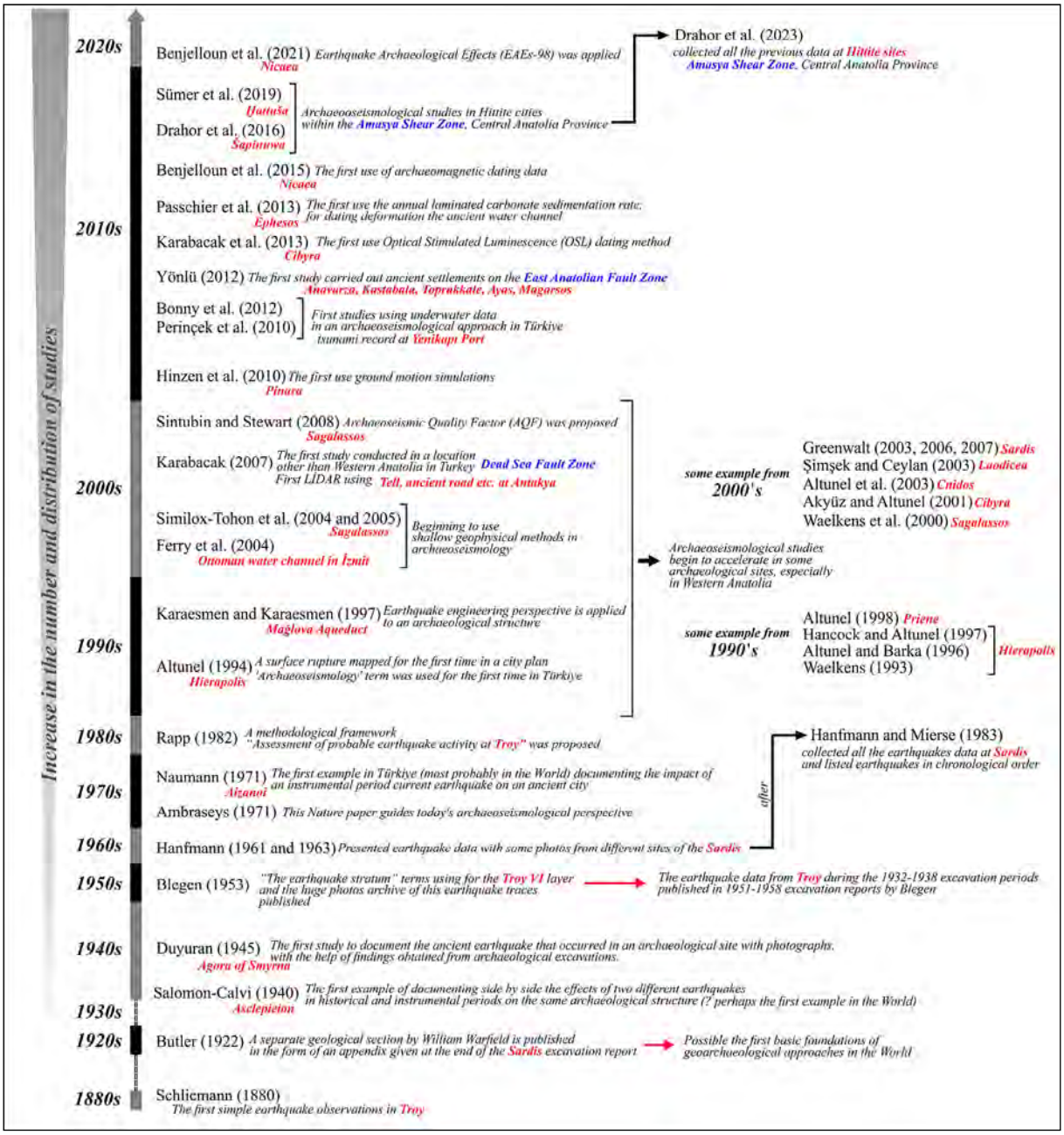

Figure 8- Chronological timeline of prominent and pioneering archaeoseismology studies carried out in Türkiye.

finite and discrete element models, engineering seismological methods, etc.) should be used more in an archaeoseismological perspective. The acceleration of scientific studies at this point seems possible by producing interdisciplinary collaborations and projects. On the other hand, one of the biggest obstacles in the development of archaeoseismology is the incorrect interpretation/incomprehension of the seismogravitational and/or seismotectonic deformation structures revealed during excavations and research in archaeological sites, and mostly restoration and deletion of traces. In this regard, it is necessary to work with experts in archaeoseismology during the systematic excavations in order not to miss these data and to evaluate and interpret them correctly. In the light of all the information summarized above, it is seen that archaeoseismology is a field that produces data sets both for active tectonic studies, archaeological research, earthquake engineering and earthquake risk analysis. Anatolia (formerly Asia

Minor) has a unique potential among the areas in the world where this discipline can be applied, due to its geological and archaeological location. However, the fact that this scientific discipline is currently little known by both geologists, archaeologists, and scientists specialized in archaeological architecture and engineering is the most important factor that reduces the number of trained scientists considerably. Along with this, the research and understanding of past earthquakes and their effects on society is of inestimble value both for our intellectual self and for the perception of the inevitable fact of living with earthquakes phenomenon. This situation seems that can only be reduced by raising society awareness and with practices within the framework implementing public measures.

The most important lesson learned about the integration of archaeoseismology into earthquake geology is that the advantages and disadvantages of this method for earthquake records do not conflict with other paleoseismological methods, on the contrary, they support and fill the gaps. When we look at the inventory created in this study, it is seen that archaeoseismological researches carried out in Türkiye are mostly concentrated in the Western Anatolian Extensional Province in tectonic terms and in Hellenistic - Roman cities, which include periods when historical period records were more productive. In this direction, earthquake data in archaeological sites, cities and civilizations in earlier periods (Neolithic, Bronze and Iron ages, etc.) should be investigated with modern archaeoseismological studies such as comprehensive study HERACLES (Hypothesis-Testing of Earthquake Ruined Argolid Constructions and Landscape with Engineering Seismology) project (Hinzen et al., 2018) related with Bronze age earthquakes performed at Greece main land and Crete. Especially to large-scale active fault zones in Anatolia (e.g. Archaeological sites close to NAFZ, EAFZ, DSFZ, ASZ, etc.) should be investigated more carefully at this point and archaeoseismological research should be increased in other important areas of the country. On the other hand, the Earthquake Archaeological Effects (EAE) classification, which we use in modern archaeoseismological studies today, has been mostly adapted to Hellenistic - Roman and later architectural structures. The application of similar classifications to civilizations such as Hittite and/or Urartu, which have monumental architectural stone structures that spread intensively in the Anatolian geography, especially in Central and Eastern Anatolia, stands out as a very important requirement in the archaeoseismological perspective.

Acknowledgements

We would like to thank to Assoc. Dr. Mustafa Avcıoğlu, Assoc. Dr. Barış Semiz, Dr. Asil Yaman, Prof. Dr. Ertuğ Öner, Prof. Dr. Murat Altuğ Erberik, Prof. Dr. Ayşegül Askan Gündoğan, head of Agora excavation Prof. Dr. Akın Ersoy, head of the Troy excavation Prof. Dr. Rüstem Aslan, head of excavation Ḫattuša Prof. Dr. Andreas Schachner, director of the Deutsches Archäologisches Institut (DAI) at İstanbul and director of the Pergamon excavation Prof. Dr. Felix Pirson and Prof. Dr. İlhan Kayan, who contributing directly or indirectly to the access of some resources while producing this publication. In addition, we also gratefully thank the excavation head of the Sardis Prof. Dr. Nick Chaill and the entire Sardis American Excavation Team for their access and support to the excavation archive. Finally, we are also indebted to thank Prof. Dr. Mahmut Göktuğ Drahor, who gave direction to archaeogeophysical studies in Türkiye and has scientific studies in almost all archaeological areas of the country, for his valuable contributions in the future approaches and suggestions section of the article. Finally, we would like to thank sincerely Prof. Dr. Klaus Hinzen, Prof. Dr. Manuel Sintubin and other anonymous reviewer whose valuable comments and useful criticisms have greatly improved the manuscript.

References

Akan, G. 2009. Rhodiapolis antik kenti ve dolayının jeoarkeolojisi ve depremselliği. Ms Thesis, Akdeniz University, 296, Antalya (unpublished).

Akan, G., Karaman, E., Köse, O. 2012. Traces of the historical earthquakes in the Rhodiapolis ancient city (Kumluca, Antalya). 65th Geological Congress of Turkey 2-6 April 2012, Ankara, 46-47.

Akyüz, S. H., Altunel, E. 2001. Geological and archaeological evidence for post–Roman earthquake surface

faulting at Cibyra, SW Turkey. Geodinamica Acta 14(1-3), 95-101.

Alexandris, A., Protopapa, E., Psycharis, I. 2004. Collapse mechanisms of masonry buildings derived by the distinct element method. In: Proceedings of the 13th world conference on earthquake engineering, vol. 59, 60.

Altınok, S., Karabacak, V., Yalçıner, C. Ç., Bilgen, A. N., Altunel, E., Kıyak, N. G. 2012. Kütahya Fay Zonu'nun Holosen aktivitesi. Türkiye Jeoloji Bülteni 55(1), 1-17.

Altunel, E. 1994. Active tectonics and the evolution of Quaternary travertines at Pamukkale, western Turkey. PhD Thesis, University of Bristol, 236, Bristol (unpublished).

Altunel, E. 1998. Evidence for damaging historical earthquakes at Priene, Western Turkey. Turkish Journal of Earth Sciences 7, 25-35.

Altunel, E. 2000. Büyük Menderes Grabeninde tarihsel depremlere ait yüzey kırıklarının belirlenmesi ve değerlendirilmesi. TÜBİTAK projesi No: YDABÇAG-372, Ocak 2000, 50.

Altunel, E., Barka, A. 1996. Hierapolis'teki arkeosismik hasarların değerlendirilmesi. Türkiye Jeoloji Bülteni 39(2), 65-74.

Altunel, E., Pınar, A. 2021. Tectonic implications of the Mw 6.8, 30 October 2020 Kuşadası Gulf earthquake in the frame of active faults of Western Turkey. Turkish Journal of Earth Sciences 30(4), 436-448.

Altunel, E., Barka, A., Akyüz, S. 2001. Gediz ve Küçük Menderes grabenlerindeki antik kentlerde tarihsel deprem hasarlarının araştırılması ve incelemesi. TÜBİTAK projesi No: YDABÇAG-199-Y098, Temmuz 2001, 41.

Altunel, E., Meghraoui, M., Karabacak, V., Akyüz, S. H., Ferry, M., Yalçıner, Ç., Munschy, M. 2009. Archaeological sites (tell and road) offset by the Dead Sea Fault in the Amik Basin, southern Turkey. Geophysical Journal International 179(3), 1313-1329.

Altunel, E., Stewart, I. S., Piccardi, L., Barka, A. A. 2003. Earthquake faulting at ancient Cnidus, SW Turkey. Turkish Journal of Earth Sciences 12, 137-151.

Ambraseys, N. N. 1971. Value of historical records of earthquakes. Nature 232(5310), 375-379.

Aydan, Ö., Kumsar, H. 2015. Assessment of the earthquake potential of the west Aegean region of Turkey based on seismicity, tectonics, crustal deformation and geo-archaeological evidence and its geotechnical aspects. Bulletin of Engineering Geology and the Environment 74, 1037-1055.

Bachmann, M., Radt, W., Schwarting, A. 2017. Die Stadtgrabung, Teil 5, Bau Z Architektur und Wanddekor. De Gruyter, 339.

Bachhuber, C., Roberts, R. G. 2009. Forces of transformation: the end of the Bronze Age in the Mediterranean. Oxbow Books, Oxford, 227.

Barış, Ş., Aydıngün, Ş., Kaya, H., Gazioğlu, C. 2021. Archeological Traces of Sixth Century Earthquakes in İstanbul Küçükçekmece Lake Basin (Bathonea) Excavations. International Journal of Environment and Geoinformatics 8(3), 386-396.

Bean, G. E. 1971. Turkey beyond the Maeander: an archaeological guide. Ernest Benn Limited, London, 267.

Benjelloun, Y. 2017. The middle strand of the North Anatolian fault in Iznik region: insights from geomorphology and archeoseismology. Phd Thesis, Université Grenoble Alpes, 303, Grenoble.

Benjelloun, Y., de Sigoyer, J., Carlut, J., Hubert-Ferrari, A., Dessales, H., Pamir, H., Karabacak, V. 2015. Characterization of building materials from the aqueduct of Antioch-on-the-Orontes (Turkey). Comptes Rendus Geoscience 347(4), 170-180.

Benjelloun, Y., De Sigoyer, J., Dessales, H., Garambois, S., Şahin, M. 2018. Construction history of the aqueduct of Nicaea (Iznik, NW Turkey) and its on-fault deformation viewed from archaeological and geophysical investigations. Journal of Archaeological Science: Reports 21, 389-400.

Benjelloun, Y., de Sigoyer, J., Dessales, H., Baillet, L., Guéguen, P., Sahin, M. 2021. Historical earthquake scenarios for the middle strand of the North Anatolian Fault deduced from archeo-damage inventory and building deformation modeling. Seismological Research Letters 92(1), 583-598.

Birinci, B. M. 2006. Hierapolis antik şehrinin arkeosismolojik açıdan incelenmesi. Ms. Thesis, Eskişehir Osmangazi University, 59, Eskişehir.

Blegen, C. W., Caskey, J. L., Rawson, M. 1951. Troy. The third, fourth, and fifth settlements. Volume II. Part 1: Text; Part 2: Plates. Princeton University Press, London, Part 1: 326p., Part 2: 315 plates.

Blegen, C. W., Caskey, J. L., Rawson, M. 1953. Troy. The sixth settlement. Volume III. Part 1: Text; Part 2: Plates. Princeton University Press, London, Part 1: 418p., Part 2: 512 plates.

Bony, G., Marriner, N., Morhange, C., Kaniewski, D., Perinçek, D. 2012. A high-energy deposit in the Byzantine harbour of Yenikapı, Istanbul (Turkey). Quaternary International 266, 117-130.

Bostock, J., Riley, H. T. 1855. The Natural History of Pliny. Translated, with copious notes and illustrations. Vol. I, cover (Books 1-5), Henry G. Bohn, London, 523.

Buchwald, H., McClanan, A. L. 2015. Churches EA and E at Sardis. Archaeological Exploration of Sardis Report 6. Harvard University Press, Cambridge, 341.

Butler, H. C. 1922. Sardis. Publications of the American Society for the excavations of Sardis. Vol. I, The Excavations, Part 1, 1910-1914. Late E. J. Brill Ltd, Leyden, 213.

Butler, H. C. 1925. Sardis. Publications of the American Society for the excavations of Sardis. Vol. II, Architecture, The Temple of Artemis, Part 1, Late E. J. Brill Ltd, Leyden, 146.

Cahill, N. 2016. Sardis 2014. 37. Kazı sonuçları toplantısı 3. cilt 11-15 Mayıs 2015, Erzurum, 147-164.

Cahill, N. 2019. Sardis, 2017. 40. Kazı sonuçları toplantısı 3. cilt 07-11 Mayıs 2018, Çanakkale, 97-116.

Caputo, R., Hinzen, K. G., Liberatore, D., Schreiber, S., Helly, B., Tziafalias, A. 2011. Quantitative archaeoseismological investigation of the Great Theatre of Larissa, Greece. Bulletin of Earthquake Engineering 9, 347-366.

Church A. J., Brodribb, W. J. 1906. Annals of Tacitus. Translated into English with notes and maps. Macmillan and Co., New York, 436.

Çetin-Yarıtaş, H. E. 2009. Termessos antik kenti ve dolayının jeolojisi arkeosismolojisi ve depremselliği. Ms Thesis, Akdeniz University, 112, Antalya.

D'Andria, F., Scardozzi, G., Spanò, A. 2008. Hierapolis di Frigia. II, Atlante di hierapolis di Frigia. Ege Yayınları, 156.

De Rossi, M. S. 1874. La antica basilica di S. Petronilla presso Roma testè discoperta crollata per terremoto. Bullettino Del Vulcanismo Italiano 1, 62-65.

Dinsmoor, W. B. 1941. An archaeological earthquake at Olympia. American Journal of Archaeology 45(3), 399-427.

Drahor, M. G. 2006. Integrated geophysical studies in the upper part of Sardis archaeological site, Turkey. Journal of Applied Geophysics 59(3), 205-223.

Drahor, M. G., Berge, A. M., Ongar, A., Ortan, A. 2016. Hitit başkenti Şapinuva'da arkeosismoloji çalışmaları. Aktif Tektonik Araştırma Grubu 20. Çalıştayı 13-15 Ekim 2016, Denizli, 21.

Drahor, M. G., Sümer, Ö., Ongar, A., Ortan, B., Berge, M. A., Süel, A., Ayyıldız, S. 2017. Şapinuva Arkeolojik Alanında 2017 Yılında Yapılan Arkeosismolojik Gözlemler. Aktif Tektonik Araştırma Grubu 21. Çalıştayı 26-28 Ekim 2017, Afyonkarahisar, 44.

Drahor, M. G., Sümer, Ö., Berge, M. A., Öztürk, C., Ongar, A., Süel, A., Schachner, A. 2023. Integrated Geoscience Investigations in Hittite Imperial Sites Affected by Earthquakes. El-Qady, G. M., Margottini, C. (Eds.). Sustainable Conservation of UNESCO and Other Heritage Sites Through Proactive Geosciences. Cham, Springer International Publishing. Springer, 463-499.

Dramis, F., Blumetti, A. M. 2005. Some considerations concerning seismic geomorphology and paleoseismology. Tectonophysics 408(1-4), 177-191.

Drews, R. 1993. The end of the Bronze Age: Changes in warfare and the catastrophe ca. 1200 B.C. Princeton University Press, New Jersey, 243.

Duyuran, R. 1945. İzmir'de Namazgâh'ta 1944 yılında yapılan kazıya ait kısa rapor. Belleten 9(35), 405-416.

Emre, Ö., Duman, T. Y., Özalp, S., Şaroğlu, F., Olgun, Ş., Elmacı, H., Çan, T. 2018. Active fault database of Turkey. Bulletin of Earthquake Engineering 16, 3229–3275.

Evans, A. 1922. New Discoveries at Knossos. The Antiquaries Journal 2(4), 319-329.

Evans, A. 1928. The Palace of Minos a comparative account of the successive stages of the early Cretan Civilization as illustrated by the discoveries at Knossos. Vol. 2, Part 1. Macmillan and Co., Lim. London, 390.

Ferrero, D. de B. 1997. Excavations and Restorations in Hierapolis During 1995. 18. Kazı sonuçları toplantısı 2. cilt 27-31 Mayıs 1996, Ankara, 85-99.

Ferry, M., Meghraoui, M., Girard, J. F., Rockwell, T. K., Kozaci, O., Akyuz, S., Barka, A. 2004. Ground-penetrating radar investigations along the North Anatolian fault near Izmit, Turkey: Constraints on the right-lateral movement and slip history. Geology 32(1), 85-88.

Freeman, C. 1996. Mısır, Yunan ve Roma Antik Akdeniz Uygarlıkları (Suat Kemal Angı çevirisi), Dost Kitapevi 2003, Anakara, 699.

Galadini, F., Hinzen, K. G., Stiros, S. 2006. Archaeoseismology: methodological issues and procedure. Journal of Seismology 10, 395-414.

Giner-Robles, J. L., Rodríguez-Pascua, M. A., Pérez-López, R., Silva, P. G., Bardají, T., Grützner, C., Reicherter, K. 2009. Structural analysis of earthquake archaeological effects (EAE): Baelo Claudia examples (Cádiz, South Spain). Field Training Course Notebook, 1st INQUA-IGCP-567 International Workshop on Earthquake

Archaeology and Palaeoseismology Vol. 2, Instituto Geológico y Minero de España.

Giner-Robles, J. L., Pérez-López, R., Silva-Barroso, P., Rodríguez-Pascua, M. Á., Bardají-Azcárate, T., Lario-Gómez, J., Garduño-Monroy, V. H. 2012. La arqueosismología como ciencia emergente. Seguridad y Medio Ambiente 128, 20-34.

Giner-Robles, J. L., Rodríguez-Pascua, M. A., Silva, P. G., Pérez-López, R. 2018. Efectos sísmicos en yacimientos arequeológicos: catalogación y cuantificación arqueosismológica. Boletín Geológico y Minero 129(1/2), 451-467.

Godley, A. D. 1928. Herodotus with an English translation. Vol. 2, cover (Books III - IV), William Heinemann, London, 415.

Godley, A. D. 1930. Herodotus with an English translation. Vol. 4, cover (Books VIII - IX), William Heinemann, London, 399.

Godley, A. D. 1938. Herodotus with an English translation. Vol. 3, cover (Books V - VII), William Heinemann, London, 569.

Greenewalt, C. H. 2003. Sardis: Archaeological research and conservation projects in 2001. 24. Kazı sonuçları toplantısı 2. cilt 27-31 Mayıs 2002, Ankara, 149-158.

Greenewalt, C. H. 2006. Sardis: Archaeological research and conservation projects in 2004. 27. Kazı sonuçları toplantısı 2. cilt 30 Mayıs-3 Haziran 2005, Antalya, 175-186.

Greenewalt, C. H. 2007. Sardis: Archaeological research and conservation projects in 2005. 28. Kazı sonuçları toplantısı 2. cilt 29 Mayıs-2 Haziran 2006, Çanakkale, 743-756.

Greenewalt, C. H., Ramage, A., Sullivan, D. G., Nayir, K., Tulga, A. 1983. The Sardis campaigns of 1979 and 1980. Bulletin of the American Schools of Oriental Research 249(1), 1-44.

Grünthal, G. 1998. European macroseismic scale 1998 (EMS-98). Centre Europèen de Géodynamique et de Séismologie, Musée National d'Histoire Naturelle, Section Astrophysique et Géophysique, Luxembourg, 99.

Hallmannsecker, M. 2020. The Ionian koinon and the koinon of the 13 cities at Sardis. Chiron 50, 1-27.

Hancock, P. L., Altunel, E. 1997. Faulted archaeological relics at Hierapolis (Pamukkale), Turkey. Journal of Geodynamics 24(1-4), 21-36.

Hancock, P. L., Chalmers, R. M. L., Altunel, E., Çakir, Z., Becher-Hancock, A. 2000. Creation and destruction of travertine monumental stone by earthquake faulting at Hierapolis, Turkey. Geological Society, London, Special Publications 171(1), 1-14.

Hanfmann, G. M. 1961. The Third Campaign at Sardis (1960). Bulletin of the American Schools of Oriental Research 162(1), 8-49.

Hanfmann, G. M. 1963. The fifth campaign at Sardis (1962). Bulletin of the American Schools of Oriental Research 170(1), 1-65.

Hanfmann, G. M., Mierse, W. E. 1983. Sardis from prehistoric to Roman times: Results of the Archaeological Exploration of Sardis 1958-1975. Harvard University Press, London, 466.

Hanfmann, G. M., Thomas, R. S. 1971. The Thirteenth Campaign at Sardis (1970). Bulletin of the American Schools of Oriental Research 203(1), 5-22.

Hinzen, K. G. 2005. The use of engineering seismological models to interpret archaeoseismological findings in Tolbiacum, Germany: a case study. Bulletin of the Seismological Society of America 95(2), 521-539.

Hinzen, K. G., Fleischer, C., Reamer, S. K., Schreiber, S., Schütte, S., Yerli, B. 2009. Quantitative methods in archaeoseismology. Archaeoseismology and Palaeoseismology in the Alpine-Himalayan Collisional Zone, 1st INQUA-IGCP-567 International Workshop on Earthquake Archaeology and Palaeoseismology 7-13 September 2009, Baelo Claudia (Cádiz, Spain), 50-51.

Hinzen, K. G., Schreiber, S., Yerli, B. 2010. The Lycian sarcophagus of Arttumpara, Pınara, Turkey: Testing seismogenic and anthropogenic damage scenarios. Bulletin of the Seismological Society of America 100(6), 3148-3164.

Hinzen, K. G., Schreiber, S., Rosellen, S. 2013*a*. A high resolution laser scanning model of the Roman theater in Pinara, Turkey–comparison to previous measurements and search for the causes of damage. Journal of Cultural Heritage 14(5), 424-430.

Hinzen, K. G., Kehmeier, H., Schreiber, S. 2013*b*. Quantitative archaeoseismological study of a Roman mausoleum in Pınara (Turkey) - testing seismogenic and rockfall damage scenarios. Bulletin of the Seismological Society of America, 103(2A), 1008-1021.

Hinzen, K. G., Schwellenbach, I., Schweppe, G., Marco, S. 2016. Quantifying earthquake effects on ancient arches, example: The Kalat Nimrod Fortress, Dead Sea fault zone. Seismological Research Letters 87(3), 751-764.

Hinzen, K. G., Maran, J., Hinojosa-Prieto, H., Damm-Meinhardt, U., Reamer, S. K., Tzislakis, J., Kemna, K., Schweppe, G., Fleischer, C., Demakopoulou, K. 2018. Reassessing the Mycenaean earthquake hypothesis: results of the HERACLES project from Tiryns and Midea, Greece. Bulletin of the Seismological Society of America 108(3A), 1046-1070.

Jones, H. L. 1917. The Geography of Strabo with an English translation. Vol. I. (cover Books I – II), William Heinemann, London, 531.

Jones, H. L. 1924. The Geography of Strabo with an English translation. Vol. III. (cover Books VI – VII), William Heinemann, London, 397.

Jones, H. L. 1927. The Geography of Strabo with an English translation. Vol. IV. (cover Books VIII – IX), William Heinemann, London, 465.

Jones, H. L. 1928. The Geography of Strabo with an English translation. Vol. V. (cover Books X – XII), William Heinemann, London, 529.

Jones, H. L. 1929. The Geography of Strabo with an English translation. Vol. VI. (cover Books XIII – XIV), William Heinemann, London, 397.

Jones, H. L. 1930. The Geography of Strabo with an English translation. Vol. VII. (cover Books XV – XVI), William Heinemann, London, 373.

Jones, W. H. S. 1933. Pausanias. Description of Greece, with an English translation. Vol. III. (cover Books VI – VIII), William Heinemann, London, 441.

Karabacak, V. 2007. Ölü deniz fay zonu kuzey kesiminin kuvanterner aktivitesi. PhD Thesis, Eskişehir Osmangazi University, 286, Eskişehir.

Karabacak, V. 2011. Geological, geomorphological and archaeoseismological observations along the Cibyra Fault and their implications for the regional tectonics of SW Turkey. Turkish Journal of Earth Sciences 20(4), 429-447.

Karabacak, V. 2016. Seismic damage in the Lagina sacred area on the Mugla Fault: a key point for the understanding of the obliquely situated faults of western Anatolia. Journal of Seismology 20, 277-289.

Karabacak, V., Altunel, E., Akyüz, S., Yönlü, Ö. 2007. Büyük Menderes Fay Zonu üzerinde normal faylanmaya bağlı özelliklerin "Yersel LİDAR" kullanılarak belirlenmesi. Türkiye Kuvaterner Sempozyumu (TURQUA) VI, 16-18 Mayıs 2007, İTÜ, İstanbul.

Karabacak, V., Yönlü, Ö., Dökü, E., Kıyak, N. G., Altunel, E., Özüdoğru, Ş., Yalçıner, Ç. C., Akyüz, H. S. 2013. Analyses of seismic deformation at the Kibyra Roman stadium, Southwest Turkey. Geoarchaeology 28(6), 531-543.

Karaesmen, E., Karaesmen, E. 1997. Arkeosismoloji ile ilgili bazı kavramların irdelenmesi. 4. Ulusal Deprem Mühendisleri Konferansı 17-19 Eylül 1997, 612-619.

Karcz, I., Kafri, U. 1978. Evaluation of supposed archaeoseismic damage in Israel. Journal of Archaeological Science 5(3), 237-253.

Karwiese, S. 1985. Das beben unter Gallien und Seine anhaltenden Folgen. Lebendige Altertumswissenschaft F. Zur Vol. Des 70, 126-131.

Koçyiğit, A. 2003. General neotectonic characteristics and seismicity of Central Anatolia. Turkish Association of Petroleum Geologist (TAPG) Bulletin Spec. Publ. 5, 1–26.

Kumsar, H., Aydan, Ö., Şimşek, C., D'Andria, F. 2016. Historical earthquakes that damaged Hierapolis and Laodikeia antique cities and their implications for earthquake potential of Denizli basin in western Turkey. Bulletin of Engineering Geology and the Environment 75, 519-536.

Kunze, E., Weber, H. 1948. The Olympian Stadium, the Echo Colonnade and an "Archaeological Earthquake". American Journal of Archaeology 52(4), 490-496.

Kürçer, A., Chatzipetros, A., Tutkun, S. Z., Pavlides, S., Özden, S., Syrides, G., Vouvalidis, K., Ulugergerli, E., Ateş, Ö. 2012. An assessment of the earthquakes of Ancient Troy, NW Anatolia, Turkey. Tectonics-Recent Advances. Sharkov, E. V. (Eds.), 171-200.

Lanciani, R. 1899. The destruction of ancient Rome: a sketch of the history of the monuments. The Macmillan Company. London, 279.

Lanciani, R. 1918. Segni di terremoti negli edifizi di Roma antica. Bullettino della Commissione Archeologica Comunale di Roma, 3-28.

Marinos P. G., Koukis G. C. 1988. The Engineering Geology Of Ancient Works, Monuments And Historical Sites: Volume 3, Part 4, Earthquakes, vibrations and other hazards in relation to the study and the protection of monuments and historical sites Preservation and protection: Proceedings of an international symposium organized by the Greek National Group of IAEG, Athens, 19-23 September 1988. Balkema. 1189-1329.

Michetti, A. M., Esposito, E., Guerrieri, L., Porfido, S., Serva, L., Tatevossian, R., Vittori, E., Audemard, F., Azuma, T., Clague, J., Comerci, V., Gurpinar, A., Mc Calpin, J., Mohammadioun, B., Morner, N. A., Ota Y., Roghozin, E. 2007. Environmental

seismic intensity scale-ESI 2007. In: Memorie Descrittive Carta Geologica d'Italia 74, Guerrieri L., Vittori E. (Eds.), Servizio Geologico d'Italia – Dipartimento Difesa del Suolo, APAT, Roma, 53.

Morris, I., Scheidel, W. 2009. The dynamics of ancient empires: State power from Assyria to Byzantium. Oxford University Press, New York, 381.

Naumann, R. 1971. Wirkungen eines Erdbebens an den antiken Bauten in Aezani. Archäologisches Anzeiger 86, 214-221.

Naumann, R., Kantar, S. 1950. Die Agora von Smyrna. Bericht über die in den Jahren 1932-1941 auf dem Friedhof Namazgâh zu İzmir von der Museumsleitung in Verbindung mit der Türkischen Geschichtskommission durchgeführten Ausgrabungen. Kleinasien und Byzanz, Walter de Gruyter & Co., Berlin, 69-114.

Negri, S., Leucci, G. 2006. Geophysical investigation of the temple of Apollo (Hierapolis, Turkey). Journal of Archaeological Science 33(11), 1505-1513.

Nur, A., Cline, E. H. 2000. Poseidon's Horses: Plate tectonics and earthquake storms in the Late Bronze Age Aegean and Eastern Mediterranean. Journal of Archaeological Science 27(1), 43-63.

Papastamatiou, D., Psycharis, I. 1996. Numerical simulation of the seismic response of megalithic monuments: preliminary investigations related to the Apollo temple at Vassai. In: Archaeoseismology, Stiros, S. C., Jones, R. E. (Eds.), Institute of Geology & Mineral Exploration and British School of Athens, Fitch Laboratory Occasional Paper 7, 225-236.

Passchier, C. W., Wiplinger, G., Güngör, T., Kessener, P., Sürmelihindi, G. 2013. Normal fault displacement dislocating a Roman aqueduct of Ephesus, western Turkey. Terra Nova 25(4), 292-297.

Pavlides, S., Caputo, R., Chatzipetros, A., Sboras, S., Koukouvelas, I., Michailidou, A., Papathanassiou, G., Valkaniotis, S., Zervopoulou, A., Basili, R., Tarabusi, G. 2014. Active faults of the broader Aegean region in the Greek database of seismogenic sources. The Gre.Da.S.S. Working Group, Spyros.

Perinçek, D. 2010. Yenikapı kazı alanının son 8000 yıllık jeoarkeolojisi ve doğal afetlerin jeolojik izleri (İstanbul-Türkiye). Maden Tetkik ve Arama Dergisi 141, 73-95.

Piccardi, L. 2007. The AD 60 Denizli basin earthquake and the apparition of Archangel Michael at Colossae (Aegean Turkey). Geological Society, London, Special Publications 273(1), 95-105.

Picón, C. A., Hemingway, S. 2016. Pergamon and the Hellenistic kingdoms of the ancient world. Metropolitan Museum of Art, New York, 346.

Pirson, F. 2017. Die Siedlungsgeschichte Pergamons–Überblick und kritische Revision. Istanbuler Mitteilungen 67, 43-127.

Rapp, G. 1982. Earthquakes in the Troad. Troy the Archaeological Geology Supplementary Monograph 4. Rapp, G. R., Gifford, J. A. (Eds.), 43-58.

Rapp, G. 1986. Assessing archaeological evidence for seismic catastrophies. Geoarchaeology: An International Journal 1(4), 365-379.

Richter, C. F. 1958. Elementary Seismology. W. H. Freeman and Company, London, 768.

Rodríguez-Pascua, M. A., Pérez-López, R., Giner-Robles, J. L., Silva, P. G., Garduño-Monroy, V. H., Reicherter, K. 2009. A comprehensive classification of Earthquake Archaeological Effects (EAE) for structural strain analysis in Archaeoseismology. Archaeoseismology and Palaeoseismology in the Alpine-Himalayan Collisional Zone, 1st INQUA-IGCP-567 International Workshop on Earthquake Archaeology and Palaeoseismology 7-13 September 2009, Baelo Claudia (Cádiz, Spain), 114-117.

Rodríguez-Pascua, M. A., Pérez-López, R., Giner-Robles, J. L., Silva, P. G., Garduño-Monroy, V. H., Reicherter, K. 2011. A comprehensive classification of Earthquake Archaeological Effects (EAE) in archaeoseismology: Application to ancient remains of Roman and Mesoamerican cultures. Quaternary International 242(1), 20-30.

Rodríguez-Pascua, M. A., Silva, P. G., Pérez-López, R., Giner-Robles, J. L., Martín-González, F., Perucha, M. A. 2013. Preliminary intensity correlation between macroseismic scales (ESI07 and EMS98) and Earthquake Archaeological Effects (EAEs). 4th International INQUA Meeting on Paleoseismology, Active Tectonics and Archeoseismology (PATA) 9-14 October 2013, Aachen, Germany, 221-224.

Sabin, P., van Wees, H., Whitby, M. 2007. The Cambridge History of Greek and Roman Warfare. Volume I: Greece, the Hellenistic World and the Rise of Rome. Cambridge University Press, Cambridge and New York, 602.

Salomon-Calvi, W. 1940. 21-22 Eylül 1939 tarihinde vukua gelen Dikili-Bergama Zelzelesi (grabî Anadolu). Türkiyedeki Zelzelelere Müteâllik Etüdler, Maden Tetkik ve Arama Enstitüsü (MTA) Yayınları, Seri B, No.5, 31-45.

Sangawa, A. 1988. Declaration of earthquake archaeology (の宣言 地震考古学). Journal of the Japanese Society for Scientific Studies on Cultural Property 16,19-26. (in Japanese)

Sangawa, A. 1993. Earthquake archaeology (地震考古学). Journal of Geography 107(7), 895-896. (in Japanese)

Schachner, A. 2019. Hattuša Efsanevi Hitit İmparatorluğu'nun İzinde. Homer Kitabevi, İstanbul, 290.

Schaeffer, C. F. A. 1948. Stratigraphie comparée et chronologie de l'Asie occidentale:(IIIe et IIe millénaires); Syrie, Palestine, Asie mineure, Chypre, Perse et Caucase, Oxford University Press, London, 653.

Schliemann, H. 1880. Ilios: The City and Country of the Trojans: the Results of Researches and Discoveries on the Site of Troy and Throughout the Troad in the Years 1871-72-73-78-79: Including an Autobiography of the Author. John Murray London, 800.

Schliemann, H. 1884. Troja: Results of the Latest Researches and Discoveries on the Site of Homer's Troy and in the Heroic Tumuli and Other Sites, made in the Year 1882 and a Narrative of a Journey in the Troad in 1881. Harper & Brothers, New York, 434.

Schreiber, S., Hinzen, K. G., Fleischer, C. 2009. An application of 3D laser scanning in archaeology and archaeoseismology: The Medieval cesspit in the archaeological zone Cologne, Germany. Archaeoseismology and Palaeoseismology in the Alpine-Himalayan Collisional Zone, 1st INQUA-IGCP-567 International Workshop on Earthquake Archaeology and Palaeoseismology 7-13 September 2009, Baelo Claudia (Cádiz, Spain), 136-138.

Schweppe, G., Hinzen, K. G., Reamer, S. K., Fischer, M., Marco, S. 2017. The ruin of the Roman Temple of Kedesh, Israel; example of a precariously balanced archaeological structure used as a seismoscope. Annals of Geophysics 60(4), 0444, 1-17.

Schweppe, G., Hinzen, K. G., Reamer, S. K., Marco, S. 2021. Reconstructing the slip velocities of the 1202 and 1759 CE earthquakes based on faulted archaeological structures at Tell Ateret, Dead Sea Fault. Journal of Seismology 25(4), 1021-1042.

Shepherd, W. R. 1923. Historical Atlas. 3rd edition. Henry Holt and Company, New York, 20 Reference Map of Asia Minor under the Greeks and Romans.

Sieberg, A. 1932. Erdbebengeographie. Handbuch der Geophysik IV(3), 688-1005.

Silva, P. G., Reicherter, K., Grützner, C., Bardají, T., Lario, J., Goy, J. L., Zozo, C., Becker-Heidmann, P. 2009. Surface and subsurface palaeoseismic records at the ancient Roman city of Baelo Claudia and the Bolonia Bay area, Cádiz (south Spain). Geological Society, London, Special Publications 316(1), 93-121.

Similox-Tohon, D., Vanneste, K., Sintubin, M., Muchez, P., Waelkens, M. 2004. Two-dimensional resistivity imaging: a tool in archaeoseismology. An example from ancient Sagalassos (Southwest Turkey). Archaeological Prospection 11(1), 1-18.

Similox-Tohon, D., Sintubin, M., Muchez, P., Vanhaverbeke, H., Verhaert, G., Waelkens, M. 2005. Identification of a historical morphogenic earthquake through trenching at ancient Sagalassos (SW Turkey). Journal of Geodynamics 40(2-3), 279-293.

Similox-Tohon, D., Sintubin, M., Muchez, P., Verhaert, G., Vanneste, K., Fernandez, M., Vandycke, S., Vanhaverbeke, H., Waelkens, M. 2006. The identification of an active fault by a multidisciplinary study at the archaeological site of Sagalassos (SW Turkey). Tectonophysics, 420(3-4), 371-387.

Sintubin, M., Stewart, I. S., Niemi, T., Altunel, E. 2009. Archaeoseismology: Past, present and future. Archaeoseismology and Palaeoseismology in the Alpine-Himalayan Collisional Zone, 1st INQUA-IGCP-567 International Workshop on Earthquake Archaeology and Palaeoseismology 7-13 September 2009, Baelo Claudia (Cádiz, Spain), 143-145.

Sintubin, M., Stewart, I. S. 2008. A logical methodology for archaeoseismology: A proof of concept at the archaeological site of Sagalassos, southwest Turkey. Bulletin of the Seismological Society of America 98(5), 2209-2230.

Sintubin, M., Muchez, P., Similox-Tohon, D., Verhaert, G., Paulissen, E., Waelkens, M. A. R. C. 2003. Seismic catastrophes at the ancient city of Sagalassos (SW Turkey) and their implications for seismotectonics in the Burdur–Isparta area. Geological Journal 38(3-4), 359-374.

Sintubin, M., Stewart, I., Niemi, N., Altunel, E. 2007. Earthquake Archaeology Archaeoseismology along the Alpine-Himalayan seismic zone. International Geoscience Programme (IGCP) project proposal 567.

Softa, M., Turan, M., Sözbilir, H. 2018. Jeolojik, Arkeolojik ve Arkeosismolojik Veriler Işığında Myra Antik Kenti'nde Tarihsel Depremlere Ait Deformasyon Verileri, GB Anadolu. Türkiye Jeoloji Bülteni 61(1), 51-74.

Söğüt, B. 2014. Stratonikeia. Turkey Through the Eyes of Classical Archaeologists, 10th Anniversary of Cooperation between Trnava University ant Turkish universities, Hrnčiarik, E. (Eds.),

Trnavská univerzita v Trnave, Filozoická Fakulta, Katedra klasickej archeológie Hornopotočná, Trnava, 27-37.

Sümer, Ö., Karagöz, O., Alak, A. 2018. Fay parametreleri ve deprem büyüklüğü arasındaki ilişkiler için yeni bir program: Faultstat. Afyon Kocatepe Üniversitesi Fen Ve Mühendislik Bilimleri Dergisi 18(3), 1089-1101.

Sümer, Ö., Drahor, M. G., Berge, M. A., Ongar, A., Schachner, A. 2019. Geoarchaeological and archaeoseismological observations in Ḫattuša: first evidence of earthquake traces from the Hittite Capital. Archäologischer Anzeiger 1, 90-96.

Sümer, Ö., Drahor, M. G., Berge, M. A., Ongar, A., Öztürk, C., Süel, A., Schachner, A., Ayyıldız, S., Gerçek, S., Aydın, M., Yağlıdere, m., Kaya, B. O. 2021. Hitit Kentlerinde Arkeosismolojik Gözlemler. XI. Uluslararası Hititoloji Kongresi 13-19 Aralık 2021, Çorum, 65.

Sümer, Ö., Drahor, M. G., Cahill, N., Gallart Marques, F. 2022. Archaeoseismology of Sardis. Aktif Tektonik Araştırma Grubu 25. Çalıştayı 1-2 Aralık 2022, İstanbul, 41-42.

Stewart, I. S., Hancock, P. L. 1994. Neotectonics. Hancock, P. L. (Ed.). Continental deformation. University of Bristol. UK, 370-409.

Stewart, I. S., Piccardi, L. 2017. Seismic faults and sacred sanctuaries in Aegean antiquity. Proceedings of the Geologists' Association 128(5-6), 711-721.

Stiros, S. C. 1988. Archaeology–A tool to study active tectonics. Eos 69(50), 1633-1639.

Stiros, S. C., Jones, R. E. 1996. Archaeoseismology. Institute of Geology & Mineral Exploration and British School of Athens, Fitch Laboratory Occasional Paper 7, 268.

Şengör, A.M.C., Görür, N., Şaroğlu, F. 1985. Strike-slip faulting and related basin formation in zones of tectonic escape: Türkiye as a case study. Strike-Slip deformation, basin formation, and sedimentation. Biddle, K. T., Christie-Blick, N. (Eds.). Society of Economic Paleontologists and Mineralogists, Tulsa, 227–264.

Şimşek, C., Ceylan, A. 2003. Laodikeia'da tespit edilen bir deprem ve Diocletianus'a ithaf edilen bir yazıt. Archivum Anatolicum 6(1), 147-163.

Tokmak, M. 2012. Earthquakes and ancient site selection in West Anatolia. PhD Thesis, Middle East Technical University, 157, Ankara.

Ünal, A. 1977. M. Ö. II. Binyıl Anadolu'sunda Doğal Âfetler. Belleten 41(163), 423-446.

Waelkens, M. 1993. Sagalassos. History and archaeology. Sagalassos I. First general report on the survey (1986–1989) and excavations (1990–1991), Acta Archaeologica Lovaniensia Monographiae 5, 37-82.

Waelkens, M., Mitchell, S., Owens, E. 1990. Sagalassos 1989. Anatolian studies 40, 185-198.

Waelkens, M., Sintubin, M., Muchez, P., Paulissen, E. 2000. Archaeological, geomorphological and geological evidence for a major earthquake at Sagalassos (SW Turkey) around the middle of the seventh century AD. Geological Society, London, Special Publications 171, 373-383.

Yalçıner, C. Ç. 2009. Investigation of buried objects with Ground Penetrating Radar: Application to archaeoseismology and palaeoseismology in the Buyuk Menderes Graben (Turkey). PhD Thesis, Eskişehir Osmangazi University, 156, Eskişehir.

Yerli, B., Schreiber, S., Hinzen, K., ten Veen, J., Sintubin, M. 2009. Testing the hypothesis of earthquake-related damage in structures in the Lycian ancient City of Pinara, SW Turkey. Archaeoseismology and Palaeoseismology in the Alpine-Himalayan Collisional Zone, 1st INQUA-IGCP-567 International Workshop on Earthquake Archaeology and Palaeoseismology 7-13 September 2009, Baelo Claudia (Cádiz, Spain), 173-176.

Yerli, B., ten Veen, J., Sintubin, M., Karabacak, V., Yalçıner, C. Ç., Altunel, E. 2010. Assessment of seismically induced damage using LIDAR: the ancient city of Pınara (SW Turkey) as a case study. Geological Society of America Special Paper 471, 157-170.

Yerli, B., ten Veen, J., Sintubin, M. 2011. Testing a logic tree approach for archaeoseismology to the ancient city of Pınara (SW Turkey). Quaternary International 242(1), 52-64.

Yönlü, Ö. 2012. Doğu Anadolu Fay Zonu'nun Gölbaşı (Adıyaman) ile Karataş (Adana) arasındaki kesiminin Geç Kuvaterner aktivitesi. PhD Thesis, Eskişehir Osmangazi University, 438, Eskişehir.

Yönlü, Ö., Altunel, E., Karabacak, V., Akyüz, S., Yalçıner, Ç. 2010. Offset archaeological relics in the western part of the Büyük Menderes graben (western Turkey) and their tectonic implications. Geological Society of America Special Papers 471, 269-279.

APPENDIX 1- Some parameters of important archaeoseismological studies carried out in Turkey. AD: Archaeological data (inscription and excavation), HEC: Historical Earthquake Catalogue, RC: Radiocarbon, L: Luminescence, C: Cosmogenic nuclide, U/Th: Uranium/Thorium series, GD: Geophysical data, PM: Paleomagnetism, GMD: Geological and morphological data, O: Other data types. No* indicates the chronological order of studies. Please follow the sites/regions from the location numbers in Table 1.

No*	Reference (s)	Tectonic Region / Related Fault or Fault Zones	Archaeological Site / Region / City	Archaeological Structure Period	Findings	Type of Work / Dating	Determined Earthquake (s)
1	Schliemann (1880 and 1884)	North Anatolian Fault Zone?, Aegean Sea ?	Troy, Çanakkale	Bronze ? / Roman?	Collapsed blocks in house wall and overturns in Corintic syenite columns	AD	pre-Hellenistic ? / Roman period
2	Butler (1922 ve 1925)	Middle part of Gediz-Alaşehir Graben System	Sardis, Manisa	Hellenistic	Restoration and strengthening traces at the Artemis Temple	AD	17 AD
3	Salomon-Calvi (1940)	Bergama Graben, Aegean Sea	Pergamon, Asklepieion, İzmir	Roman	He states that how ancient earthquake effected the Asklepieion systematically destroyed the temple pillars and how the pillars that were erected afterwards were not affected by the 1939 earthquake	AD,HEC	? / 1939
4	Duyuran (1945); Naumann and Kantar (1950)	İzmir Fault ?	Agora of Smyrna, İzmir	Early Byzantine ?	Earthquake findings in the trench around the Basilica in addition sloppy restorations with spolia pieces used for the reconstruction of the Agora	AD, HEC	153 AD ? / 178 AD
5	Blegen et al. (1951 and 1953)	North Anatolian Fault Zone?, Aegean Sea ?	Troy, Çanakkale	Bronze	Findings at Troy III, IVb, IVc, Vc and VI layers	AD	mid 13th century BC
6	Schaeffer (1948)	Eastern Mediterranean Basin	Predominantly Ugarit sites, for Anatolia Troy, Boğazköy (Ḫattuša), Alacahöyük and Tarsus	Mostly Bronze	In particular, it evaluates earthquake data within the chronology of Palestine, Syria, Persia, Caucasus, Cyprus, Aegean and Anatolian areas separately	AD	2100 – 2200 BC / 1365 BC 2 main earthquakes; 1610 – 1620 BC Hiatus ?
7	Hanfmann (1961); Hanfmann and Mierse (1983)	Middle part of Gediz-Alaşehir Graben System	Sardis, Manisa	Roman and Byzantine	Demonstrates a simple probabilistic earthquake chronology by identifying fires and deformational structures of different areas and periods at Sardis	AD	17 AD / 7th / 12th/ 16th or 17th centuries
8	Ambraseys (1971)	Eastern Mediterranean Basin	Western Anatolia, especially with 17 AD earthquake which was affecting the Gediz River and its surroundings, and Istanbul, A regional-scale study addressing the relationship between historical and instrumental period earthquakes			HEC	17 AD / Earthquakes affecting İstanbul
9	Bean (1971)	Büyük Menderes Graben System and its eastern termination	Tralleis, Hierapolis	Roman (Imperial)	Based only on historical records	HEC	27 BC ? – 14 AD Tralleİs 60 AD Hierapolis
10	Naumann (1971)	Emet – Gediz Fault Zone	Aizanoi, Kütahya	-	Overturned columns and damaged building walls	-	1970 Gediz Earthquake
11	Ünal (1977)	Hittite , Hatti and Ugarit regions ?	Ugarit, Šamuḫa (Kayalıpınar), Ninova	Late Hittite	Based on Hittite tablets and literature	AD	Hatti period ? / 1365 BC / 1290 BC
12	Rapp (1982 and 1986)	North Anatolian Fault Zone?, Edremit Fault Zone?	Troy, Çanakkale	Troy VI (~ BC 1800 -1300)	Various destructions in Troy VI layer	AD, HEC	1365 BC ?

APPENDIX 1- *continued*

13	Karwiese (1985)	Küçük Menderes Graben System, Aegean Sea, Ephesus Fault ?	Ephesus, İzmir	Roman	Deformations of the 2nd house at terrace houses and 6th and 7th settlements; Numismatic data belonging to the Gallienan period; the changes of buildings after the earthquake.	AD, HEC	3rd quarter of the 3rd century; 262 AD Aegean Sea earthquake?
14	Waelkens et al. (1990); Waelkens (1993)	Fethiye Burdur Fault Zone, its northeastern termination	Sagalassos, Burdur	Hellenistic – Roman	Restoration of the Temple of Apollo Clarios after a probable earthquake, Deformations in ? Roman Bath and ? Hellenistic aqueducts	AD	138-140 BC
15	Altunel (1994)	Eastern parts of the Gediz-Alaşehir and Büyük Menderes graben systems	Hierapolis, Denizli	Roman	Various deformations on archaeological structures along the active NW-SE line passing through the city, hot water outlets and travertines, etc.	AD, HEC, GMD	60 AD ?
16	Altunel and Barka (1996)	Hierapolis fracture zone		Roman and Byzantine	Damages in architectural structures of different periods	AD, HEC, GMD	60 AD and 1354 ?, 1702(1703) ?, 1717 ?
17	Ferrero (1997)	Gediz-Alaşehir and Büyük Menderes graben systems ?		Byzantine	Based on the abandonment of some Byzantine structures and Doric Building	AD	early 7th century ?
18	Hancock and Altunel (1997)	Hierapolis Fault Zone		Roman and Byzantine	Damages in architectural structures of different periods	AD, HEC, GMD	60 AD and 4th century ?; 7th century ? or 14th century ?
19	Altunel (1998)	Western part of the Büyük Menderes Graben System	Priene, Aydın	Hellenistic - Roman	Deformations at the Holy Hall, Street, Agora and Temple of Athena	AD, HEC, GMD	Earthquake(s) in the 12th century AD or after
20	Altunel (2000)	Büyük Menderes Graben System	Priene and Miletos, Aydın		Some deformations in Miletos and Priene	AD, HEC	~ 350 BC / 26-25 BC / 60 AD
21	Hancock et al. (2000)	Hierapolis Fault Zone	Hierapolis, Denizli	Roman and Byzantine	Damages in architectural structures of different periods	AD, HEC, GMD	excluding 60 AD, no specific earthquake is given
22	Waelkens et al. (2000)	The northeast end of the Fethiye Burdur Fault Zone, Kırkkavak Fault ?	Sagalassos, Burdur	Hellenistic - Byzantine	Mainly Neon Library floor, Theatre, upper Agora, and other architectural structures	AD, GD	Second half of the 1st century AD / mid 3rd century AD / first quarter 6th century AD / mid 7th century AD
23	Altunel et al. (2001)	Gediz and Küçük Menderes Graben systems	Ephesus, Sardis and Philadelphia	Mostly Roman	Deformations and various repairs some architectural structures for 3 ancient cities	AD, GD	17 AD / 4th century / 1595 / 1928 / 1969
24	Akyüz and Altunel (2001)	Burdur - Fethiye Fault Zone, Kibyra Fault Zone	Cibyra, Burdur	Roman - Byzantine	Damages at the Stadium and other architectural structures in the city	AD, HEC, GMD	417 AD
25	Altunel et al. (2003)	Datça Peninsula, Knidos Fault	Cnidos, Muğla	Hellenistic - Byzantine	Deformations in the architectural structures of different periods in the city, especially the Temple of Aphrodite and the Demeter Sanctuary	AD, HEC, GMD	Between 2nd - 3rd century BC / 459 AD
26	Greenewalt (2003; 2006; 2007)	Middle part of Gediz-Alaşehir Graben System	Sardis, Manisa	Roman - Byzantine	Traces of a possible surface faulting event that destroyed the structures in Field 55	AD	7th century AD or later
	Drahor (2006)				Using geophysical methods at Field 55	GD	
27	Sintubin et al. (2003)	The northeast end of the Fethiye Burdur Fault Zone, Isparta–Eğirdir Fault Zone ? / Ağlasun mountain front ?	Sagalassos, Burdur	Hellenistic - Byzantine	Damages in different architectural structures of the city	AD, GMD	early 6th century AD / mid 7th century AD

APPENDIX 1- *continued*

28	Şimşek and Ceylan (2003)	Eastern parts of the Gediz-Alaşehir and Büyük Menderes graben systems	Laodicea, Denizli	-	Emphasizes that many earthquakes affect the city based on historical and archaeological data	AD, HEC	27 BC / 47 AD / 60 AD / end of 3rd or beginning of 4th centuries AD / 494 AD
29	Ferry et al. (2004)	North Anatolian Fault Zone, İzmit Segment	Nicaea, İzmit	Ottoman water channel	Displacement data of a buried Ottoman water channel	AD, GD	After 1591 AD three (3) earthquakes
30	Similox-Tohon et al. (2004)	The northeast end of the Fethiye Burdur Fault Zone, Reactive active normal fault passing through Sagalassos	Sagalassos, Burdur	Hellenistic - Byzantine	Interpretations on six resistivity profiles	AD, GD, GMD	mid 7th century AD
31	Similox-Tohon et al. (2005)			Byzantine	Trench-based archaeoseismological data	AD, GMD Problematic U/Th	6th or 7th century AD
32	Birinci (2006)	Pamukkale Fault, Hierapolis Fault Zone	Hierapolis, Denizli	Roman and beyond	Geological observations on archaeological structures and travertine channels	AD, HEC, GMD	60 AD/ 494 AD / 7th century AD / 1354 AD
	Negri and Leucci (2006)	Hierapolis Fault Zone ?	Hierapolis, Denizli	Hellenistic - Roman	Active normal fault determined under the Temple of Apollo using geophysical methods	AD, GD	No specific earthquake is noted
33	Similox-Tohon et al. (2006)	The northeast end of the Fethiye Burdur Fault Zone ? Theater and Necropolis fault segments	Sagalassos, Burdur	Hellenistic - Byzantine	By using many techniques, then all data is combined going for an interpretation	AD, GMD, GD, O	~ 500 AD / mid or second half of the 7th century AD
34	Karabacak (2007)	Northern extension of the Dead Sea Fault Zone, Hacıpaşa and Karasu faults	Structures such as tells, ancient roads, castles, Antakya	Pre-Hittite, Hittite and Late Roman	Deformation analyses on the structures such as mounds, ancient roads, castles by using instrumental measurement techniques (geophysics and geodesics)	AD, GMD, GD, O, RC	526 AD / 859 AD / 1408 AD / 1822 AD / 1872 AD
35	Piccardi (2007)	Hierapolis Fault Zone	Hierapolis and Colossae, Denizli	Roman (Imperial)	Deformations on Nymphaeum, Plutonium , correlation of tectonic data with historical/mythological data	AD, HEC, GMD	60 AD
36	Sintubin and Stewart (2008)	The northeast end of the Fethiye Burdur Fault Zone	Sagalassos, Burdur	Hellenistic - Byzantine	By compiling the data of previous archaeoseismological studies in the city, they propose a new measurement method in practice entitled Archaeoseismic Quality Factor (AQF)		They note that the earthquake hypothesis in Sagalassos contains some weakness and uncertainty and needs to be re-evaluated
37	Akan (2009), Akan et al. (2012)	Rhodiapolis Fault ?	Rhodiapolis, Antalya	Hellenistic - Roman	Deformations in various archaeological structures	AD, GMD	141 AD / 7th century AD
38	Altunel et al. (2009)	Northern extension of the Dead Sea Fault Zone, Hacıpaşa Segment	Amik Plain, Antakya	Pre-Hittite, Hittite	Cut and offset by the fault; a mound settlement dating to ~ 5000 BC and an ancient road dating to ~ 2000 BC	AD, GMD, GD, O	1408 AD / 1872 AD
39	Çetin-Yarıtaş (2009)	Termessos Fault	Termessos, Antalya	Roman ?	Deformations in architectural structures; such as Theatre, bath, Corinthian Temple etc.	AD, GMD	?
40	Yalçıner (2009)	Büyük Menderes Graben System	Archaeological structures at the northern part of the graben	Roman - Ottoman	Offsets on Ramazan Paşa Bridge, Roman wall and road	GMD, GD	-
41	Perinçek et al. (2010)	North Anatolian Fault Zone	Yenikapı, İstanbul	Byzantine	Tsunami and shipwreck findings	AD, GMD, RC	557 AD
42	Hinzen et al. (2010)	Fethiye Burdur Fault Zone ?	Pinara, Muğla	Classical	Deformation analyses on the Arttumpara Sarcophagus	AD, O	?
43	Yerli et al. (2010)			Classical - Byzantine	Deformations on the Roman Theatre	AD, O	?

APPENDIX 1- *continued*

44	Yönlü et al. (2010)	Western part of the Büyük Menderes Graben System	Ramazanpaşa Bridge, Priene, Aydın	Hellenistic-Ottoman	Deformations on different architectural structures in the city and the Ottoman bridge	AD, GMD, O	1846 AD
45	Karabacak (2011)	Fethiye Burdur Fault Zone, Kibyra Segment	Cibyra, Burdur	Hellenistic - Roman - Byzantine	Deformations on mainly Stadium and Theatre, and minor other architectural structures	AD, GMD, HEC, GD, O	417 AD / after 7th century AD
46	Yerli et al. (2011)	Fethiye Burdur Fault Zone	Pinara, Muğla	Classical - Byzantine	They're testing the archaeological logic tree method set for the city, and reveal Archaeoseismic Quality Factor (AQF); They assumed low seismic hazard potential of the region needs serious reconsideration.		
47	Tokmak (2012)	Western Anatolia	Various ancient cities	The relations between active faults and seismicity with morphological, lithological and distance/density parameters in the locations where ancient cities were established are examined			
48	Yönlü (2012)	Southwest extension of the East Anatolian Fault Zone	Anavarza, Kastabala, Toprakkale, Ayas, Magarsos	Roman	Deformations in different architectural structures belonging to different archaeological periods	AD, GMD, GD, O, HEC, RC, L	?
49	Altınok et al. (2012)	Kütahya Fault Zone	Seyitömer Mound, Kütahya	Neolithic – Bronze	Seyitömer Mound and trench-based paleoseismological data	AD, GMD, O, L	~ 6000 BC / ~ 1800 BC
50	Bony et al. (2012)	North Anatolian Fault Zone	Yenikapı, İstanbul	Byzantine	Tsunami and shipwreck findings	AD, GMD, RC	557 AD
51	Kürçer et al. (2012)	Troy and Kumkale faults	Troy, Çanakkele	-	Trench-based paleoseismological data	RC	> 760 BC / 130 – 780 AD / 1000 AD – 1300 AD; 3 or 2 earthquakes
52	Hinzen et al. (2013a,b)	Fethiye Burdur Fault Zone ?	Pinara, Muğla	Roman	Deformations in the Roman theater and mausoleum	AD, O	Deformation analysis and numerical data of the event
53	Karabacak et al. (2013)	Fethiye Burdur Fault Zone	Cibyra, Burdur		Deformations in Stadium and other architectural structures	AD, GMD, L	10 – 11th century AD
54	Passchier et al. (2013)	Büyük Menderes Graben System, İçme Tepe Fault	South of Ephesus, Kusadası	Roman (Imperial)	Vertical offset exceeding 3 m in Roman water channels	AD and annual carbonate lamination	earthquake after the second half of the 2nd century AD, probable 178
55	Söğüt (2014)	Muğla and Yatağan faults ?	Stratonikeia, Muğla	Byzantine	Collapsed city street	AD	Street rebuilt during the between 4th-5th century AD
56	Aydan and Kumsar (2015)	Normal faults of Western Anatolia Province ?	Magnesia, Ephesus, Sardis, Smyrna	-	Deformations in different architectural structures in different cities	AD, HEC	17 AD / 10th century AD
57	Benjelloun et al. (2015)	Northern extension of the Dead Sea Fault Zone, Antakya-Samandağ corridor	Antioch water channels, Antakya	Roman	Deformation and restoration of ancient water channels	AD, RC, PM, O	?
58	Buchwald and McClanan (2015)	Middle part of Gediz-Alaşehir Graben System	Sardis, Manisa	Byzantine	They attributes the destruction of “Church E” to the earthquake and relates it to the 1595 earthquake in historical earthquake data	AD, HEC	1595 AD
59	Cahill (2016 ve 2019)			Roman	The monumental arched structure collapsed and hit the floor and left a trace	AD	?
					Deformations at Area 55		Probably the early 6th century AD
60	Kumsar et al. (2016)	Pamukkale Fault Zone and Laodikya Fault	Hierapolis and Laodicea, Denizli	Roman - Byzantine	NE and SW oriented collapsed walls and columns and channels affected by surface rupture	AD, HEC	early 7th century AD
61	Drahor et al. (2016 ve 2017)	Amasya Shear Zone ?	Šapinuwa, Çorum	Middle Hittite	Systematic deformations in probable Middle Hittite buildings	AD, GD, GMD	after 14th century BC earthquake(s) ?

APPENDIX 1- *continued*

62	Karabacak (2016)	Muğla Fault	Lagina sanctuary, Stratonikeia, Muğla	Roman – Early Byzantium	Deformations on Propylon, Sunaki Stoa, Temple and Chapel	AD, GMD, RC, L	just after the 4th century AD
63	Bachmann et al. (2017)	Western Anatolian and/or Aegean Sea faults?	Pergamon, Asklepieion, İzmir	Roman	Some destructions observed in Room 4 of Building Z at the Acropolis	AD	Probably 178 AD ?
	Pirson (2017)				Based on the many changes in the city and decline in settlement activities		
64	Benjelloun (2017)	Middle branch of the North Anatolian Fault Zone	Nicaea, İznik	Hellenistic -Byzantine	Combining and interpreting deformation elements in different architectural structures and different data in the study	AD, GMD, O, RC, C	AD: 3rd century / 13th century / after mid 15th century Dating: 527 – 787 AD / 858 – 1097 AD
65	Stewart and Piccardi (2017)	Aegean Region and Greece	Ephesus, Hierapolis, Delphi, Knidos etc.	Bronze - Byzantine	Various deformations in some architectural structures	AD, GMD	various earthquakes from the literature
66	Benjelloun et al. (2018)	Middle branch of the North Anatolian Fault Zone	Nicaea water channels, İznik	Roman - Modern	Interpretations based on the repairs in the buildings	AD, GMD, GD	1065 AD ?
67	Softa et al. (2018)	Kale and Kekova faults ?	Myra, Antalya	Classical - Byzantine	Deformations in architectural structures around the Harbour and Theatre	AD, GMD, HEC	141 AD ?/ 240 AD ? / 344 AD ?
68	Sümer et al. (2019)	Amasya Shear Zone ?	Ḫattuša, Çorum	Early Hittite	Traces of systematic deformation in the Great Temple	AD, GMD	after 16th century BC earthquake(s)
69	Hallmannsecker (2020)	Western Anatolia	Sardis, Manisa	Roman	Approach to the 17 AD earthquake on an inscription found in Sardis	AD	17 AD
70	Barış et al. (2021)	Northern branch of the North Anatolian Fault Zone	Bathonea, Küçükçekmece Lake, İstanbul	Late Roman – Early Byzantine	Deformations in Cistern and tunnels	AD, GD, HEC, O	6th century AD earthquakes
71	Altunel and Pınar (2021)	Aegean Sea, Kusadasi Bay, Ephesus Fault ?	Ephesus, İzmir	Roman ?	Possible deformations in the Terrace houses, the Celsus Library and the Domitian Temple	AD	-
72	Benjelloun et al. (2021)	Middle branch of the North Anatolian Fault Zone	Nicaea, İznik	Roman - Ottoman	Deformations in defence walls, towers, Yeşil Mosque and different architectural structures and dating the repairs; in addition, the damages are evaluated in the light of EAEs criteria	AD, GMD, O, RC	3 different earthquake probabilities before and after 1331 AD
73	Sümer et al. (2022)	Middle part of Gediz-Alaşehir Graben System	Sardis, Manisa	Roman - Byzantine	They make an approach by evaluating their own observations, data in the literature and the historical earthquake catalogues.	AD, HEC	17 AD / early 7th century AD ? / 1595 / 1771 / 1845 AD
74	Sümer et al. (2021), Drahor et al. (2023)	Amasya Shear Zone ? or North Anatolian Fault Zone ?	Ḫattuša and Šapinuwa, Çorum	Hittite	The deformations at the Ḫattuša and Šapinuwa; make a relative approach according to the age of the architectural structures in the cities	AD	after the 15th-14th centuries BC earthquake(s) ?

Bulletin of the Mineral Research and Exploration

http://bulletin.mta.gov.tr

Assessing groundwater quality in semi-arid conditions: a geographic information systems-integrated approach using water quality index

Rihab CHOUGAR[a, b], Fethi BAALI[a, b], Riheb HADJI[c, d*], Lassad GHRIEB[f], Amor HAMAD[a, b, e] and Younes HAMED[g]

[a] *Department of Earth and Univers Sciences, Faculty of Exact Sciences and Natural and Life Sciences, Echahid Larbi Tebessi University, Tebessa12002, Algeria*

[b] *Laboratory of Water and Environment; Faculty of Exact Sciences and Natural and Life Sciences, Echahid Larbi Tebessi University, Tebessa12002, Algeria*

[c] *Department of Earth Sciences, Institute of Architecture and Earth Sciences, Farhat Abbas University, Setif, Algeria*

[d] *Laboratory of Applied Research in Engineering Geology, Geotechnics, Water Sciences, and Environment, Farhat Abbas University, Setif, Algeria*

[e] *International Association of Water Resources in the Southern Mediterranean Basin, Tunisia*

[f] *Department of Earth and universe science, Life Sciences, Guelma University, Guelma 24000, Algeria*

[g] *Department of Earth Sciences, Faculty of Sciences of Gafsa, University of Gafsa, Tunisia*

Research Article

Keywords:
Freshwater Demands, Water Quality Index WQI, Aquifer, Hydrogeological Processes, Chemical Parameters.

ABSTRACT

Meeting freshwater demands in water-scarce regions is imperative, given challenges like hydric stress, urbanization, aridity, and population growth. This study focuses on the Tebessa aquifer system, a critical water source facing escalating demands. A primary objective is to identify actionable management strategies to improve groundwater quality dynamics in semi-arid regions. The methodology involves a comprehensive assessment of groundwater health using the Water Quality Index (WQI) approach. This method integrates diverse parameters influenced by intensive agricultural and industrial activities. Additionally, spatial relationship analysis, facilitated by Geographic Information System (GIS) technology, is employed to gain insights into complex hydrogeological processes. The multi-parameter strategy implemented results in water quality maps that highlight various ions, revealing spatial disparities and assigning quality priority classes from 'Good' to 'Poor' across the groundwater. The research, conducted in the semi-arid Tebessa-Morsott Plain, encompasses field and laboratory investigations to delineate hydrochemical traits, including alkalinity, salinity, and heightened ion concentrations. The results of the study contribute to scientific understanding by uncovering interrelationships and spatial intricacies, offering valuable insights for water resource governance. The effectiveness of the methodology, incorporating WQI and GIS, is demonstrated in the comprehensive evaluation of groundwater quality. Ultimately, this research provides a foundation for informed decision-making and sustainable management of groundwater resources in semi-arid regions.

Received Date: 24.08.2023
Accepted Date: 29.04.2024

Citation Info: Chougar, R., Baalı, F., Hadji, R., Ghrieb, L., Hamad, A., Hamed, Y. 2024. Assessing groundwater quality in semi-arid conditions: a geographic information systems-integrated approach using water quality index. Bulletin of the Mineral Research and Exploration 174, 129-143. https://doi.org/10.19111/bulletinofmre.1475323

**Corresponding author: Riheb HADJI, hadjirihab@yahoo.fr*

1. Introduction

Groundwater is a critical source of potable water, especially in semiarid regions where scarce and unpredictable precipitation necessitates heavy reliance on this resource. The resilience of groundwater reserves in these areas is vital for communities facing water scarcity. However, the sustained viability of this resource hinges on its quality, and ensuring its purity is imperative for public health. Contaminants, both natural and anthropogenic, can compromise suitability for consumption, necessitating a comprehensive understanding of groundwater quality for effective management strategies.

Rigorous investigations by researchers such as Drias and Toubal (2015), Kallel et al. (2018), Hamad et al. (2018*a, b*; 2021*a, b*), Elubid et al. (2019), Zeqiri et al. (2019), Nekkoub et al. (2020), Kerbati et al. (2020), Besser et al. (2021) and Brahmi et al. (2021) have highlighted water-related challenges in the study area and neighbouring regions, emphasizing issues of water availability, quality and sustainability.

Comprehensively assessing groundwater quality within the Tebessa aquifer system, a primary source for various needs, is essential. Challenges such as hydric stress, climatic aridity, rapid urbanization, and population growth have led to overexploitation and degradation of aquifer quality. This study focuses on factors contributing to groundwater quality decline to contribute to a deeper scientific understanding and develop sustainable solutions.

The Water Quality Index (WQI) method serves as a pivotal tool, offering a concise representation of overall water health by synthesizing diverse parameters. It enables policymakers, scientists, and resource managers to gauge water pollution extent, track trends, and allocate resources for remediation strategies, fostering a standardized framework for evaluating water quality.

Geographic Information Systems (GIS) technology, renowned for systematizing and analysing geographical data, emerges as a foundational instrument in hydrogeological modelling. Coupled with the WQI, GIS provides a dynamic framework for assimilating water quality parameters into comprehensive spatial analyses, aiding in effective resource management and policy formulation.

Research on water scarcity in the semi-arid region of North Africa, as evidenced by the works of Hamed et al. (2018, 2023), Bensoltane et al. (2021), Benmarce et al. (2021, 2023), and Ncibi et al. (2021, 2022), underscores the urgency and complexity of the addressing water scarcity issues. The study employs a multiparameter approach, including pH, Total Dissolved Solids (TDS), and crucial ions, synthesized and assimilated using GIS capabilities, resulting in meticulously constructed maps. These maps provide insights into spatial variations, culminating in a unified integrated map stratified into priority classes, representing a pragmatic depiction of groundwater quality across the studied region.

The overarching objective of this study is to comprehensively assess and enhance the understanding of groundwater quality in semiarid regions, particularly Tebessa. The primary aim is to evaluate groundwater quality, identify key influences, integrate spatial and analytical approaches, and formulate management strategies. The findings are expected to inform evidence-based policies and strategies to mitigate risks associated with water scarcity and preserve water resources critical for human well-being in environmentally sensitive areas.

2. Study Area

The geological context of North Africa forms an integral segment within the broader framework of African geology. This intricate geological setting holds paramount significance in unraveling the geological history and dynamics of the African continent (Rouabhia et al., 2004; Bagwan et al., 2023; Sankar et al., 2023; Orabi et al., 2023). In the border region between Algeria and Tunisia, all the collapse trenches intersect atlas structures of the Late Lutetian age. The extensional phase of the Miocene is evidenced by the formation of the Oulad Soukies, Foussana-Kasserine trenches, and the El Ma Labiod basin. The substrate of the Tebessa and Hammamet trenches is composed of a mosaic of horsts and grabens. Four successive stages have been identified during the development of the Tebessa trench: The

first stage occurred during the Lower Villafranchian (Upper Pliocene). The second stage occurred during the Upper Villafranchian. The third stage occurred at the end of the Middle Pleistocene. And the fourth stage occurred at the end of the Upper Pleistocene. The subsidence process is still ongoing, as evidenced by three seismic events in 1995. This is parallel to the uplifting of the graben margins, where the subsurface sank in the central part during the final collapse stage. This ongoing geodynamic activity sheds light on the complex tectonic evolution of the region.

The Tebessa-Morsott plain (35°24' to 35°35' N latitude and 7°50' to 8°10' E longitude) is situated in the northeastern region of Algeria at 28 km from the international border, and 230 km from the Mediterranean Sea. Spanning an area of 974.4 km², this basin stands as a host to significant aquifers that play a crucial role in the region (Figure 1). The region is marked by a semi-arid climate featuring hot and arid summers, contrasting with cold winters. The annual precipitation ranges from 200 mm to 350 mm, indicative of the region's arid nature. The summer temperatures can surge to 45°C.

The Tebessa-Morsott plain belongs to the Merdja subwatershed and is drained by the Oued Ksob stream. It boasts an elongated North-West to South-East orientation and encompasses a vast depression hemmed in by mountainous terrain. The altitudinal variation spans from 1712 meters to 700 meters, adhering to the geological structure of the North Auresian (Aures Nememcha) region within the Saharan Atlas.

Numerous researchers have diligently explored the geological context of the study region, as evidenced by the works of Mouici et al. (2017), Tamani et al. (2019), Boulemia et al. (2021), Zerzour et al. (2020; 2021), Taib et al. (2022; 2023), Mahleb et al. (2022), Chibani et al. (2022), Benyoucef et al. (2023) and Zighmi et al. (2023). The region is characterized by the Triassic diapirs of Jebel Jebissa, constituting the oldest geological outcrop in the Tebessa region. These formations consist of sandstone clay passing to gypsum limestone. A substantial Plio-Quaternary infill within the Tebessa Collapse Ditch substantiates the existence of a considerable groundwater reservoir in the region. It consists of sand, alluviums, and limestone pebbles. The Maastrichtian carbonate formations outcrop in the South-West and North-East edge of the basin, whereas the Turonian limestone appears in the East (Figure 2). These serve as important karstic reservoirs of the region. Because of their significant depth in the center of the basin, the potential of these reservoirs remains untapped within the plain.

3. Materials and Methods

3.1. Field and Laboratory Investigations

In February 2019, a comprehensive groundwater sampling campaign was executed across three distinct locations: Merdja, Bekkaria and Hammamet. This operation aimed to assess the hydrochemical characteristics of the sampled groundwater. The collected groundwater samples underwent an analysis to ascertain their chemical composition and properties.

Analytical scrutiny was conducted in the laboratory setting, employing standardized methodologies outlined by the American Public Health Association (APHA) in the year 1995. The range of eight key parameters was meticulously investigated in each groundwater sample. Calcium (Ca^{+2}), Mg^{+2}, bicarbonate (HCO_3^-), chloride (Cl^-), sulfate (SO_4^{-2}), potassium (K^+), sodium (Na^+), and major cations (Ca^{+2},Mg^{+2}, Na^+, and K^+) formed the focal points of the investigation. The determination of major cations (namely calcium, sodium, magnesium and potassium) was achieved via the utilization of the ICP-Mass spectrometer method. The quantification of bicarbonate (HCO_3) content involved a volumetric titration process employing hydrochloric acid (HCl) as the reagent. For the assessment of sulfate, a spectrophotometric turbidimetry method was employed, while chloride (Cl^-) content was quantified using a volumetric titration procedure involving silver nitrate ($AgNO_3$) and potassium dichromate ($K_2Cr_2O_7$). Moreover, bicarbonate (HCO_3) and carbonate (CO_3) concentrations were evaluated through Portamess analysis using titration with hydrochloric acid (HCl), alongside the utilization of phenolphthalein and methyl orange as indicator reagents (Selvam et al. 2013). This method yielded a dataset that improves our kind of the hydrochemical composition of the sampled groundwater across these locations.

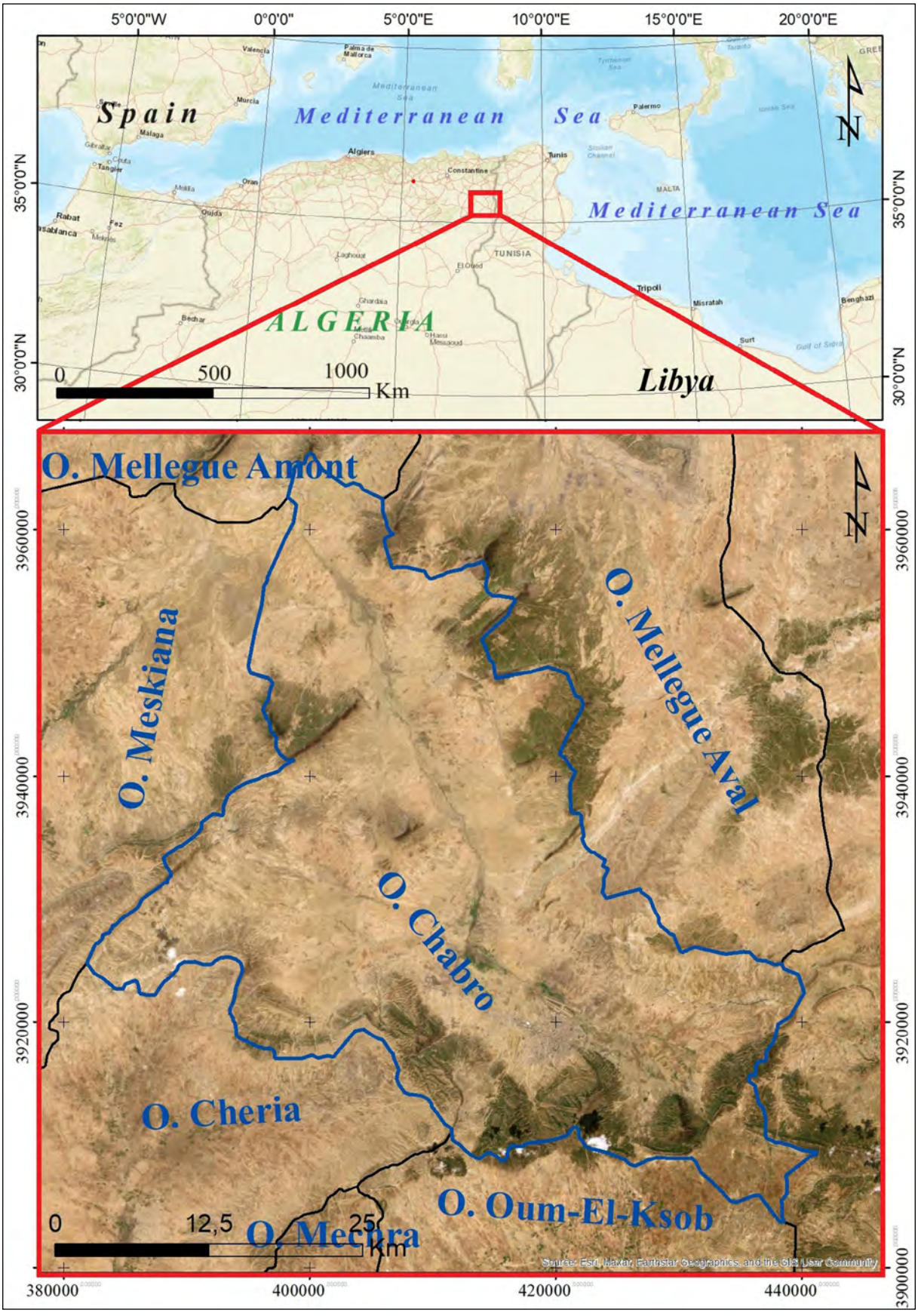

Figure 1- Geographic location of the study area.

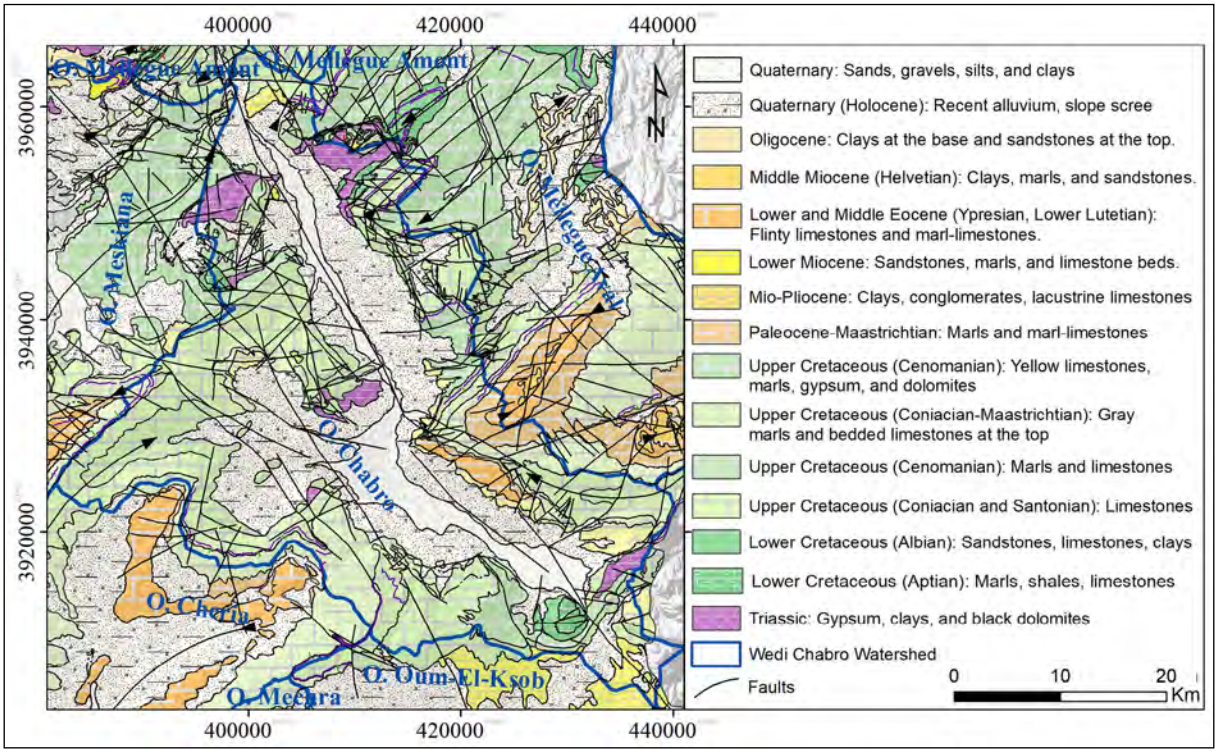

Figure 2- Simplified geological map of study area.

3.2. Geospatial Data Collection, Integration, and Interpolation

The accurate determination of sampling points, encompassing their precise latitude, longitude, and elevation coordinates, was achieved through the utilization of the GARMIN 12-Channel GPS device in the fieldwork. These geographical coordinates, once established, were combined with the groundwater parameters following preparation within the Excel-pro Program. This dataset was subsequently imported into a GIS platform, serving as the foundation for further analytical and digitization processes. The dataset, now in the form of point data, was integrated into the ArcGIS 10.8 software, where it constituted a distinct point layer. To facilitate advanced analyses and visualization, a geo-database was established. This facilitated the generation of spatial distribution maps that depicted the prevalence of selected water quality parameters across the studied region (Bairu et al., 2013). Spatial interpolation, a technique pivotal in environmental sciences, involves predicting values at unknown points based on known values at neighbouring points. Among the plethora of interpolation methods, two widely employed ones are Inverse Distance Weighting (IDW) and Ordinary Kriging (OrK). Both methods fundamentally rely on the concept of spatial autocorrelation, wherein samples that are spatially proximate tend to exhibit similar characteristics.

The implementation of IDW and OK necessitates the determination of observation quantities for predictions. In this context, the search window's scope should encompass these observations, thus encapsulating an area surrounding the point of prediction. The configuration of this search window is determined based on empirical knowledge pertaining to the phenomenon being investigated (Zarco-Perello and Simões, 2017). IDW method estimates data values for unknown locations by averaging the available values from sampled data points (Setianto and Triandini, 2013).

3.3. Calculation of WQI

To assess the water quality of the basin, the WQI is a valuable tool that summarizes multiple water parameters into a concise numerical representation. This index method is particularly aligned with the

guidelines for drinking water quality established by the World Health Organization (WHO). By converting an array of complex variables into a singular one- or two-digit number, the WQI simplifies the interpretation of extensive monitoring data. Water quality indices offer a streamlined means of monitoring and managing water quality. They serve as a convenient instrument for assessing trends in regional water quality and aiding decision-makers in evaluating the efficacy of specific interventions aimed at improving water quality (Li et al., 2019). The computation of the WQI involves four sequential steps. In the initial step, each of the nine water quality parameters is assigned a weight (W_i) based on its relative significance in determining the overall quality of water for drinking purposes. Notably, the assignment of weights was informed by their individual importance, parameters such as chloride, sulfate, and sodium were assigned a weight of 3, while calcium, magnesium, bicarbonate, and potassium were assigned a weight of 2 (Table 1).

The subsequent step involves the calculation of the relative weight (W_i) according to the Equation 1:

$$w_i = \frac{w_i}{\sum_{i=1} w_i} \quad (1)$$

Where "Wi" represents the relative weight, "wi" is the weight of each parameter, and "n" is the number of parameters.

Following this, a quality rating scale (qi) is assigned to each parameter (Equation 2). This scale is derived by dividing the concentration (Ci) of each chemical parameter in a water sample by its standard (Si) as outlined by WHO guidelines.

$$qi = (Ci / Si) \times 100 \quad (2)$$

Equation (2) captures this rating, with qi signifying the quality rating, Ci representing the concentration of each chemical parameter in milligrams per liter (mg/l), and Si denoting the WHO drinking water standard for each parameter according to WHO guidelines. The Sub-Index (SI) for each parameter (i) is subsequently computed using the (Equation 3):

$$SIi = Wi\ qi \quad (3)$$

The overall WQI is obtained by summing the individual SIi values (Equation 4):

$$WQI = \Sigma\ SIi \quad (4)$$

The calculated WQI values are generally categorized into five distinct classes: Excellent, good, poor, very poor, and unfit for drinking purposes (Table 2). This classification aids in communicating the quality of groundwater samples, thus supporting informed decision-making (Tiwari et al., 2014).

Table 2- Classification of WOI range and category of water.

WQI Range	Category of water
<50	Excellent water
50-100	Good water
100-200	Poor water
200-300	Very Poor water
>300	Unfit for drinking purpose

4. Discussions

The assessment of groundwater quality holds significant importance in environmental evaluation.

Table 1- Relative weight of chemical parameters.

Chemical parameters	WHO Standard	Weight(wi)	Relative weight(Wi)
Na^+	200	3	0.17
Ca^{2+}	75	2	0.12
K^+	12	2	0.12
Cl^-	250	3	0.17
SO_4^{-2}	250	3	0.17
HCO_3^-	120	2	0.12
Mg^{2+}	50	2	0.12
Total		Σwi = 17	ΣWi=0.99

Key statistics for 16 groundwater samples have been compiled through chemical analyses, as outlined in Table 3. Furthermore, the correlation matrix analysis, presented in Table 4, provides insights into the complex relationships among various groundwater quality parameters.

The analysis gives a comprehensive snapshot of key statistical parameters for water quality in groundwater samples, shedding light on the range, central tendency, and variability of various constituents. The maximum and minimum values highlight the broad spectrum of concentrations, indicating substantial variability in the groundwater composition. Mean values provide an average measure for each parameter, showcasing the typical concentration levels. Standard deviations quantify the dispersion around the mean, elucidating the consistency or variability in the dataset. Medians offer a central value, indicating the middle point in the ordered dataset and providing a robust measure of central tendency. Table 4, the correlation matrix, unveils the intricate relationships between groundwater quality parameters. Notably, the correlation coefficients signify the degree and direction of associations between different ions. The strong positive correlation between Ca^{+2} and Cl^{-} suggests a potential common source or geochemical processes linking these ions. Additionally, the correlations help identify potential influences or interactions, providing valuable insights for groundwater management and environmental assessment. These results contribute to a nuanced understanding of groundwater characteristics, aiding in the formulation of strategies for resource preservation and contamination prevention in the studied area.

In the study area the ions examined, namely HCO^{-3}, SO_4^{-2}, Cl^{-}, Ca^{+2}, Mg^{+2}, K^{+}, and Na^{+}, a noteworthy observation is the relatively low variability exhibited by their concentrations. Specifically, the bicarbonate content fluctuates between 173.24 and 341.16 mg/l, sulfate ranges from 57.60 to 500 mg/l, calcium ranges from 45.62 to 161 mg/l, potassium varying from 2.70 to 7.5 mg/l, sodium spanning 12.50 to 23.10 mg/l and magnesium varying between 17.01 and 61 mg/l. Of particular significance is the elevated concentration of chloride, demonstrating a wide variability from 37.99 to 291.3 mg/l. Examining the interrelationships between parameters. The chloride content is strongly correlated with magnesium (R= 0.62) and calcium (R = 0.61) These correlations can indeed indicate an increase in groundwater salinity underscore augmented groundwater salinity, such

Table 3-Normal statistics of water quality parameters of groundwater samples.

STATISTICS	K(mg/l)	Mg(mg/l)	Ca(mg/l)	Na(mg/l)	Cl(mg/l)	SO_4(mg/l)	HCO_3Meq/l
Maximum	7.5	61	161	23.10	291.3	500	341.16
Minimum	2.70	17.01	45.62	12.50	37.99	57.60	173.24
Average	5.23	37.31	94.27	17.88	147.06	294.70	261.94
Standarddeviation	1.47	14.29	28.70	3.03	76.89	125.15	55.24
Median	4.90	35.49	84.16	17.88	141.80	290	261.94

Table 4- Correlation matrix analysis result of the groundwater quality parameters.

Parameters	**Mg^{+2}**	**K^{+}**	**Ca^{+2}**	**Na^{+}**	**SO_4^{-2}**	**HCO_3^{-}**	**Cl^{-}**
Mg^{+2}	1						
K^{+}	-0.25	1					
Ca^{+2}	0.61	-0.36	1				
Na^{+}	-0.02	0.44	0.12	1			
SO_4^{-2}	-0.20	0.28	-0.13	0.05	1		
HCO_3^{-}	0.37	-0.48	0.28	-0.31	0.09	1	
CL^{-}	0.62	-0.21	0.59	-0.07	-0.46	0.02	1

findings provide valuable insights into the complex hydrochemical interactions at play within the Merdja aquifer region. By juxtaposing statistical analyses, correlation evaluations, and parameter concentrations, this study offers a comprehensive understanding of the groundwater quality dynamics within the investigated area. These insights contribute not only to the scientific understanding of the aquifer's hydrochemistry but also to the broader objectives of water resource management and environmental protection.

4.1. Spatial Variability Physicochemical Parameter

Calcium: Groundwater contains calcium due to the dissolution of carbonate formations surrounding the aquifer and it is also influenced by the presence of gypsum marl, dolomite minerals and evaporative deposits. The MCL for Ca^{+2} in drinking water is 75 mg/l. Observed Ca^{+2} concentrations range from 45.62 to 161 mg/l. The spatial distribution map portraying calcium concentrations has been formulated and is illustrated in Figure 3.

Sodium: It appears that sodium ions come from the leaching of Triassic gypsum formations near Djebissa. The gypsiferous marl forming the rock substrate of the aquifer generates these ions through ion exchange and evaporation processes. The MCL for Na+ in drinking water is set at 200 mg/l. The measured Na+ concentrations range from 12.5 to 23.10mg/l. A spatial map depicting the spatial variability of sodium concentrations is presented in Figure 3.

Potassium: The presence of potassium in groundwater is attributed to the use of fertilizers in nearby agricultural lands The MCL for K^+ in drinking water is defined as 12 mg/l. The observed K^+ concentrations range from 2.7 to 7.50 mg/l. A spatial map illustrating potassium concentration variations has been formulated and is exhibited in Figure 3.

Magnesium: The presence of magnesium due to the dissolution of dolomite limestones formations. The MCL for SO_4^{-2} in drinking water is set at 50 mg/l. The observed SO_4^{-2} concentrations span from 17.01 to 61 mg/l. A spatial map depicting the distribution of sulphate concentrations has been constructed and is presented in Figure 3.

Sulphate: the presence of sulphate it attributed to the dissolution of gypsum within gypsiferous marls and the leaching of evaporites and atmospheric deposition, industrial discharges. The MCL for SO_4^{-2} in drinking water is set at 250 mg/l. The observed SO_4^{-2} concentrations span from 57.6 to 500 mg/l. A spatial map depicting the distribution of sulphate concentrations has been constructed and is presented in Figure 3.

Chloride: Chloride content arises from the leaching of evaporites as well as sand, clay and gypsum deposits covering a significant basin area. Additionally, industrial activities contribute to chloride concentration. The MCL for Cl- in drinking water is established at 250 mg/l. The observed Cl^- concentrations range from 37.99 to 291.30 mg/l. A spatial map portraying the spatial distribution of chloride concentrations has been formulated and is displayed in Figure 3.

Bicarbonate: Bicarbonate is present due to the dissolution of carbonate formations that surround the aquifer. The MCL for HCO_3^- in drinking water is specified as 120 mg/l. Observed HCO_3^- concentrations span from 173.24 to 341.16 mg/l. A spatial map outlining the spatial distribution of bicarbonate concentrations has been developed in Figure 3.

4.2. Mapping Groundwater Quality Index

The generation of the groundwater quality map (Figure 4) entailed is based on the classification process framework outlined in Table 5, and executed using ArcGIS software.

The intricate spatial distribution of groundwater quality is a product of various interacting factors, including lithological characteristics, hydrodynamic behaviour of groundwater, prevailing climatic conditions, influx of wastewater, and potential sources of pollution.

Integral to this endeavour is the creation of a WQI map, a visual representation that encapsulates a comprehensive synthesis of water quality parameters. This is due to the Kriging geostatistical technique renowned for its ability to yield spatial interpolations of complex datasets. The WQI values were judiciously

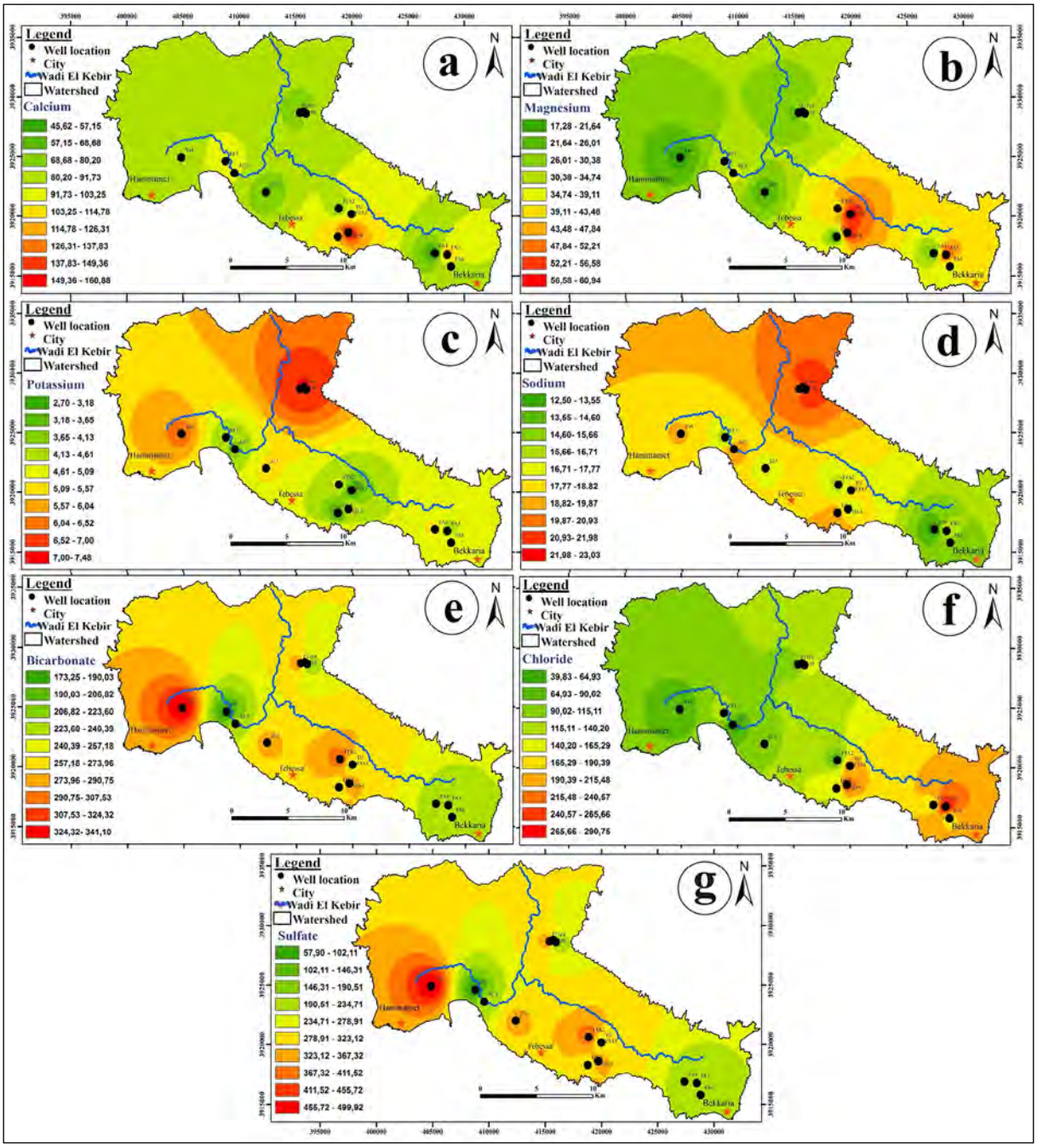

Figure 3- Spatial distribution of physiochemical parameters: a) Calcium (Ca^{+2}); b) Magnesium (Mg^{+2}); c) Potassium (K^{+}); d) Sodium (Na^{+}); e) Bicarbonate (HCO_3^{-}); f) Chlorite (Cl^{-}); g) Sulfate (SO_4^{-2}).

classified into four distinct ranges, namely excellent water (<50), good water (50-100), poor water (100-200), and very poor water (200-300).

The classification of the water in the study area is good except for well Q3-4 which is characterized by poor quality.

This insightful geospatial analysis accentuates the intricate interplay of myriad factors influencing groundwater quality distribution. Such revelations hold far-reaching implications, particularly in the realms of resource management and environmental safeguarding. The synergy of water quality indices, advanced geostatistical methodologies, and GIS tools

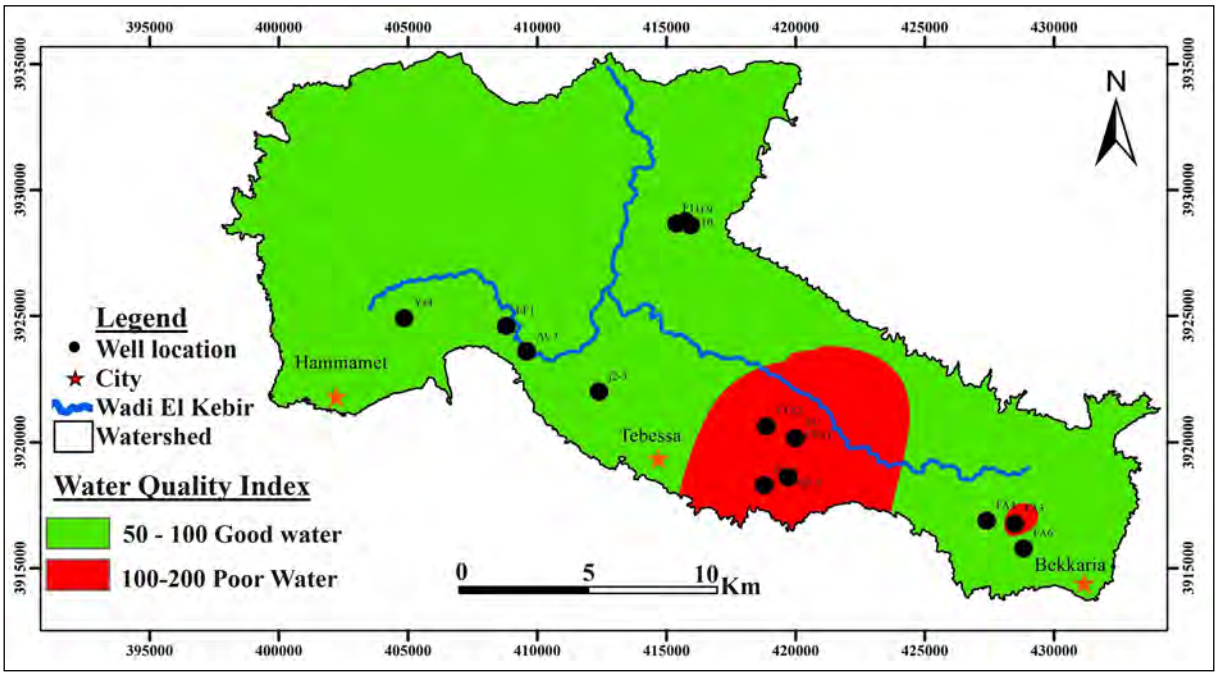

Figure 4- Spatial distribution map of water quality index in Merdja plain.

Table 5- Qi, SI_i, WQI and water classification of each groundwater samples of study area.

Sample	Na^+		Ca^{+2}		K^+		Mg^{+2}		Cl^-		SO_4^{-2}		HCO_3^-		WQI	Class
	Qi	SLi	Qi	SLi	Qi	SLi	Qi	SLi	Qi	SLi	Qi	SLi	Qi	SLi		
EF1	8.05	1.37	133.60	16.03	35.83	4.30	62.22	7.47	56.72	9.64	23.04	3.92	162.67	19.52	62.25	Good
j2-3	8.50	1.45	89.33	10.72	43.33	5.20	44.22	5.31	44.52	7.57	139.20	23.66	181.98	21.838	75.74	Good
AC3	10.00	1.70	122.83	14.74	32.50	3.90	72.90	8.75	18.12	3.08	84.48	14.36	223.67	26.84	73.37	Good
FA3	8.55	1.45	172.93	20.75	35.83	4.30	113.54	13.62	116.52	19.81	71.20	12.10	224.68	26.962	99.00	Good
FA4	6.25	1.06	60.83	7.30	44.17	5.30	46.24	5.55	66.40	11.29	90.80	15.44	204.35	24.522	70.46	Good
FA6	7.35	1.25	105.80	12.70	40.83	4.90	70.00	8.40	68.30	11.61	92.00	15.64	233.38	28.006	82.50	Good
FTA1	9.15	1.56	134.67	16.16	24.17	2.90	121.06	14.53	90.48	15.38	103.68	17.63	196.00	23.52	91.67	Good
FTA2	7.95	1.35	99.39	11.93	40.00	4.80	82.40	9.89	24.08	4.09	168.00	28.56	284.30	34.116	94.74	Good
T3	10.75	1.83	106.83	12.82	59.17	7.10	87.50	10.50	40.00	6.80	138.00	23.46	244.00	29.28	91.79	Good
TU	6.90	1.17	103.25	12.39	31.67	3.80	76.20	9.14	23.64	4.02	111.20	18.90	281.62	33.794	83.22	Good
Q3-4	8.35	1.42	214.67	25.76	40.83	4.90	122.00	14.64	102.00	17.34	138.40	23.53	264.17	31.7	119.29	Poor
Q5-6	9.90	1.68	149.33	17.92	22.50	2.70	36.00	4.32	55.20	9.38	116.00	19.72	274.17	32.9	88.63	Good
Ys4	9.45	1.61	112.21	13.47	52.50	6.30	40.08	4.81	28.36	4.82	200.00	34.00	144.37	17.324	82.33	Good
F10	11.55	1.96	100.47	12.06	62.50	7.50	70.98	8.52	59.96	10.19	120.00	20.40	172.83	20.74	81.37	Good
F9	10.95	1.86	114.36	13.72	55.00	6.60	67.10	8.05	73.99	12.58	27.95	4.75	170.83	20.5	68.07	Good
F11	9.45	1.61	101.53	12.18	57.50	6.90	34.02	4.08	15.20	2.58	180.00	30.60	163.43	19.612	77.57	Good
EF1	8.05	1.37	133.60	16.03	35.83	4.30	62.22	7.47	56.72	9.64	23.04	3.92	162.67	19.52	62.25	Good

culminate in a holistic understanding that guides strategic decision-making processes and contributes to the sustainable management of vital water resources.

5. Determination of chemical facies

5.1. Piper diagram

According to the ionic relationship between the hydrochemical parameters in the study area and their distribution by plotting the major cations and anions on the Piper trilinear diagram, it is observed that there are two dominant facies: Calcic sulphate and calcic chloride Due to the dissolution of carbonate formations and gypsum.

5.2. The origins of chemical elements

The calcium often originates from geological formations rich in minerals such carbonate and gypsum, these geological formations play a crucial role in the presence and availability of calcium in the environment the analysis of diagram shows that 5 out of 16 samples have a carbonate origin (Figures 5, 6, 7 and 8).

The presence of chloride and sodium is linked to the dissolution of triassic formations. The diagram indicates the existence of another source of sodium in the product when water interacts with clay minerals leading to the fixation of calcium ions after the release of tow sodium ions.

Salinity is associated with the dissolution of evaporate or carbonate formations and Base Exchange as suggested by the interpretation of previous diagram.

6. Results

The preservation of groundwater quality is pivotal for sustaining life in semiarid regions heavily reliant on this precious resource. This study underscores the intricate interplay of factors impacting groundwater quality within the Tebessa-Morsott plain of North-eastern Algeria. The aquifer's vulnerability to contamination, coupled with escalating demands, compels a comprehensive assessment to ensure its sustainability.

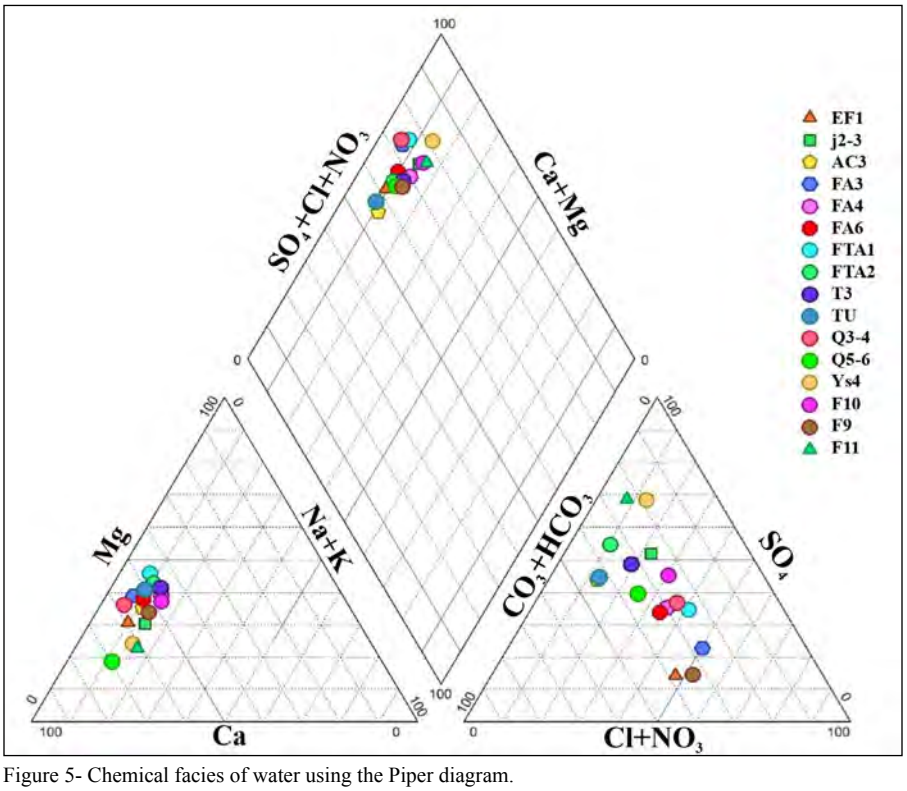

Figure 5- Chemical facies of water using the Piper diagram.

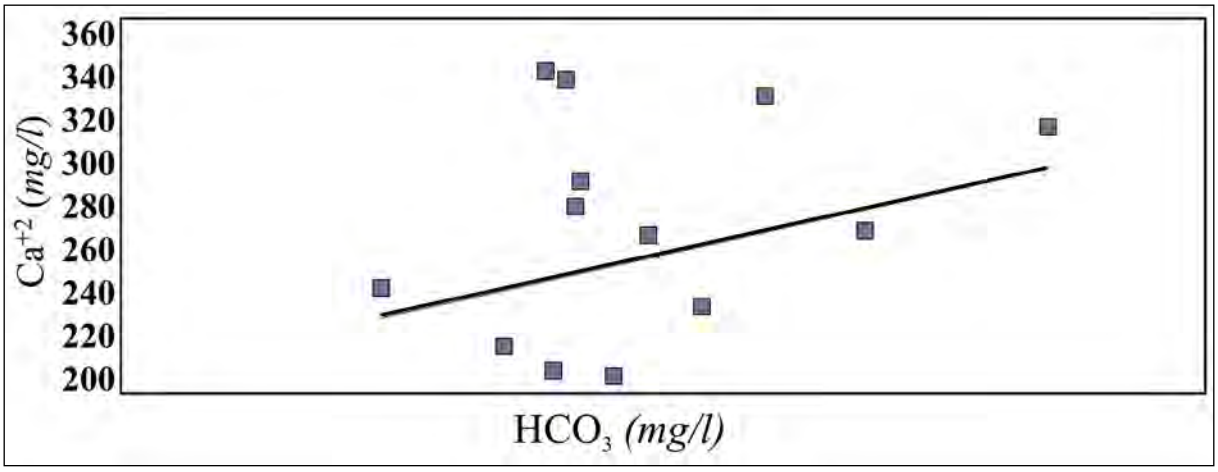

Figure 6- Ca^{+2} vs HCO_3^- in Merdja plain.

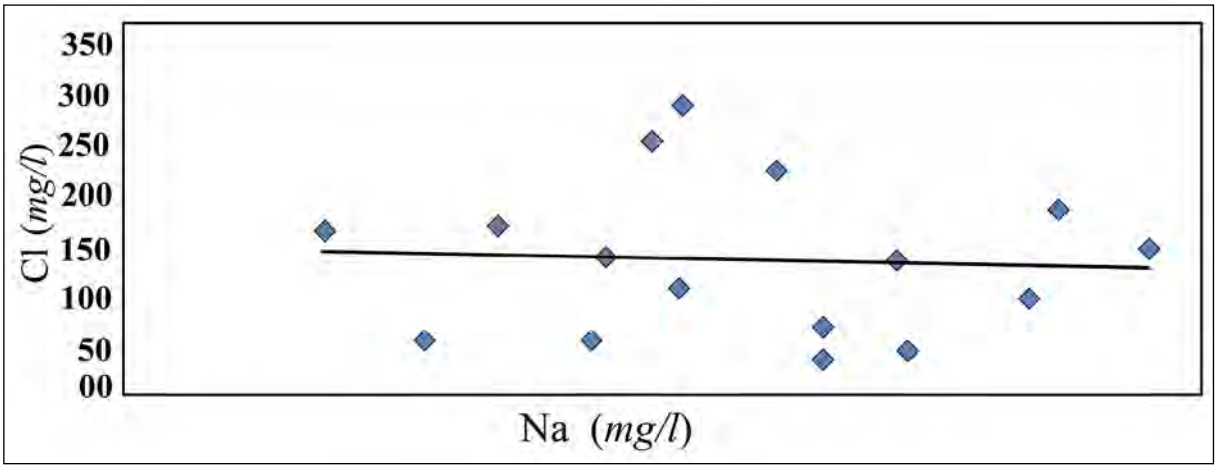

Figure 7- Cl^- vs Na^+ in Merdja plain.

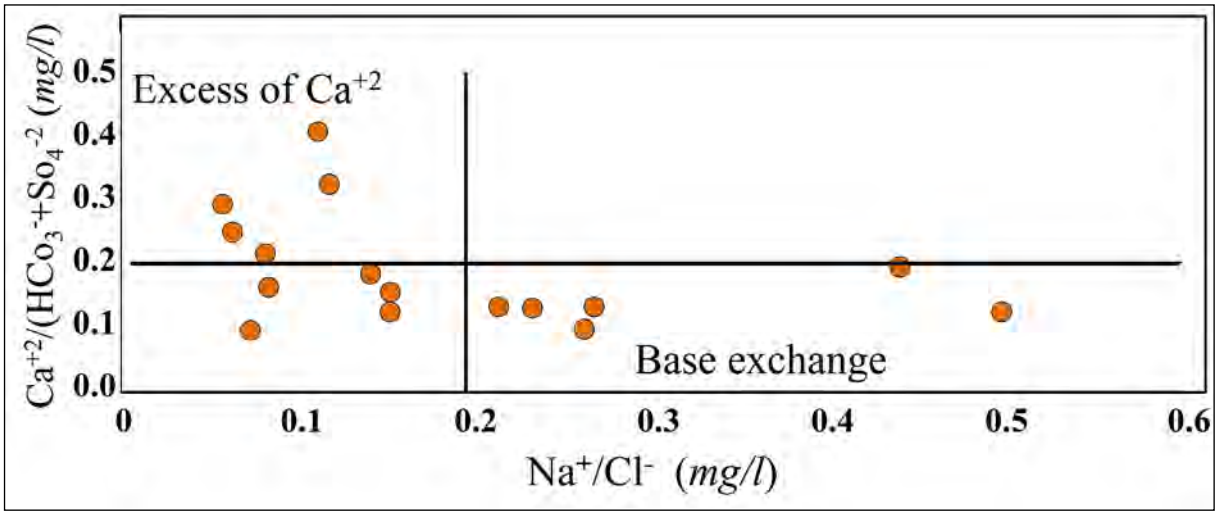

Figure 8- Base Exchange in the Merdja plain.

Groundwater quality is not only a product of natural processes but is also profoundly influenced by anthropogenic activities. Increased agricultural practices, accentuated by chemical pesticide use, contribute to the degradation of water quality. Complex interactions between the aquifer and surrounding soil, lithology, and climatic conditions further exacerbate the challenge. Understanding these dynamics is essential for crafting effective management strategies.

The WQI serves as a powerful tool for quantifying water quality. This method simplifies complex data into a single numerical value, allowing for easy interpretation and informed decision-making. Integrating GIS amplifies this approach, enabling spatial analyses that unveil trends and patterns, aiding resource management and policy formulation.

Results underscore the significance of calcium, sodium, potassium, sulphate, chloride, and bicarbonate concentrations in groundwater. Strong correlations reveal intricate relationships, shaping the hydrochemical landscape. By mapping these parameters, spatial nuances become apparent, guiding targeted interventions.

Crucially, the WQI map reflects the intricate web of influences on groundwater quality. Wells with excellent water quality (WQI <50) are identified, while those with poor and very poor quality signal intervention needs. This geospatial understanding supports resource allocation and decision-making processes.

The study's objective to enhance understanding aligns with sustainable management aspirations. Its findings inform policies, interventions, and strategies vital for navigating the challenges of water scarcity. By synergizing scientific rigor, geospatial analysis, and multidisciplinary insights, this study paves the way for safeguarding groundwater quality in semiarid regions, ensuring the continued availability of this invaluable resource for generations to come.

Addressing the multifaceted challenges of water scarcity and declining groundwater quality in semiarid regions necessitates a comprehensive approach. Integrated management strategies, involving collaboration between government agencies, local communities, and scientific institutions, should encompass regulatory measures to control pollution sources while promoting sustainable practices. A robust groundwater monitoring network is crucial for tracking water quality changes over time, fostering transparency and informed decision-making. Incorporating climate resilience strategies, education on sustainable water practices, economic incentives, and cross-border collaboration can enhance groundwater preservation efforts. Sustained research and innovation are vital to understanding complex interactions and developing effective solutions. Policy integration across sectors ensures holistic management, ensuring equitable and sustainable use of groundwater resources while considering environmental protection and land use. By embracing these recommendations, stakeholders can navigate the challenges posed by water scarcity and safeguard the availability of safe water for current and future generations.

Acknowledgments

This work was overseen by the IAWRSMB -Tunisia and the Laboratory of Applied Research in Engineering Geology, Geotechnics, Water Sciences, and Environment, Setif 1 University.

References

Bagwan, W. A., Gavali, R. S., Maity, A. 2023. Quantifying soil organic carbon (SOC) density and stock in the Urmodi River watershed of Maharashtra, India: Implications for sustainable land management. Journal of Umm Al-Qura University for Applied Sciences, 1-17.

Bairu, A., Tadesse, N., Amare, S. 2013. Use of geographic information system and water quality index to assess suitability of groundwater quality for drinking purposes in Hewane areas, Tigray, Northern Ethiopia. Ethiopian Journal of Environmental Studies and Management, 6 (2), 110-123.

Benmarce, K., Hadji, R., Zahri, F., Khanchoul, K., Chouabi, A., Zighmi, K., Hamed, Y. 2021. Hydrochemical and geothermometry characterization for a geothermal system in semiarid dry climate: The case study of Hamma spring (Northeast Algeria). Journal of African Earth Sciences, 182, 104285.

Benmarce, K., Hadji, R., Hamed, Y., Zahri, F., Zighmi, K., Hamad, A., Gentilucci M., Ncibi, K., Besser, H. 2023. Hydrogeological and water quality analysis

of thermal springs in the Guelma region of North-Eastern Algeria: A study using hydrochemical, statistical, and isotopic approaches. Journal of African Earth Sciences, 205, 105011.

Bensoltane, M. A., Zeghadnia, L., Hadji, R. 2021. Physicochemical Characterization of Drinking Water Quality of the Communal Water Distribution Network in Souk Ahras City/Algeria. Civil Engineering Research Journal, 12 (02).

Benyoucef, A. A., Gadri, L., Hadji, R., Slimane, H., Mebrouk, F., Hamed, Y. 2023. Empirical graphical and numerical model for the schematization of underground mining operations in the heterogeneous rock masses, case of Boukhadra mine, Algeria. Arabian Journal of Geosciences 16 (3), 165.

Besser, H., Dhaouadi, L., Hadji, R., Hamed, Y., Jemmali, H. 2021. Ecologic and economic perspectives for sustainable irrigated agriculture under arid climate conditions: An analysis based on environmental indicators for southern Tunisia. Journal of African Earth Sciences, 104134.

Boulemia, S., Hadji, R., Hamimed, M. 2021. Depositional environment of phosphorites in a semiarid climate region, case of El Kouif area (Algerian–Tunisian border). Carbonates and Evaporites, 36 (3), 1-15.

Brahmi, S., Baali, F., Hadji, R., Brahmi, S., Hamad, A., Rahal, O., Zerrouki, H., Saadali B., Hamed, Y. 2021. Assessment of groundwater and soil pollution by leachate using electrical resistivity and induced polarization imaging survey, case of Tebessa municipal landfill, NE Algeria. Arabian Journal of Geosciences, 14 (4), 1-13.

Chibani, A., Hadji, R., Hamed, Y. 2022. A combined field and automatic approach for lithological discrimination in semi-arid regions, the case of geological maps of bir later region and its vicinity, Nementcha mounts, Algeria. Geomatics, Landmanagement and Landscape (4), 7–26.

Drias, T., Toubal, A. C. 2015. Cartographie de la vulnérabilité a la pollution de la nappe alluviale de Tebessa-Morsott (bassin versant de l'Oued Ksob) extrême est algérien. LARHYSS Journal P-ISSN 1112-3680/E-ISSN 2521-9782, (22), 35-48.

Elubid, B., Huang, T., H. Ahmed, E., Zhao, J., M. Elhag, K., Abbass, W., Babiker, M. 2019. Geospatial distributions of groundwater quality in Gedaref state using geographic information system (GIS) and drinking water quality index (DWQI). International journal of environmental research and public health, 16 (5), 731.

Hamad, A., Baali, F., Hadji, R., Zerrouki, H., Besser, H., Mokadem, N., Legrioui R., Hamed, Y. 2018*a*. Hydrogeochemical characterization of water mineralization in Tebessa-Kasserine karst system (Tuniso-Algerian Transboundry basin). Euro-Mediterranean Journal for Environmental Integration, 3 (1), 7.

Hamad, A., Hadji, R., Bâali, F., Houda, B., Redhaounia, B., Zighmi, K., Legrioui, R., Brahmi S., Hamed, Y. 2018*b*. Conceptual model for karstic aquifers by combined analysis of GIS, chemical, thermal, and isotopic tools in Tuniso-Algerian transboundary basin. Arabian Journal of Geosciences, 11 (15), 409.

Hamad, A., Abdeslam, I., Fehdi, C., Badreddine, S., Mokadem, N., Legrioui, R., Hadji R. Hamed, Y. 2021*a*. Vulnerability characterization for multi-carbonate aquifer systems in semiarid climate, case of Algerian–Tunisian transboundary basin. International Journal of Energy and Water Resources, 1-14.

Hamad, A., Hadji, R., Boubaya, D., Brahmi, S., Baali, F., Legrioui, R., Abdeslam, I., Hidouri, B., Hamed, Y. 2021*b*. Integrating gravity data for structural investigation of the Youkous-Tebessa and Foussana-Talah transboundary basins (North Africa). Euro-Mediterranean Journal for Environmental Integration, 6 (2), 1-11.

Hamed, Y., Hadji, R., Redhaounia, B., Zighmi, K., Bâali, F., El Gayar, A. 2018. Climate impact on surface and groundwater in North Africa: A global synthesis of findings and recommendations. Euro-Mediterranean Journal for Environmental Integration, 3 (1), 25.

Hamed, Y., Hadji, R., Ahmadi, R., Ayadi, Y., Shuhab, K., Pulido-Bosch, A. 2023. Hydrogeological investigation of karst aquifers using an integrated geomorphological, geochemical, GIS, and remote sensing techniques (Southern Mediterranean Basin-Tunisia). Environment, Development and Sustainability, 1-33.

Kallel, A., Ksibi, M., Dhia, H. B., Khélifi, N. (Eds.). 2018. Recent advances in environmental science from the Euro-Mediterranean and surrounding regions: proceedings of Euro-Mediterranean Conference for Environmental Integration (EMCEI-1), Tunisia 2017. Springer International Publishing.

Kerbati, N. R., Gadri, L., Hadji, R., Hamad, A., Boukelloul, M. L. 2020. Graphical and Numerical Methods for Stability Analysis in Surrounding Rock of Underground Excavations, Example of Boukhadra Iron Mine NE Algeria. Geotechnical and Geological Engineering, 1-9.

Li, H., Smith, C. D., Wang, L., Li, Z., Xiong, C., Zhang, R. 2019. Combining spatial analysis and a drinking water quality index to evaluate monitoring data. International journal of environmental research and public health, 16 (3), 357.

Mahleb, A., Hadji, R., Zahri, F., Chibani, A., Hamed, Y. 2022. Water-Borne Erosion Estimation Using the Revised Universal Soil Loss Equation (RUSLE) Model Over a Semiarid Watershed: Case Study of Meskiana Catchment, Algerian-Tunisian Border. Geotechnical and Geological Engineering, 1-14.

Mouici R, Baali F, Hadji R, Boubaya D, Audra, P., Fehdi, C., Cailhol, D., Jaillet, S., Arfib, B. 2017. Geophysical, Geotechnical, and Speleologic assessment for karst-sinkhole collapse genesis in Cheria plateau (Algeria). Mining Science, 24, 59-71.

Ncibi, K., Hadji, R., Hajji, S., Besser, H., Hajlaoui, H., Hamad, A., Mokadem, N., Ben Saad, A., Hamdi, M., Hamed, Y. 2021. Spatial variation of groundwater vulnerability to nitrate pollution under excessive fertilization using index overlay method in central Tunisia (Sidi Bouzid basin). Irrigation and Drainage.

Ncibi, K., Mastrocicco, M., Colombani, N., Busico, G., Hadji, R., Hamed, Y., Shuhab, K. 2022. Differentiating Nitrate Origins and Fate in a Semi-Arid Basin (Tunisia) via Geostatistical Analyses and Groundwater Modelling. Water, 14 (24), 4124.

Nekkoub, A., Baali, F., Hadji, R., Hamed, Y. 2020. The EPIK multi-attribute method for intrinsic vulnerability assessment of karstic aquifer under semi-arid climatic conditions, case of Cheria Plateau, NE Algeria. Arabian Journal of Geosciences, 13 (15), 1-15.

Orabi, O. H., El-Sabbagh, A., Mansour, A. S., Ismail, H., Taha, S. 2023. Foraminifera study for the characterization of the Campanian/Maastrichtian boundary in Gebel Owaina, Nile Valley. Journal of Umm Al-Qura University for Applied Sciences, 1-19.

Rouabhia, A., Baali, F., Kherici, N., Djabri, L. 2004. Vulnérabilité et risque de pollution des eaux souterraines de la nappe des sables miocènes de la plaine d'El Ma El Abiod (Algérie). Science et changements planétaires/Sécheresse, 15 (4), 347-352.

Sankar, T. K., Ambade, B., Mahato, D. K., Kumar, A., Jangde, R. 2023. Anthropogenic fine aerosol and black carbon distribution over urban environment. Journal of Umm Al-Qura University for Applied Sciences, 1-10.

Selvam, S. I. J. D., Mala, R. I. J. D., Muthukakshmi, V. 2013. A hydrochemical analysis and evaluation of groundwater quality index in Thoothukudi district, Tamilnadu, South India. International Journal of Advanced Engineering Applications, 2 (3), 25-37.

Setianto, A., Triandini, T. 2013. Comparison of kriging and inverse distance weighted (IDW) interpolation methods in lineament extraction and analysis. Journal of Applied Geology, 5 (1).

Taib, H., Ben Abbas, Ch., Khiari, A., Hadji, R. 2022. Geomatics-based assessment of the Neotectonic landscape evolution along the Tebessa-Morsott-Youkous collapsed basin, Algeria, eomatics, Landmanagement and Landscape (3), 131–146.

Taib, H., Hadji, R., Hamed, Y., Bensalem, M. S., Amamria, S. 2023. Exploring neotectonic activity in a semiarid basin: A case study of the Ain Zerga watershed. Journal of Umm Al-Qura University for Applied Sciences, 1-14.

Tamani, F., Hadji, R., Hamad, A., Hamed, Y. 2019. Integrating Remotely Sensed and GIS Data for the Detailed Geological Mapping in Semi-Arid Regions: Case of Youks les Bains Area, Tebessa Province, NE Algeria. Geotechnical and Geological Engineering, 1-11.

Tiwari, A. K., Singh, P. K., Mahato, M. K. 2014. GIS-based evaluation of water quality index of ground water resources in West Bokaro Coalfield, India. Current world environment, 9 (3), 843.

Zarco-Perello, S., Simões, N. 2017. Ordinary kriging vs inverse distance weighting: Spatial interpolation of the sessile community of Madagascar reef, Gulf of Mexico. Peer J, 5, e4078.

Zeqiri, R. R., Riheb, H., Karim, Z., Younes, G., Mania, B., Aniss, M. 2019. Analysis of safety factor of security plates in the mine" Trepça" Stantërg. Mining Science, 26, 21.

Zerzour, O., Gadri, L., Hadji, R., Mebrouk, F., Hamed, Y. 2020. Semi-variograms and kriging techniques in iron ore reserve categorization: Application at Jebel Wenza deposit. Arabian Journal of Geosciences, 13 (16), 1-10.

Zerzour, O., Gadri, L., Hadji, R., Mebrouk, F., Hamed, Y. 2021. Geostatistics-Based Method for Irregular Mineral Resource Estimation, in Ouenza Iron Mine, Northeastern Algeria. Geotechnical and Geological Engineering, 1-10.

Zighmi, K., Zahri, F., Hadji, R., Benmarce, K., Hamed, Y. 2023. Polymetallic mineralization hosted in the Neogene sedimentary strata of the Algerian Tellian Range: A comprehensive overview. Mining of Mineral Deposits, 17 (2), 20-27.

Bulletin of the Mineral Research and Exploration

http://bulletin.mta.gov.tr

Economic heavy minerals in the stream sediments of wadi Shaàb, southern coast of the Red Sea, Egypt; characterization and upgrading for investigation of their potential recovery

Mona FAWZY[a*], Mostafa BAYOUMI[a], Hassan SHAHIN[a], Bahaa EMAD[a], Abdel Hay EL SHAFEY[a], Marwa ABDEL-AZEEM[a], Ahmed ISMAIL[a], Asmaa EL-MOGHAZY[b] and Mohamed DIAB[a]

[a] *Nuclear Materials Authority, P. O. Box 530, Maadi, Cairo, Egypt*

[b] *Geology Department, Faculty of Science, Helwan University, Ain Helwan, 11795, Cairo, Egypt*

Research Article

Keywords:
Heavy Minerals, Red Sea Coast, Gravity Concentration, Magnetic Separation, Potential Recovery, Material Balance.

ABSTRACT

The southern coast of the Red Sea is one of the most promising areas for the occurrence of economic minerals. Therefore, studying the characterization and evaluation of these minerals in the Wadi Shaàb Quaternary sediments and investigating their ability to concentrate and physically separate using economical and ecofriendly techniques is the main goal of this work. The results showed that the representative sample contains an average of 0.06% ilmenite, 0.08% zircon, 0.07% rutile, 0.07% leucoxene, 0.008% cassiterite, 0.004% xenotime, 0.0004% monazite, 0.022% almandine garnet, and 0.46% magnetite. The recovery of economic heavy minerals was applied using a combination of wet-gravity technique via shaking table and magnetic separation using high intensity magnetic separator. The results demonstrated the success of gravity separation in raising the grade from 7.63% to 45.03% in a yield of 13.74% out of the original sample, and also valuable metallurgical recoveries that higher than 89% for tabling multi-stages (rougher and scavenging) was obtained. Concentrated mineral fractions of magnetite, ilmenite, almandine, heavy silicates, and the non-magnetic fraction bearing zircon and rutile were obtained using a high intensity magnetic separator at different ampere range.

Received Date: 06.10.2023
Accepted Date: 24.04.2024

1. Introduction

Zircon, ilmenite, rutile, and garnet are economic heavy minerals used as raw materials for nuclear energy production and also in the manufacture of metallurgical and engineering industrial products (Grosz and Schruben, 1994; Fawzy et al., 2022*a*), in addition to that, monazite and xenotime contain critical metals such as rare earth elements (REE) that have high-tech applications.

Normally, processing of heavy mineral sands does not require crushing and grinding operations, which reduces cost and saves energy (Jordens et al., 2013). Most mineral beneficiation techniques for sand raw material begin with gravity separation by exploiting the density differences between heavy and their associated light minerals, which consist mainly of quartz and feldspar (Moscoso-Pinto and Kim, 2021; Fawzy, et al., 2022*b*; Diab, et al., 2022). After gravity separation, highly magnetic minerals (ferromagnetic as magnetite) can be separated from the obtained heavy minerals using low intensity magnetic separator (LIMS) and also paramagnetic minerals can be separated from diamagnetic minerals via high intensity

Citation Info: Fawzy, M. M., Bayoumi, M. B., Shahin, H., A., Emad, B., M., Abdel-Azeem, M. M., Ismail, A. M., El-Moghazy, A. F., Diab, M. 2024. Economic heavy minerals in the stream sediments of wadi Shaàb, southern coast of the Red Sea, Egypt; characterization and upgrading for investigation of their potential recovery. Bulletin of the Mineral Research and Exploration 174, 145-165. https://doi.org/10.19111/bulletinofmre.1472786

**Corresponding author: Mona FAWZY, mm1_fawzy@yahoo.com*

magnetic separator (HIMS), electrostatic or flotation separation techniques can be also implemented depending on the properties of each mineral to be separated (Rejith, and Sundararajan, 2018; Fawzy, 2018; 2021*a*; *b*). Regarding magnetic separation, the mining industry is currently using this process for ore processing, material screening and mineral purification (Iranmanesh, and Hulliger, 2017). Therefore, it is essential to decide on the mineral processing that can recover the valuable heavy minerals (VHMs) with a fast and efficient processing rate. This research focuses on the efficient recovery of the economic heavy minerals in the stream sediments of the Wadi Shaàb area. Among their valuable minerals, we can find hematite, magnetite, ilmenite, leucoxene, xenotime, monazite, rutile, cassiterite, and zircon. To achieve the heavy mineral recovery, this study considered two sequential mineral beneficiation processes: Magnetic separation after gravity concentration techniques via variable magnetic field strengths to optimize the recovery and final grade of each VHMs.

2. Geological Setting and Sampling

The Wadi Shaàb area is located at the southeastern corner of Egypt about 30 km south Shalateen city between latitudes of 22° 33′ and 22° 55′ N, and longitudes of 35° 21′ and 36° 00′ E (Figure 1). The geomorphological units that were recorded in the study area are: high mountains, isolated hills, piedmont plain, alluvial fans, coastal plain and hydrographic basins (Yousef, et al., 2009). The high mountains of Wadi Shaàb area are composed mostly of ophiolitic rocks, metasediments, metavolcanics and related volcanoclastic, tonalite-granodiorite as well as biotite-muscovite granite. The piedmont plain and alluvial fans consist mainly of coarse sand, gravel, and pebbles which changed eastward to become fine to medium sand and silt. The coastal plain is represented mainly by sand sheets, sand dunes and sabkha deposits that parallel to the shoreline.

Systematic sampling patterns were carried out for the studied stream sediments of the Wadi Shaàb. Nineteen samples were obtained through pits arranged in two profiles in the middle of Wadi Shaàb (Figure 1). The pits are of about 50 cm diameter and 70 -100 cm depth and 1- 6 km apart (Figure 2).

3. Methodology

Each studied sample for the Wadi Shaàb stream sediments was prepared firstly by proper mixing and splitting into representative sub-samples to undergo various characterization tests, such as determination of grain size distribution, total heavy mineral (THM) concentration, measurement of apparent density. One test sample representing the area under investigation was equipped with a mass of about 15 kg by mixing an equal amount of each sample thoroughly. Various characterization tests were carried out for this sample in order to complete the physical concentration and separation of economic heavy minerals from the stream sediments. The methodology flowchart is shown in Figure 3. The grain size distribution analyses of the studied samples were performed by using mechanical sieve shaker with set of sieves with mesh diameters of 2.0, 1.0, 0.5, 0.250, 0.125, and 0.063 mm (ASTM codes). Each size fraction was weighed, and its distribution recorded. While the apparent density measurements were carried out by weighing the sample then pouring it inside a graduated cylinder, after that compacted well to simulate the presence of the sample in nature. The density values obtained from dividing the mass of the sample by its volume.

Heavy liquid separation tests were carried out using bromoform ($CHBr_3$; density 2.89 g/cm^3) with the aim of separating heavy minerals from the associated light minerals, which mainly consist of quartz and feldspar (densities 2.65 and 2.56 g/cm^3 respectively). This test was performed by placing 50 g of each sample in a separating funnel with the bromoform, stirring for 5 minutes and allowing it to stand for 15 minutes. Next, the heavy and light mineral fractions were separated, rinsed with acetone, dried and weighed. Each obtained heavy fraction was subjected to grain size distribution analyses and magnetic fractionation tests using mechanical sieve shaker and Carpco High Intensity magnetic separator (HIMS) respectively. Additionally, an Olympus stereo binocular microscope was also used to prepare and select pure mineral grains by hand picking. The mineralogical characterization for the obtained picked heavy mineral grains was carried out in this work via X-ray diffraction (XRD) instrument and environmental scanning electron microscope

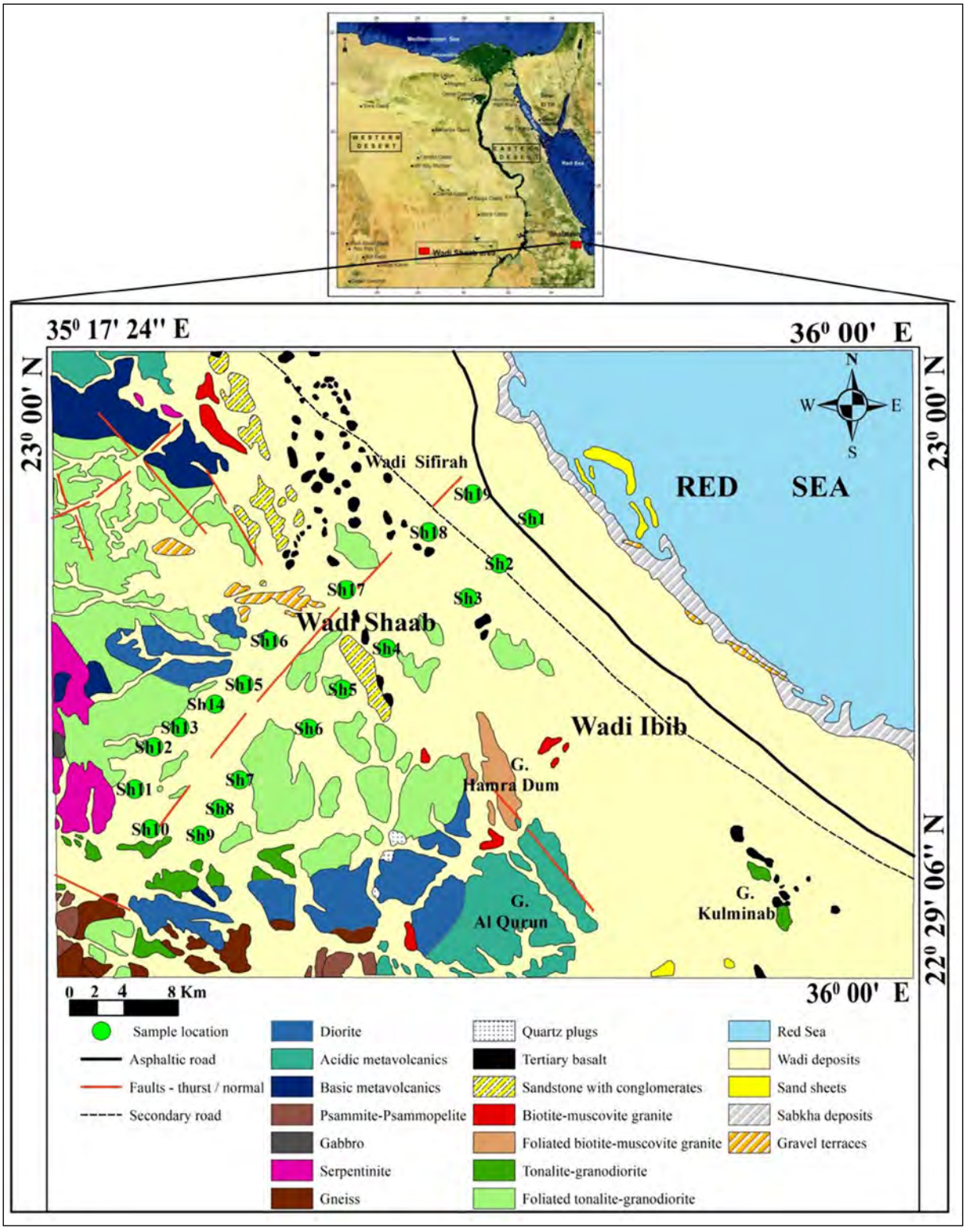

Figure 1- a) Location map of Shaàb area, and b) Geological map showing sampling locations of the Wadi Shaàb area, south Eastern Desert of Egypt (Modified after EGSMA, 2002).

Figure 2- Field photo showing the sampling techniques at the Wadi Shaàb area.

(SEM) (a Philips Model XL 30) that supplied with energy dispersive spectrometer (EDS) unit.

Chemical assays of the Shaàb samples were determined using an energy-dispersive X-ray fluorescence (EDXRF) Rigaku spectrometer with polarized optics. EDXRF is one of the most convenient and fast analytical methods suitable for working in physical beneficiation field (Rydberg, 2014; Zhao et al., 2020). The schematic flowsheet of heavy mineral estimation using EDXRF spectrometry was depicted at Figure 3.

Physical beneficiation experiments for the Shaàb test sample were carried out firstly via wet-gravity technique using shaking table (Wilfley, No. 13) to minimize the associated gangue (quartz and feldspar) at the lowest possible level. The obtained heavy concentrates were subjected to low intensity magnetic separator to separate magnetite. Free-magnetite heavy concentrates were subjected to high-intensity magnetic separator (Carpco, Model MLH, 13 III-5" 15) for separating paramagnetic from diamagnetic minerals. Magnetic separation processes were carried out at different magnetic currents of intensity at 0.8, 1.5, and 2 .5 A, pre-optimized factors of a medium air gap of 1.5 cm, average air gap of 1.5 cm, magnetic roll speed of 30 rpm and finally at

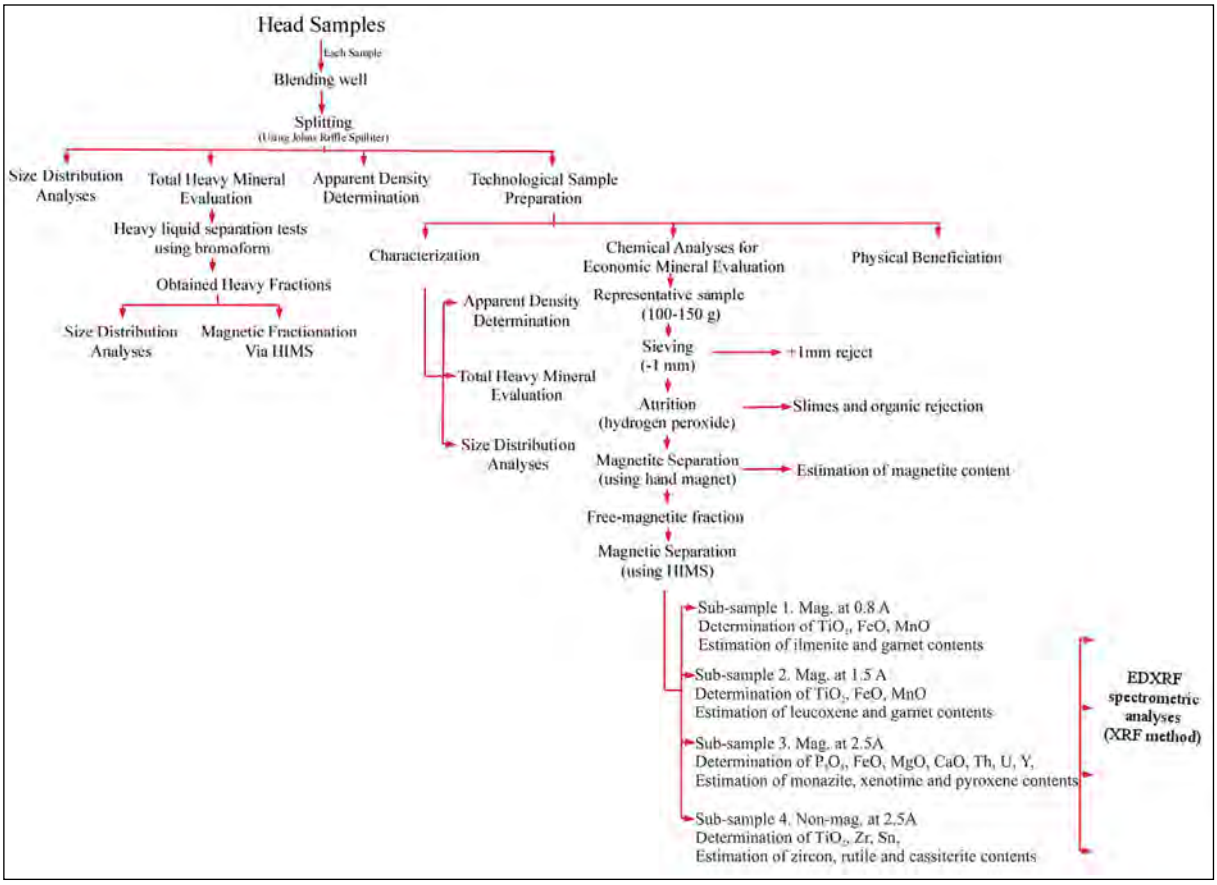

Figure 3- Methodology flow-sheet.

a feed rate of 39.2 g/min. About 100 grams of the obtained gravity concentration products (concentrate and tail) were subjected to bromoform separation test for heavy mineral assay estimation.

4. Results and Discussion

4.1. Sample Characterization

The EDXRF analyses for Shaàb head representitive sample were shown in Table 1, the head assays of the main oxides showed contents of Fe_2O_3 is 2.85% and TiO_2 is 0.41%. The highest trace elements are zirconium (355 ppm), Cr (435 ppm), and Ni (366 ppm) while Zn, Y, Pb, Cu, Nb, and Sn showing their low contents.

Size distribution analysis is the most important physical parameter that has a significant impact on the separation efficiency using various physical beneficiation techniques. Many research papers confirmed that the highest percentage of heavy minerals liberation was found in the size fraction less than 250 µm (Rahman et al., 2015; Hegde et al., 2006; Shalini et al., 2020; Paltekar et al., 2021). Grain size distribution analyzes results of the Wadi Shaàb head samples (Sh 1-19) as well as test sample (Sh tech.) were presented in Figure 4. It showed a high degree of homogeneity and the mean values confirmed that the highest percentage (73.4% mass) of the samples size is retained in a size ranging from 1 to 0.063 mm while the gravel and very coarse sand fractions were about 23.26% mass, and the silty size fraction was calculated as 3.33% mass. For Shaàb sample (Sh tech.), it was 73.03% mass for size range from 1to 0.063mm, 24.71% mass for the gravel and very coarse sand fraction, and 2.27% mass for the silty size fraction.

Table 1- EDXRF analyses of Shaàb head bulk sample.

Major Oxides (%)						**Trace Elements (ppm)**										
Fe_2O_3	CaO	TiO_2	P_2O_5	K_2O	MnO	Zr	Cr	Ni	Co	V	Zn	Y	Pb	Cu	Nb	Sn
2.85	2.32	0.41	0.09	0.81	0.05	355	435	366	110	142	65	21	11	28	11	58.9

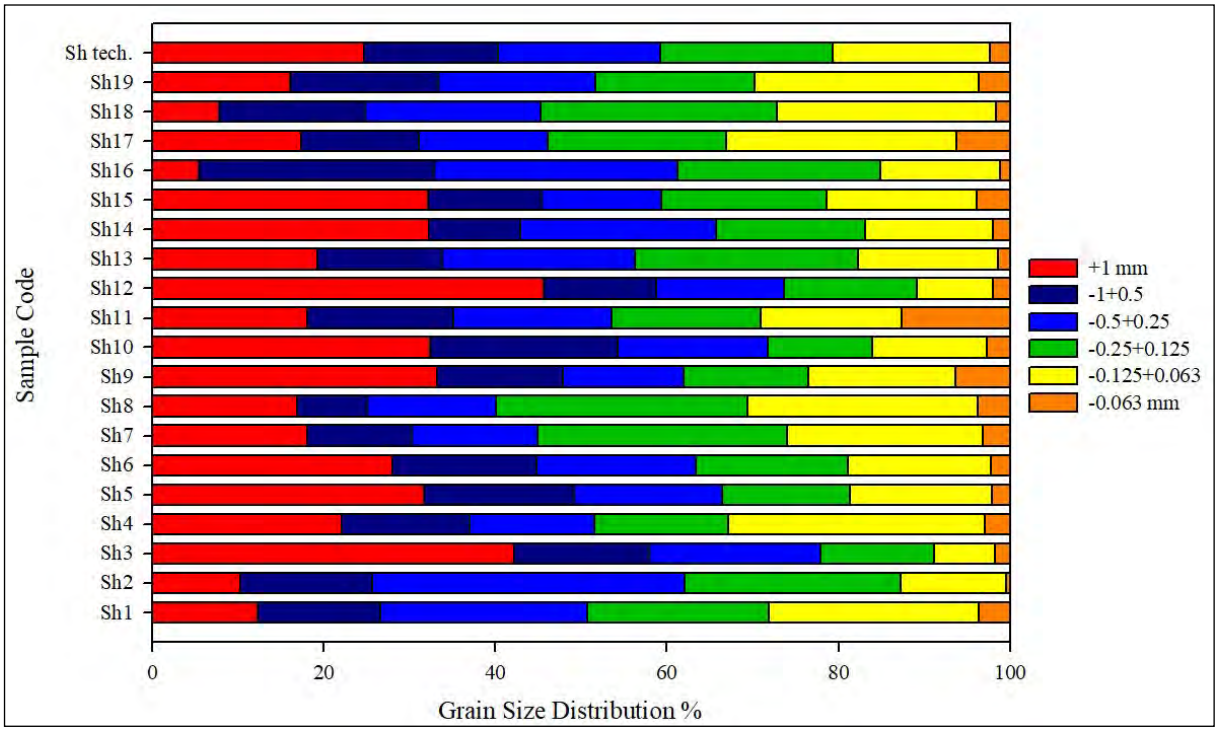

Figure 4- Grain size distribution analyses for the Shaàb stream sediment samples.

The apparent density values were used as evidence for the presence of heavy mineral concentrations in the studied samples; in addition to using these values for estimation the reserves of heavy minerals in the area under investigation (Fawzy et al., 2022*a*, *b*; Diab et al., 2022). As for the apparent density measurements of the Wadi Shaàb samples which were shown in Figure 5, the values ranged between 2.46 g/cm^3 for sample no.10 (Sh10) to 1.21 g/cm^3 for Sh14, with an average of about 1.86 g/cm^3 and the value of the Shaàb sample was 1.83 g/cm^3. Compared to the typical values of dry density of ordinary sand, which is estimated at 1.5 g/cm^3 (Yu et al., 2023), this indicates that the raw Shaàb sand contains heavy minerals in a higher proportion than ordinary sand. The content of the heavy minerals in each sample was determined using a heavy liquid separation (bromoform) technique, and the results were showed in Figure 6. The results confirmed that the total heavy mineral content in the Shaàb samples ranged between 2.91% mass for Sh 9 and 11.24% mass for Sh 13, with an average of about 8.00% mass and 7.63% mass for Sh tech.

The obtained heavy mineral fractions were studied for size distribution analysis and the results were presented in Figure 7, the mean results (for 19 samples) showed that 96.08% mass of the HMs retained in the size range 1 to 0.063 mm while zero percent of HMs in the size fraction greater than 1mm and 3.91% mass of HMs presented in silt size fraction (-0.063 mm). The results for the Shaàb test sample were as follows, 96.86% mass of HMs kept in size fraction -1+0.063 mm, 0% mass in +1mm size fraction, and 3.13% mass of the HMs in silty fraction. Figure 7 also shows that the mineral fraction (-0.125 + 0.063mm) is the largest fraction that retains heavy minerals (about 40%), followed by fraction (-0.25 + 0.125 mm) that retained about 30% of the heavy minerals.

Microscopic examination for the picked heavy mineral grains using Stereo-binocular microscope

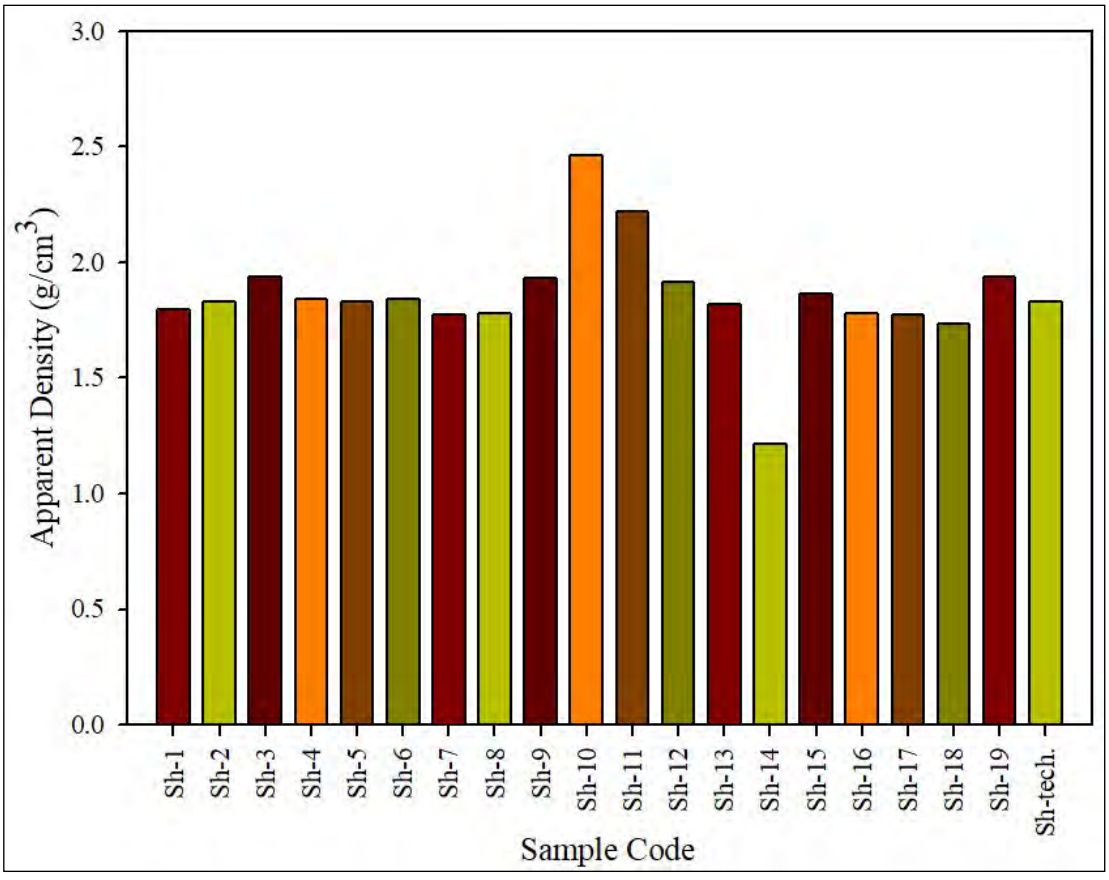

Figure 5- Apparent density measurements in the Wadi Shaàb stream sediment samples.

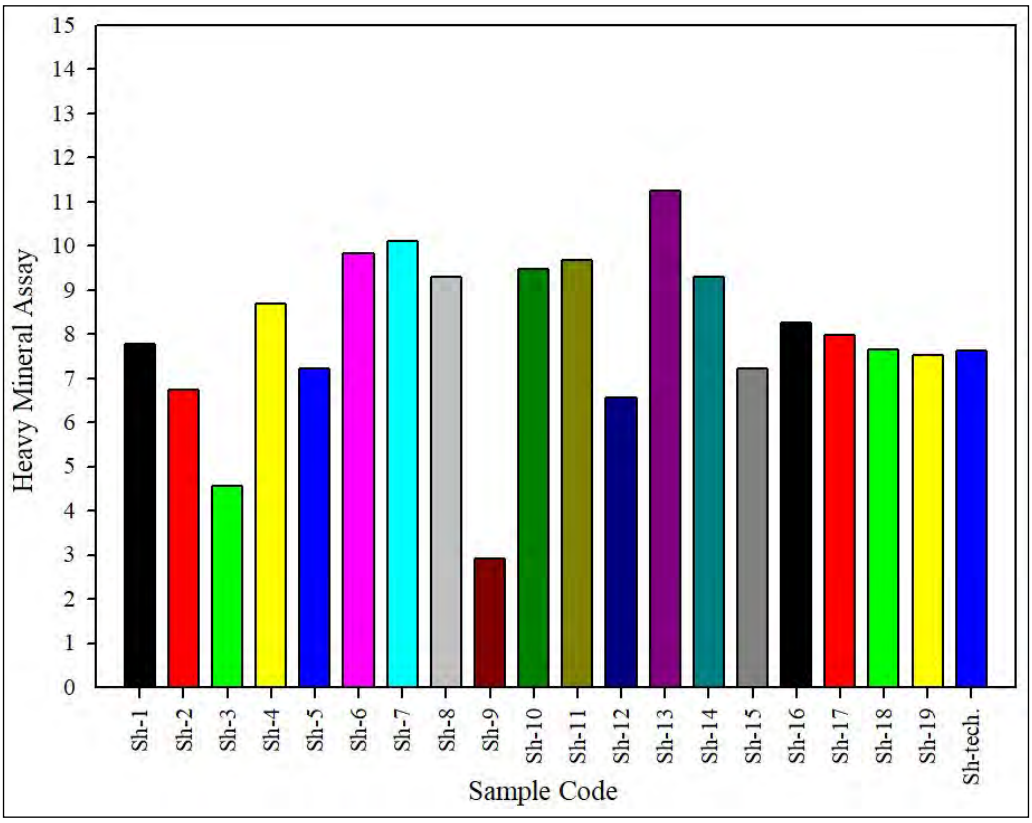

Figure 6- Heavy mineral distribution analyses for the Shaàb samples.

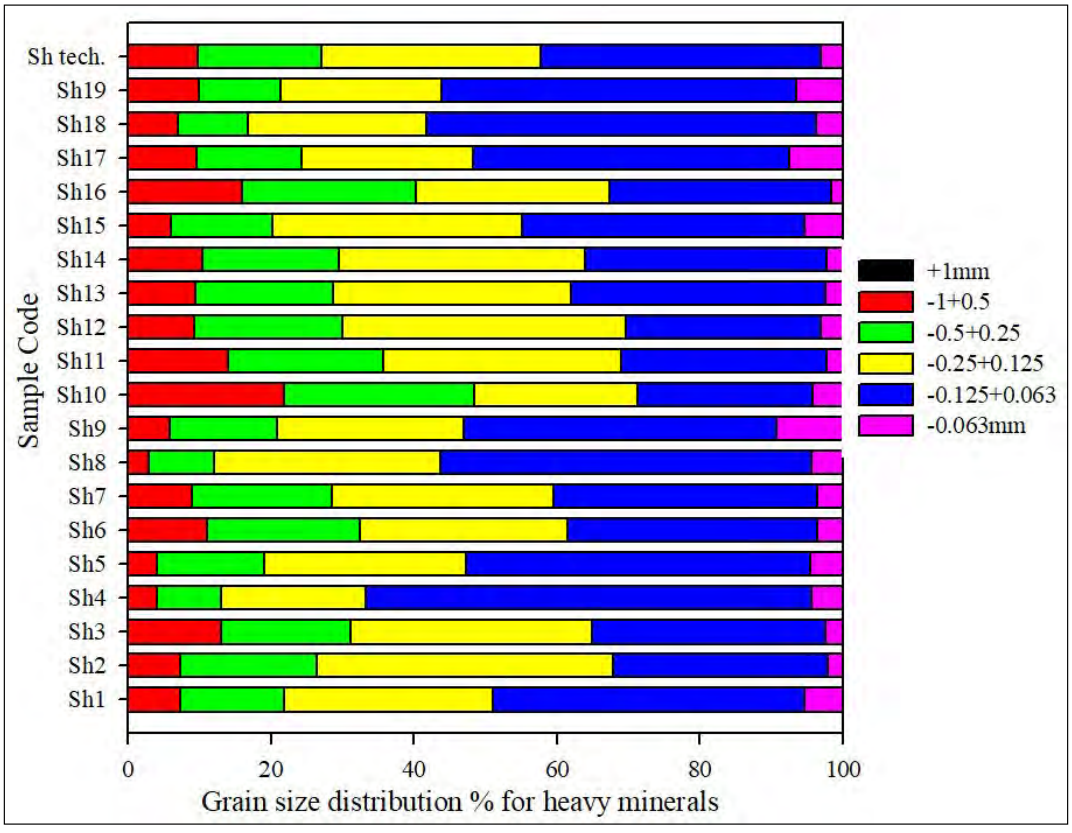

Figure 7- Size distribution analyses for the Shaàb heavy mineral fractions.

then SEM analyses that supplied with EDS unit revealed the presence of a large group of economic heavy minerals that were listed as follows; ilmenite (Figure 8a), leucoxene (Figure 8b), rutile (Figure 8c), sphene (Figure 8d), zircon (Figure 9a), Zn-Sn-Pb mineral (Figure 9b), Zn mineral (Figure 9c), xenotime (Figure 10a), monazite (Figure 10b), cassiterite (Figure 10c).

For detailed mineralogical study, magnetic fractionation for the separated heavy minerals was conducted using HIMS magnetic separator. Each heavy mineral sample was magnetically separated into five fractions (magnetic at 0.04A, 0.8A, 1.5A, 2.5A, and non-magnetic at 2.5A). Each fraction was weighted and calculated with respect to the percentage of heavy minerals and the results are presented in Figure 11. The magnetic fractionation results manifested that the magnetic fraction at 1.5A represents the highest value ranging from 30.61% mass for Sh 14 to 58.93% mass for Sh 7 with an average of about 46.19% mass followed by the magnetic fraction at 2.5A, where the values ranged between 8.29 % mass for Sh 4 to 27.94% mass for Sh 14 with an average of 17.76% mass. While the non-magnetic fraction at 2.5A has values between 10.48% mass for Sh 6 to 24.85% mass for Sh 14 with an average of 17.12% mass. The magnetic fraction at 0.8A, its value ranged between 8.79 to 26.10% mass with an average of 14.15% mass. As for the lowest value of magnetic fractionation, it had a magnetic fraction of 0.04A which ranged from 2.09 to 7.81% mass with an average of 4.78% mass. With regard to the Shaàb test sample, the magnetic fractionation results were as follows; 54.61% mass for magnetic fraction at 1.5A, 26.61% mass for magnetic fraction at 2.5A, 4.03% mass for non-magnetic fraction at 2.5A, 8.44% mass for magnetic fraction at 0.8A, and 6.32% mass for magnetic fraction at 0.04A (Figure 11).

EDXRF analyses for the oxides and elements of different magnetic fractions for the Shaàb test sample were shown in Table 2. The data of analyses as well as magnetic fractionation results in order to compute the contents heavy minerals assuming their stoichiometric composition, revealed that the content of ilmenite reaches 0.06%, zircon is 0.08%, rutile is 0.07%, leucoxene is 0.07%, cassiterite is 0.008%, xenotime is 0.004%, monazite is 0.0004%, heavy silicates is 0.53%, almandine is 0.022%, and magnetite represents 0.46%.

The mineralogical confirmation of the magnetic fractionation of the Wadi Shaàb representative sample was conducted via x-ray diffraction analyses and the diffractograms for the various fractions were depicted in Figure 12 and Figure 13. Figure 12a showed that the magnetic fraction at 0.04 amps contains mainly magnetite, hematite, and antigorite which have ASTM Card No. 76-1849, 58-599, and 44-1447 respectively. While the magnetic fraction at 0.8 amps was mainly composed of ilmenite, hematite and actinolite which have ASTM Card No. 03-778, 01-1053 and 85-2157 respectively (Figure 12b). The alteration product of ilmenite (leucoxene), actinolite, almandine, quartz and traces of rutile separated as magnetic fraction at 1.5 amps and have ASTM Card No. 03-778, 85-2157, 74-1553, 85-789, and 72-1148 respectively (Figure 12c).

Magnetic separation at 2.5 amps proved the presence of epidote, actinolite, and monazite, which have ASTM Card No. 17-514, 85-2157, and 46-1295 respectively (Figure 13a), while the non-magnetic fraction at the same amperes showed the presence of zircon, rutile, cassiterite, and diopside, which have ASTM Card No. 81-588, 72-1148, 77-449 and 83-98 respectively (Figure 13b).

4.2. Beneficiation Processes

Zircon, rutile, ilmenite and other economic minerals are found all over the world, but not always in high grade concentrations. Therefore, low-grade ores can be exploited by raising their grades via various physical beneficiation processes.

The beneficiation processes of the Shaàb test sample was firstly carried out by raising the grade of heavy minerals through the shaking table in order to get rid of quartz and feldspar as much as possible. The obtained heavy mineral concentrate was fed as feed to different magnetic separators to differentiate the minerals according to their magnetic response.

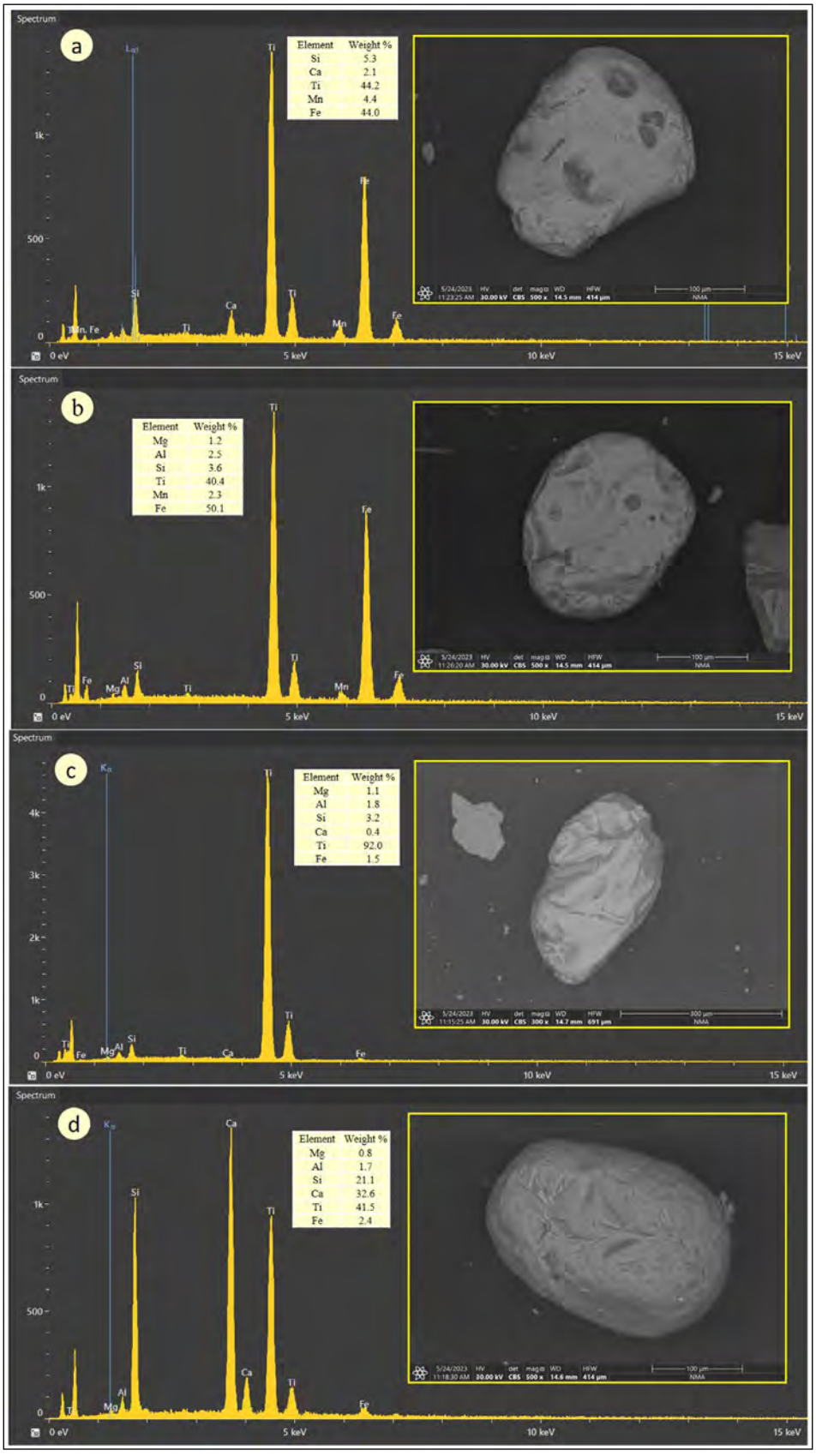

Figure 8- Back-scattered electron (BSE) images and corresponding EDS spectra showing; a) ilmenite, b) leucoxene, c) rutile, and d) sphene.

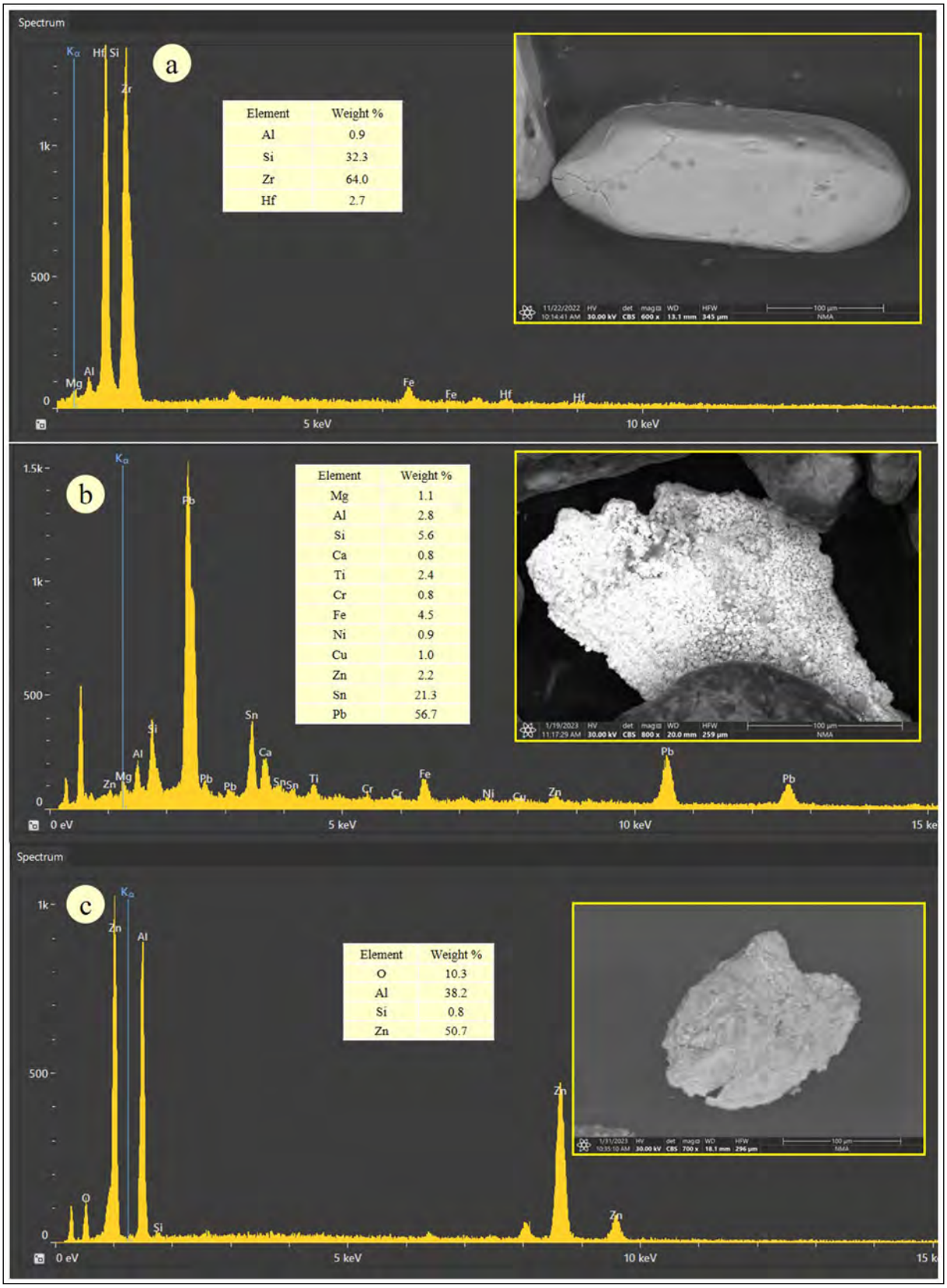

Figure 9- BSE images and corresponding EDS spectra showing; a) zircon, b) Zn-Sn-Pb mineral, and c) Zn-mineral.

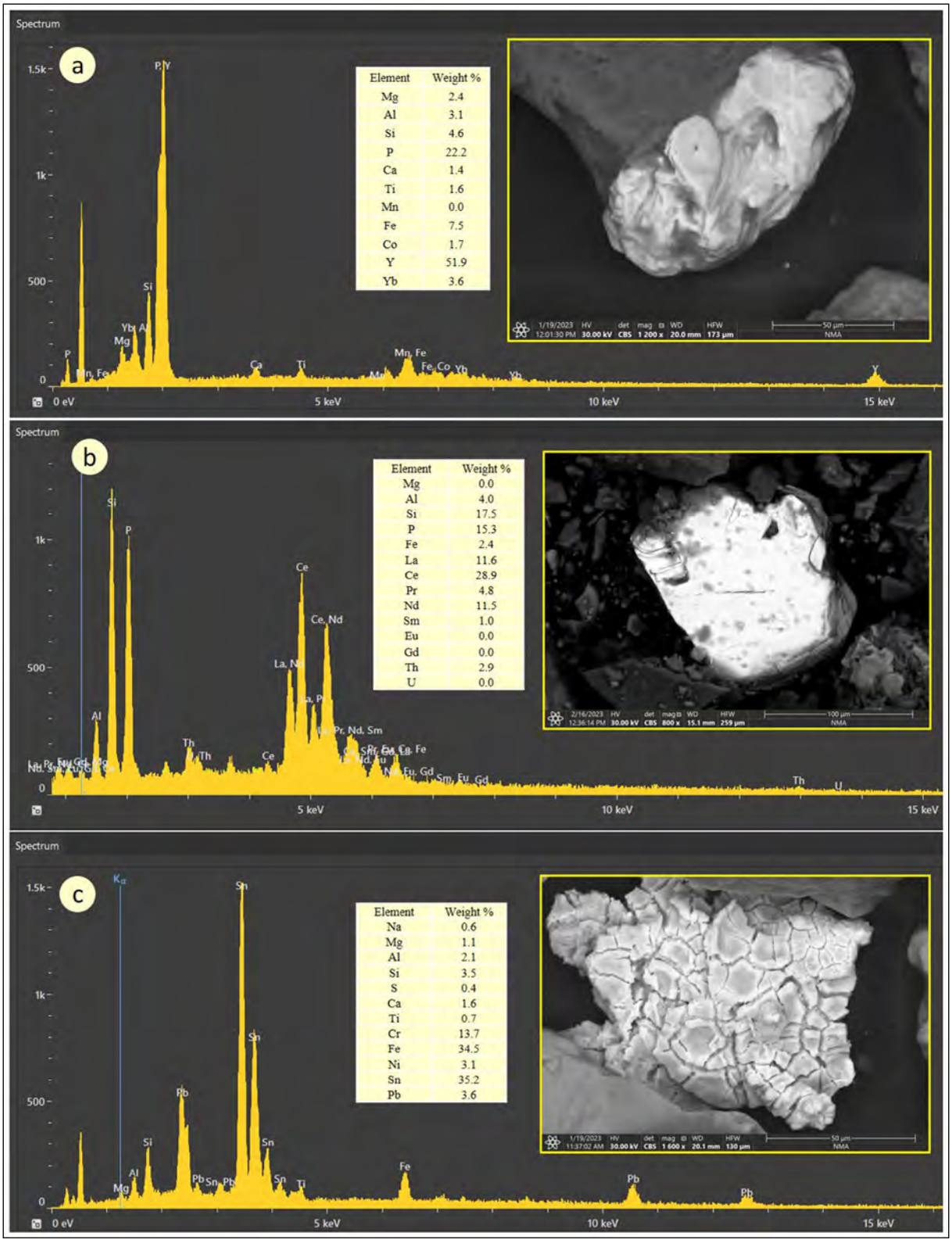

Figure 10- BSE images and corresponding EDS spectra showing; a) xenotime, b) monazite, and c) cassiterite.

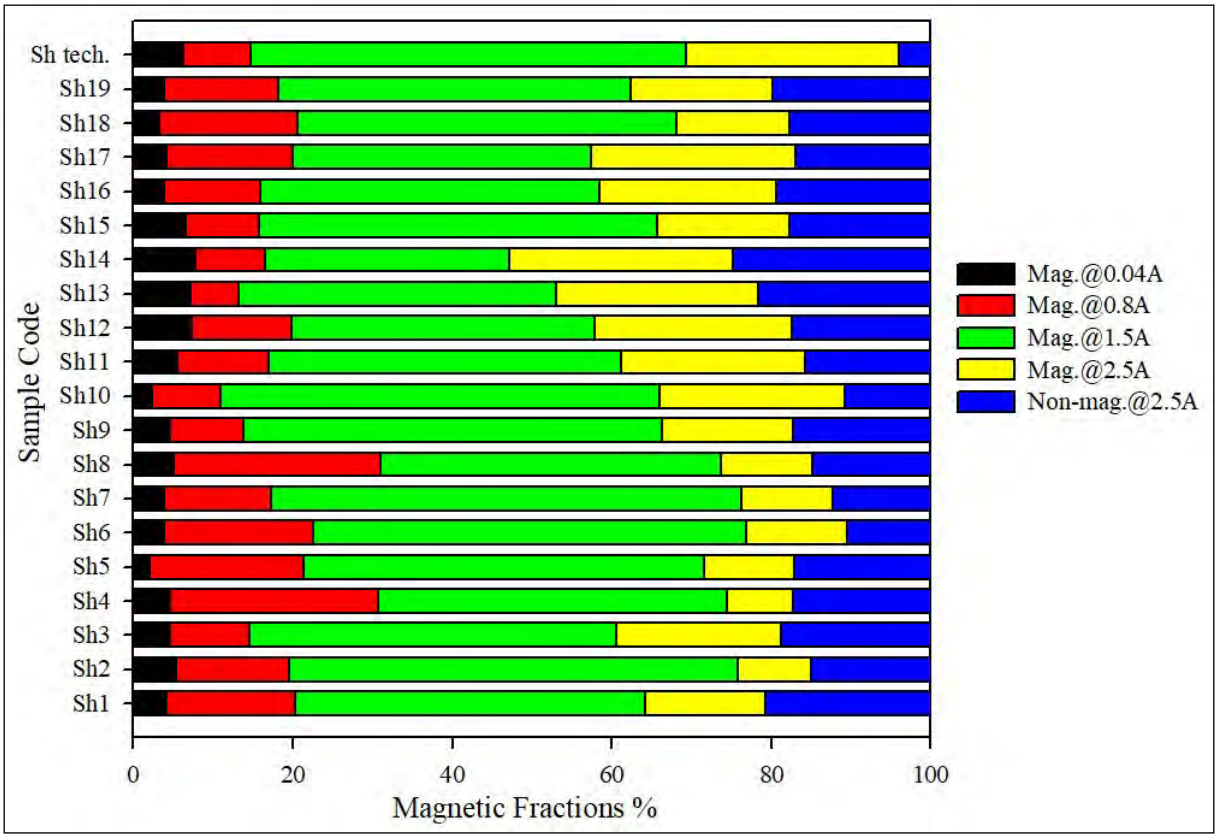

Figure 11- Magnetic fractionation for heavy mineral fractions in the Shaàb samples via DHIMS.

Table 2- EDXRF analyses of the Shaàb test sample after magnetic fractionation.

Shaàb Sample after Magnetic Separation	**Mag. Fr. @0.8A**	**Mag. Fr. @1.5A**	**Mag. Fr. @2.5A**	**Non-mag. Fr. @2.5A**
Major Elemental Oxides in %				
Fe_2O_3	9.3	10.8	8.12	0.932
CaO	1.14	3.32	3.81	2.27
TiO_2	1.44	1.13	0.887	0.167
P_2O_5	0.0755	0.08	0.084	0.087
K_2O	0.161	0.976	0.724	1.07
MnO	0.142	0.232	0.16	0.024
Trace Elements in ppm				
Cr	2740	490	563	46
Ni	1750	336	285	55
Co	510	327	280	37
V	324	339	266	45
Zn	114	191	143	42
Y	18	80	45	16.6
Pb	11	10	10.5	15.2
Cu	<0.1	80	<0.1	13.6
Th	<0.1	<0.1	9.5	<0.1
U	<0.1	<0.1	<0.1	<0.1

4.2.1. Shaking Table Concentration

Heavy minerals were concentrated from the sand by exploiting differences in mineral density via a rougher stage followed by multi-stages of scavengers through Wilfley Shaking Table No. 13 (Fawzy et al., 2022*a*, *b*). The rougher stage was carried out under optimum conditions of 134 g/min feed rate, 14 liters/min water flow rate, stroke length of 1.5 cm, and inclination angle of 9°, while the multi-scavenging stages were carried out under operating conditions of 140 g/min feed rate, water flow rate of 17.5 liters/min., 2 cm stroke length, and inclination angle of 11°. It is clear from the aforementioned values that the scavenging stages have greater values for operating conditions than those for the roughing stage, due to the higher content of light minerals and lower content of heavy minerals during the scavenging stages. About 50 g representative sample of the

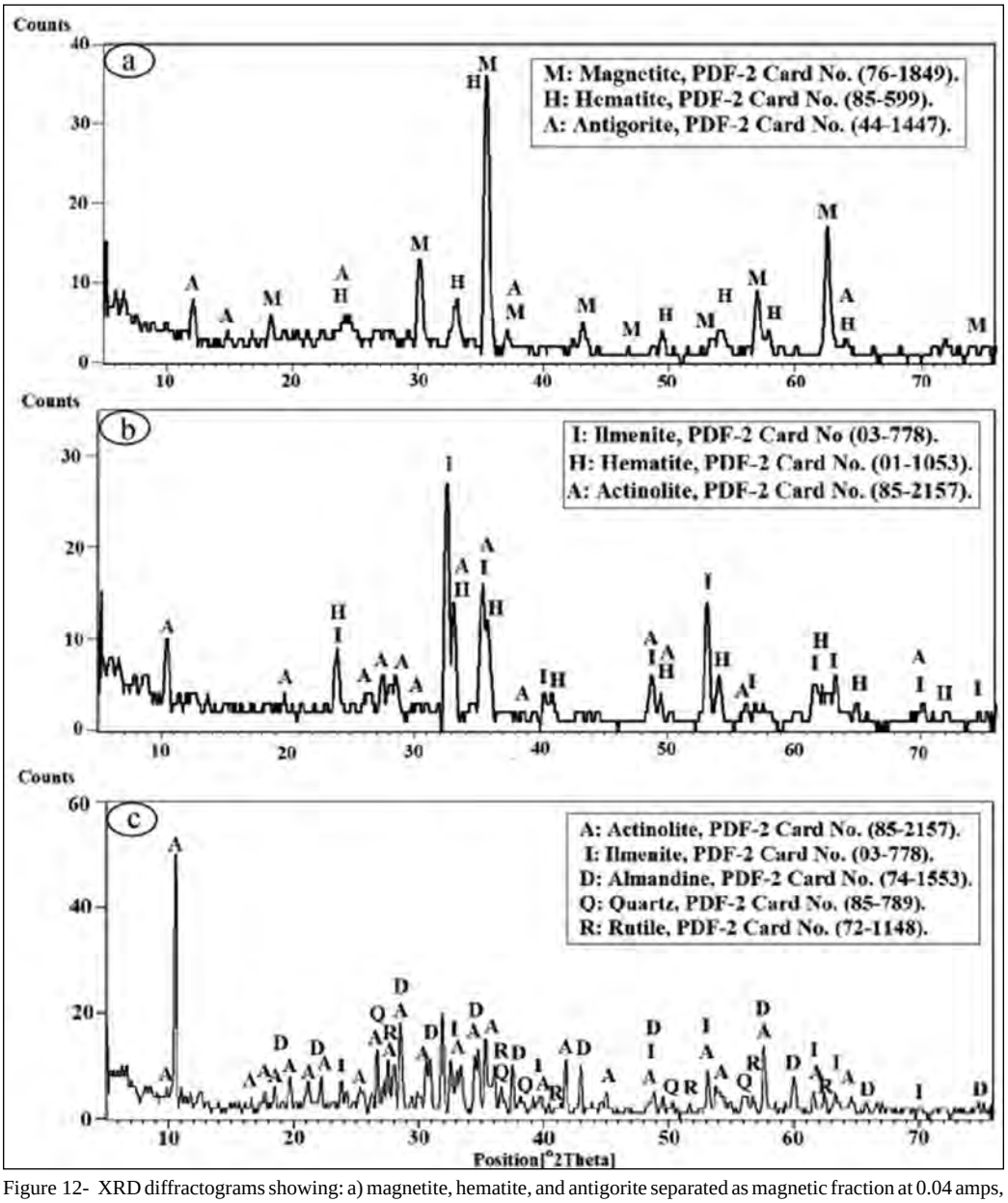

Figure 12- XRD diffractograms showing: a) magnetite, hematite, and antigorite separated as magnetic fraction at 0.04 amps, b) ilmenite, hematite, and actinolite separated at 0.8 amps as magnetic fraction, and c) almandine, ilmenite, actinolite, quartz, and rutile separated at 1.5 amps as magnetic fraction of the Wadi Shaàb representative sample.

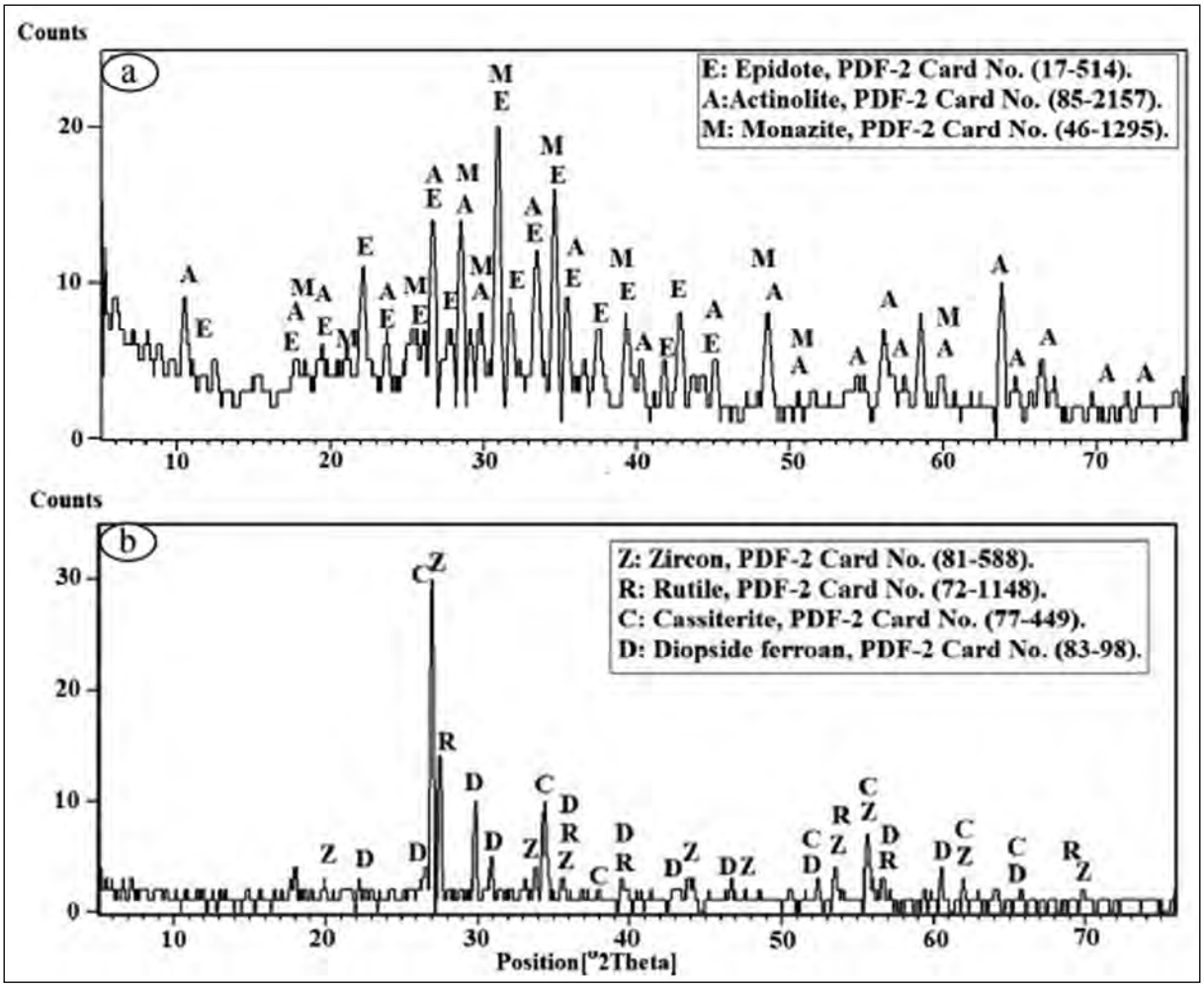

Figure 13- XRD diffractograms showing: a) epidote, actinolite and monazite separated fraction at 2.5 amps as magnetic, and b) zircon, rutile, cassiterite, and diopside separated at 2.5 amps as non-magnetic fraction of the Wadi Shaàb representative sample.

tabling products (concentrate and tail) were used in the bromoform-separation test to estimate the heavy mineral material balance and the data were presented at Table 4.

It is clear from the results shown in Table 3 that the heavy mineral assay increased from 7.63% of the feed sample to 45.03% in the concentrate after multi-stages gravity separation, while the heavy mineral recovery in the roughing stage reached to 62.64% and increased

Table 3- Material balance of the different products of gravity concentration via shaking table for Shaàb head sample.

Products of Tabling		Yield (%)	Heavy Mineral Assay (%)	Heavy Mineral Recovery (%)
Concentrate	Roughing stage	8.99	53.17	62.64
	Scavenging Round 1	3.45	47.79	21.63
	Scavenging Round 2	1.3	31.17	5.31
	Total Concentrate	13.74	45.03	89.58
Tail	Total	86.26	1.53	10.42
Feed	Total	100	7.63	100

Table 4- Feed and concentrate grade EDXRF analyses as well as enrichment ratio (E.R.) for the Shaàb test sample as results of gravity concentration via shaking table.

	Feed Grade	Concentrate Grade	Enrichment Ratio (E.R.)
Major Oxides in %			
Fe_2O_3	2.85	7.78	2.73
CaO	2.32	4.6	1.98
TiO_2	0.41	1.34	3.27
P_2O_5	0.087	0.125	1.44
K_2O	0.81	0.66	0.81
MnO	0.0537	0.15	2.79
Trace Elements in ppm			
Cr	377	1550	4.11
Zr	355	849	2.39
Ni	150	221	1.47
Co	110	279	2.54
V	142	253	1.78
Zn	65	119	1.83
Y	21	55	2.62
Pb	11	14	1.27
Cu	28	33	1.18
Th	<0.1	12.6	126
U	<0.1	11.2	112

to 89.58% after two stages of scavenging in a yield of 13.74% out of the feed sample.

EDXRF spectrometric analysis of final concentrate versus head sample analysis and enrichment ratio values are presented in Table 4 where the enrichment ratio values which were estimated by dividing the concentrate grade by the feed grade (c/f) and the resulting value indicates how many times the concentrate has element concentration relative to the feed. The enrichment ratio values for major elements such as Fe_2O_3 and TiO_2 showed a clear improvement and increased by 2.73% for Fe_2O_3 and 3.27 for TiO_2. As for the trace elements such as Zr, Cr, Co, Y, U, and Th, they showed high enrichment ratio values, as a result of doubling of the content of minerals bearing them as magnetite, ilmenite, rutile, sphene, zircon, xenotime, almandine, and monazite in the concentrate.

4.2.2. Magnetic Separation

The heavy mineral fractions were used as feed for LIMS for separation of magnetite as a ferromagnetic mineral fraction and the non-magnetic fraction were subjected to HIMS to fractionate free-magnetite mineral fraction into paramagnetic and diamagnetic fractions. Four magnetic fractions were resulted; magnetite fraction, paramagnetic fraction separated at 0.8A, paramagnetic fraction separated at 1.5A, and paramagnetic fraction at 2.5A. Non-magnetic fraction separated at 2.5A was also obtained.

Magnetite Separation: Using a low intensity magnetic separator, magnetite is the separation product of this fraction and it represents about 0.30% mass of the heavy mineral fraction. The magnetite fraction was confirmed by SEM analyses where the Back-scattered electron (BSE) image with corresponding energy dispersive spectrum (EDS) and its stereo microscopic image were shown at Figures 14a, b respectively. The SEM data for magnetite as separate grain was depicted in Figure 14c.

Magnetic Fraction at 0.8A: Ilmenite is the main target mineral for separation in this fraction using HIMS at 0.8A that represents about 2.58% mass of the heavy mineral fraction. The BSE image and its corresponding EDS for this fraction as well as the stereo microscopic images are shown at Figure 15a, b respectively, they were clarified that the main content is iron (38.0%), titanium (27.4%), and silicon (18.8%), this means that ilmenite is the main constituents with traces of almandine garnet. Ilmenite as a separate grain was presented in Figure 15c.

Magnetic Fraction at 1.5 A: Garnet and leucoxene are the main essential minerals for separation in this fraction that represents about 2.18% mass of the heavy fraction of the Shaàb sample. The SEM data shown in Figure 16a as well as the stereo microscopic image shown in Figure 16b proved that leucoxene and almandine with traces of heavy silicates are the main minerals that have been occurred. SEM data concerning almandine is shown in Figure 16c.

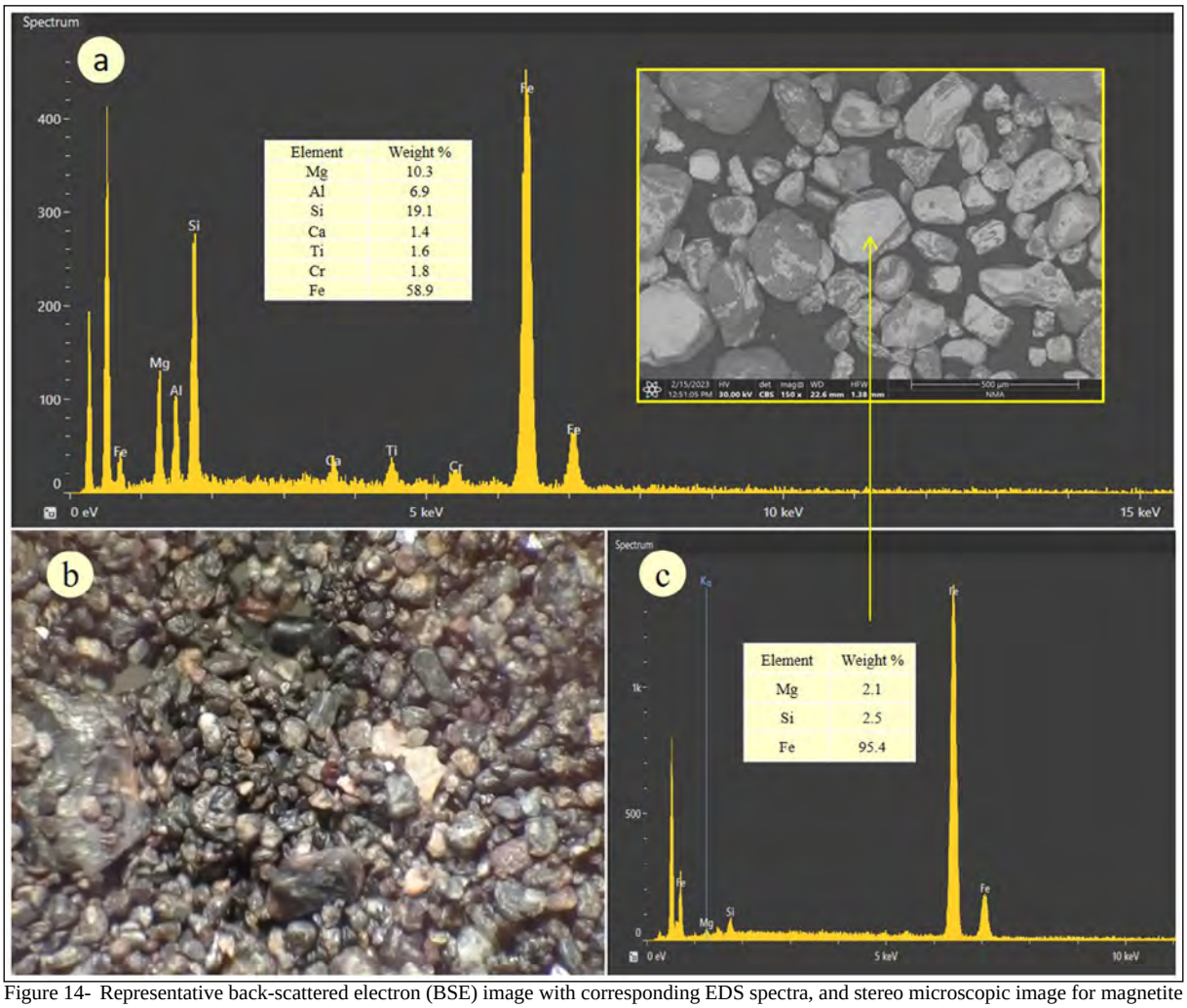

Figure 14- Representative back-scattered electron (BSE) image with corresponding EDS spectra, and stereo microscopic image for magnetite fraction a), b) respectively and c) for magnetite.

Magnetic Fraction at 2.5 A: Heavy silicates as pyroxene, amphibole and epidote are the target mineral for separation in this fraction as well as traces of monazite and xenotime. This heavy fraction represents about 1.49% mass of the heavy concentrate. The SEM results (Figure 17a) and stereo microscopic image (Figure 17b) proved that this fraction contains mainly heavy silicate minerals, in addition to the presence of monazite confirmed in Figure 17c.

Non-magnetic Fraction at 2.5 A: Non-magnetic minerals such as zircon, rutile, sphene, and cassiterite are the main heavy minerals can be separated at this fraction. This fraction represents about 7.19% mass of the heavy mineral fraction. The SEM data in Figure 18a proved that the main elemental content is Ti (32.0%), Si (29.4%), Ca (22.8%), and P (1.8%). The stereo microscopic image in Figure 18b as well as SEM data in Figures 18c, d, and e confirmed that zircon, rutile, and cassiterite are the essential minerals in this fraction.

A schematic sequence for processing and separating economic heavy minerals from the Shaàb stream sediments sample with material balance is presented as a flow-sheet in Figure 19.

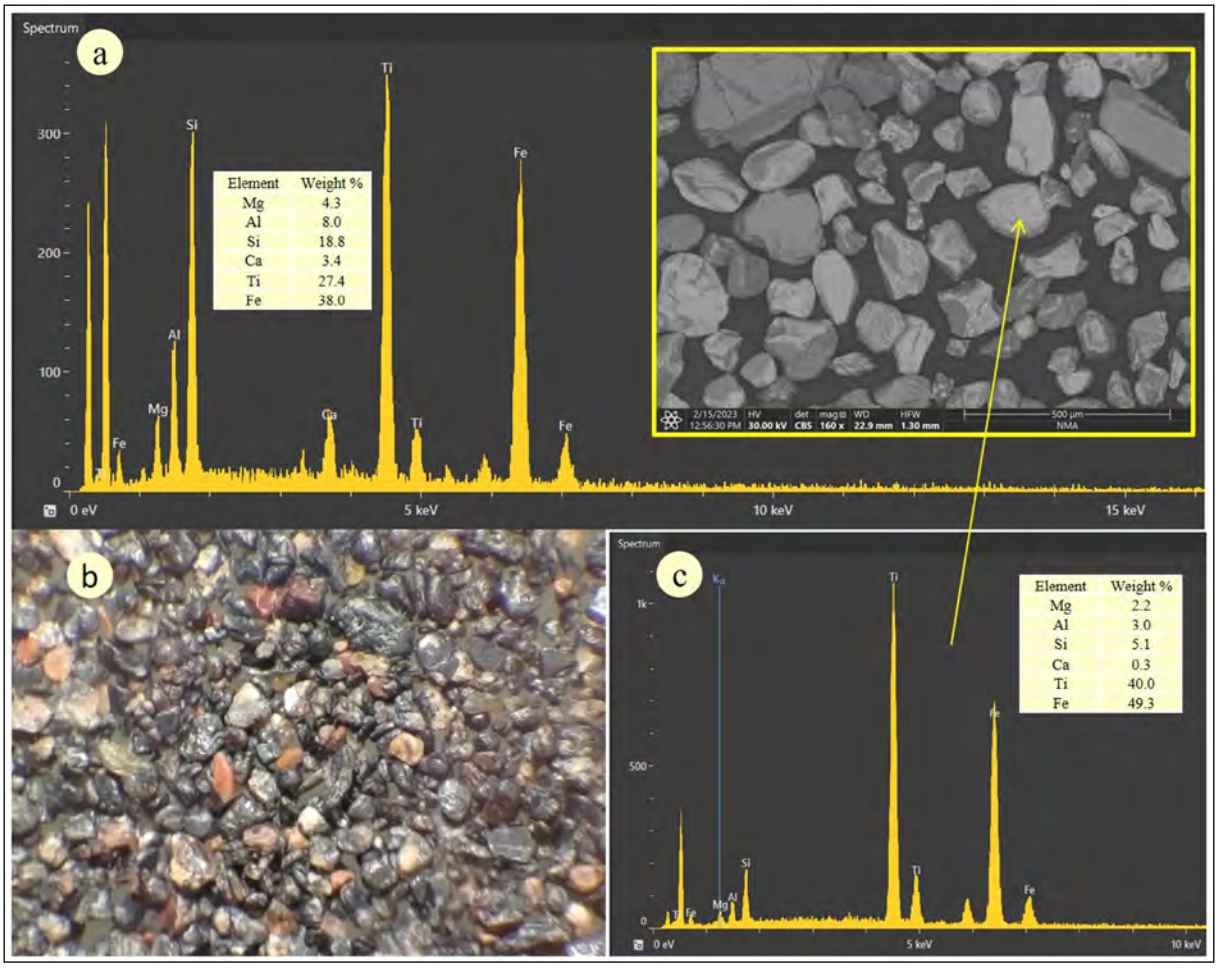

Figure 15- Representative BSE image with corresponding EDS spectra, and stereo microscopic image for magnetic fraction at 0.8A a), and b) respectively and c) for ilmenite.

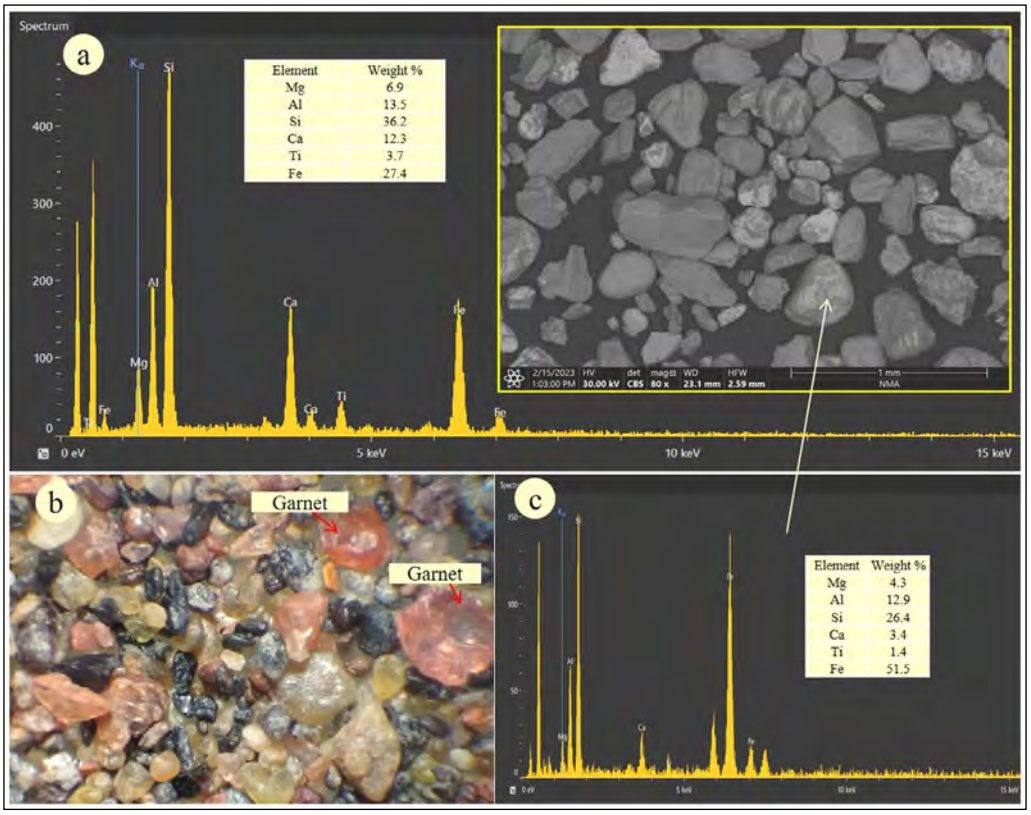

Figure 16- Representative BSE image with corresponding EDS spectra, and stereo-microscopic image for magnetic fraction at 1.5A a), b) respectively, and c) for almandine.

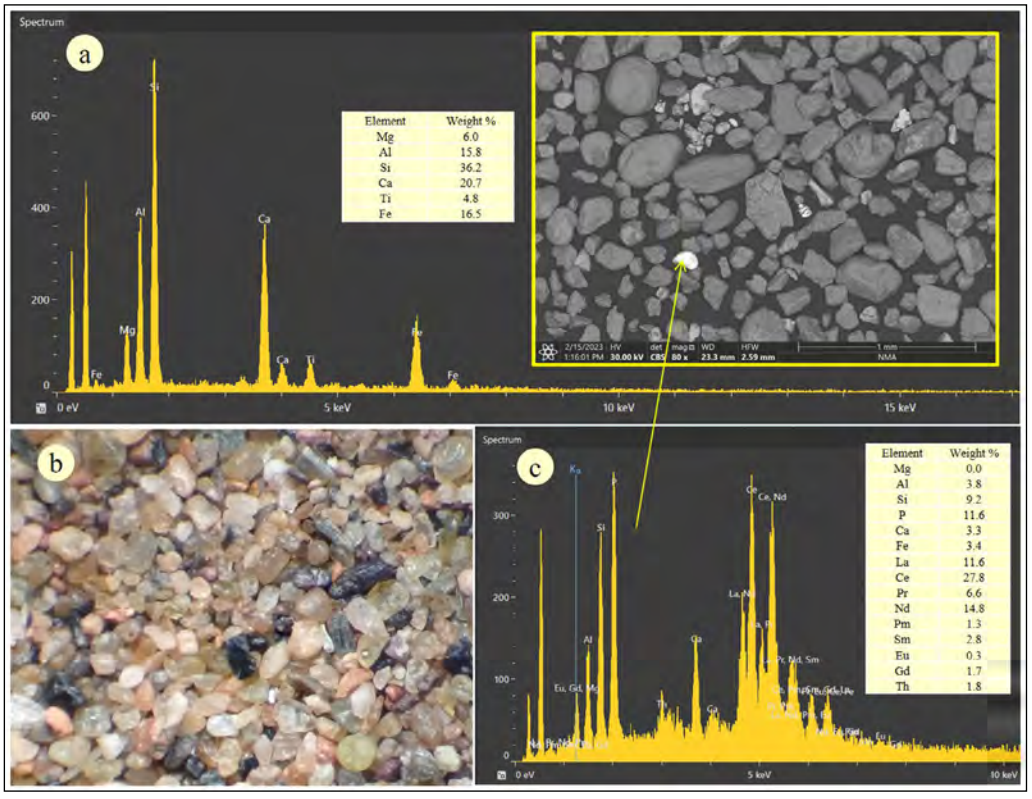

Figure 17- Representative BSE image with corresponding EDS spectra, and stereo microscopic image for magnetic fraction at 2.5A a), and b) respectively, and c) for monazite.

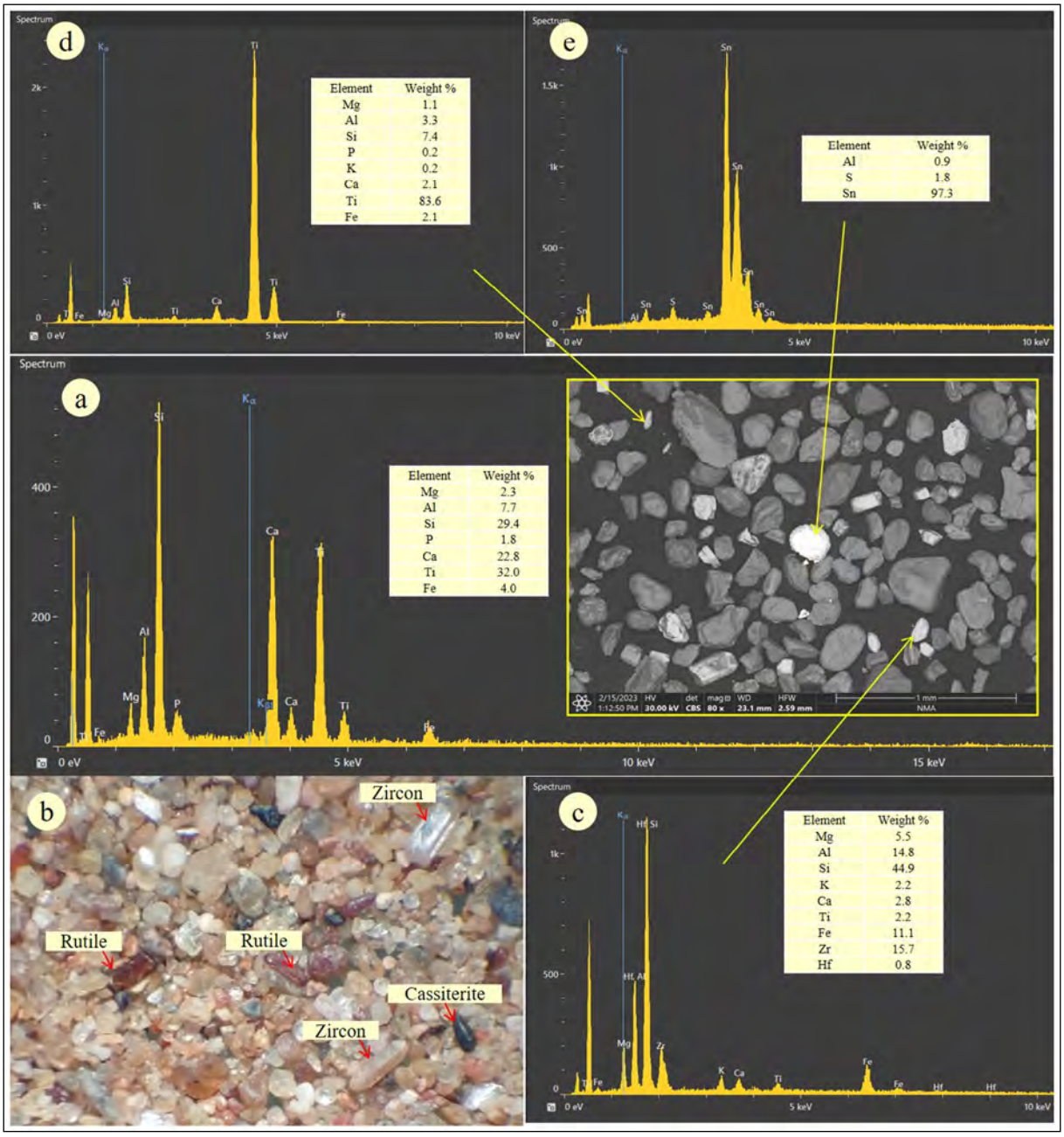

Figure 18- Representative BSE image with corresponding EDS spectra, and stereo icroscopic image for non- magnetic fraction at 2.5A a), and b) respectively, c) for zircon, d) for rutile, and e) for cassiterite.

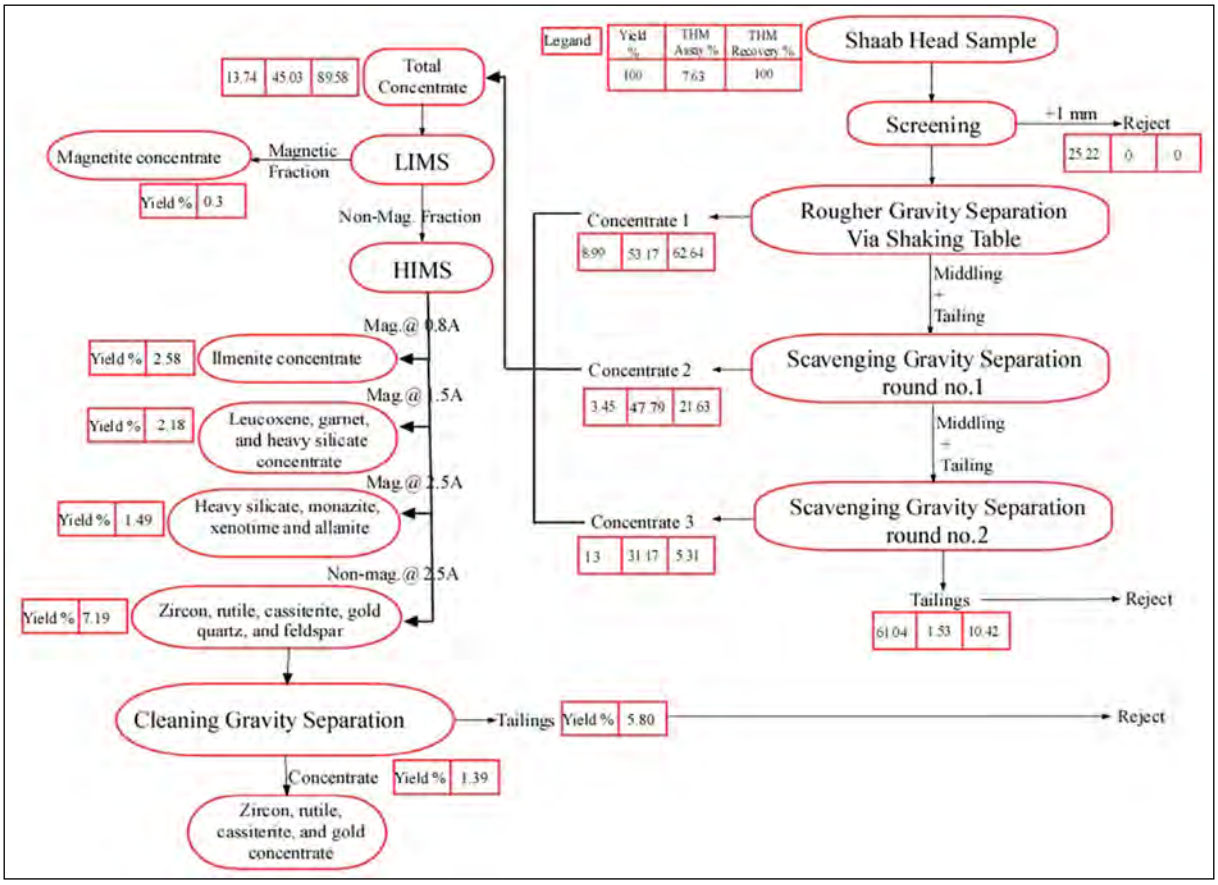

Figure 19- Flow-sheet with material balance for recovery of economic heavy minerals from Shaàb test sample.

5. Results

Mineralogical investigation of the Wadi Shaàb stream sediments revealed the presence of total heavy minerals content ranged from 2.91% mass to 11.24% mass with an average of about 8.00% mass. Microscopic examination supplemented with (XRD) and (SEM) analyses confirmed the presence of ilmenite, leucoxene, rutile, sphene, zircon, Zn-Sn-Pb minerals, xenotime, monazite and cassiterite. The estimated reserve of the economic heavy minerals within the Wadi Shaàb stream sediments can be summed up as follows; magnetite 3850 tons, zircon 669 tons, rutile 585 tons, leucoxene 585 tons, ilmenite 502 tons, almandine 184 tons, cassiterite 66 tons, xenotime 33 tons and monazite 3 tons. Physical upgrading processes of VHMs from the Wadi Shaàb stream sediments was successfully performed in this study using wet gravity concentration in conjunction with magnetic separation. The total heavy mineral assay increased from 7.63% to 45.03% after two rounds of the scavenging concentration step following the roughing step in a yield of 13.74% out of the original sample. Magnetite is the separation product of this fraction using a low intensity magnetic separator. DHIMS succeeded in fractionate free-magnetite mineral fraction into paramagnetic and diamagnetic fractions.

Acknowledgement

The authors gratefully acknowledge the support and assistance provided by our institution (Nuclear Materials Authority).

References

Diab, M., Abu El Ghar, M. A., Gaafar, I. M., El shafey, A. M., Hussein, A.W., Fawzy, M. M. 2022. Potentiality of Physical Upgrading for Valuable Heavy Minerals from Sermatai Area, Egypt. Journal of Mining and Environment 13, 1, 15-32.

EGSMA 2002. Egyptian geological survey and mining; geologic map of the Marsa Shaab, quadrangle, Egypt, scale 1:250 0000. Geological Survey, Cairo, Egypt.

Fawzy, M. M. 2018. Surface characterization and froth flotation of fergusonite from Abu Dob pegmatite using a combination of anionic and nonionic collectors. Physicochemical Problems of Mineral Processing 54(3), 677-687.

Fawzy, M. M. 2021*a*. Separation of fine beryl from quartz via magnetic carriers by the aiding of non-ionic surfactant. Physicochemical Problems of Mineral Processing 57(2), 14-23.

Fawzy, M. M. 2021*b*. Flotation separation of dravite from phlogopite using a combination of anionic/ nonionic surfactants. Physicochemical Problems of Mineral Processing 57(4), 87-95.

Fawzy, M. M., Abu El Ghar, M. S., Gaafar, I. M., El Shafey, A. M., Diab, M., Hussein, A. W. 2022*a*. Diit Quaternary Stream Sediments, Southern Coast of the Red Sea, Egypt: Potential Source of Ilmenite, Magnetite, Zircon, and Other Economic Heavy Minerals. Mining, Metallurgy and Exploration 39:655–667.

Fawzy, M. M., Abu El Ghar, M. S., Gaafar, I. M., El shafey, A. M., Diab, M., Hussein, A. W. 2022*b*. Recovery of valuable heavy minerals via gravity and magnetic separation operations from Diit Quaternary stream sediments, southern coast of the Red Sea, Egypt. International Conference on Chemical and Environmental Engineering, Journal of Physics: Conference Series; 2305 012020.

Grosz, A. E., Schruben, P. G. 1994. NURE geochemical and geophysical surveys; defining prospective terranes for United States placer exploration (No. 2097). USGPO; for sale by US Geological Survey, Information Services, Retrieved February 26, 2014.

Hegde, VS., Shalini, G., Kanchanagouri D. G. 2006. Provenance of heavy minerals with special reference to ilmenite of the Honnavar beach, central west coast of India. Current Science (00113891) 91 (5).

Jordens, A., Cheng, Y. P., Waters, K. E. 2013. A review of the beneficiation of rare earth element bearing minerals. Mineral Engineering 2013, 41, 97–114.

Iranmanesh, M., Hulliger, J. 2017. Magnetic separation: Its application in mining, waste purification, medicine. biochemistry and chemistry. Chemical Society Reviews 2017, 46, 5925–5934.

Moscoso-Pinto, F., Kim, H. S. 2021. Concentration and Recovery of Valuable Heavy Minerals from Dredged Fine Aggregate Waste. Minerals 11, 49.

Paltekar, M., Hegde, VS., Hulaji, S., Pratihari, AR., Korkoppa, MM. 2021. Geochemistry of heavy minerals from Uttara Kannada beach sediments, West Coast of India: An insight into provenance studies. Journal of Sedimentary Environments 6, 693-705.

Rahman, M. A., Zaman, M. N., Biswas, P. K., Sultana, S., Nandy, P. K. 2015. Physical separation for upgradation of valuable minerals: A study on sands of the Someswari river. Bangladesh J. Sci. Ind. Res. 50(1), 53-58, 2015

Rejith, R. G., Sundararajan, M. 2018. Combined magnetic, electrostatic, and gravity separation techniques for recovering strategic heavy minerals from beach sands. Marine Georesources & Geotechnology 35, 959–965.

Rydberg, J. 2014. Wavelength dispersive X-ray fluorescence spectroscopy as a fast, non-destructive and cost-effective analytical method for determining the geochemical composition of small loose-powder sediment samples, Journal of Paleolimnology 52:265–276.

Shalini, G., Hegde, V. S., Soumya, M., Korkoppa, M. M. 2020. Provenance and Implications of Heavy Minerals in the Beach Sands of India's Central West Coast, Journal of Coastal Research 36 (2), 353-361.

Yousef, A. F., Salem, A. A., Baraka, A. M., Aglan, O. Sh. 2009. The impact of geological setting on the groundwater occurrences in some wadis in Shalatein-Abu Ramad area, south Eastern Desert, Egypt. European Water 25 (26), 53-68.

Yu, C., Cheng, Jing-J., Jones, L., Wang, Y., Faillace, E., Loureiro, C., Chia, Y. 2023. Data collection handbook to support modeling the impacts of radioactive material in soil. 10.2172/10162250.

Zhao, W. Z., Lu, B., Yu, J. B, Zhang, B. B., Zhang, Y. 2020. Determination of sulfur in soils and stream sediments by wavelength dispersive X-ray fluorescence spectrometry. Microchemical Journal 156:104840.

Publication Rules for the "Bulletin of the Mineral Research and Exploration"

1. Purposes

- To contribute to the establishment of scientific communication issues in earth sciences both in Türkiye and internationally.
- To contribute to economic (mining, oil and gas, geothermal etc.), environmental and social (geoheritage etc.) studies in Türkiye and in the World.
- To make the earth science scientific research and applications made by the MTA on publicly known,
- To use the bulletin as an effective tool in the international publication exchange by keeping it at a high level in terms of quality, scope and format,

2. Scope-Attribute

In order for manuscripts to be published in the Bulletin of the Mineral Research and Exploration, they must have at least one of the following qualifications:

2.1. Research Articles and Reviews

2.1.1. Original Scientific Researches

- Such articles cover original scientific research and its results that contribute to the fundamental issues of earth sciences, research and evaluation of underground resources, and examine the environmental problems in terms of earth sciences,
- It covers research that apply new approaches and methods in solving problems related to earth sciences.

2.1.2. Review Articles

- They cover studies that compile previous research on subjects of earth sciences with a critical approach and put forward a new opinion on that subject.

2.2. Criticism and Response Articles

- Articles that criticize all or part of an article of the bulletin in the latest issue are published in the following first issue, if submitted within six months at the latest from the date of publication digitally.
- Before the publication, review articles are sent to the responsible author of the criticized article to make a response.
- If the criticism is not responded within foreseen time, the criticism letter is published alone, subsequent replies are not published. Replies are not allowed to be re-criticized.
- In criticizing and replying, scientific discussion and ethical rules should be followed. Criticism and response manuscripts should not exceed four pages, including figures, if available.

2.3. Brief Notes

- In "Brief Notes" section of the Bulletin of the Mineral Research and Exploration, the brief, objective and concise articles reflecting the data obtained from scientific researches and applications carried out in the area of earth sciences or new findings related to previously unknown geosciences in Türkiye are given place.
- The articles arranged in the "Brief Notes" section are published without waiting in the first or in the second issue the latest, after the date they are sent to the Chair of the Editorial Board in order to ensure rapid communication.
- Articles requested to be published in the "Brief Notes" section should not exceed four pages, including all figures and tables.

3. Submission and Acceptance for Manuscripts

- The manuscripts submitted to be published in the Bulletin of the Mineral Research and Exploration should be prepared in ENGLISH in accordance with the Publishing Rules of the Bulletin of the Mineral Research and Exploration, and submitted via electronic application at http://dergi.mta.gov.tr/index.php.
- The manuscript must not have been previously published partially or completely elsewhere (except in abstract form).
- Manuscripts submitted with the request for publication in the Bulletin of the Mineral Research and Exploration should not exceed 30 pages, including all illustrations. The articles exceeding 30 pages can be published if deemed appropriate by referees and editors.
- In the submitted manuscript, the number of figures and tables should be given in proportion to the main text in a ratio of 1/3.
- Corresponding author is asked to suggest at least three referees for the evaluation of the manuscript. (The proposed referees and the authors should not have any joint work within the last two years).

- Manuscripts that do not comply with the Publishing Rules for the Bulletin of the Mineral Research and Exploration in terms of quality and form are directly returned without being examined in terms of content.
- Manuscripts deemed appropriate in terms of format are sent to at least two expert referees for review by the Editorial Board of the Bulletin of the Mineral Research and Exploration.
- Authors should make the referee corrections and suggestions sent to them within 20 days and upload to the system.
- Comments from referees are evaluated by the Editors and associated editors. Manuscripts deemed necessary to be corrected are sent back to the authors with a request for correction. Whether the suggested corrections have been made or not is checked by the Editorial Board.
- In the revision proposals given by the editors and referees, if there are suggestions that are not accepted by the author and have not been corrected, a report explaining the reason for rejecting these suggestions by the author should be sent to the Editorial Board together with the corrected copies.
- After the last control at the printing stage, the pre-print of the manuscript is sent to the authors in pdf format and the printing control is requested.
- Articles, not accepted for publication are not returned to the authors, for the unpublished articles, a letter is written to the responsible author indicating the reason for rejection.

4. Language and Period of Publication

- The Bulletin of the Mineral Research and Exploration is published three times a year, each issue as being in English (printed and online) and in Turkish (online) languages.
- The spelling rules of the Turkish Language Association are valid for the spelling rules for the Turkish issue. However, in spelling of the words related to earth sciences, the spelling forms of technical terms are used in accordance with the decision of the Editorial Board (For example; underground, ground, earth's crust, etc.).

5. Spelling Draft

- The text of the manuscripts to be sent for the first review with the request to be published in the Bulletin of the Mineral Research and Exploration should be written in A4 (29.7 x 21 cm) size, word format, Times New Roman 10 pt., normal with 2.0 line spacing.
- At the bottom, top, left and right of the page 2.5 cm indent must be left. Formulas that require the use of special letters and symbols should be presented in computer media.
- In all subtitles, the initials of all words must be capital. First degree headings to be used in the article should be written in Times New Roman, 10 pt., bold and left aligned by giving numbers. Secondary headings should be written in Times New Roman, 10 pt., normal font and left aligned by giving numbers. Third-degree headings should be written in Times New Roman, 10 pt., italic font and left-aligned by giving numbers. Fourth-order headings should be written in Times New Roman, 10 pt., italic, aligned to the left, without giving numbers, and the text should continue after the title without a colon and a paragraph (see example article: www.dergi.mta.gov.tr).
- One blank line should be left after paragraphs in the text.
- Paragraph headings should be written 0.5 mm indentation.
- One article should respectively contain;

  -Title

  -Author's Name and Surname and * sign

  - Abstract

  - Keywords

  - Introduction

  - Main Text

  - Discussion

  - Results

  - Acknowledgements

  - Reference sections.
- Line and page numbers must be added to the article text.

5.1. Title of the Article

- The title should reflect the subject of the article as briefly, clearly and adequately as possible. Subjects that are not sufficiently covered in the article should not be included in the title. The first letter of the title

should be capitalized and the other words should be in lowercase letters (except for proper names) in Times New Roman, 10 pt. and bolded.

5.2. Author Name, Address and E-Mail Address

- The first name of the authors should be in lowercase (except the first letter), and the surname should be in capital letter and without any title.
- Only the name of the organization should be specified in the occupational address after the name and surname of the authors (position should not be specified).
- ORCID number should be taken from www.orcid.org and placed under the address.
- In articles written by more than one author, numbers should be placed on surnames of the authors, the address information should be included in the bottom line with a single line spacing. In this section, the corresponding author of the article should be indicated by using an asterisk (*) and the corresponding author's e-mail, telephone and other contact information must be provided.
- Abbreviations should not be used in writing the author's name and address. Addresses should be given in Turkish in Turkish publication (online) and in English in English publication (printed).

5.3. Abstract

- Abstract should be written at a level that can be understood without referring to the other parts of the article.
- The abstract should be organized as a brief presentation of the sections in the article, reflect the purpose of the article, be informative, and should be written in a way to emphasize new data and results on the subject.
- Short and simple sentences should be used in writing the abstract.
- In the abstract, there should not be any reference to other parts and illustrations of the article or to other articles.
- Information not mentioned in the main text should not be included in the abstract.
- The abstract should not exceed approximately 200 words and should be written as a single paragraph.
- Abstract should be written in Times New Roman, 10 pt., normal text with single line spacing.
- "ABSTRACT" should not be placed for the articles to be included in "Brief Notes" section.
- The English abstract should be given under the heading "ABSTRACT".

5.4. Keywords

In order to facilitate searches, five keywords that will indicate the general content of the article should be selected and specified in this section. Words used in the title should not be repeated.

5.5. Introduction

- In this section, the necessary information for preparatory and facilitative to understand the article such as the purpose of the study, its location, methods of study and previous reviews on the subject should be given.
- If an unusual way is followed in naming, classification and abbreviations within the text of the manuscript, its reason should be stated in this section.
- Each of the topics to be included in this section can create a separate paragraph or a subtitle can be given for each of them when necessary (e.g. method, material, terminology and etc.).
- This section can again be used when reminder information is needed to facilitate the understanding of the article (e.g. statistical information, formulas, experimental or application methods and etc.).

5.6. Main Body of Article

- Constitutes the main body of the article.
- In this section, the data, findings and opinions that are intended to be transferred to the reader on the subject are mentioned.
- The data used in other parts of the article such as "Abstract", "Discussions", "Results" originate from this part.
- Care should be taken not to deviate from the purpose stressed in the "Introduction" section of the article when dealing the topics. Information that does not contribute to the achievement of the purpose of the article or that is not used to reach the conclusion should not be included.
- All data used in this section and all opinions put forward should be proven by the findings obtained from the studies or based on a source by reference.

• The way and method to be followed in handling the topics vary according to the characteristics of the topics covered.

• Subject headings in necessary numbers with different stages should be used in this section.

5.7. Discussions

• The data and findings objectively conveyed in the "Main Text" section of the article should be discussed by the author in this section. Discussions should be separate from the "Results" section.

5.8. Results

• New data and findings obtained from the review that constitutes the subject of the article should be stated concisely and concretely in this section.

• Subjects that are not adequately addressed and / or covered in the main text should not be included in this section.

• The results can be given as items in order to emphasize the research results and make the expression understandable.

5.9. Acknowledgements

• In this section, important contributions in the realization of the study, which is the subject of the article, are indicated. An attitude that will distract this section from its main purpose should not be taken in the Acknowledgements.

Contribution should be stated as short and concise as possible to the persons and/or organizations that provided assistance (reading, writing, language assistance, etc.) during the research, and should not take an attitude that would distract this section from its main purpose.

5.10. References

• In this section, only the documents mentioned in the article should be included in complete.

• Abbreviations should be avoided in naming the publications and journals.

• The mentioned documents should be written in Times New Roman and 9 pt.

• The first line of the references should be written as justified to the left margin of the page, and the other lines should be written by giving a hanging indent value of 1.25.

• The references should be listed in alphabetical order, taking into account the surnames of the authors.

• If one author has more than one work in the same year, lowercase alphabet letters should be used right after the year of publication and the letters should be italic (e.g. Saklar, 2011*a*, *b*).

• If more than one document of the same author is cited, first his / her single-name publications in chronological order, then double-names according to the chronological order, and then multi-names according to chronological order should be given.

For example:

Corradini, C. 2007. The conodont genus Pseudooneotodus Drygant from the Silurian and Lower Devonian of Sardinia and the Carnic Alps (Italy). Bollettino-Societa Paleontologica Italiana 46 (2/3), 139-148.

Corradini, C., Serpagli E. 1999. A Silurian conodont biozonation from late Llandovery to end Pridoli in Sardinia (Italy), In Serpagli (Ed.), Studies on conodonts: Proceedings of the 7th European Conodont Symposium. Bollettino della Società Paleontologica Italiana 37 (2-3) (1998), 255-273.

Corradini, C., Corriga, M. G. 2010. Silurian and lowermost Devonian conodonts from the Passo Volaia area (Carnic Alps, Italy). Bollettino della Società Paleontologica Italiana 49 (3), 237-253.

Corradini, C., Corriga, M. G. A. 2012. Pridoli – Lochkovian conodont zonation in Sardinia and the Carnic Alps: implications for a global zonation scheme. Bulletin of Geosciences 87 (4), 635-650.

Corradini, C., Leone, F., Loi, A., Serpagli, E. 2001.Conodont Stratigraphy of A Highly Tectonised Silurian-Devonian Section in The San Basilio Area (Se Sardinia, Italy). Bollettino Della Societa Paleontologica Italiana 40 (3), 315-323, 1 Pl.

Corradini, C., Pondrelli, M., Serventi, P., Simonetto, L. 2003. The Silurian cephalopod limestone in the Monte Cocco area (Carnic Alps, Italy): conodont biostratigraphy. Revista Española de Micropaleontologia 35 (3), 285-294.

Corradini, C., Corriga, M. G., Männik, P., Schönlaub, H. P. 2015. Revised conodont stratigraphy of the Cellon section (Silurian, Carnic Alps). Lethaia 48 (1), 56-71.

- If documents of different authors with the same surname are mentioned, they should be written in alphabetical order, considering their first names.
- If documents of different author(s) with the same surname are mentioned in the same year, they should be cited as given below. Same publication rule should be applied for the single author.

For example:

"Usta, M., Yetiş, C., Nazik, A. 2018. Anamur (Mersin) dolayının stratigrafisi ve Kambriyen yaşlı kuvarsitler ile dolomitlerin endüstriyel hammadde potansiyeli. Çukurova Üniversitesi Fen ve Mühendislik Bilimleri Dergisi 35, 6, 11-22, Adana"

should be cited as (Usta, M. et. al., 2018)

"Usta, D., Ateş, Ş., Çoban, M., Deveci, Ö, Sağlam, F.M. 2014. Adıyaman-Sincik-Hilvan arasındaki bölgenin stratigrafisi ve kaya türü özellikleri. 67. Türkiye Jeoloji Kurultayı Bildiri Özleri, Ankara, 98-99"

should be cited as (Usta, D. et. al., 2018)

"Usta, M. 2018. Anamur (Mersin) dolayının stratigrafisi ve Kambriyen yaşlı kuvarsitler ile dolomitlerin endüstriyel hammadde potansiyeli. Çukurova Üniversitesi Fen ve Mühendislik Bilimleri Dergisi 35, 6, 11-22, Adana"

should be cited as (Usta, M., 2018)

"Usta, D. 2014. Adıyaman-Sincik-Hilvan arasındaki bölgenin stratigrafisi ve kaya türü özellikleri. 67. Türkiye Jeoloji Kurultayı Bildiri Özleri, Ankara, 98-99"

should be cited as (Usta, D., 2018)

- If the document is in a periodical publication (if it is an article), information about the document is given in the following order: Authors ' surname, first letters of the authors' first names. Year of publication. The name of the article. The name of the publication in which the article was published, volume number and / or issue number with the first letters in capital, the numbers of the first and last page of the document. Punctuation marks like comma and etc. after journal names should not be used.
- In the examples below, the information about the mentioned documents is organized according to different document types, taking into account the punctuation marks.

For example:

Gürsoy, M. 2017. Munzur Dağları Alt Miyosen çökelleri mollusk topluluğu ve paleoekolojisi (Doğu Anadolu, Türkiye). Maden Tetkik ve Arama Dergisi 155, 75-99.

Pamir, H. N. 1953. Türkiye'de kurulacak bir Hidrojeoloji Enstitüsü hakkında rapor. Türkiye Jeoloji Bülteni 4 (1), 63-68.

Robertson, A. H. F. 2002. Overview of the genesis and emplacement of Mesozoic ophiolites in the Eastern Mediterranean Tethyan region. Lithos 65, 1-67.

- If the document is a book: authors' surnames, authors' first names. Year of publication. Title of the book with capital letters. The name of the publishing organization or the name of the publication in which the document was published, the volume and / or issue number, and the total number of pages of the book should be specified, respectively.

For example:

Einsele, G. 1992. Sedimentary Basins. Springer Verlag, 628.

Ketin, İ., Canıtez, N. 1956. Yapısal Jeoloji. İTÜ, 308.

Meriç, E. 1983. Foraminiferler. Maden Tetkik ve Arama Genel Müdürlüğü Eğitim Serisi, 26, 280.

- If the document is published in a book containing the articles of various authors, the usual order for the document included in a periodical publication is followed until the end of the document title. Then the editors' surnames and initials and the abbreviation of the editor word "Ed." is written in parentheses. Then, the title of the book in which the document is located is written with the first letters in capital letters. Name of publishing organization. The place of publication, the volume number of the publication in which the document was published, and the numbers of the first and last pages of the document should be written.

For example:

Anderson, L. 1967. Latest information from seismic observations. Gaskell, T. F. (Ed.). The Earth's Mantle. Academic Press. London, 335-420.

Göncüoğlu, M. C., Turhan, N., Şentürk, K., Özcan, A., Uysal, S., Yalınız, K. 2000. A geotraverse across northwestern Türkiye. Bozkurt, E., Winchester, J. A., Piper, J. D. A. (Ed.). Tectonics and Magmatism in Türkiye and the Surrounding Area. Geological Society of London. Special Publication, 173, 139-162.

- If it is desired to specify the name of a book in which the writings of various authors are collected as a document; following the surnames and names of the book's editors, in parentheses the "Ed." statement is written. Year of publication. Title of the book with capital letters. The name of the publishing organization or the name of the publication in which the document was published, the volume and / or issue number and the total number of pages of the book should be specified.

For example:

Gaskel, T. F. (Ed.). 1967. The Earth's Mantle. Academic Press, 520.

- If the document is "published abstract", information about the document is given in the following order: Authors' surnames, authors' first names. Year of publication. Name of the document (paper). The name, date and place of the meeting where the paper is published, and the first and last page numbers in the book containing the abstract should be written.

For example:

Öztunalı, Ö., Yeniyol, M. 1980. Yunak (Konya) yöresi kayaçlarının petrojenezi. Türkiye Jeoloji Kurumu 34. Bilim Teknik Kurultayı, Ankara, 36.

Yılmaz, Y. 2001. Some striking features of the Anatolian geology. 4. International Turkish Geology Symposium, 24-28 Eylül 2001, Adana, 13-14.

- If the mentioned document has not been published like report, lecture notes and etc., the word "unpublished" should be written at the end of the information about the document in parentheses after the information about the document is given in the usual order for the document in a periodical publication.

For example:

Akyol, E. 1978. Palinoloji ders notları. EÜ Fen Fakültesi Yerbilimleri Bölümü, 45, İzmir (unpublished).

Özdemir, C., Biçen, C. 1971. Erzincan ili, İliç ilçesi ve civarı demir etütleri raporu. Maden Tetkik Arama Genel Müdürlüğü, Rapor No: 4461, 21, Ankara (unpublished).

- For unpublished courses, seminars and similar notes, the course organizer after document name. The place of the meeting. Title of the book and relevant page numbers should be given.

For example:

Walker, G.R., Mutti, E. 1973. Turbidity facies and facies associations. Society for Sedimentary Geology Pacific Section Short Course. Annaheim. Turbitides and Deep Water Sedimentation, 119-157.

- If the document is a thesis; author's surname, initial of the author's first name. Year of publication. Name of the thesis. The type of the thesis, the university where it was given, the total number of pages, its province and the word "unpublished" are written in parentheses.

For example:

Akıllı, H. 2019. Polatlı-Haymana (Ankara) civarı sıcak sularının izotop jeokimyası (δ18O, δD, 3H, δ13C, δ34S, 87Sr/86Sr) ve ana iz element bileşimleri ile incelenmesi. PhD Thesis, Ankara University, 255, Ankara (unpublished).

Argun Aktan, Ö. 2019. Marmara Denizi Batı Kıta Sahanlığı Yüzeysel Çökellerinde Jeojenik ve Antropojenik Ağır Metal Zenginleşmesine Yönelik Araştırmalar (Şarköy Kanyonu, KB Türkiye). MSc Thesis, Ankara University, 179, Ankara.

- Anonymous works should be arranged according to the publishing institution.

For example:

MTA. 1964. 1/500.000 ölçekli Türkiye Jeoloji Haritası, İstanbul Paftası. Maden Tetkik ve Arama Genel Müdürlüğü, Ankara.

• For the documents that are in print, no date is put after the name of the author, the name of the article and the source to be published should be specified and the word “in print” and / or “in review” should be written at the end (in parentheses).

For example:

Ishihara, S. The granitoid and mineralization. Economic Geology 75th Anniversary (in press).

• Information downloaded from the Internet should be given in the form of the name of the institution, its web address, and the date on which the web address was accessed. Turkish references should be given directly in Turkish and should be written in Turkish characters.

For example:

ERD (Earthquake Research Department of Türkiye). http://www.afad.gov.tr. 3 March 2013.

• While citing the source, the original language should be adhered to, and the title of the article should not be translated.

6. Illustrations

• All of the drawings, photographs, plates and tables used in the article are referred to as “illustrating”.

• Illustrations should be used when their use is unavoidable or when they make the subject easier to understand.

• In the selection and arrangement of the format and size of the illustrations, an attitude should be made to prevent loss of space as much as possible considering the page length and layout of the bulletin.

• The number of illustrations used should be proportional to the size of the text.

• All illustrations should be submitted in separate files regardless of the text.

• Abbreviations should not be used in illustration explanations in the text and should be numbered in the order of mention within the text.

• Photographs and plates must be submitted as a computer file in which all details can be seen for the examination of the article, with EPS, TIFF or JPEG extension and at least 300 dpi resolution.

6.1. Figures

• Drawings and photographs other than the plate to be included in the article are evaluated together as “Figure” and numbered in the order of mention in the text.

• The figures should be prepared in computer considering the dimensions of a single column width as 7.4 cm or double column width as 15.8 cm. The figure area with its caption should not exceed 15.8x21 cm.

• While preparing the figures, unnecessary details should not be included and care should be taken not to use more space than necessary for the transfer of information.

• In figure descriptions, a space should be left after the word “Figure” is written, and the number is given in the usual sequence number, followed by a hyphen (-) and a space again, and a description of the relevant figure should be written. If the figure legend exceeds the bottom lines, the following lines should to be written after the “Figure 1-” statement alignment. Figure descriptions should be created as follows, without exceeding the edges of the figure and justified on both sides.

For example:

Figure 1- The district of Sandıklı (Afyon); a) geological map of the southwest, b) the general vertical section of the study area (Seymen, 1981), c) Türkiye’s most important neotectonic structures (modified from Koçyiğit, 1994).

• Drawings should be drawn in computer properly, clean and with care.

• The use of thin lines that may disappear when minimized in figures should be avoided.

• Symbols or letters used in all drawings should not be less than 2 mm (7 pt.) in Times New Roman.

• All standardized symbols used in the drawings should preferably be explained in the drawing, if they are too long then they should be explained in the figure below.

• Bar scale should be used in all drawings and the north direction should be indicated on all maps.

• The name of the author, description of the figure, figure number should not be included in the drawing.

- Photographs should reflect the aims of the subject and should be in adequate numbers.
- Figures should be framed.

6.2. Plates

- Plates should be used in cases where multiple photographs are required to be printed together on a special paper.
- Plate dimensions must be equal to the size of the bulletin's usable area of the page.
- Figure numbers should be written under each of the figures on the plate and bar scale should be used.
- Original plates must be attached to the final copy to be submitted in the case of acceptance of the manuscript.
- Figures and plates should be numbered among themselves and independently. Figures should be numbered with Latin numerals and plates with Roman numerals (eg Figure 1, Plate I).
- There should be no explanation text on the figures inside the plate.

6.3. Tables

- All tables should be arranged in word format and should be prepared in Times New Roman.
- Tables should not exceed the size of 15x8 cm together with the table caption.
- Table explanations should be created without exceeding the edges of the figure and justified as in the example below.

For example:

Table 1- Hydrogeochemical analysis results of geothermal waters in the study area.

7. Nomenclature and Abbreviation

- Abbreviations must be in the accepted international or national form. Unusual nomenclature and abbreviations that are not standardized in the article should be avoided. In cases where it is deemed necessary to use such nomenclature and abbreviations, the way and method followed should be explained.
- There should not be a dot between the words initials used in standard abbreviations (such as MTA, DSİ).
- Abbreviations of geography aspects should be made in English (N, S, E, W, NE and etc.).

The word group to be abbreviated should be written clearly where it is mentioned first time and the abbreviation should be given in parentheses, then only the abbreviated form should be written throughout the article.

- Systems with international validity (m, inch, etc.) should be used as the unit of measure. Decimals should be separated with commas in Turkish articles and with a period in English articles.
- The names of figures, plates and tables in the article should not be abbreviated. For example, "As seen in the generalized stratigraphic section of the region (Figure 1) …….".

7.1. Chronostatigraphic and Geochronologic Nomenclature

- "International Chronostratigraphic Chart" (https://stratigraphy.org/chart), which is updated annually by the International Stratigraphic Committee, should be taken into consideration in chronostratigraphic and geochronological nomenclature.
- Position within a chronostratigraphic unit can be expressed in adjectives indicating the position, for example: lower, middle, upper and etc. When using these adjectives, it should be decided whether the lower, middle and upper distinction is formal / informal in the International Chronostratigraphic Chart.

For example:

lower Miocene, Upper Holocene and etc.

- When stating the time where a geochronological unit is, temporal adjectives such as; early, middle, late and etc. are used. When using these adjectives, the International Chronostratigraphic Chart should be taken into consideration to decide whether the adjectives begin with capital or lowercase letters.

For example:

early Miocene, Late Holocene etc.

7.2. Paleontological Nomenclature and Spelling of Fossil Names

- Original names of fossils should be used.

For example:

Nummulites with limestone

• Fossil genus and species names are written in italics, cf., aff. and gr. etc. expressions are written as normal (perpendicular). When writing fossil names for the first time, the surnames of the people who identify them and the year in which they were first defined should be written. In later uses, the surnames and the year in which they are defined may not be written. The surnames and dates of identifiers coming at the end of the fossil names are not references, they should not be included in the mentioned documents.

For example:

Alveolina aragonensis Hottinger, 1960 not a reference.

Alveolina cf. *aragonensis* Hottinger, 1960 not a reference.

Alveolina aff. *aragonensis* Hottinger, 1960 not a reference.

Alveolina gr. *aragonensis* Hottinger, 1960 not a reference.

• After the first use of the same genus in the text is written clearly, it can be abbreviated as in the example so that it will not be confused with another genus in later use.

For example:

Alveolina aragonensis, A. polathensis, A. ellipsoidalis etc.

• If the date is in parentheses after the person describing it after the name of the fossil in the text, this is a reference and should be included in the mentioned documents.

For example:

Alveolina aragonensis Hottinger (1960) is a reference.

• The following rules should be taken into account when writing the systematic paleontologic section.

a. First of all, genus, species and subspecies to be identified should be written in hierarchical order like the order, upper family, family type species and so on. Later, the species to be described should be written together with the surnames and date of the people who defined the subspecies name. If there is a photograph of the described fossil, the plate or figure with the photograph should be added under the fossil name. The names of the authors listed here are not references, so they are not included in the reference.

For example:

Order: Foraminiferida Eichwald, 1830

Superfamily: Alveolinacea Ehrenberg, 1839

Family: Alveolinidae Ehrenberg, 1839

Type Genus: *Borelis* de Montfort, 1808

Type Species: *Borelis melenoides* de Montfort, 1808
= *Nautilus melo* Fichtel and Moll, 1798

Borelis vonderschmitti (Schweighauser, 1951)

(Plate II, Figure 3-5 or Figure 3A-H).

b. Similar or synonyms (synonym) list should be left-aligned in chronological order. The page and figure number of the synonymous fossil in the relevant study should be included in the synonymous list. Authors in the synonymous list are references and must be included in the references.

For example:

1951 *Neoalveolina vonderschmitti* **Schweighauser**, page 468, Figures 1-4.

1974 *Borelis vonderschmitti* (Schweighauser), **Hottinger**, page 67, plate 98, Figures 1-7.

c. After the synonymous list is given, the definition, explanations (similarities and differences), dimensions, material, stratigraphic distribution (according to the characteristics of the fossil) should be written.

d. If the fossil is defined for the first time (new species) in the systematic paleontology section, the origin of the name, holotype, type locality, material, description, explanation (similarity and differences), age and geographical distribution, dimensions (according to the features that define the fossil) should be written. Photographs of the fossil identified for the first time by the authors must necessarily be placed in plates or figures.

e. Bar scale indicating the size of fossils must be used definitely in plates / figures.

8. References

• In the references to be made in the Main Text, only the surnames of the authors and the publication year of the mentioned article should be specified. Referencing should be arranged according to one of the following examples:

• Referring to a publication with a single author (in chronological order):

-Altınlı (1972, 1976) defined the Bilecik sandstone in detail.

It is known that the fold axes of the Devonian and Carboniferous units around İstanbul are N-S trending (Ketin, 1953, 1956; Altınlı, 1999).

• Referring to a publication with two authors:

- The upper parts of the unit include Ilerdian fossils (Sirel and Gündüz, 1976; Keskin and Turhan, 1987, 1989).

• Referring to a publication with more than two authors:

- According to Caner et al. (1975), the Alıcı formation reflects the conditions of fluvial environment.

- Unit disappears by wedging towards E (Tokay et al., 1984).

• Referring to a reference in another publication:

It is known that Lebling mentioned about the existence of Liassic around Çakraz (Lebling, 1932; Charles, 1933).

• When referring to the works of the authors with the same surname in the same year, referring the authors' first names by writing their initials:

- Many studies have been done in the field of structural geology in the study area (Gutnic et al., 1979; Yılmaz A., 1983; Yılmaz, İ., 1983; Poisson et al., 1984 etc.).

9. Prints Sent to Authors

Two copies of the relevant issue published in the Bulletin of the Mineral Research and Exploration are sent to the authors.

10. Terms of Publication and Copyrights

• Some or all of the articles to be published in the Bulletin of the Mineral Research and Exploration should not have been published before.

• Authors who submit a publication to the Bulletin of the Mineral Research and Exploration are deemed to have accepted the bulletin's publication rules in advance.

• The copyright of the manuscripts accepted for publication and converted into publications belongs to the General Directorate of Mineral Research and Exploration (MTA).

The authors of the study sign the relevant forms within the scope of the provisions specified in the Regulation of the Editorial Board regarding the transfer of copyright and submit them to the Editorial Board. After the publication of the article, MTA may pay royalty fees to the authors of the article for their declarations within the scope of the "Regulation on the Editorial and Processing Fees to be paid by the Public Organizations and Institutions".

NOTE: Information and forms about Bulletin of the Mineral Research and Exploration can be accessed from the website: http://dergi.mta.gov.tr/index.php.